An acoustic investigation of microbubble response to medical imaging ultrasound pulses

David H. Thomas

A thesis submitted for the degree of Doctor of Philosophy.
The University of Edinburgh.
2009

To my parents.

Abstract

Ultrasound contrast agents have the ability to provide locally increased echogenicity, improving the sensitivity and specificity of images. Due to the unique interaction of microbubbles with the imaging ultrasound field, contrast ultrasonography offers both improved diagnostic techniques, and the potential therapeutic uses of gene and drug delivery through the use of targeted agents. By enhancing the contrast at the tissue-blood interface, an improved image of the structure of organs can be achieved, which is useful in many areas of medical ultrasound imaging. Monitoring the flow of contrast agent in the blood stream also offers information on the degree of blood perfusion into an organ or microvasculature.

Present knowledge of the interaction of microbubbles with ultrasound is far from complete. The full potential of contrast agents in improving diagnostic and therapeutic techniques has therefore not yet been achieved. The nonlinear and dynamic properties of microbubble response offer potentially large improvements in contrast to tissue ratio, through intelligent pulse sequence design and/or improved signal processing. Due to various drawbacks of populations studies, only by studying the response from single microbubbles can the interaction be fully understood. The variations of microbubble size and shell parameters within a typical sample of contrast agent dictate that a large number of single scatterer data are necessary to obtain information on the variability of microbubble response, which is not possible with current optical systems.

This thesis aims to be a contribution to the understanding of contrast behaviour in response to medical imaging ultrasound pulses. A fully characterized microacoustic system, employing a wide-band piezoelectric transducer from a commercial ultrasound imaging system, is introduced, which enables the measurement of single scattering events. Single microbubble signals from two commercially available contrast agents, Definity® and biSphere™, have been measured experimentally in response to a range of clinically relevant imaging parameters. The data has been analyzed, together with the results from appropriate theoretical models, in order to gain physical insight into the evolution and dynamics of microbubble signals.

A theoretical model for the lipid shelled agent Definity has been developed, and the predicted response from a real sample of single microbubbles investigated. Various characteristics of resonant scatter have been identified, and used to distinguish resonant scatter in experimental acoustic single bubble data for the first time. A clear distinction between the populations of resonant and off-resonant scatter has been observed for a range of incident frequencies and acoustic pressures. Results from consecutive imaging pulses have been used to gain understanding of how initial size, shell material and encapsulated gas may effect the lifetime of a microbubble signal. The response to a basic pulse sequence is also investigated, and an alternative processing method which takes advantage of observed behaviour is presented.

Improved understanding of the contrast-ultrasound interaction will provide the basis for improved signal processing tools for contrast enhanced imaging, with potential benefits to both diagnostic techniques and microbubble manufacture.

Declaration of originality

I hereby declare that the research recorded in this thesis, and the thesis itself, was composed and originated entirely by myself, except where otherwise stated, in the Department of Medical Physics and Medical Engineering, at The University of Edinburgh.

David H. Thomas

Acknowledgments

I wish to acknowledge support from the Engineering and Physical Sciences Research Council (UK) in the form of a PhD scholarship related to the research of the Biologically Inspired Acoustics Systems (BIAS) group in the Basic Technology Programme.

I would like to gratefully acknowledge the enthusiastic supervision of Dr. Vassilis Sboros during this work. I thank Prof. Norman McDicken and Mr. Tom Anderson for their advice, support and many technical discussions. Padraig Looney and Mairead Butler have both given valuable help to the theoretical and experimental work presented in this thesis.

The theoretical model used in Chapter 3 was originally developed by Nikos Pelekasis and Kostas Tsiglifis, and was realised in MATLAB for comparison with experimental data by Padraig Looney and Robin Steel.

Thanks also to the Postgraduates of the Medical Physics group for the help and welcome distractions they've offered, and to the departmental secretary Irene Craig, who is truly irreplaceable. I am grateful to all my friends, in Edinburgh and beyond, for making it all worthwhile.

Finally, thanks to my parents for their understanding and encouragement when it was most needed.

Contents

List of figures

List of tables

Chapter 1
Introduction to ultrasound contrast agents

1.1 Introduction

Contrast enhancement is used in a broad range of medical imaging techniques, including computed tomography (CT) and magnetic resonance imaging (MRI), to improve the sensitivity and specificity of images. Due to the unique interaction of ultrasound contrast with the imaging ultrasound field, contrast ultrasonography offers both improved diagnostic techniques, and the potential therapeutic uses of gene and drug delivery through the use of targeted agents[2].

The diagnostic advantages of contrast enhanced ultrasound imaging lie in the ability of the agent to provide locally increased echogenicity. By enhancing the contrast at the tissue-blood interface, an improved image of the structure of organs can be achieved, which is especially useful in echocardiography. Monitoring the flow of contrast agent in the blood stream also offers information on the degree of blood perfusion into an organ or microvasculature.

1.2 Historical development

Contrast enhancement of ultrasound images was originally observed, inadvertently, by cardiologist Dr Charles Joiner in the mid-1960s. During a routine injection of saline into the aortic root, he performed an echo cardiography scan and noticed bright echoes in the M-mode image. This effect was published by Gramiak and Shah in 1968, who observed that agitated green dye produced similar signals[3], allowing the chambers of the heart to be imaged. Enhancement was seen with different solutions, and the echogenicity of small air bubbles in the solutions were recognized to be the cause. However, the free air bubbles created by such agitation are not stable, and will quickly dissolve back into the solution (a $2\mu\mathrm{m}$ air bubble requires only 8ms to fully dissolve[4]). When used in vivo they are not able to pass through the lungs. Although this makes them useful in the diagnosis of heart defects such as cardiac shunts[5] (Figure 1.1,

page 23), they have limited value as intravenous agents. More than two decades passed before agents were developed that had the ability to remain intact after injection long enough to survive pulmonary circulation. To ensure that bubbles survive to reach the left ventricle of the heart, and thus provide useful image enhancement, methods were developed that protected the bubble so that they would not dissolve in the blood or be eliminated by their passage through the lungs. By introducing a shell to stabilize the bubbles the diffusion of gas into the solution can be reduced, and the local pressure a bubble can sustain before dissolving can be increased. Substituting air (as the encapsulated gas) with a less soluble high density gas also increases the bubble's survival within the blood stream to several minutes, and potentially several passes through the circulation system[2,4].

The first commercially available agent that survived pulmonary passage to provide useful echo enhancement of the heart was Albunex (Molecular Biosystems, San Diego, US), which consists of air bubbles, with an average size of $4\mu m$, surrounded by an albumin shell[6]. Acoustic in vitro experiments with the agent showed that the bubbles were not behaving as simple Rayleigh scatterers but as harmonic oscillators, resonating at the frequencies used to image them[7]. These first acoustic experiments highlighted the potential for improved imaging techniques, and the need for greater understanding of the properties of encapsulated microbubbles in the presence of ultrasound. Early in vitro work with clinical concentrations showed that the oscillations of individual microbubbles were nonlinear, and imaging the second harmonic component of scatter offers potential improvements in contrast to tissue ratio[8].

Since the development of these early agents, several kinds of gases and shell materials have been found to be suitable for use in contrast agents. Table 1.1, (page 24) summarizes currently available contrast agents, showing their constituent materials and average sizes.

1.3 Clinical applications

Imaging blood flow is of diagnostic value for a wide range of diseases including cancer and cardiovascular disease. The scattered signal from blood in the circulation arises mainly from red blood cells ($6 - 8\mu\mathrm{m}$ in size)[9], and is correspondingly very weak compared to that from surrounding tissues. The use of microbubbles as ultrasound contrast agents offers significant improvement in signal amplitude.

Clinical applications of microbubbles as contrast agents have been reviewed extensively[10,11],

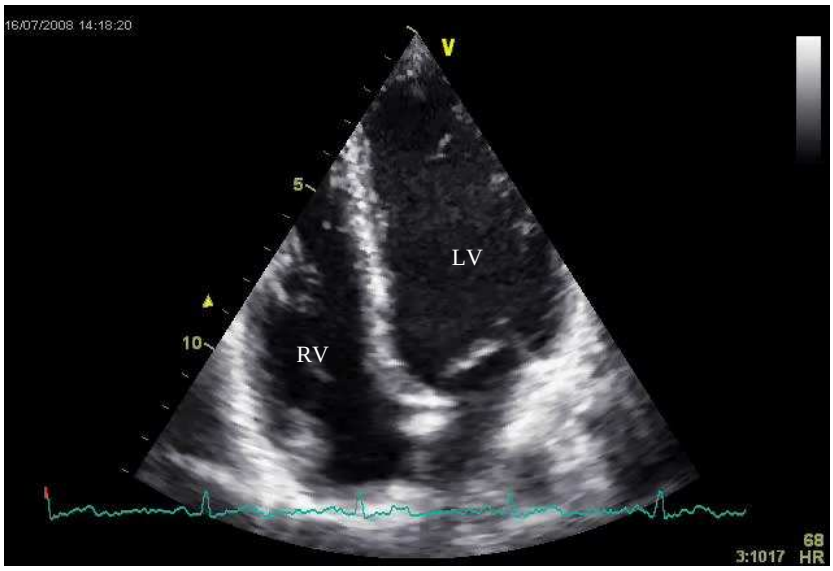

(a) Pre-contrast injection

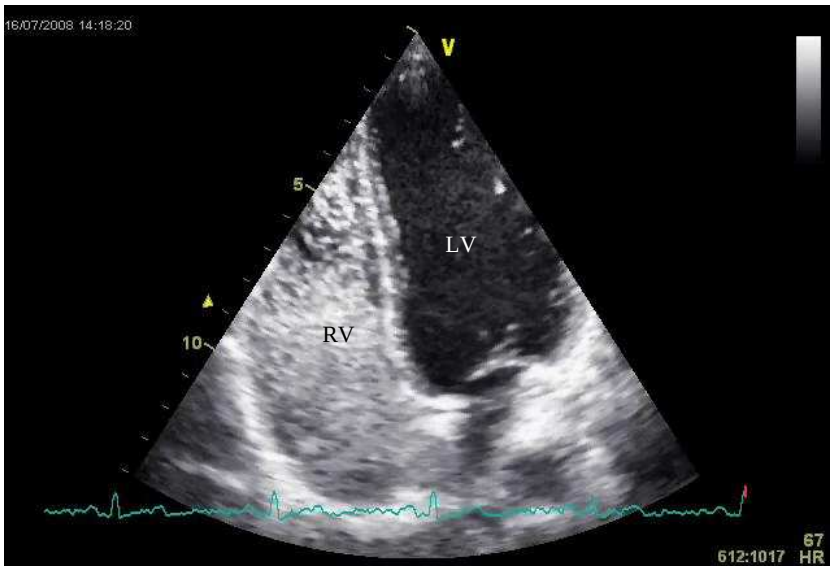

(b) Post-contrast injection

Figure 1.1: *An echocardiogram showing the heart in an apical view (left side of the heart is on the right of the image). Agitated saline injected into the blood stream can be imaged with ultrasound, when passing through the right ventricle (RV). (a) shows the heart before contrast injection. Post-contrast injection (b), blood in the RV contains the agitated saline, which produces bright echoes. As the unshelled air bubbles do not survive passage through the lungs, no contrast is observed in the left ventricle (LV). This is diagnostically useful, as it confirms correct formation of the atrial septum, but no left-sided cardiac morphology is available, due to the fragility of unshelled-microbubbles. Images courtesy of Audrey White, NHS, Department of Cardiology, Western General Hospital, Edinburgh.*

Name	Shell	Gas	Mean size (μm)
Albunex	Albumin	Air	4.3
Quantison	Albumin	Air	N/A
Optison	Albumin	Octafluoropropane	4.5
MP1950	Lipid	Decafluorobutane	2
PESDA	Albumin	Decafluorobutane	4.7
Definity	**Lipid/Surfactant**	**Octafluoropropane**	**1.1-3.3**
Imagent	Lipid/Surfactant	Nitrogen	6(median)
SonoVue	Lipid	Sulfur hexafluoride	2(median)
BR14	Lipid	Perfluorobutane	2.6
Levovist	Lipid/Galactose	Air	2-4
biSphere	**Polylactide/Al**	**Nitrogen**	**3**
Acusphere	Polylactide	Perfluoropropane	N/A
Sonazoid	Lipid/Surfactant	Perfluorobutane	2.2
ST68-PFC	Lipid/Surfactant	Decafluorobutane	1.8
Sonavist	Cyanoacrylate	Air	N/A

Table 1.1: *Commercial contrast agents, showing their constituent shell materials and encapsulated gases. The two agents investigated in Chapter 3 onwards are highlighted in bold*[1].

and the main uses (namely heart, liver and kidney imaging) are outlined below.

1.3.1 Heart imaging

Several studies support contrast enhanced ultrasound as a 'bedside' heart imaging tool due to its high resolution, mobility and ability to accurately assess the outcome of treatment through accurate measurement of heart tissue variability[12–16]. Contrast enhanced ultrasound imaging is routinely used in patients which are difficult to image with conventional ultrasound. Significantly improved sensitivity in the measurement of left ventricular cavity dimensions and wall motion assessment can be achieved[11], allowing greater confidence in diagnoses based on such measurements. Myocardial contrast echocardiography (MCE) is used to provide capillary flow measurement, as the majority of the blood volume within the myodcardium is microvasular, which can provide direct information on the heart pathology and function[11]. Diagnoses related to vascular defects can be attained through analysis of relative differences in image contrast within the myocardium, and a qualitative assessment of location and spatial extent of a such defects can be achieved[17]. Observation of normal wall motion and perfusion in MCE can accurately exclude myocardial ischemia, making this a very useful diagnostic tool[11]. More recent studies show that MCE with addition of dobutamine injection(a drug used to induced 'stress' in the heart muscles) can diagnose coronary artery disease even in the absence of wall motion

abnormalities[18]. MCE can also be used to assess the success of various therapeutic techniques, for example patients with acute myocardial infarction who have undergone primary coronary stenting (PCS). The final infarct size, and thus risk of coronary occlusion following therapy can be assessed and compared with original vascular defects[19]. Collateral blood flow within an ischemic area of the heart can be measured using contrast enhanced ultrasound, and can be related to the potential for tissue to recover. This can therefore potentially be used for determining the treatment procedure in such cases, and thus avoiding otherwise potentially unnecessary surgical procedures[20].

At the current time myocardial contrast echocardiodraphy has a definite clinical role to play in a diagnostics at hospitals worldwide (including here at Edinburgh), and although uptake is currently limited in some countries by licensing issues and by cost, it can provide a cost-effective alternative to more expensive imaging techniques such as CT and MRI.

1.3.2 Liver imaging

Knowledge of the vascularity in liver can be of great value in identifying focal liver lesions. Conventional ultrasound imaging of liver lesions is difficult as many of the lesions have similar levels of echogenicity to the surrounding liver tissue[21]. Doppler techniques are limited in the sensitivity and specificity of detecting blood flow within small tissues and cannot detect blood flow in microvessels. Thus, contrast enhancement offers a far superior imaging modality in the liver, with temporal and spatial resolutions better than those available with other clinical imaging systems[21].

As well as identification of lesions, the intensity and temporal characteristics of contrast enhancement can be used to help in the characterization of malignant lesions[21–24], as the tissue type directly effects the vascular volume within the region. Contrast ultrasound is used as an initial screening tool for liver metastases with a sensitivity between $83 - 92\%$. It can often detect metastases not seen in CT and generally offers a comparable confidence to that of MRI[22,23]. Tumour viability can be measured by pre- and post-treatment contrast imaging of heptocellular carcinoma, in order to asses vascularity[25,26].

Liver imaging is at present the most clinically advanced area of CEUS. Lesion characterisation is possible with accuracy similar to that obtainable with CT or MR[27–29].

1.3.3 Other uses

While the above applications are the main clinical uses for contrast enhanced ultrasound, a number of diagnostic areas have the potential to be improved by the use of contrast enhancement. Infarctions caused by blockage of the blood supply to tissues within the spleen are easily detectable this way, and is especially useful in trauma medicine[30]. In the kidney contrast enhanced ultrasound has been shown to be highly sensitive in a variety of diagnostic techniques; for example renal screening for artery stenosis[31]. The assessment of blood flow may prove useful in patients with diabetes, who are especially vulnerable to microvascular disease[32]. There is also potential for atherosclerotic plaques to be imaged with contrast enhanced ultrasound in the coronary and carotid arteries[33].

1.4 Microbubble physics

Increased contrast from in vivo microbubbles is due to the high scattering cross section of the contrast agent material, together with bubble resonance phenomena, providing increased scatter in comparison to the surrounding tissue. If the radius of a single scatterer R is much less than the distance r to the source of the ultrasound ($R << r$), the received signal intensity I_s is directly proportional to the incident pulse intensity I_i and the scattering cross section (σ) of the scatterer, as defined by the Born approximation[34]:

$$I_s = \frac{I_i \sigma}{4\pi R^2}. \tag{1.1}$$

1.4.1 Scattering cross section

The simplest model of sound scattering from small particles was formulated by Lord Rayleigh, in his book "The Theory of Sound"[35]. According to Rayleigh's model (assuming the size of the single scatterer is much less than the wavelength λ of the incident pulse), the cross section of a linear scatterer is given by[34]:

$$\sigma = \left[\frac{4}{9}\pi R_0^2 (kR_0)^4\right]\left[\left(\frac{\kappa_s - \kappa}{\kappa}\right)^2 + \frac{1}{3}\left(\frac{3(\rho_s - \rho)}{2\rho_s - \rho}\right)^2\right], \tag{1.2}$$

where R_0 is the radius of the scatterer, $k = 2\pi/\lambda$ is the wavenumber, κ_s is the compressibility

of the scatterer, κ is the compressibility of the surrounding medium, ρ_s is the density of the scatterer, and ρ is the density of the surrounding medium. Although this is not a suitable model for describing the behaviour of encapsulated gas bubbles, as neither absorption of sound energy or bubble resonance are accounted for, it gives an indication why bubbles are so effective at producing contrast.

Scattering cross section σ increases with frequency to the fourth power, scatterer size to the sixth power, and compressibility squared. For a fixed frequency and scatterer size, the cross section is therefore dependent solely on compressibility and density[36]. For a solid scatterer, it can be assumed that $\kappa_s << \kappa$ and $\rho_s >> \rho$, and the above equation becomes:

$$\sigma = [A]\left[\left(\frac{-\kappa}{\kappa}\right)^2 + \frac{1}{3}\left(\frac{3\rho_s}{2\rho_s}\right)^2\right], \tag{1.3}$$

where [A] represents the relationship between the wavelength and the radius of the scatterer. Therefore for a solid scatterer, the terms of compressibility and density both cancel, and the second bracket becomes a proportionality term equal to 1.75. For a gas bubble, the compressibility and density relations are reversed. Assuming $\kappa_s >> \kappa$ and $\rho_s << \rho$, the above equation becomes:

$$\sigma = [A]\left[\left(\frac{\kappa_s}{\kappa}\right)^2 + \frac{1}{3}\left(\frac{3(-\rho)}{-\rho}\right)^2\right], \tag{1.4}$$

which for an air bubble in water ($\kappa_s = 2.3 \times 10^{-4}$, $\kappa = 4.6 \times 10^{-11}$, $\rho = 1$) the proportionality term becomes approximately 2×10^{13}, far greater than that for a solid in the same liquid. A low density gas therefore maximizes the cross section of a fixed radius scatterer in response to a fixed driving frequency.

1.4.2 Linear resonance

Microbubbles have properties unique in their role as medical contrast agents, in that they interact with the imaging modality, and as such provide increased contrast in comparison with a static scatterer of the equivalent size and scattering cross section. Rayleigh's model above does not take this into account. In response to a typical medical imaging pulse, the small amplitude radial oscillations of a free bubble in a liquid can be modelled using linear theory of simple har-

monic oscillators. As the bubble is disturbed from its equilibrium radius, the enclosed volume of gas acts as a spring, with the compression or expansion of the gas giving rise to a force acting against the change in volume[8]. Inertia arises from the mass of liquid surrounding the gas[37] being displaced by the oscillation of the bubble. The oscillations are damped by various effects, including viscosity, radiation and heat exchange. Resonance frequency of a bubble radius R_0, is thus approximated by:

$$f_0 = \frac{1}{2\pi R_0}\sqrt{\frac{3\gamma P_0}{\rho_0} + \frac{2(3\gamma - 1)\sigma}{\rho_0 R_0}}, \tag{1.5}$$

where γ is the adiabatic ideal gas constant, and P_0 is the hydrostatic pressure in the surrounding liquid, ρ_0 is the density of the liquid, σ is the surface tension at the gas liquid interface, as originally described by Minnaert[38] (although damping effects will add additional terms[39]). Minneart's results were published with respect to the sound emitted from air bubbles in water. Comparing the 'babbling of a brook' and the sound of a dripping tap to the corresponding sounds emitted from tuning forks, he was able to calculate the resonance frequencies of each.

This expression of resonance relates frequencies on the order of typical medical imaging frequencies ($1 - 10\mathrm{MHz}$) equivalent to bubbles with initial radii of $5\mu\mathrm{m}$ or less. The scattering cross section of a bubble at resonance can be effectively up to three orders of magnitude greater than the equivalent geometric cross section[36], thus greatly increasing the contrast effect from in vivo microbubbles driven at resonance. Resonance has the potential to reduce the dependence on the sixth power of the radius (Equation 1.2) to an insignificant contribution to the scattered signals.

The presence of an encapsulating shell on a free gas bubble acts to dampen the oscillations, and thus increases the resonance frequency[40]:

$$f_r = \sqrt{f_0^2 + \frac{S_{shell}}{4\pi^2 m}}, \tag{1.6}$$

where f_r is the resonance frequency of the encapsulated bubble, f_0 resonance frequency of a free bubble, S_{shell} is the shell stiffness, and $m = 4\pi {R_0}^3 \rho$. Table 1.2 (page 29) shows the effect of the shell on the resonance frequency of various contrast agents, calculated from the above equation and assuming a perfectly elastic homogeneous shell of constant thickness[40].

The values differ between the contrast agents due to the differing shell properties, as outlined further in Section 1.7.

Radius (μm)	Air	Sonovue	Albunex	Quantison
0.5	9.4	21.0	57.0	127.0
1.0	3.8	7.7	50.0	45.0
2.5	1.3	2.2	5.2	11.0
5.0	0.6	0.9	1.9	4.0

Table 1.2: *Resonance frequency (MHz) of different ultrasound contrast agents, calculated from Equation 1.6, assuming a perfectly elastic homogeneous shell of constant thickness*[40].

1.4.3 Nonlinear modeling

While the above equations show analytical formulations of linear resonance, there is no analytical formula for the nonlinear case observed in microbubble scatter. It has been shown that a strongly nonlinear response can be expected from bubbles driven by ultrasound, with contributions from harmonic, sub- and ultra-harmonic frequencies present in the scattered signals[41]. Such nonlinear resonance behaviour can only be evaluated by numerical calculations and approximations.

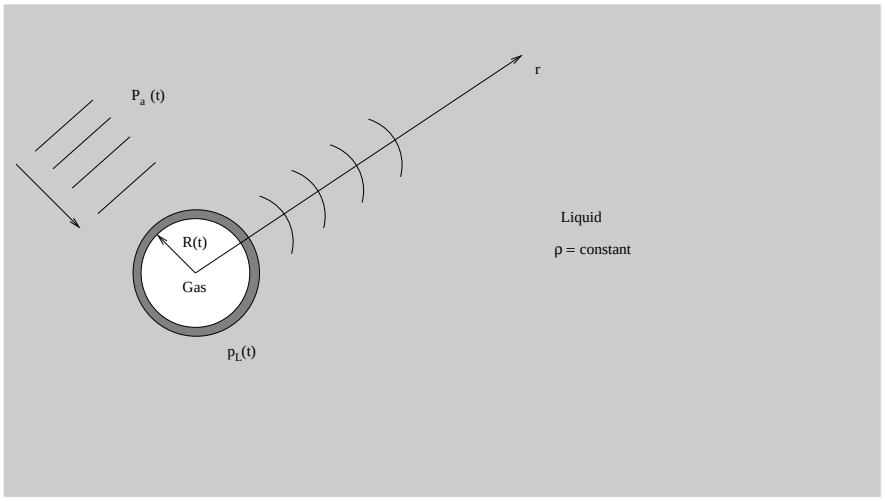

Figure 1.2: *Illustration of a bubble in a liquid. $R(t)$ is the radius of the bubble, $p_L(t)$ is the pressure in the liquid at the bubble surface, $P_a(t)$ is the incident driving pressure, and ρ is the density of the liquid (assumed to be constant).*

The Rayleigh-Plesset model (Equation 1.7, page 30) is the simplest nonlinear equation of motion for a gas bubble in a liquid[8], and is frequently used in the literature. Originally formulated

by Lord Rayleigh in 1917 following his work studying the destructive effect of the collapse of bubbles around ship propellers[42], it was rewritten to include a driving incident pressure by Plesset[43] in 1949. It describes the radial oscillations of an ideal spherical gas bubble in an infinite incompressible fluid, as illustrated in Figure 1.2 (page 29) . It does not include any energy loss caused by the radiation of sound, although from linear theory it can be shown that damping from viscosity in the liquid (which is accounted for) is a much larger factor for bubbles less than $10\mu\mathrm{m}$ at frequencies $f_0 < 10MHz$[8].

$$\rho R\dot{R} + \frac{3}{2}\rho\dot{R}^2 = p_L - p_0 - P_a(t) \tag{1.7}$$

Where R is the bubble radius; p_L is the pressure in the liquid at the bubble surface; p_0 is the static pressure in the liquid; and $P_a(t)$ is the driving sound field.

Other models have since been developed, which include additional terms for describing the compressibility of the liquid and the various damping mechanisms. Three commonly used nonlinear models are:

- RPNNP model (an extension of the Rayleigh Plesset model, named by Lauterborn[41] for its developers Rayleigh,Plesset, Noltingk, Neppiras, and Poritsky)
- Trilling model[44]
- Keller-Miksis model[45]

The RPNNP model (Equation 1.8) uses additional terms to the Rayleigh Plesset model to include the effects of the gas in the bubble, a constant vapour pressure, surface tension, and liquid viscosity.

$$\rho R\ddot{R} + \frac{3}{2}\rho\dot{R}^2 = p_0\left(\frac{R_0}{R}\right)^{3\gamma} + p_\nu - p_0 - \frac{2\sigma}{R} - \delta_{tot}\omega\rho R\dot{R} - P_a(t) \tag{1.8}$$

Where ρ is the density of surrounding liquid; R is microbubble radius (with initial radius R_0); p_0 is the pressure inside the bubble; p_ν is the vapour pressure; P_a is the incident acoustic pressure; ρ is the surface tension; ω is the angular frequency of incident pulse; δ_{tot} is the total damping coefficient; γ is the polytropic exponent

The Trilling model (Equation 1.9)[44] is based on work done studying gas bubbles from underwater explosions, and relies on the acoustic approximation that the speed of sound is constant, and as such independent of acoustic pressure. In response to a driving pressure $P_a(t)$, the model can be expressed as below:

$$\rho\ddot{R}R\left(1-2\frac{\dot{R}}{c}\right)+\frac{3}{2}\rho\dot{R}^2\left(1-\frac{4}{3}\frac{\dot{R}}{c}\right)=\frac{R}{c}\dot{p_L}-\frac{R}{c}\dot{P_a}(t)-p_0+P_a(t)-p_L \tag{1.9}$$

The Keller-Miksis equation (Equation 1.10)[44] is based upon similar assumptions to the Trilling model, and was developed by Keller and Kolodner[46] and later modified by Keller and Miksis[45] to include an incident field $P_a(t)$:

$$\rho R\ddot{R}\left(1-\frac{\dot{R}}{c}\right)+\frac{3}{2}\rho\dot{R}^2\left(1-\frac{1}{3}\frac{\dot{R}}{c}\right)=\left(1+\frac{\dot{R}}{c}\right)P(t)+\frac{R}{c}\dot{P} \tag{1.10}$$

where:

$$P(t)\equiv\left(P_{st}+\frac{2\sigma}{R_0}+P_{shell}\mid_{R_0}\right)\left(\frac{R_0}{R}\right)^{3\gamma}-\frac{2\sigma}{R}-P_{shell}\mid_R-P_a(t)-p_0 \tag{1.11}$$

Where P_{shell} is defined by a specific shell model, incorporating terms for shell viscosity and surface tension.

The Trilling and Keller-Miksis equations differ from the Rayliegh-Plesset in their derivation, by assuming a finite speed of sound in the liquid, and also by allowing for acoustic radiation. It has been shown that the differences between results in the Trilling and Keller-Miksis are small, and that both are successful in modeling encapsulated microbubbles with relevant diameters[8]. For acoustic pressures that are applicable in diagnostic ultrasound imaging, the Keller-Miksis model has been shown to provide most accurate results[47].

Similar results have been calculated from different theoretical formulations. The Gilmore model[48] accounts for a pressure dependent speed of sound in the liquid, and the Flynn model[49] includes thermal processes in the gas. More recently, models have been formulated which update the above equations to account for various experimentally observed behaviours; for example compression dominated behaviour in lipids has been modelled by Marmottant et al[50], showing good agreement with experimental data.

From these differential equations for the bubble radius as a function of time, the scattered pressure can be calculated by using the Bernoulli equation to relate pressure to the velocity of the bubble wall, as originally expressed by Vokurka[51] in 1985. The scattered pressure in the far field P_s, at a distance r can be expressed as:

$$P(r) = \frac{\rho R}{r}\left(R\ddot{R} + 2\dot{R}^2\right) \tag{1.12}$$

In this way, theoretical models of microbubble behaviour can be directly compared to both acoustic and optical experimental measurements, allowing significant physical insight.

1.5 Current microbubble detection schemes

Current microbubble knowledge has been used to design various pulse sequences and signal processing methods to exploit the difference between tissue response and nonlinear microbubble response.

Nonlinear microbubble response leads to increased contrast to tissue ratio when the contrast agent is imaged at twice the incident frequency, and this has led to the development of second harmonic imaging as an imaging technique. However, due to significant overlap between the components of fundamental and second harmonic scatter (especially for short imaging pulses at low frequencies), filtering techniques are not able to sufficiently remove linear tissue echoes. Harmonics are also created by nonlinear propagation and tissue scatter, which limits the efficiency of harmonic imaging in increasing the contrast. Subharmonic imaging also attempts to filter out the tissue echoes, and takes advantage of subharmonic components of microbubble scatter. While this avoids tissue generated signals, subharmonic signals are relatively weaker than fundamental and higher harmonics, and the use of a lower frequency reduces the resolution of the images.

The fact that microbubbles not only interact with the imaging field, but can also be destroyed by it, led to the development of intermittent pulsing schemes. Alternating an intermittent high amplitude pulse with a series of imaging pulses leads to destruction of microbubbles, followed by perfusion of contrast back into the imaging area. This gives increased contrast to tissue ratio, and the potential for blood volume and flow velocity measurements[52]. Inaccuracies arise from incomplete and nonuniform destruction of microbubbles, however, as disruption is not constant

within a distribution of initial bubble sizes[53].

More advanced imaging techniques have been proposed which rely on sequences of imaging pulses to remove the tissue echo, and are suitable for real time imaging. Pulse amplitude modulation (PAM) relies on the linearity of tissue echoes in response to pulses of increasing amplitude. Nonlinear microbubble signals are not proportionate to the amplitude of the imaging pulse, allowing cancellation of tissue echoes only, by applying appropriate gains to the signals[54]. Pulse inversion (PI) relies on the cancellation of linear tissue response from two phase inverted pulses, leaving only nonlinear microbubble response[55], due to the differences between compression and expansion. A combination of both phase inversion and amplitude modulation (PIAM) gives additional contrast enhancement at low mechanical index (MI), but can lead to the creation of artifacts in the resulting image. Although these techniques have been shown to give potential improvements in contrast to tissue ratio and resolution, they currently do not take full advantage of the nonlinear contrast response, due to the diversity of response within a microbubble distribution. Pulse sequences also reduce the frame rate, due to increased number of transmitted pulses needed to produce each imaging frame, which reduces the amount of real time diagnostic information available.

Continuous real time imaging requires that microbubbles survive in the blood stream long enough to be diagnostically useful. This can be achieved by imaging at low mechanical index (MI), but this reduces the signal to noise ratio (SNR), when compared to high MI imaging pulses. The use of coded excitation and frequency modulated chirps can limit the peak pressures, allowing increased energy to be transmitted without increasing microbubble destruction, but the increased SNR comes with an axial resolution trade off[56]. Combining chirps with pulse sequences (e.g. PIAM), has been shown to give improved SNR for microbubbles at resonance[57], as the microbubble response from increasing and decreasing frequency chirps are not time-reversed copies. However, decoding the responses introduces reduction in axial resolution, and the potential improvements are again currently limited due to the diversity of response within a microbubble distribution.

Further experimental work is needed to test the efficiency of these pulse sequences, to identify possible improvements. As a sample of contrast agent contains a distribution of scatter[58], pulse sequences designed using the results from real acoustic data will be necessary in order to fully exploit the nonlinearities of microbubble response, and adaptive signal processing techniques may be required to take advantage of different behaviours for different applications.

1.6 Contrast agent studies: methodologies

The complex interaction of a sample of contrast agent with the incident imaging pulse leads to many difficulties in understanding their behaviour. In order to build and test an adequate theoretical model for the interaction, experimental data need to be acquired; the quantification of microbubble response to ultrasound is currently an important research area. A variety of experimental in vitro techniques have been developed to study the responses of both microbubble populations and single scattering events, using both acoustic and optical imaging. More recently additional imaging techniques have been developed to interrogate the physical characteristics of microbubbles, such as electron microscopy[59] and atomic force microscopy[60]. Three common types of experimental setups reported in the literature are outlined below.

1.6.1 High concentration measurements

Both attenuation and scattering information can be gained from investigation of populations of scatterers. Measuring acoustic attenuation as a function of frequency is the simplest method of characterizing contrast agent response. A system for such has been described by de Jong et al[61] (Figure 1.3 , page 35), which compares the acoustic attenuation through a suspension of contrast agent with a reference measurement without contrast. Similar systems have been described to measure the acoustic backscatter from high concentrations, which have allowed various imaging techniques to be characterized, including B-mode imaging[8], 2nd harmonic imaging[62,63] and pulse inversion imaging[55,64]. While the overall resonance behavior of a sample can be deduced from a sample of microbubbles[37,65], the size distribution of any given sample makes it difficult to extract information on the physical and acoustic properties of single scatterers[66,67]. Any acoustic signals measured are distorted by transducer effects, as well as frequency dependent scattering and attenuation within the sample. Most studies use "microbubble density less than that required to cause shadowing"[62], which in general relates to concentrations greater than 10^4 microbubbles per ml of suspension. Self attenuation adds complexity to the analysis, which is limited by further complications such as multiple scatter and bubblebubble interactions[68].

1.6.2 Single bubble acoustic measurements

The study of scattering events by single microbubbles has the potential to offer increased knowledge of the bubble-ultrasound interaction, and thus improved signal processing techniques,

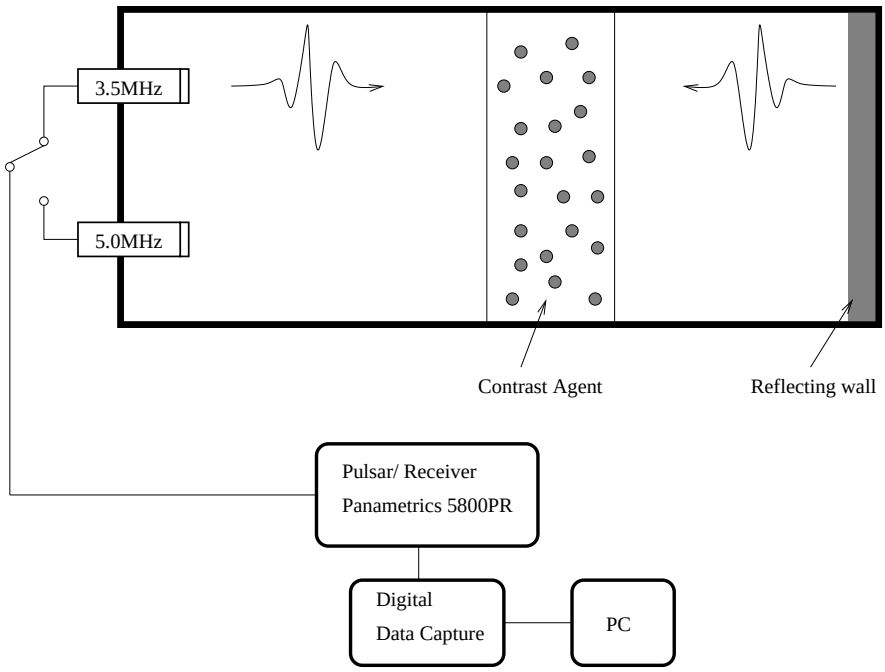

Figure 1.3: *Measurement system for acoustic attenuation spectra of suspensions of contrast agents, as described by de Jong et al*[61].

leading to advances in diagnostic imaging techniques. Advances in transducer design have led to the measurement of single bubble scattering events being possible, and various experimental systems have been described[69–73] using low concentrations of contrast agents together with direct scatter measurement[74–77], signal decorrelation[4,78], and monitoring of scatter with high frequencies[79]. Previous systems have used either flow chambers to produce free bubble scatter, which may suffer from alignment limitations due to beam properties, or phantoms employing tubes to control the flow of contrast agent solutions, which may have pressure-related effects due to the effect of the tube[80]. It has been shown that while single microbubble echoes can be detected, not all bubbles give a response[71].

In order to extract the absolute pressure emitted from a single bubble, the system must be well characterized and carefully calibrated in order to take into account the transducer transform function, and frequency dependent attenuation[81].

1.6.3 Optical microscopy

Optical microscopy experiments have provided information on the radial oscillations of microbubbles, and thus the acoustic emissions and frequency response can be calculated. They are based on high speed optical systems, and have the ability to image single microbubbles, usually held stationary in a phantom/tube. One such system, the 'Brandaris128' camera has enabled the first and only direct observations of single microbubble resonance to date[81]. The Brandaris128 (Figure 1.4) is a high-speed camera that combines a customized rotating mirror camera frame with a series of image detectors, allowing 128 consecutive image frames to be acquired at a maximum frame rate of 25MHz. This gives sufficient temporal resolution to produce two dimensional images of microbubble oscillations over several periods of incident ultrasound, and is currently the state of the art[82]. Other systems are available with equal or better temporal resolution[83], but suffer from a limited number of frames allowing images to be acquired for only a few ultrasound periods[84]. Although the optical resolution of these systems has improved greatly since their introduction, microbubble oscillation thresholds have been detected close to their optical limit[80], leading to uncertainty about the level of minimum response which can be detected[2]. Limitations also exist in the two dimensional imaging techniques used in current systems. Potential off-axis asymmetric oscillations have been predicted[85] which may lead to significant variations in the emitted signals. This limits the usefulness of radial measurements at predicting acoustic emissions.

1.7 Contrast agent studies: results

1.7.1 Response to ultrasound

While theoretical models predict various behaviours of oscillating bubbles, the main body of present knowledge has been gleaned from in vitro and in vivo experiments of both single and populations of bubbles.

Microbubble behaviour is generally considered to be defined by three regimes of response. In response to low acoustic pressures, microbubbles respond in a linear fashion. However, in contrast to this view, linear behaviour has not been observed for single bubble optical measurements[80], and nonlinear behaviour has been observed even at very low acoustic pressures ($< 10kPa$)[62,86]. In response to medium acoustic pressures ($100kPa - 1MPa$), nonlinear oscillations are predicted and have been observed by many investigators. Nonlinear behaviour has

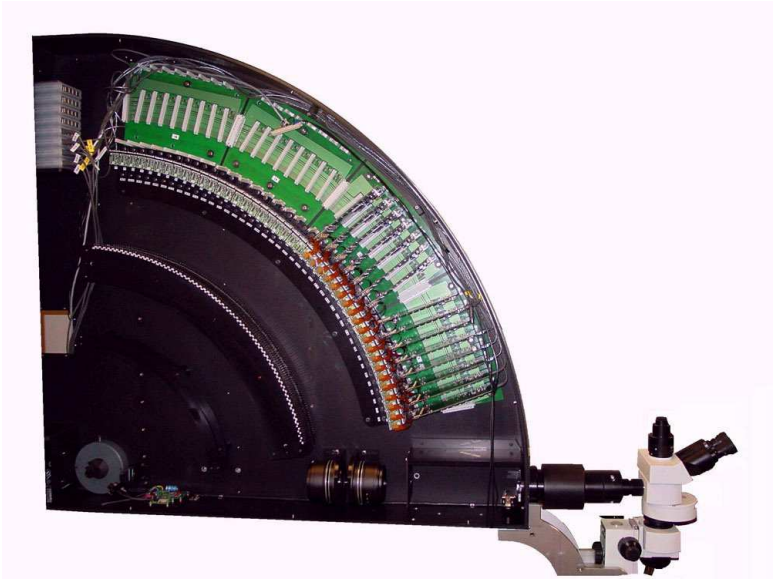

(a)

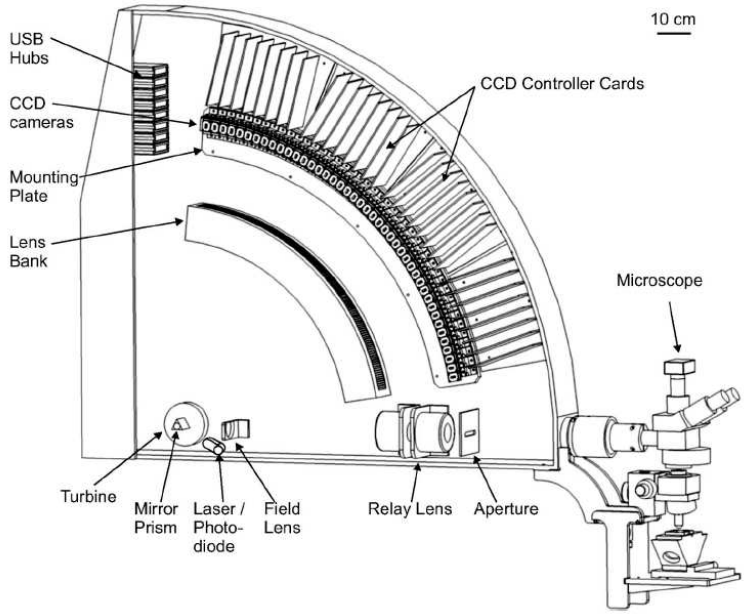

(b)

Figure 1.4: *Photograph (a) and illustration (b) of the Brandaris128 system, showing the high speed camera setup. A customized rotating mirror camera frame is combined with a series of charge coupled device (CCD) image detectors, allowing 128 consecutive image frames to be be acquired at a maximum frame rate of 25MHz. Sufficient resolution is achieved to produce two dimensional images of microbubble oscillations over several periods of incident ultrasound. This system is currently the state of the art*[82]*. Images courtesy of Nico de Jong, Thorax Center Biomedical Engineering, Rotterdam, The Netherlands.*

been confirmed with optical techniques by showing that relative microbubble expansion is proportional to peak negative pressure[80]. Single bubble experiments have shown that a threshold exists for the onset of scatter[80], which leads to the numbers of bubbles which contribute to scatter being dependent on the incident acoustic pressure[71]. At higher pressures optical measurements have led to observation of bubble disruption, as a result of violent effects such as gas-jet formation[53], ultrasound-induced coalescence of two or more microbubbles[53,53], fragmentation of a microbubble into smaller bubbles[4,53,87–91] and acoustically-driven diffusion[4,91,92], which leads to transient response[4,92]. Smaller bubbles have been shown to be more likely to succumb to these violent processes, due to larger relative radial expansion.

Measurement of the spectral response of microbubbles is more complicated than assessing the response from varying acoustic pressures. The frequency response of the transducer causes accurate calibration to be necessary to measure the full spectral response, and define the relative magnitudes of any harmonic components present. Due to the fragility of microbubbles, the destructive affects of pulses need to be accounted for when using multiple pulses to measure the response from multiple frequencies.[2]. As outlined above, the ability of microbubbles to resonate in the imaging field is unique among contrast agents. Although peak spectral response from a population of scatterers can be measured[37] (indicating resonant behaviour is present within the population), direct measurement of single bubble resonance is more difficult, and has only been observed using optical techniques[81]. The effect of shell viscosity and elasticity on the predicted resonance frequency of lipid shelled microbubbles has been measured in this way. Theoretical predictions of subharmonics in the scattered signal when a bubble is driven at twice its resonant frequency have also been confirmed[93].

1.7.2 Microbubble Shell

Although a wide variety of experimental shell materials have been investigated for use in contrast agents, the agents currently available (Table 1.1) generally consist of either a soft lipid based shell which allows a large amount of oscillation, or a harder albumin shell which is more brittle, and has been shown more likely to crack under insonation. The effect of the shell on the acoustic emissions of microbubbles has been the subject of many theoretical and experimental studies, but it has proved difficult to define absolutely the mechanical properties of the shell with acoustic experiments alone, because of both the fragility of the shell and the sensitivity of currently available acoustic systems. Previous results in the literature have shown that Quan-

tison, an albumin based scatterer, shows neither visible oscillation nor destruction in response to ultrasound imaging pulses[65], although scatter from single bubbles has been observed[58,65,71]. This suggests that scatter observed is due to gas escaping from the bubbles, as a result of slight disruptions in the shell which cannot be observed optically. The number of single scatterers observed to give a response has been shown to be directly related to the incident acoustic pressure[71], and a minimum threshold pressure has been calculated from acoustic transmission and scattering measurements, at which gas release is caused[94]. Significant differences in the response to increasing acoustic pressures has been shown for lipid encapsulated bubbles, again suggesting a significant shell contribution to scatter[71].

Fast optical microscopy of single microbubbles under insonation offers additional information on the effect of the shell. Lipid shelled microbubbles have been shown to retain their structural integrity at low acoustic pressures, where disruption of albumin shelled bubbles has been detected. This difference, it has been suggested, arises from the molecular bonds which make up the respective shell materials. The van der Waals bonds in lipids give rise to the ability to 'repair' themselves[95] after a moderate disruption, in comparison to the more rigid and larger cross-linked covalent bonds which make up the protein molecules in albumin and prevent repairable deformations taking place. Borden et al[96] used the results from optical measurements to describe the behaviour of a lipid shell as a "heterogeneous shell morphology ... domains persist as islands on the bubble surface as the gas core expands, then fold and straighten out like an accordion as the shell collapses and expands back to the resting radius". Decay of both lipid and Albumin shelled microbubbles has been observed through both diffusion[4,92] and fragmentation[95,97], although on differing time scales and in response to differing acoustic pressures (as described here in Chapter 6). Compression dominated behavior has been observed in optical measurements in lipid shelled agents only[50,80], and has been related to buckling of the lipid shell (theoretical models have been produced which confirm this as a potential explanation)[50].

Different formulations of lipid shell exist and, although they have been shown to provide differing resilience to the destructive effects of incident pulses, depending on their thickness[4,90], no differences have been observed in the emitted acoustic signals between them. For harder Albumin shelled agents differences have been observed in the threshold needed to detect acoustic signals, leading to differences in the numbers of scatterers detected at a single acoustic pressure in three different formulations of biSphere, depending on the composition of the shell[88]. Dependence of gas release on the initial radius of single bubbles measured using optical tech-

niques has also been observed, suggesting both shell thickness and the presence of defects are dependent on size. It has been shown that Quantison and biSphere show evidence of gas release in response to high acoustic pressures[97,98], which leads to nonlinear emissions not observed at lower MIs. Linear signals at low acoustic pressures can therefore be related to lack of shell disruption or oscillation.

Other imaging methods offer future potential improvements to understanding the effect of the shell, including electron microscope imaging[59] and atomic force microscopy[99], but accuracy is currently uncertain due to distortions to the molecular structure of the shell materials.

1.7.3 Microbubble Gas

The stability of an encapsulated microbubble is dependent on the solubility of the gas, as well as the aforementioned shell properties. Lipid shells are permeable and thus microbubbles composed of such are only stable if the encapsulated gas is non-soluble in the surrounding liquid. On the other hand, Albumin shells are more rigid, and have increased resistance to both diffusion and oscillation. It is generally understood that acoustic emissions from such bubbles are due to ultrasound-induced cracks leading to the oscillation of the released encapsulated gas[72,92], and as such the lifetime of the bubble is dependent on the rate at which the free gas diffuses into the surrounding liquid. Optison (an albumin shelled agent), for example, shows evidence of gas diffusion on time scales ($< 1s$) similar to that of a free bubble of the same gas (octafluoropropane) undergoing static diffusion[92].

Perfluorochemicals are the gases currently used in many contrast agents (Table 1.1), because of both the high molecular weight and the increased concentration gradient between the gas in the bubble and the liquid. While a $2\mu\mathrm{m}$ air bubble requires only 8ms to fully dissolve in water[4], a similar sized free bubble of decafluorobutane has a dissolution time of approximately $200\mathrm{ms}$. Experiments have shown that this increased resilience holds for insonated microbubbles in the bloodstream, by comparing the lifetime of similar shelled bubbles of differing constituent gases[100]. As such, the decay of various contrast agents can be affected by the microbubble environment, specifically the hydrostatic pressure and the gas content of the surrounding liquid. While air-filled Quantison has shown increased decay in degassed suspensions compared to air-saturated suspensions[101], octafluoropropane filled Definity shows no such dependence. Another effect of gas transfer through the shell is termed ‘rectified diffusion’. This is related to gases dissolved in the surrounding liquid being forced into the bubble due to a pressure gradient

set up by the incident pressure, and has been observed experimentally in a limited number of cases. Light scattering techniques have been used to observe Sonazoid bubbles grow over the course of several pulses[102], although this has not yet been observed in single bubble acoustic measurements.

1.8 Thesis outline

1.8.1 Aims of thesis

Microbubbles provide a view of blood flow and the microvasculature which cannot be achieved with conventional ultrasound imaging. The assessment of such flow provides an invaluable indicator to a large number of diseases, as demonstrated by the large number of applications that are now available in clinical practice. Quantitative information of microvasculature blood flow is highly desirable in the diagnosis and treatment evaluation of a number of diseases, and has the potential to add large benefits to both diagnosis and patient care. At present, the techniques available are not of sufficient quality or accuracy to span the range of potential clinical uses, as present knowledge of the interaction of microbubbles with ultrasound is far from complete. As such the full potential of contrast agents in improving diagnostic and therapeutic techniques has not yet been achieved. The nonlinear and dynamic properties of microbubble response offer potentially large improvements in contrast to tissue ratio, through intelligent pulse sequence design and/or improved signal processing. As a result of the various drawbacks of populations studies[103], only by studying the response from single microbubbles can the interaction be fully understood (as outlined in Section 1.6.1). Because of the variations of microbubble size and shell parameters within a typical sample of contrast agent, large amounts of single scatterer data are necessary to obtain information on the uniformity of microbubble response, which is not possible with current optical systems.

Therefore, the aims of this thesis are:

- To develop a well-characterized micro-acoustic system, with which large amounts of single bubble RF data can be collected from commercially available contrast agents, in response to a variety of clinically relevant imaging parameters.
- To analyze such data, in comparison with the results from relevant theoretical models, in order to gain physical insight into the response of microbubbles to ultrasound.

Improved understanding of the contrast-ultrasound interaction will provide the basis for improved signal processing tools for contrast enhanced imaging, with potential benefits to both diagnostic techniques and microbubble manufacture.

1.8.2 Structure of thesis

- Chapter 1 has introduced ultrasound contrast agents as a way to improve diagnostic imaging. Theoretical basis for contrast enhancement has been discussed and the theoretical modeling of microbubble response introduced. Previous results have been discussed in the light of present understanding of the microbubble-ultrasound interaction.

- Chapter 2 describes the calibration and characterization of the ultrasound system used in the experimental system. The system is based upon a Philips Sonos 5500 (Philips Medical Systems, Andover, MA) ultrasound research machine. A membrane hydrophone system (Precision Acoustics Ltd., Dorchester, UK) is used to calibrate the incident acoustic field, and well-characterized sub-millimeter solid scatterers are used to calibrate the receiver.

- Chapter 3 develops a theoretical model for the lipid shelled contrast agent Definity® (Lantheus Medical Imaging,N Belarica, MA), and investigates the predicted response from a real distribution of single microbubbles.

- Chapter 4 presents experimental single bubble data for Definity®, in response to a variety of incident frequencies and acoustic pressures. The experimental system, based on a hydrodynamically focused flow tank, is described in detail. A comparison between experimental results and the theoretical results presented in Chapter 3 is made.

- Chapter 5 presents theoretical and experimental data for the albumin shelled contrast agent biSphere™ (Point Biomedical Corp., San Carlos, CA), again in response to a variety of incident pulse parameters.

- Chapter 6 investigates the effect of consecutive imaging pulses on microbubble response, and presents experimental results from Definity® and biSphere™. The lifetime and evolution of signals is investigated, and comparisons with theoretical data are used to infer how the microbubble response is affected by diffusion and destruction.

- Chapter 7 introduces a basic pulse sequence design (pulse amplitude modulation), and

presents experimental results for a variety of imaging parameters. The response of single bubble scatter is investigated, and an alternative processing method which takes advantage of observed behaviour is presented.

- Chapter 8 presents conclusions and areas for future research.

Chapter 2
Calibration of ultrasound parameters

2.1 Aim of chapter

This chapter describes the calibration and characterization of the ultrasound system used in the in vitro experiments in subsequenct chapters. This is to be done in order to develop a well-characterized micro-acoustic system, with which large amounts of single bubble RF data can be collected from commercially available contrast agents, in response to a variety of imaging parameters. The system is based upon a Philips Sonos 5500 (Philips Medical Systems, Andover, MA) ultrasound research machine. A membrane hydrophone system (Precision Acoustics Ltd., Dorchester, UK) will be used to calibrate the incident acoustic field, and well-characterized sub-millimeter solid scatterers used to calibrate the receiver.

2.2 Introduction

In any experimental setup, the performance and tolerances of the setup must be fully known in advance. In our experiments, there are two independent systems of interest; the environment in which measurements are taken, specific to the ultrasound contrast agents (for example dilution, pressure, speed of flow and physical parameters which effect the microbubble structure over time), and the ultrasound equipment being used to excite them and measure their response. This chapter covers the calibration of the ultrasound system.

The main parameters of a diagnostic ultrasound pulse relate to frequency, focus, pulse length and acoustic pressure. The output is limited in peak rarefactional pressure by the mechanical index (MI), in order to ensure no adverse biological effects are caused by the imaging beam. The rational behind this is to avoid inertial cavitation in tissue (the index quantifies the likelyhood of such an onset). MI is defined as the peak rarefactional pressure (P_{neg}) of an ultrasound wave propagating in a uniform medium divided by the square root of the transmitted center frequency (f_0), as stated in Equation 2.1. Below an MI of 0.7 it is very unlikely that inertial

caviation will occur[104]), and is thus considered clinically safe. For an incident frequency of 1MHz, this relates to an acoustic peak rarefactional pressure of 700kPa.

$$MI = \frac{\mathrm{p}_{neg}}{\sqrt{f_0}}, \tag{2.1}$$

2.3 Phillips Sonos 5500 Imaging System

The Sonos 5500 system employs wideband phased array transducers. In order to maintain relevance to clinical results, a modified version of this commercially available system was used in the experiments. A 'back-door' control system was fitted to allow precise and selective control of the transmit and receive parameters, and an R.F. data capture board with a sampling rate of 19.63MHz fitted to capture data directly from the scanner's on-board receive amplifier. Custom software (Acoustic Frame Link©, McKee D. Poland, Philips Medical, Andover, MA, US) was used, which interfaces with the hardware and stores acoustic frame data sets as binary data files, allowing further analysis.

2.4 Calibration of transmit parameters

2.4.1 Introduction

While it is possible to use a single element transducer together with custom built receiver electronics to produce a reliable ultrasound system, a clinical system will always have certain in-built differences, which may contribute to producing differing results from a distribution of microbubbles. For example, the transducers used by the Phillips Sonos in this investigation are wide band phased arrays, containing an array of crystals, each controlled by delay circuitry. The receiver electronics in a clinical scanner are likely to have higher sensitivities than a 'home made' system, due to the quality of the electronics, and the use of proprietary techniques by the scanner manufactures. The use of such transducers and receiver system dictates that a thorough calibration is necessary to ensure that the desired beam is produced, and is not affected by any imaging parameters which the scanner uses to form an image.

In order to produce a beam with similar characteristics across a range of frequencies, the ultrasound beam was measured for a range of acoustic pressures and frequencies. The transducers

used are wideband phased arrays containing 192 elements (in the orientation as shown in Figure 2.1). Using four transducers with overlapping frequencies, a frequency range of 1-11MHz was achieved, as follows;

- S3=1-4 MHz
- S4=1.5-5.5 MHz
- S8=2.0-9.0 MHz
- S12=3.5-11 MHz

Acoustic pressures commonly used in contrast ultrasound imaging were chosen for calibration[105].

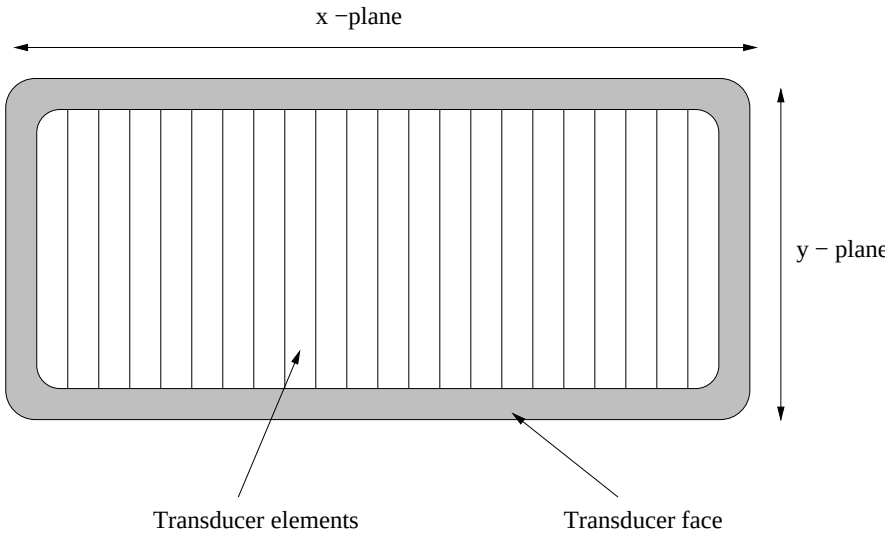

Figure 2.1: *Orientation of the phased array transducers.*

2.4.2 Method

Calibration of transmit pulses was done using a membrane hydrophone measurement system. The acoustic pressure was varied from 187kPa to 1500kPa, with suitable experimental values chosen so as to cover all studies described in this thesis.

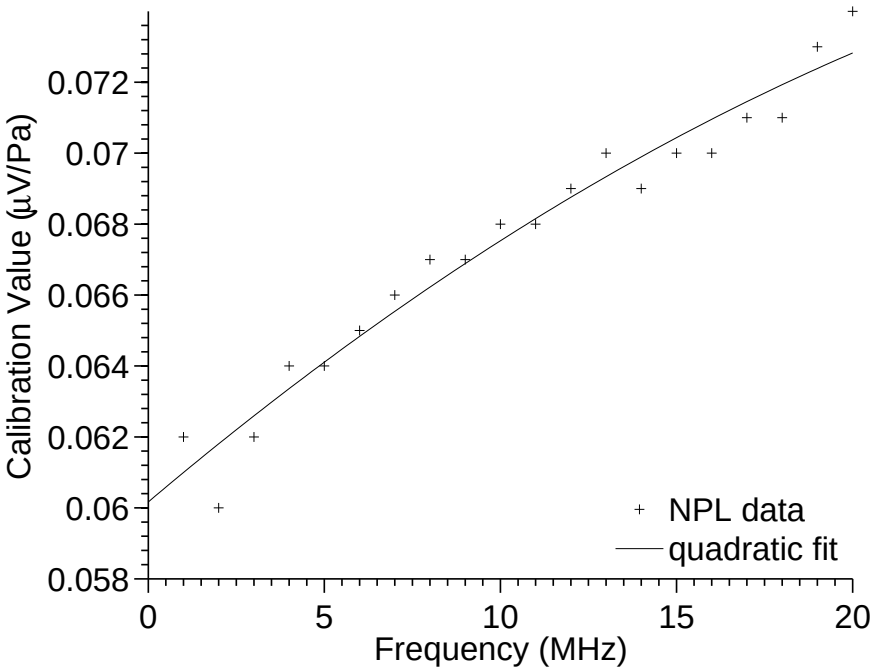

Figure 2.2: *Sensitivity of the Precision Acoustics Hydrophone, as provided by the NPL calibration certificate. Values have a* 7% *uncertainty.*

2.4.2.1 Experimental setup

The system consisted of a polyvinylidene fluoride (PVDF) membrane hydrophone (Precision Acoustics Ltd, Dorchester, UK) with active element of diameter $0.2\mathrm{mm}$ in combination with a submersible pre-amplifier, DC coupler unit and a 50Ω in-line shunt, connected to a digital oscilloscope with a sampling rate of 50MHz. The system was supplied with a National Physical Laboratory calibration certificate, providing calibration data over the range 1-40MHz in 2MHz increments, and a 50Ω terminator was used to ensure collaboration between the calibrated data and the measured data. The National Physical Laboratory (NPL) calibration sheet provided a frequency specific calibration value ($\mu\mathrm{V}/\mathrm{Pa}$), with 7% uncertainty over the relavent frequency range. This was used to convert the output voltage of the hydrophone system to an equivalent acoustic pressure[106]. The twenty calibration values were fitted to a quadratic curve over a range of 15MHz, as shown in Figure 2.2. Acoustic pressures were measured as a function of peak negative voltage, from an average value of 128 samples (unless the specific time base requirements of the measurement required a variation of this method, for example in comparing various pulse sequences). The signals recorded by the oscilloscope were stored as text files on a laptop connected via USB link, for further analysis.

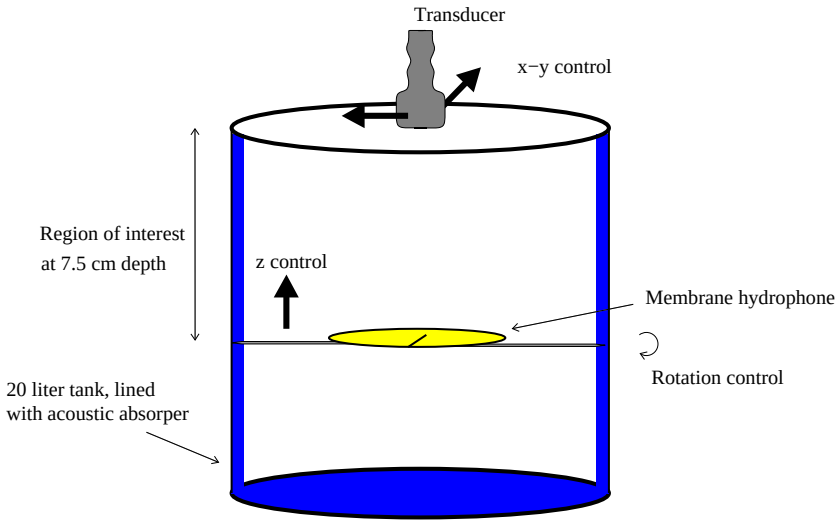

Figure 2.3: *Diagram of the experimental setup used to calibrate the ultrasound system.*

A 20 liter cylindrical tank was used for measurements (Figure 2.3). It was filled with pre-boiled degassed water at room temperature, and lined with a layer of acoustic absorber (to reduce stray reflections of the ultrasound beam). A custom designed combined transducer and hydrophone holder was used, to allow precision alignment of the hydrophone element with the center of the ultrasound beam. This holder consisted of a clamp to securely hold the transducer face perpendicular to the hydrophone, connected to a micromanipulator which allowed precise movement of the transducer. The hydrophone was placed in a specially designed holder clamped into a metal frame, which had a z-axis height adjustment mechanism similar to a micromanipulator system, and the ability to rotate in the vertical plane in order to fine-tune the alignment with the transducer. The effect of the metal frame channeling surrounding radio frequency noise into the system was shown to be negligible. This setup allowed the hydrophone to be repeatedly positioned at the same depth, and also gave a rudimentary mechanism to produce beam plots through the focus of the transducer.

The hydrophone was submersed for a minimum of one hour before measurements were taken, to ensure the stability of the hydrophone voltage output (as recommended by the manufacturers), and also to allow any remaining air bubbles in the tank to collect on the hydrophone. These were then removed by gently flushing a syringe near the surface of the hydrophone.

When measuring the transmit pulse, each transducer was clamped at the top of the tank, on an x-y stage. The translation that this x-y stage allows relates to the elements of the transducer

as shown in Figure 2.1. With the hydrophone in position directly below the transducer, the transducer was aligned so as to produce the maximum peak negative voltage output from the transducer, as monitored on a digital oscilloscope. A standard alignment pulse was chosen for each transducer, at the lower end of the bandwidth, with a frequency and acoustic pressure to ensure a stable six cycle output pulse, the maximum amplitude of which could be easily determined from the hydrophone output. Six cycle pulses were chosen as they are long enough to contain sufficient spectral clarity, but short enough to investigate a spatially sparse distribution of bubbles. In a typical clinical use, B-mode imaging applications use very short pulses to ensure high axial resolution (2 to 3 cycles), while Doppler ultrasound applications use longer lasting pulses (5 to 20 cycles)[107] to provide a more narrow spectrum of ultrasound frequencies, due to the reciprocal relationship between pulse duration and pulse bandwidth. Although six cycles is slightly longer than the average B-mode imaging pulse used in a clinical scanner, it was chosen as it has been used previously in the literature in similar studies to give a stable non-transient response from contrast agents at clinical imaging frequencies and pressures[80], while being sufficiently similar to a typical imaging pulse to remain clinically relevant. For the S3 transducer a 6 period pulse of 550kPa peak negative pressure, at a frequency of 1.6MHz, was chosen as shown in Figure 2.4. Acoustic pressures were measured as a value of peak negative amplitude.

2.4.2.2 Scanner control

The scanner itself is controlled by utilizing a combination of 'front-end' controls and 'back-door' commands provided by the scanner manufacturer, under a confidentiality agreement. Settings necessary to change for diagnostic imaging use, such as transmitted power, image size and focus depth, are controlled by various knobs and touch screens, as used in a clinical setting. Other more specific beam properties can be controlled by back-door commands, not usually accessible in a clinical environment (used for research and development purposes only). By entering a sequence of commands into the user interface, the specifics of the output beam can be controlled, as so;

- *'Xfreq 1.6'*; An incident frequency of 1.6MHz.
- *'Pulses = 6'*; Pulse length of 6 cycles.

The main controls used to control the pulse were as follows;

- Frequency
- Pulse length
- Frame rate (including a triggering system based on a set time interval)
- Line rate (time delay between successive insonations within one frame)
- Sector Size
- Transmit Power (-dB)
- Line angle, including parallel lines
- Pulse Sequences.

As some of these controls are interrelated, the calibration of the scanner relates to a specific sequence of commands, which was used throughout calibration and all later bubble experiments. These controls were in addition to front-end scanner controls which controlled the gain, focal point positioning, pulse repetition rates, frame rates and any triggering settings applied to the imaging pulses. The scanner was switched on one hour in advance of measurements, as recommended by the manufacturers. The scanner settings were set at the typical clinical settings, and kept the same throughout the calibration and experimental phases. Image sector depth was set to $9\mathrm{cm}$, with a focus at $6\mathrm{cm}$ (unless stated otherwise). The region of interest at which the beam was calibrated was chosen to be beyond the focus, so as to present a near-plane wave for small targets such as microbubbles. This ensured that the pressure profile was not centered with a sharp peak, and that positioning errors become less significant. A calibration depth of $7.5cm$ was chosen in most situations. Gain settings were chosen so as to give the best signal to noise ratio without introducing any compression of received signals by the scanner, as explained in the next section.

2.4.2.3 Transmit parameters

The range of frequencies available was determined by the bandwidth of the various transducers that were used. The four transducers used are termed S3, S4, S8, S12, a nomenclature based around the approximate value of center frequency of the bandwidth (e.g. S3 usable range from 1MHz to 4MHz). The frequency resolution was limited by the scanner 'ratio' value, relative to the digitization rate. A frequency step of approximately 100kHz was achieved at the lower

frequencies in the S3 transducer, increasing up to approximately 1MHz at the upper end of the frequency range in the S12. The four transducers overlapped in bandwidth, giving coverage from 1.5MHz up to approximately 11MHz. A range of acoustic pressures were measured, from 187kPa to 1500kPa. This range was limited to 187kPa by the noise level of the hydrophone system.

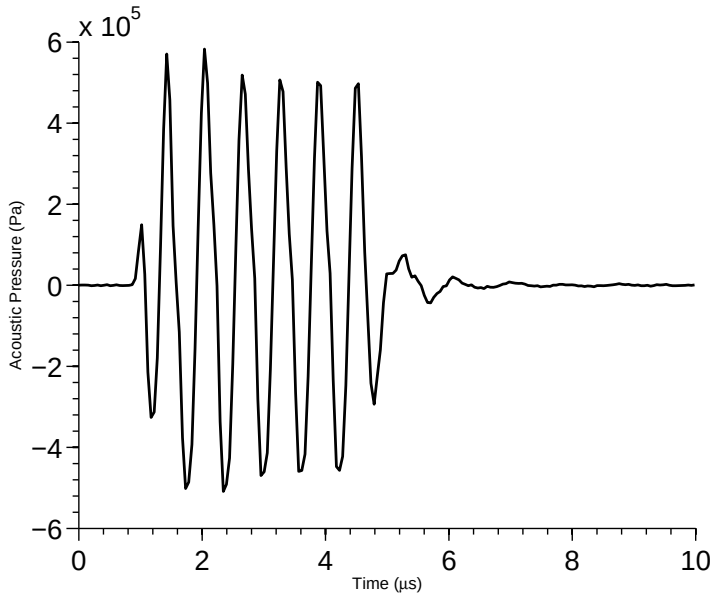

Figure 2.4: *Standard alignment pulse for the S3 transducer as measured by the Precision Acoustics hydrophone; a six cycle pulse of 550kPa peak negative pressure, at a frequency of 1.6MHz.*

2.4.3 Results

The hydrophone set-up was used to assess two aspects of the ultrasound beam. A beam plot was done for each transducer in order to determine the spatial characteristics of the beam. Once these are known, the most favourable position for microbubble measurements to be carried out can be chosen, in terms of comparison to clinical conditions and accuracy and repeatability of measurements.

2.4.3.1 Beam plots

The beam width was plotted along the axial direction, in order to characterize the variation of pressure along the width of the beam. A micromanipulator was used to translate the transducer,

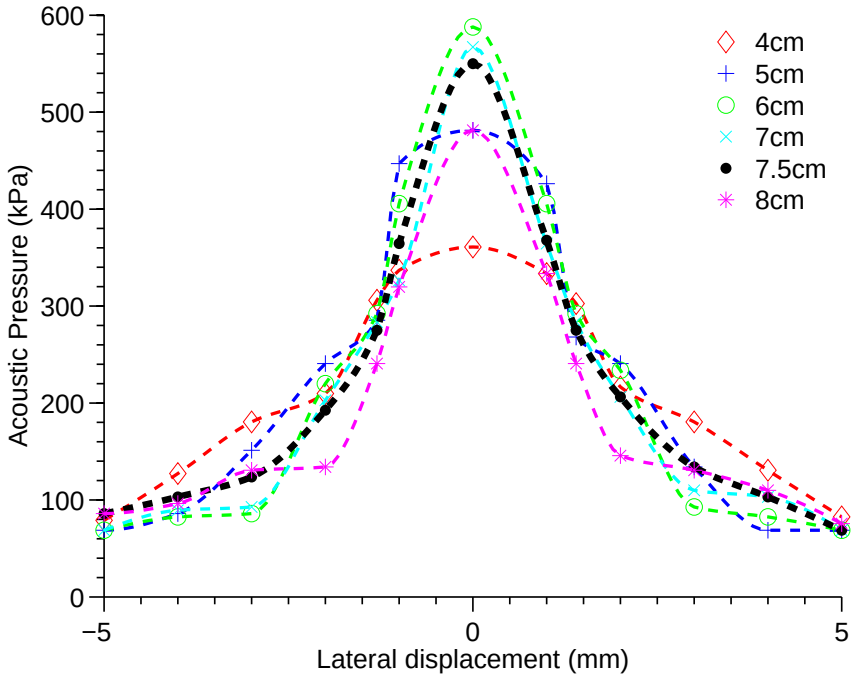

Figure 2.5: *Beam plots of the S3 transducer, as measured by the membrane hydrophone at a range of depths. Focus depth is set to 6cm, and the output power set to give 550kPa at 7.5cm (1.6MHz six cycle pulses). The different plots show how the beam profile changes with depth, and with lateral displacement from the center of the beam. The center of the beam has variation of just* 6% *in the peak acoustic pressure from 6cm to 7.5cm.*

moving the beam across the face of the hydrophone. Measurements were taken translating the transducer through both the x and y axis (axis orientation shown in Figure 2.1) at a number of depths, so as to measure the beam shape before and after the focus of the beam. From the hydrophone measurements, values of acoustic pressure were calculated, and plotted to give the beam profile for each transducer, as shown in Figure 2.5.

This data was then used, along with the dimensions of the individual transducer faces, to choose suitable regions of interest for experiments. The desired regions should be after the focal points, so as to present a plane wave to the target, but should also not be too tightly focused in either x or y direction so as to make positioning errors critical. A region as close to the focus region as possible is desired, to give maximum sensitivity. As can be seen in Figure 2.5, the S3 transducer has a suitable region thus at approximately 7.5cm from the face, 1.5cm after the focal point. The center of the beam has variation of just 6% in the peak acoustic pressure from 6cm to 7.5cm. For the S12, the frequency range is much higher, and as such the effective penetration of a stable beam at diagnostic amplitudes is much less (around 5cm at 550kPa and 10MHz). With a focal point of 2.5cm, the beam is more tightly focused than that of the S3, S4 and S8, and so a region of interest is chosen to be at 3.0-4.0cm. In all transducers, the scan focus (x-dimension) was chosen to be close to the elevation focus (y-dimension, measurements not shown), to ensure a plane wave after focus.

2.4.3.2 Frequency response

Once the regions of interest had been chosen, and a list of suitable frequencies had been determined, the frequency response of each transducer were individually calibrated at a range of clinically relevant acoustic pressures.

The desired frequency was chosen using the required back door commands, and the scanners transmit voltage (dB's) was adjusted to give hydrophone response which equated to the required acoustic peak negative pressure. The scanner output voltage in mV was noted, along with various characteristics of the measured pulse, including values of peak-to-peak pressure, peak positive pressure, and the frequency of the pulse as measured by the oscilloscope, as an independent check on the frequency settings of the scanner.

The shape of the pulse produced by the scanner, as recorded by the hydrophone, was variable across the frequency range, being more stable in the center of each transducer's frequency

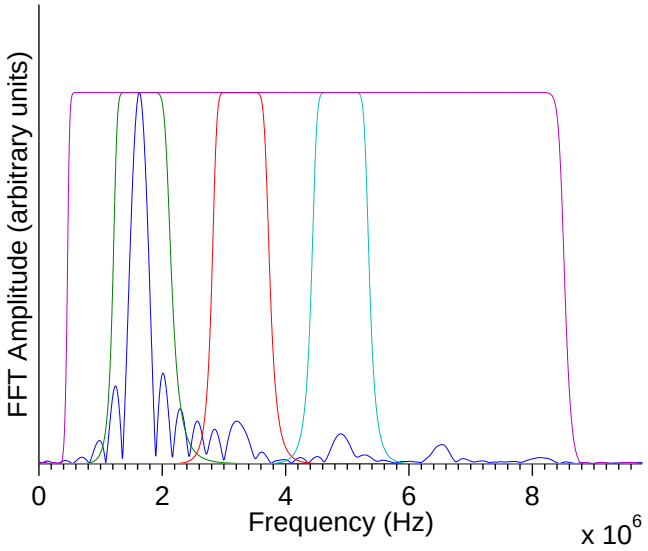

Figure 2.6: *Discrete Fourier transform of the standard alignment pulse for the S3 transducer (a 6 period pulse of 550kPa peak negative pressure at a frequency of 1.6MHz). Elliptical filters centered at the fundamental, second harmonic and third harmonic shown within a bandpass filter to remove high frequency noise.*

range, where smooth sinusoidal pulse trains can be seen corresponding to each pulse emitted by the transducer. At the lower edges of the range, the pulses become more jagged and triangular, containing 2nd and 3rd harmonic frequencies.

Once the transmit pulses were recorded and stored, they were converted into a comma separated value (CSV) text format which could easily be analyzed in MATLAB® (Mathworks). Time base information was also stored by the oscilloscope, giving a two column array containing time-voltage. Using the calibration data shown in Figure 2.2, this was converted to time-acoustic pressure data. The signals were corrected for offset, and filtered to remove high frequency noise (above five times the input frequency). The signals were resampled to a rate of 19.63MHz to give equivalence with signals received from the Sonos scanner. In order to determine the frequency components of the signals, the Fourier transform of the RF signal was taken using the MATLAB discrete Fourier transform (FFT) command, and the fundamental and harmonic frequencies identified. These data were used together to create elliptical filters to separate out the fundamental, second and third harmonic components within the signals (Figure 2.6).

A fourth-order elliptical filter was chosen as it was found to give the flattest response over the

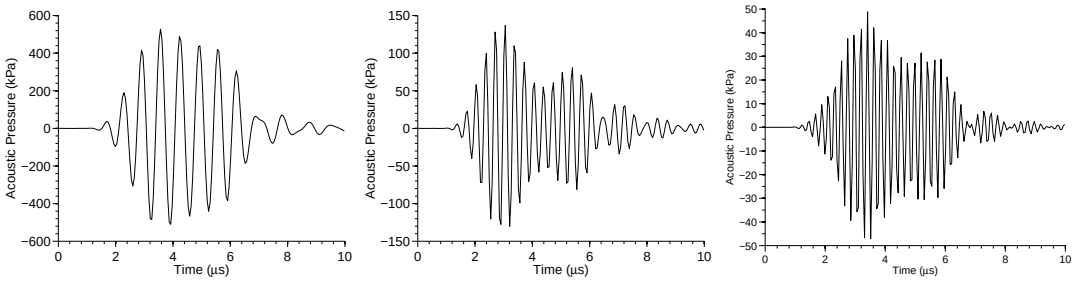

(a) Fundamental component (b) 2nd Harmonic component (c) 3rd Harmonic component

Figure 2.7: *Filtered signals of the standard alignment pulse for the S3 transducer (1.6MHz, 550kPa six cycle pulses), showing the fundamental (a), 2nd harmonic (b), and 3rd harmonic (c) components, produced using the filters shown in Figure.2.6.*

required frequency range. Initially a static passband of $\Delta f = 800kHz$ was used across the full frequency range, but this was found to be inadequate at coping with the varying bandwidth (full-width-half-maxima of the FFT response) of the transmitted frequencies. The filters are required to be wide enough in the frequency domain to include the full bandwidth of the spectral component, and retain the time domain characteristics of the R.F. data, whilst being narrow enough to avoid overlap with the spectral components. Both criteria were empirically found to be satisfied by a value $\Delta f = 0.6 f_0$.

The filters were transformed into the frequency domain and plotted to ensure correct alignment with the original signal, then used to separate out the three frequency components (fundamental, 2nd and 3rd harmonic). Figure 2.6 shows the FFT of the standard alignment pulse for the S3 transducer (1.6MHz 6 cycle pulse, 550kPa peak negative pressure), with elliptical filters centered at the fundamental, second harmonic and third harmonic. Thus for each input frequency and acoustic pressure, four signals are derived to be used as a calibration basis; raw RF data, and fundamental, 2nd harmonic and 3rd harmonic components. The increased harmonic components of the signal as introduced by nonlinear propagation through the water can be seen[108]. The measurement of each signal was repeated five times to ensure correct alignment. An 'energy density' -like value was calculated for each of the component, as defined in Equation 2.2;

$$\int_{t_{min}}^{t_{max}} |P_f(t)|^2 dt, \tag{2.2}$$

where f is the frequency component.

Energy density is a term used for the amount of energy stored in a given system or region of space per unit volume, depending on the context. In analysing single microbubble signals, an assumption of constant length of signal (in the time domain) cannot be made, so the duration of the signal is included in the above calculation, giving units of Pa^2s. This allows signals of differing lengths to be compared absolutely (which could not be done, for example with root mean squared pressure RMS).

A suitable indexing scheme was used to name and store the signals for ease of recall and further use within MATLAB scripts. The calibrated acoustic pressure values for each of the four transducers are shown in Figure 2.8, showing that a good overlap in frequencies is available for both the transmitted fundamental and second harmonic frequency components. At least three values of well calibrated third harmonic signal are also recorded for each transducer.

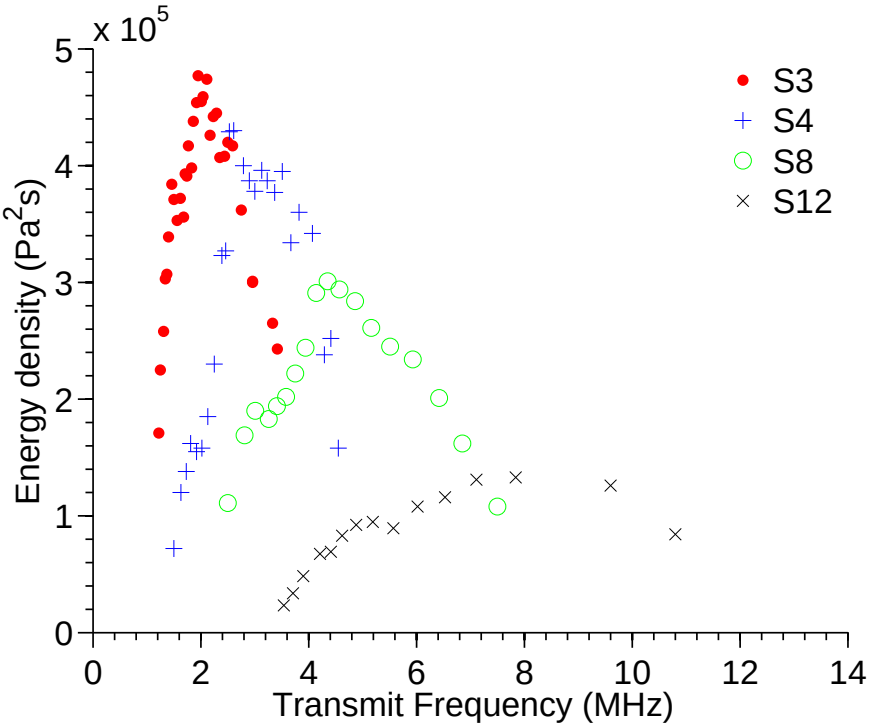

Figure 2.8: *Calibrated fundamental energy densities for each of the transducers (550kPa, six cycle pulses), showing good coverage across the range of frequencies 1-10MHz.*

2.5 Calibration of receive parameters

2.5.1 Introduction

Once the transmit parameters are well characterized, it is necessary to calibrate the receive function of the system, in order to produce quantitative results.

In B-mode ultrasound imaging, two-dimensional images of tissue are created based on the intensity of the signals received from echoes. Due to attenuation of the acoustic energy of the incident and reflected waves during propagation, the amplitude of these signals decrease with depth. The amount of amplification (gain) applied to the signal is typically adjusted to compensate for this effect. Gain adjustment in the axial direction is known as time gain compensation (TGC). In addition to TGC, lateral gain compensation (LGC) can be used to adjust the gain setting as a function of the lateral position. This is useful in echocardiogram applications where cardiac tissues that run parallel to the ultrasound beam often do not produce strong echoes; increasing the gain within these selected image sectors only, allows the cardiac tissue to be emphasized while leaving the chambers dark. TGC and LGC are one of the first processing stages to be applied to the received RF signal, and as such is known as a 'pre-processing' step. The RF signals captured from the scanner, using the custom hardware AFLink data capture described above, thus include an adjustment for TGC and LGC.

In order to fully calibrate the receiver, the affect of the various gains on the received signal needs to be characterized. By measuring the response from a known scatterer for each transmit parameter, an absolute receive calibration can be achieved, and the data collected from the AFLink software calibrated. This was done using a method similar to that presented by Sboros et al[75], and an improved method is presented here. Previous studies have used transducer spectral sensitivity data[109], or "perfect" planar reflectors[40,94] in order to normalize backscatter data, but inaccuracies exist due to the range of acoustic pressures contained within the transmit beam due to its finite width. As the scattered signals from perfect reflectors will be significantly greater than those from single scatterers, it is necessary to assume linearity of response, which may not be true for all regimes of scatter. The use of a single submillimeter scatterer measurements avoids these drawbacks. It has been shown that by using a reference material all transducer effects can be eliminated by creating a backscattering coefficient, to compare transmitted and received signals[110]. The use of single Rayleigh scatterers (much less than a wavelength in size) allows point characterization of the receive field. As the scatter from small solid spheres

has been comprehensively covered in previous literature, and can be well predicted[111,112], an absolute point-characterization of the receive field can be attained by combining theoretical predictions with accurate measurements of solid sphere scatter.

2.5.2 Method

2.5.2.1 Experimental setup

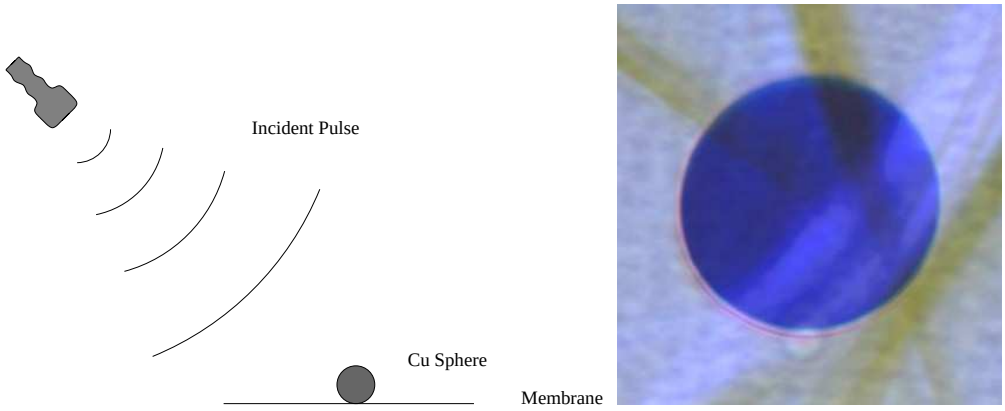

(a) Diagram of experimental setup

(b) Microscope photograph of a $45\mu m$ diameter copper sphere

Figure 2.9: *Experimental setup used to calibrate receive parameters*

Original work was done by experimentally measuring the scatter from sub-millimeter copper spheres dropped toward an upward facing transducer in a suitably designed water tank[75]. This allowed well defined receive curves to be produced. In order to improve the method, in both accuracy and duration of measurement, it was decided to attach the copper spheres to a suitable thin membrane, as shown in Figure 2.9. Not only did this allow easier alignment of the transducer with the sphere, but also repeat measurements of a single sphere using different transmit variables were now possible.

Single copper spheres were chosen as scatterers to be used as a target in the calibration experiments. Sub-millimeter spheres of copper are readily available, with the relevant parameters (density and speed of sounds within the material) of copper well known. Sub-millimeter spheres with a purity of 99%, and a maximum size of $150\mu\mathrm{m}$, from Goodfellows Ltd (Cambridge, UK) were used.

A variety of thin-film membranes were investigated to find the most suitable material. Ideally

the thinnest membrane should give the least echo, but a smooth and taut surface could not be achieved with a membrane below a thickness of $10\mu\mathrm{m}$, A $12\mu\mathrm{m}$ polyester membrane was chosen (Preservation Equipment ltd, Norfolk, UK). This membrane was then placed onto a $10\mathrm{cm}$ diameter holder and glued into place. To fix the copper spheres in place, a poly-L-lysine solution was used. Once applied to the membrane surface and allowed to evaporate, a thin film of acoustically transparent glue-like material remains. A single copper sphere in a small amount of water dropped onto the surface of this solution and allowed to dry becomes sufficiently attached to remain in place for up to two to three days. With a copper sphere attached like this, a series of calibration measurements can be taken, and the dimensions of the copper sphere can be accurately measured (to within $0.1\mu\mathrm{m}$) using an optical microscope.

The experimental set-up consisted of an optically guided placement of the spheres onto the membrane, followed by a specially designed tank to measure the ultrasound scatter. A small batch of spheres with average radius $45\mu\mathrm{m}$ (Goodfellows Ltd, Cambridge, UK) was dispersed in a small dish containing purified and boiled water. The dish was placed under an inverted microscope (Nikon Diaphot, Tokyo, Japan) and an individual sphere collected into an assisted conception micropipette with $150\mu\mathrm{m}$ internal diameter, using a manual injector. The position of the pipette was controlled using a micromanipulator (MMN-333, Narishige International Ltd, London, UK). The dish was removed and replaced by the membrane in its plastic holder, and the copper sphere released from the micropipette, along with approximately $0.1\mathrm{ml}$ of water, onto the area previously treated with poly-L-lisine. Once the water had evaporated, the attachment of the sphere was tested by repeated submersion into a tank of water, and an image of the captured sphere then acquired under the microscope using a CCD-camera (XC- 77CE Sony, Tokyo, Japan). The size and approximate roundness of each sphere was assessed using imaging software (Image-Pro Plus, Media Cybernetics Inc., Silver Spring, MD, USA), and any spheres with more than a 5% departure from roundness were rejected from further measurement.

The membrane was then introduced into the measuring tank, which allowed successive alignment of the sphere first by optical microscope, then by ultrasound measurement. Combined optical and acoustic measurement gives increased confidence that the desired single scatterer is measured, avoiding unwanted echoes from any bubbles or dust particles which may be attached to the membrane. The two imaging modalities were separated in the tank to allow precise characterization of the acoustic field as described above, and to minimize reflections from surfaces other than the membrane. The section of the tank in which acoustic measurements were made

was lined with Aptflex F28 acoustic absorber (Precision Acoustics, Dorset, UK) to minimize stray reflections. The optical axis of the microscope was aligned with the transducer through the use of a membrane holder attached to a one dimensional translation axis. In this way a single sphere can be imaged and aligned in the microscope, then translated into the ultrasound field (approx $300\mathrm{mm}$ translation), whereby the transducer, attached to a 3-axis micromanipulator, can be aligned to place the copper sphere in the center of the ultrasound field (assessed by achieving the maximum echo from the copper sphere in the field of view). This system has also been used by Butler et al[113,114] to successfully image attached microbubbles, using both optical and acoustic methods.

The scanner transmit settings were set to the same as those used in the transmit calibration experiments, and the receiver gain set to a relatively high overall gain of 194 (arbitrary units), for initial measurements. A range of different transmit and receive settings was used to record backscatter information from a range of differently sized spheres. As the scatter from a sphere is dependent on its radius according to the sixth power at the frequencies used[112], and as such spheres of different radii give a large range of response, it was determined that six differently sized spheres provide an adequate sample size to determine the mean and the population standard deviation. In order to produce a receive calibration across the frequency range, a series of measurements were made for increasing transmit frequencies (approximately 10 frequencies were measured for each transducer used), at three different transmit amplitudes (300kPa, 550kPa and 1100kPa). Each sphere measurement was repeated three times, with each sphere being realigned between measurements, and checked for deviation from mean values (any outliers were ignored, and if a set of measurements had more than 25% outliers the entire set was rejected). This gave a set of 18 measurements for each transducer.

2.5.2.2 Comparison with theoretical values

Once backscatter information has been recorded, the receive function of the transducer can be calibrated. This is done by direct comparison with the theoretical backscatter values, calculated using Hickling's analysis of Faran's theory for the backscatter from solid elastic spheres. A full analysis of the receiver calibration at a point, including the full theoretical derivation, can be found in Sboros et al[75].

The copper sphere echoes were analyzed in MATLAB, and a sum squares technique used to identify the echo from the background noise (the results shown in Figure 2.10(a)). The signals

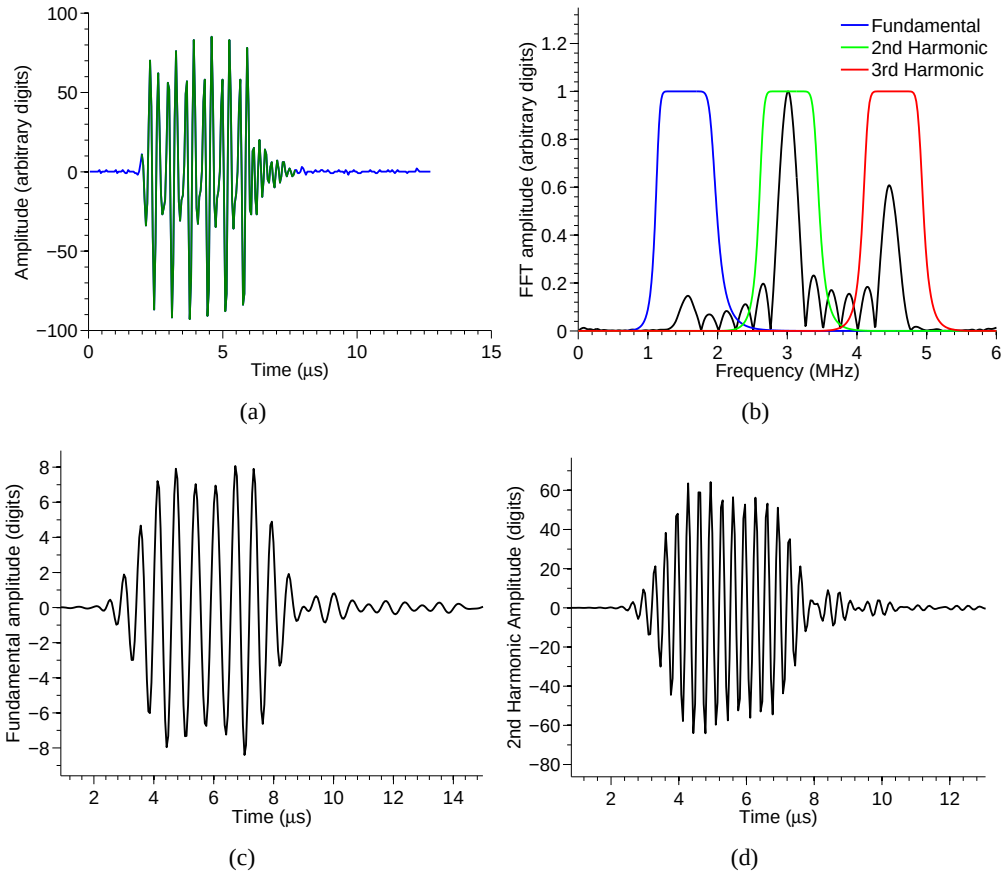

Figure 2.10: *(a) RF Signal from a $53\mu\mathrm{m}$ copper sphere in response to a 1.6MHz 550kPa six cycle pulse (signal is uncalibrated, with arbitrary units of amplitude). Fourier transform with elliptical filters (b), and the filtered components of the fundamental (c) and 2nd harmonic (d) are shown (arbitrary units).*

were filtered to remove any offset, and again to identify the fundamental and second harmonic components, using the same filter parameters used to analyze the transmit pulses. The energy density of each harmonic component was calculated, using Equation 2.2. Note that the spectral components can be treated separately as solid spheres are linear scatterers, and as such one transmit pulse corresponds to a series of calibration values (fundamental, 2nd harmonic, third harmonic, etc.).

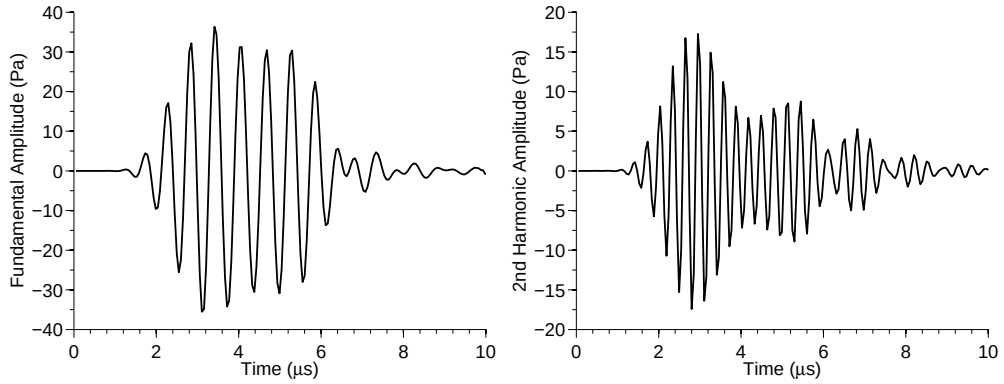

Figure 2.11: *Theoretical fundamental (a) and 2nd harmonic (b) scattered signals from a* $53\mu\mathrm{m}$ *copper sphere, in response to a 1.6MHz 550kPa six cycle pulse, as calculated using Hickling's analysis.*

The transmit pulses, treated with an identical analysis, are used to calculate the components of each harmonic frequency that are incident at the same position as for the copper sphere measurements. The ratio of the spectral densities of the scattered signals to the respective components of the incident pulse is a backscattering-cross-section-like (BSCS) physical quantity. This was then compared with the theoretical BSCS, calculated using Hickling's analysis[112], using the same experimental conditions. The theoretical scatter from a $53\mu\mathrm{m}$ copper sphere calculated in this way is shown in Figure 2.11. The ratio of the two BSCS produces the required point-calibration, and allows the ratio of "digits squared" (arbitrary unit measurement of the scanner system) over Pa squared to be calculated for a specific frequency. This spectral calibration curve can be used to convert any further measurements into absolute values of Pascals.

2.5.3 Results

As described above, by comparing a theoretically scattered pulse to an echo measured experimentally, a calibration curve can be produced across the frequency spectrum.

Alignment of the copper sphere within the ultrasound beam was determined to be crucial to producing reliable repeat measurements of backscatter. It was observed that the receive sensitivity was higher for signals received at the harmonics of the transmit signal, and as such any small misalignments had greater effect on amplitude of the 2nd and 3rd harmonic signals received than the fundamental components. It was surmised that this relates to the size and focus of the receive beam at the position of measurement, which is controlled by the electronic focusing of signals, applied upon receive.

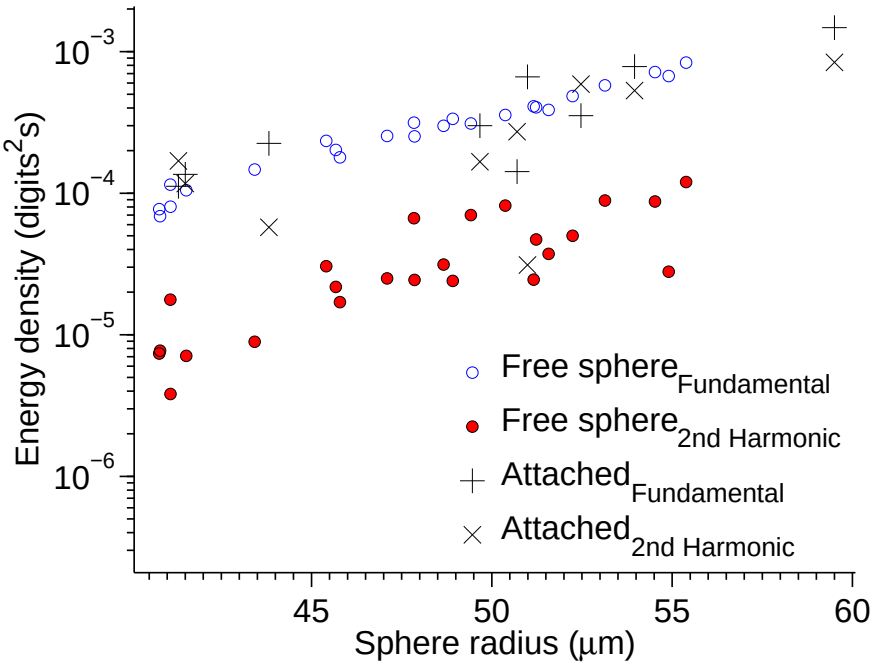

Figure 2.12: *Solid sphere scatter comparison between free and attached spheres, in response to 1.6MHz, 550kPa six cycle pulses. Fundamental components of scatter are similar in free and attached copper spheres. Attached spheres display increased energy of scatter at the second harmonic as compared to the fixed sphere scatter, suggesting misalignment of the dropping apparatus. Scanner gain = 94 units in both experiments.*

Measurements were initially taken to confirm that the attached sphere measurements were similar to free sphere measurements, and to ensure that the membrane had no impact on the solid

sphere scatter. Copper spheres were dropped toward the transducer, and scatter individually measured. Fundamental signals from free spheres (energy densities shown in Figure 2.12) are not significantly different to the equivalent attached spheres signals. The energy of second harmonic components for the free spheres however are slightly below the attached, which may be due to slight mis-positioning of the dropping apparatus. This will affect the harmonic components greater than the fundamental, as the second harmonic beam has a narrower focus. As the receiver is more sensitive at the higher frequencies, this results is a lower calibration value at the second harmonic for free spheres, whereas the mis-alignment is not observed to affect the fundamental calibration values. This shows the value of the improved attached-sphere set-up in producing a more accurate and reliable receiver calibration. Figure 2.12 also shows the dependence of energy of scatter on scatterer size.

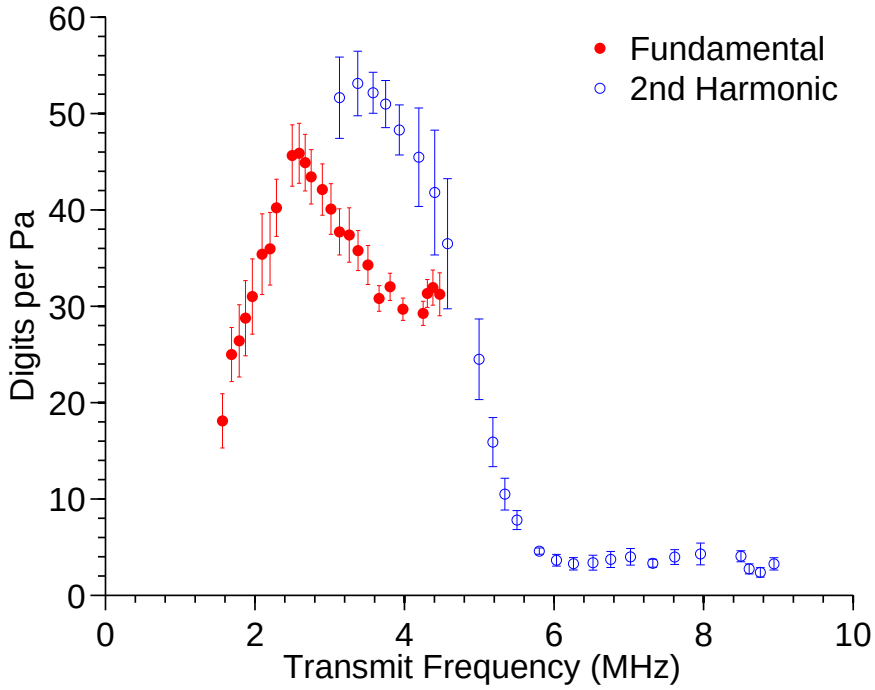

Figure 2.13: *S4 calibration data in digits per Pa, from a series of 18 spheres dropped toward the transducer. Scanner is at high gain settings. The non overlapping fundamental and second harmonic can be clearly seen as a result.*

Results from attached spheres are expected to produce a smooth curve for receive calibration of the S3 transducer (transmit frequency range of 1.2MHz to 3.5MHz), with overlapping fundamental and second harmonic frequencies[75]. However, at the peak receiver sensitivity, the fundamental calibration curve in all four transducers was found to be below the level of the

second harmonic. This departure between the fundamental and second harmonic frequency curves was observed to be greater in the higher frequency transducers, which displayed higher levels of overall gain. Figure 2.13 shows the results from the S4 transducer. The fundamental curve peaks at 2.59MHz at 46dPa (digits per Pa), whereas the second harmonic curve peaks at 3.38MHz, at a higher value of 53dPa, giving an offset of 17dPa at this peak receive sensitivity. The amount of overlap was observed to reduce when the overall gain settings of the scanner were reduced. Figure 2.14 shows how the overall gain level affects the ratio between the calibration values at 3MHz and the second harmonic energy density at a transmit frequency of 1.5MHz in the S4 transducer (the data is produced from a $53\mu\mathrm{m}$ sphere) and similar results for the S8 transducer. In order to produce a smooth spectral calibration curve, this ratio should be close to one (so that the fundamental and harmonic curves overlap), but as can be seen in Figure 2.13 the value drops sharply once the overall gain level (combination of TGC, LGC) is increased beyond approximately 150 (arbitrary units) in the S4, and 100 in the S8. This effect is caused by compression of the sphere signals when the signal amplitude is close to the threshold of the gain amplifier. At higher gain settings sphere signals are therefore subject to a nonlinear receiver response. The signals at the fundamental peak sensitivity are of larger amplitude than the signals at peak second harmonic, and thus a reduced fundamental calibration value is calculated, as seen above. By measuring the effect of various gain settings on the size of received signal it was possible to define the minimum size of signal at which this affect is seen. Figure 2.15 shows the RF signals from a $53\mu\mathrm{m}$ sphere at differing gain levels. The signals measured at gain levels that compression effects are observed (greater than 150) are an order of magnitude greater than any single microbubble signals measured, ensuring that bubble signals will not be subject to compression.

A gain level of 94 units was chosen for further calibration, as this gave a constant calibration value across the range of sphere sizes measured, and produced smooth spectral calibration curves across the full frequency range in each transducer.

2.5.3.1 Calibration results

Once suitable gain settings were identified, the transducers were calibrated across the full frequency range, and the receiver calibration values of digits/Pa calculated using point scatterer measurements and calculations, as shown in Figures 2.16-2.19. At the maximum of the respective transducer bandwidths the calibration becomes unreliable, as can be seen by the second

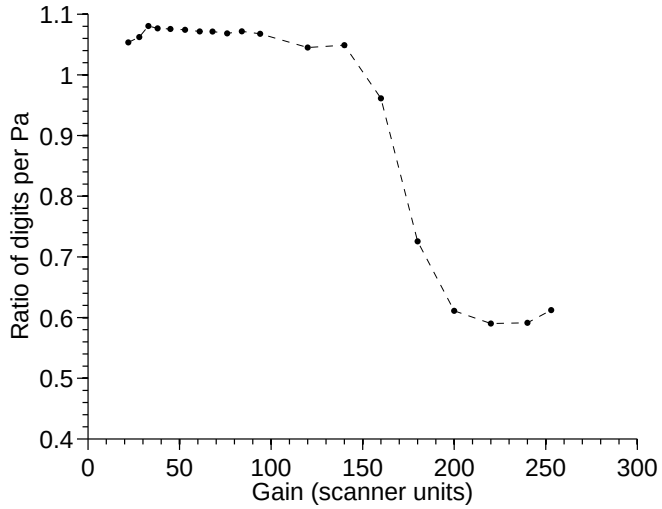

(a) S4 Ratio of fundamental (1.5MHz) to second harmonic (3MHz) calibration values at peak sensitivity.

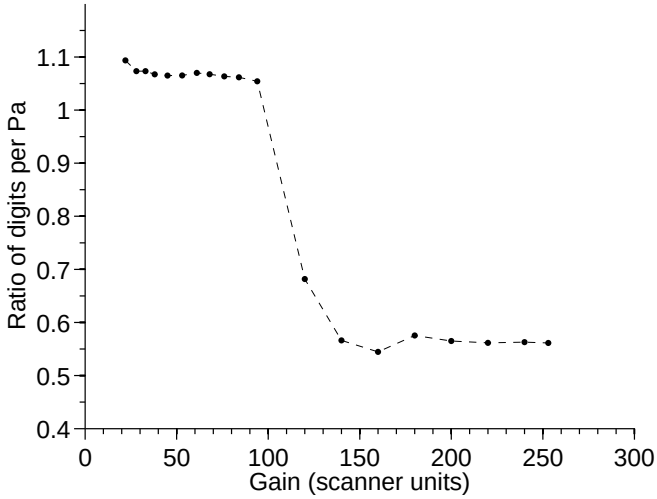

(b) S8 Ratio of fundamental (2.75MHz) to second harmonic (5.5MHz) calibration values at peak sensitivity.

Figure 2.14: *Calibration data showing ratio of fundamental to second harmonic calibration values (dPa) at peak sensitivity, for S4 and S8 transducers, calculated using a* $53\mu m$ *copper sphere. The ratios, which should be approximately one, show a sharp drop off at higher gains where the sphere signals are compressed. The S8 has an overall higher level of gain applied, and as such shows this drop off at lower levels of gain.*

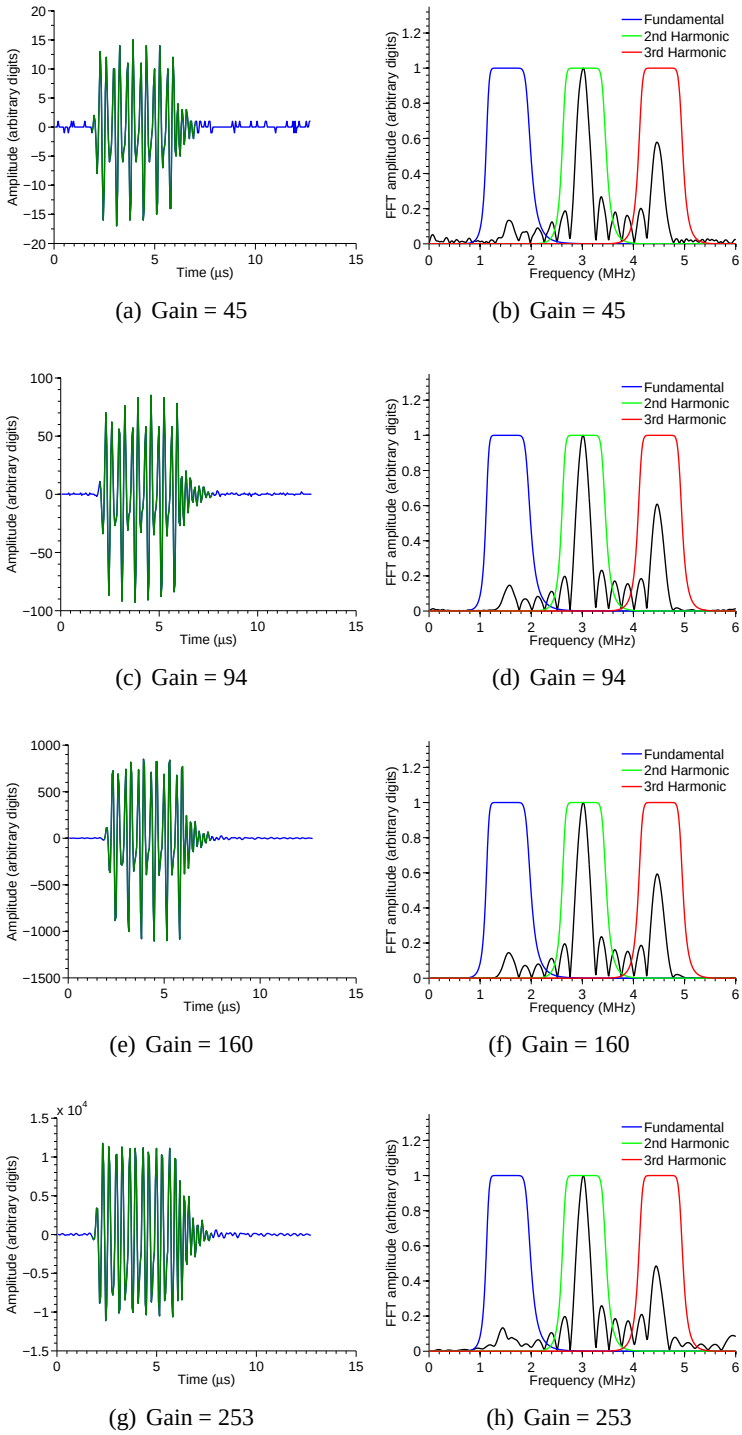

(a) Gain = 45 (b) Gain = 45

(c) Gain = 94 (d) Gain = 94

(e) Gain = 160 (f) Gain = 160

(g) Gain = 253 (h) Gain = 253

Figure 2.15: *RF signals from a* $53\mu\mathrm{m}$ *copper sphere in response to 1.6MHz 550kPa six cycle pulse, at varying gain levels. Compression of the signal (as evident in Figure 2.14) occurs at gains greater than 150 (Figures (e)-(h)), as can be seen in the reduction of the fundamental component of scatter. This corresponds to RF amplitudes greater than 1000 digits, which is an order of magnitude greater than the amplitudes of bubble signals.*

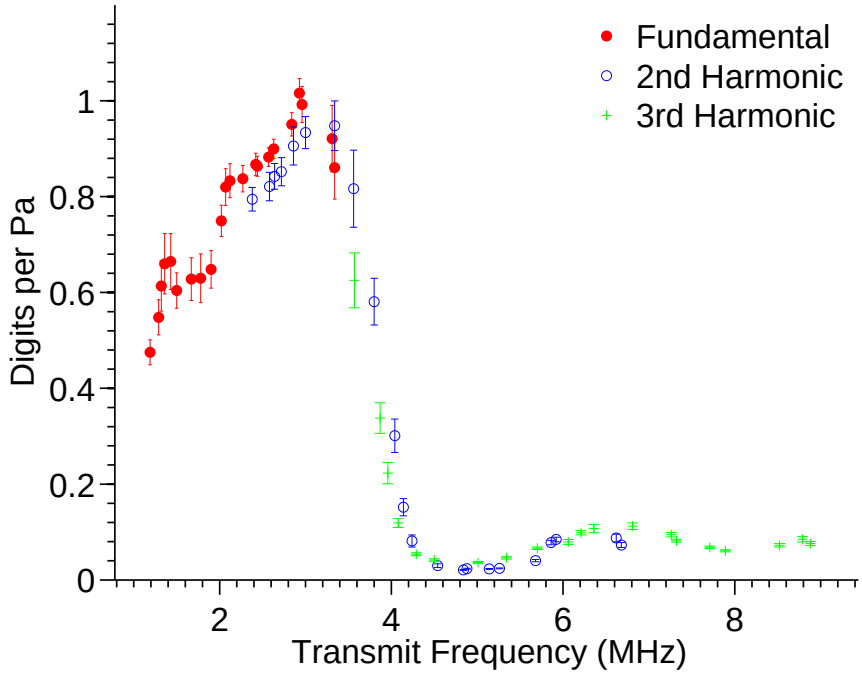

Figure 2.16: *Receive calibration of S3 transducer, shown in digits per Pa (error bars of standard error).*

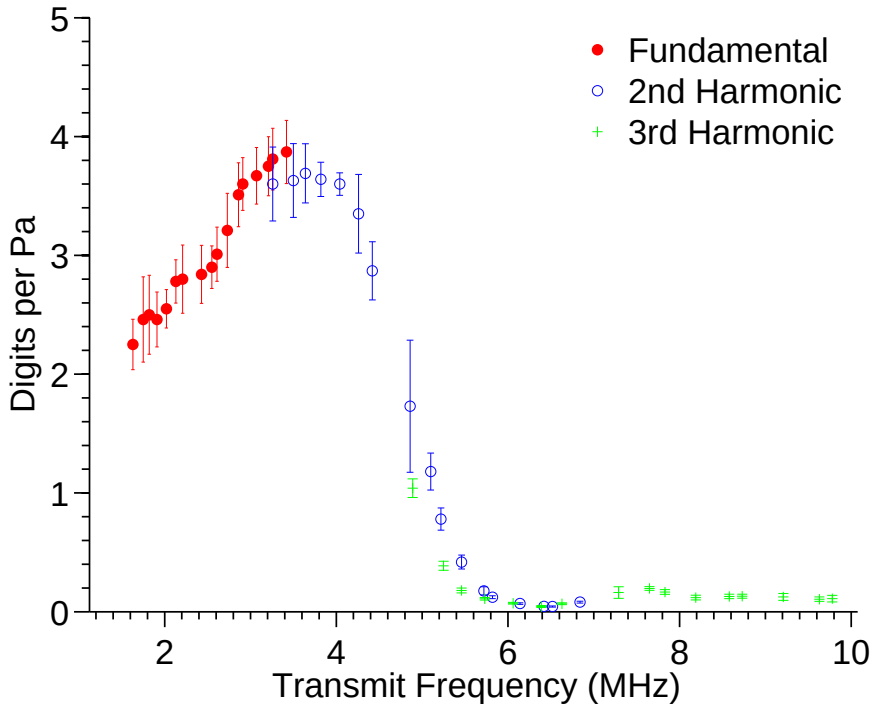

Figure 2.17: *Receive calibration S4 transducer, shown in digits per Pa.*

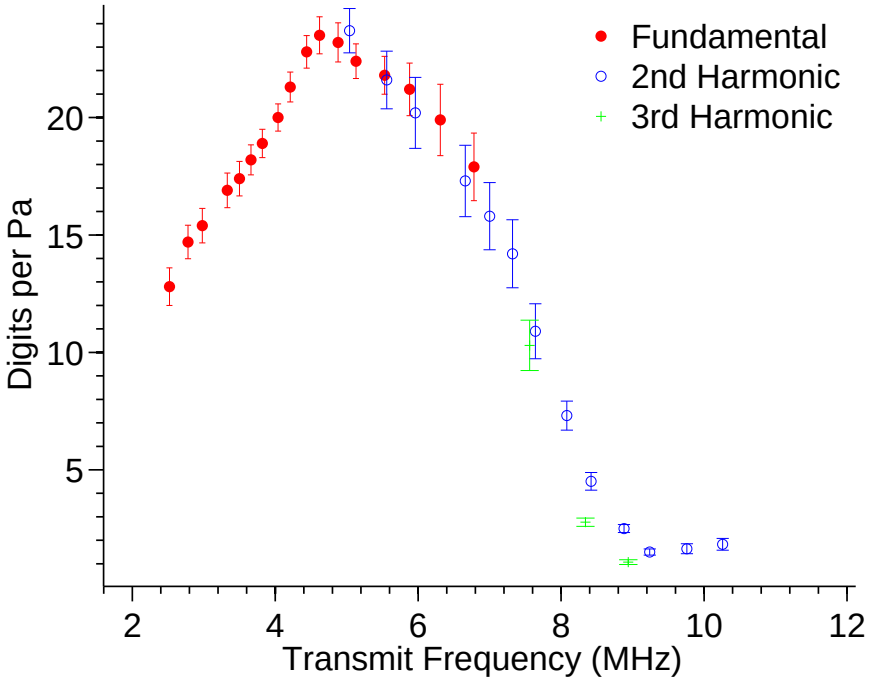

Figure 2.18: *Receive calibration S8 transducer, shown in digits per Pa.*

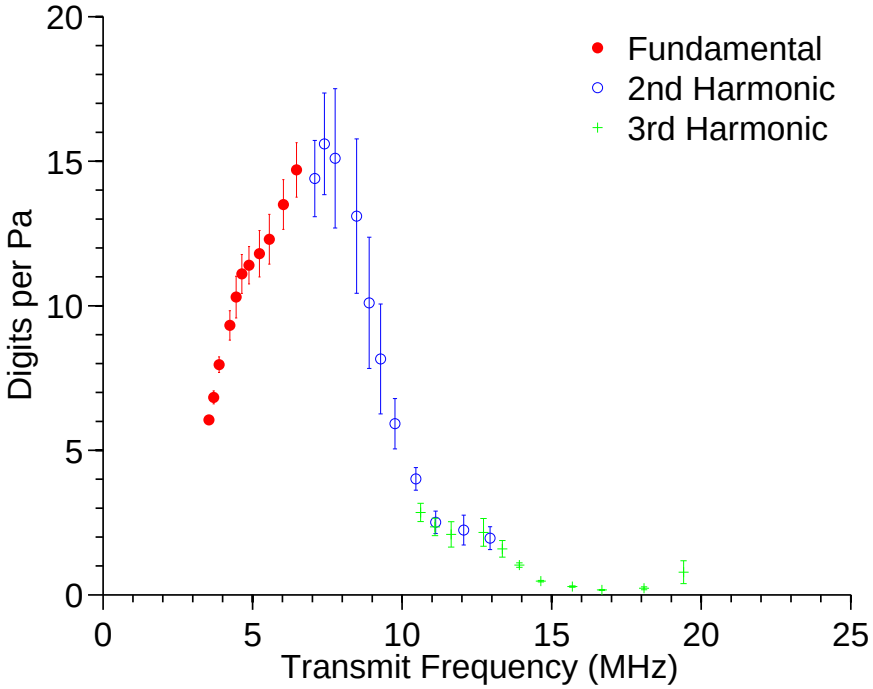

Figure 2.19: *Receive calibration S12 transducer, shown in digits per Pa.*

local maximum in the 2nd and 3rd harmonics at approximately 6.5MHz in the S3 transducer. This is does not indicate increased sensitivity, but is due to the noise created by the electronics.

2.6 Chapter summary

The transmit and receive parameters of the four wideband phased array transducers to be used in this thesis were characterized. Ultrasound beams were plotted, and suitable regions for experimentation were chosen. The transmit calibration has been used to produce well characterized beams with which to interrogate bubble response at a variety of clinical frequencies and acoustic pressures, and the receive calibration has been used to produce quantitative calibration for use with single bubble measurement across a wide range of acoustic parameters.

Chapter 3
Theoretical response of the contrast agent Definity®

3.1 Introduction

Studying the response of microbubbles is vital to fully understand the behaviour of such scatterers, and subsequently developing improved imaging schemes. This will in turn lead to improved diagnostic techniques which can address some of the clinical issues raised in Chapter 1. Presented here is a multi-method investigation into the single pulse response of the imaging contrast agent Definity® (Lantheus Medical Imaging). A theoretical model based upon a Keller-Miksis type equation[45] has been developed to model the motion of the bubble wall. From this, the pressure waves emitted by the bubble can be calculated by using the Vokurka equation[51]. Model parameters were set to mimic a typical soft shelled Definity microbubble. These results are displayed so as to allow comparison with detailed experimental measurements of Definity microbubbles (Chapter 4), and an experimentally measured size distribution has been used to allow direct comparison. A variety of imaging parameters are used in order to identify any frequency or pressure dependent effects, and the effect of changing various shell parameters on these results has been investigated.

3.2 Aim of chapter

The aim of this chapter is to investigate the characteristics of resonant scatter, as predicted by a current theoretical model, in order to identify such behaviour in the experimental results, and thus confirm the validity of the model. This resonance behaviour is the integral part of ultrasound contrast which allows improved diagnostic imaging, but is not yet fully exploited in current imaging schemes, which are based upon theoretical results from basic approximations of microbubble behaviour. Clinical agents contain a relatively wide distribution of microbubble sizes, and current clinical pulses used (typically designed for B-mode imaging) can only excite a small proportion of these bubbles. As such the true potential for improved contrast

and resolution has not been reached, and the following results and conclusions may aid in the development of pulsing schemes which can increase the proportion of microbubbles which are at resonance, therefore increasing the contrast to tissue ratio achieved. Single bubble multi-method investigations such as this also have the potential to discover bubble-specific responses which will be masked by large concentration studies, and thus lay the groundwork for novel contrast imaging schemes. Also, only by combining experimental and theoretical results in this way can the predictions of a model be tested, and thus improved upon.

This chapter contains an investigation into the time and frequency components of response from a distribution of single microbubbles, and as such presents novel results. The variation in large numbers of single bubble response is rarely addressed in the literature, and the time-domain response of single bubbles is also rarely investigated. By combining these two methods in order to allow a resonance response to be definitively identified in single bubble response, single bubble measurements offer a powerful tool to optimise the scatter from a distribution of microbubbles (by identifying optimum transmit parameters), and thus to maximimise the contrast to tissue ratio achievable in diagnostic techniques. In single bubble optical measurements, when the size of each bubble is easily measured, it is possible to identify single bubble resonant scatter, and this is also the case in large concentration bubble measurements, as the incident parameters can be easily changed to find the corresponding maximum resonance response. However, this has not been done previously in single bubble acoustic measurements, as neither can the bubble size be easily measured (without affecting the acoustic response), nor can different incident pulses easily be transmitted upon the same microbubble without affecting its integrity. The results below (and in Chapter 4) present an alternative method for identifying resonance behaviour.

3.3 Theoretical model

The first theoretical studies of the dynamics of bubbles date back to Lord Rayleigh[42,115], who in 1917 looked at the destructive effects of cavitating bubbles on ship propellers. In 1933 Minnaert[38] undertook a combined experimental and theoretical study of the sound emitted from bubbles. More recent studies have developed more sophisticated models for the behaviour of oscillating encapsulated bubbles under the influence of ultrasound. As described in Chapter 1, the use of a theoretical model to simulate the motion of the bubble wall in this way gives an insight into the physical mechanisms that are present, and in turn can help to define the behaviours observed experimentally. The results from such a model which are specifically

relevant to the physical characteristics of Definity, a Keller-Miksis type equation[45] using a Mooney Rivlin shell model[116], are investigated here.

3.3.1 Physical parameters of microbubbles

It is known that Definity contains microbubbles with a soft lipid outer shell (perflutoro-lipid), and a non-soluble gas core (octoflouropropane), as described in Chapter 1. Various physical characteristics, for example shell material stiffness and gas density, can be estimated and be used to define parameters upon which the shell dynamics can be modeled[8]. While these parameters can be estimated from bulk material properties, the accuracy of these estimates become a limitation in how accurately the model predicts the response of microbubbles. For example, material properties such as shell thickness are on the order of nanometers, and so cannot be defined absolutely with current technology, although advances in tools such as atomic force microscopy[60] offer promising improvements. Variations of up to 150% in maximal excursions of optically identical bubbles have been previously measured[117], due to differences in elastic properties of individual bubble's shells, which will lead to large variations in the signals produced from a distribution of bubbles. Comparison between experimental and theoretical results may lead to improved estimates in the variation of individual shell parameters.

The main parameters used in the shelled models to describe the behaviour of the encapsulating lipid shell are the shell thickness (d_s), shell stiffness (G_s) and the shell viscosity (η_s)[118]. G_s and η_s have been previously measured for Definity using ultrasound attenuation measurements[40,61]. The values for these are here initially chosen to be 15nm, 50MPa and 1Pas respectively, as calculated from a mean of various experimental measurements presented in the literature (for example,[119] define $G_s \approx 180\mathrm{MPa}$ and $\eta_s \approx 0.9\mathrm{Pas}$, whereas[120] define $G_s \approx 15\mathrm{MPa}$ and $\eta_s \approx 0.05\mathrm{Pas}$. The shell thickness estimates vary from 1nm up to 20nm, with the majority of the literature settling on 15nm, as defined above). The effect of varying these parameters will be briefly investigated later, where relevant.

3.3.2 Size distribution

In order to accurately estimate the response from a sample of microbubbles, the size distribution from which the sample is taken is needed. Once activated, a vial of Definity contains a maximum of 1.2×10^{10} microbubbles per milliliter (equivalent to $150\mu\mathrm{l/ml}$ of encapsulated

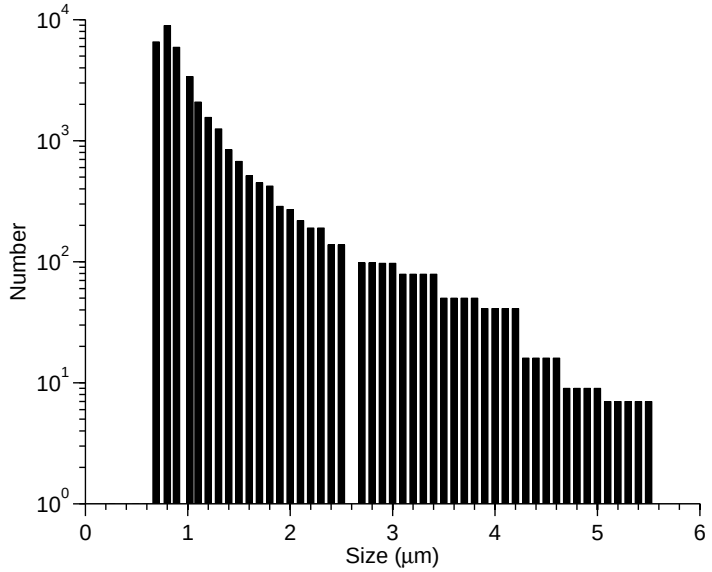

Figure 3.1: *Size distribution of 35380 Definity microbubbles, as measured using a laser diffraction technique (Malvern Mastersizer), accurate to within* $0.1\mu\mathrm{m}$.

gas), with an average diameter of 1.1-3.3um. The data sheet supplied with the agent quotes microbubble size distribution as 98% with a diameter less than 10um, with a maximum diameter of 20um. A Malvern Mastersizer (Malvern Instruments, Worcs., UK) was used to measure the size distribution of a sample of bubbles, with a resolution of $0.1\mu\mathrm{m}$, to produce diameter curves from $0.7 - 5.5\mu\mathrm{m}$, as shown in Figure 3.1. The Malvern Mastersizer measures particle diameters between $0.02 and 2000\mu\mathrm{m}$, and relies upon laser diffraction to determine the size distribution of the suspension. The size distribution calculation relies upon the premise that there is an inverse relationship between the size of the particle and the angle at which the particle scatters laser light. An absorption of 0.1 and refractive index of 1.4 were chosen for the analysis of the microbubble suspensions, as used previously in the literature[121]. These high concentrations are used in clinical trials either by bolus injection ($10\mu\mathrm{l/kg}$) or by infusion (1.3mL of activated Definity diluted in 50mL saline, injected at a rate of $4\mathrm{mL/min}$). In order to produce single bubble data this must be diluted further, to allow single scattering events to be imaged. It was calculated that a dilution of over 10,000 by volume was necessary, and has been verified experimentally[68]. The distribution shown in Figure 3.1 shall be used in this study to estimate the response from a distribution of Definity single scatterers.

3.3.3 Equations used in the model

A Keller-Miksis type equation was used to model the motion of the bubble wall. It has been shown that this produces similar results to the alternative Rayleigh-Plesset model[45]. The equations of motion for the liquid, derived from the conservation equations for mass and momentum, allow ordinary differential equations to be derived for the bubble radius as a function of time. The Keller-Miksis equation[45] models the surrounding liquid by assuming linear compressibility, and has the advantage over the Rayleigh-Plesset model by including a finite speed of sound in the surrounding liquid, which allows the model to account for radiation damping[8]. This has been shown by Prosperetti[47] to be especially relevant in the case of intermediate Mach numbers, as is the case for the pressures used in diagnostic ultrasound. The equation used here to model the motion of the bubble wall takes the form;

$$\rho R\ddot{R}\left(1-\frac{\dot{R}}{c}\right)+\frac{3}{2}\rho\dot{R}^2\left(1-\frac{1}{3}\frac{\dot{R}}{c}\right)=\left(1+\frac{\dot{R}}{c}\right)P+\frac{R\dot{P}}{c} \tag{3.1}$$

where

$$P\equiv\left(P_{st}+\frac{2\sigma}{R_0}+P_{shell}|_{R_0}\right)\left(\frac{R_0}{R}\right)^{3\gamma}-\frac{2\sigma}{R}-P_{shell}|_R-P_a(t)-P_{st} \tag{3.2}$$

The P_{shell} term relates to the behaviour of the shell, as defined by the shell model described below. $P_a(t)$ is the incident acoustic pressure (kPa), and P_{st} is the hydrostatic pressure ($P_{st} = 103\mathrm{kPa}$). Surface tension equals $\sigma = 0.0728\mathrm{Nm}^{-1}$, and the ratio of specific heats $\gamma = 1.4$. Other variables used are viscosity of water $\eta_L = 0.001\mathrm{Pas}$, density of water $\rho = 1000\mathrm{kgm}^{-3}$ and speed of sound in water $c = 1500\mathrm{ms}^{-1}$.

3.3.4 Choice of shell model

The various models described in Chapter 1, predict many characteristics of microbubble behaviour, but are limited by the definitions they take for the material's mechanical behaviour. These "Hookean models" (i.e. models that use Hooke's Law to define this property) use a simplified definition for the elasticity modulus of the material, which ignores the changes in the shell material with varying mechanical index (MI). For most materials this is not the case, and they will exhibit a varying elasticity modulus when subject to increasing pressures or fre-

quencies. This can lead to deviations in predicted results from measured behaviour due to differences in values for membrane elasticity, which directly determines the microbubble's dynamic behaviour. Depending on the way the elasticity modulus varies, there are two different types of models that can depict the dynamics of microbubble wall motion. Materials, such as rubber, whose stress-strain relationship exhibits a decrease in gradient as the incident pressure increases are termed strain softening materials, and can be modeled using the Mooney-Rivlin Law. Materials whose stress-strain ratio increases at a greater amount as the deformations increase, which corresponds to an increase apparent elasticity modulus, are termed strain hardening. Such materials should be defined using a model that is able to describe this type of behaviour, such as the Skalak law[85]. The importance of the choice of model to define these material properties has been shown in the literature[116]. In the results presented here, a Mooney Rivlin shell model will be used, as suggested previously to be relevant for Definity[116], which behaves as a softer-shelled agent at larger amplitudes.

The Mooney-Rivlin model defines the shell properties as follows;

$$P_{Shell} \equiv \frac{2d_{Se}G_S}{R}\left(1-\left(\frac{R_0}{R}\right)^6\right)\left(1+B\left(\left(\frac{R}{R_0}\right)^2-1\right)\right)+\frac{12\dot{R}\eta_S d_S}{{R_0}^2} \tag{3.3}$$

Where, similar to the strain hardening Skalak model, the variable B is a measure of strain softening of the shell. Here this will be set to $B = 0$, for large amounts of softening corresponding to the nature of a Definity phospholipid shell.

3.3.5 Resonance frequency

The equations above lead to the bubble's resonance frequency being dependent upon a variety of factors. At low amplitudes, i.e. in the linear case, for a bubble of initial radius R_0, the frequency of resonance is defined as;

$$f_{Res} = \frac{1}{2\pi R_0\sqrt{\rho}}\sqrt{f_0^2-\frac{\nu^2}{2\rho R_0^2}} \tag{3.4}$$

The frequency f_0 is defined as;

$$f_0 \equiv \sqrt{\left(\frac{2\sigma}{R_0} + P_{st}\right) 3\gamma + 12 G_S \frac{d_S}{R_0} - \frac{2\sigma}{R_0}} \tag{3.5}$$

As can be seen in Equation 3.5, the resonance radius is dependent upon the shell stiffness parameter G_S. However, as the incident pressure is increased, the bubble's behaviour becomes nonlinear, and this linear relationship breaks down[118]. The incident pressure will therefore have an effect on the resonance frequency, and this is shown in more detail below. Resonance frequency and radius is defined as that at which peak fundamental scatter is obtained, unless otherwise stipulated.

3.4 Methodology

The above equations have been implemented as a simulation model using MATLAB(R2007b, Mathworks). Matlab code was developed based upon original work by N. Pelekasis, K. Tsiglifis (Department of Mechanical Engineering, University of Thessally, Volos, Greece)[85]. The associated ordinary differential equations have been solved for a variety of initial bubble radii R_0 using a Runge-Kutta method, and in response to a variety of experimentally measured imaging pulses, applied by the ODE solver 'ode23.m' in MATLAB, and implemented in Matlab by P. Looney (Medical Physics, The University of Edinburgh, Edinburgh, UK). The Matlab scripts to solve the differential equations were written by P. Looney, but all subsequent analysis (and corresponding Matlab scripting) was performed by the author of this thesis. The contrast agent bubble is described by its initial radius and its shell properties, and the ODE solver calculates the radial dynamics of the bubble. Using a typical PC (for example Intel Core2 Duo 2.2GHz) the required calculation time is around one minute for each six cycle ultrasound response, giving calculation times of around two hours for a distribution of 100 bubbles. The Vokurka equation[51] (Equation 3.6) is then used to calculate the scattered pressure P from each bubble, at a distance $r = 0.075m$ from the microbubble (as measured experimentally).

$$P(r) = \frac{\rho R}{r}(R\ddot{R} + 2\dot{R}^2) \tag{3.6}$$

An experimentally measured size distribution is used to produce a sample of initial bubble radii, allowing direct comparison with experimental results. The calculated bubble responses have been decomposed into the various components of harmonics using the same filters defined

in Chapter 2, and the results are analyzed below.

3.5 Results

The equations above were used to calculate the bubble dynamics in response to real transmit pulses (measured using the membrane hydrophone system as detailed in Chapter 2). The results for the Mooney Rivlin strain softening model are presented. Results are presented in an 'energy density' -like value, as defined previously in Chapter 2, where;

$$\int_{t_{min}}^{t_{max}} |P_f(t)|^2 dt, \tag{3.7}$$

where f is the frequency component.

In all subsequent text, this shall be refered to as the unit of 'energy density', in units of Pa^2s.

3.5.1 Mooney Rivlin results

The variations in energy density, as predicted by the Mooney Rivlin strain softening model in response to a 1.6MHz, 550kPa six cycle typical imaging pulse are shown in Figure 3.2, with the RF, fundamental and second harmonic components plotted. Fundamental and second harmonic scatter have been concentrated on here, as clinical imaging schemes are yet to implement higher harmonic imaging, due to drawbacks in transducer technology. Bubble signals have been calculated with a radial resolution of 0.02μm, and a clear resonance peak (maximum fundamental scatter) at initial radius of $R_0 = 4.54\mu$m can be seen. The amount of harmonic components in the respective bubble's responses differs significantly from below to above resonance, and the position of these energy-radius curves will change with the resonance radius as the frequency is increased. Here, at 1.6Mhz, the peak in fundamental scatter, which is the stronger component ($0.0112\mathrm{Pa}^2\mathrm{s}^{-1}$ at $R_0 = 4.54\mu$m), is shifted with regards to the peak in second harmonic response ($0.0028Pa^2s^{-1}$ at $R_0 = 3.56\mu m$) by $0.82\mu m$, indicating that maximum overall response occurs at a relatively reduced harmonic. This shift is due to second harmonic resonance occurring at $R_0 = 3.56\mu$m (where the prime resonance frequency is twice that of the incident frequency)[122]. The proximity of the two resonance peaks (fundamental and second harmonic) is dependent on both incident frequency and acoustic pressure, due to nonlinearities increasing with mechanical index. Although the second harmonic peak is not directly identifiable in the RF

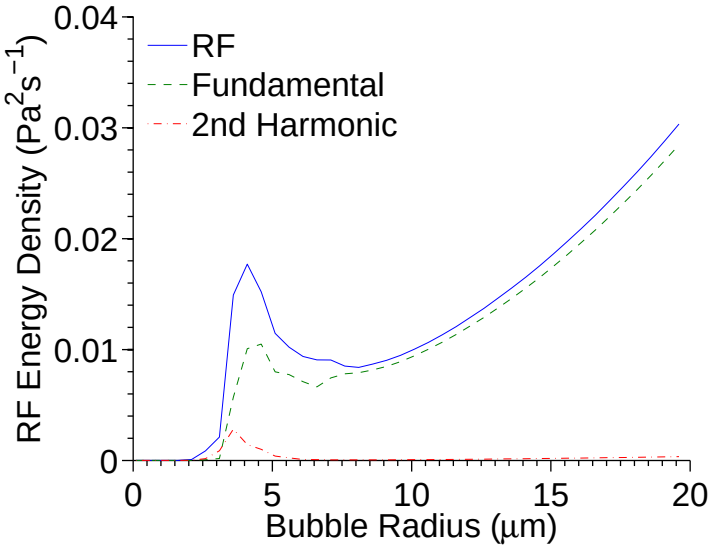

(a) Responses for bubbles with radii $R = 0.1 - 20\mu\text{m}$.

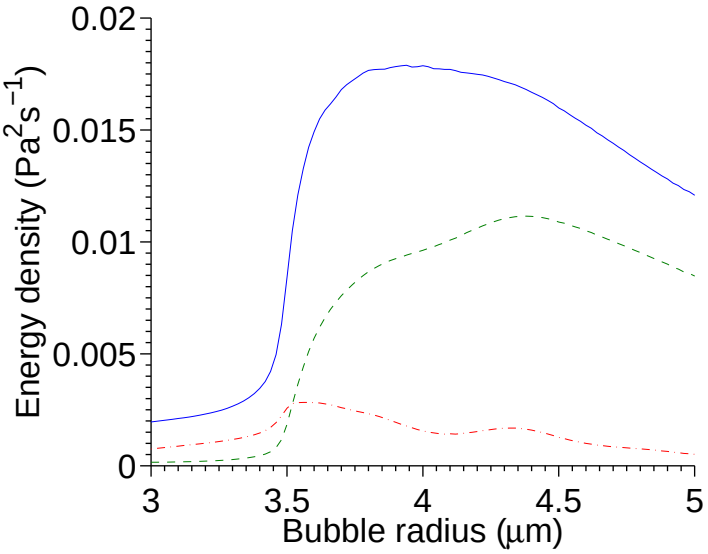

(b) Responses for bubbles with radii $R = 3 - 5\mu\text{m}$.

Figure 3.2: *Variation in energy density as predicted by the Mooney-Rivlin strain softening model, in response to a 1.6MHz, 550kPa six cycle pulse, as measured by a membrane hydrophone. The graphs show how the fundamental and 2nd harmonic peak scatter is off-set. 3.2(b) is an expanded version of 3.2(a), showing in detail how the energy densities vary as the bubble radius approaches resonance.*

data (as it is 'over-shadowed' by the tail of fundamental resonance peak), its presence leads to the region of harmonic dominated scatter for bubbles with initial radii less than $R_0 = 3.62\mu\mathrm{m}$.

Figures 3.3 shows the radial response, R.F. scattered pressure and fundamental component of scatter from three example bubbles; below resonance, at resonance and above resonance (where resonance refers to maximum fundamental scatter). At resonance the radial response, and thus the scattered pressure wave, is dominated by the expansion phase of the bubble, with an expansion to compression ratio ($E/C_R = R_{max}/R_{min}$) of over 7. The time-frequency representation of these signals, as calculated by the short time Fourier transform (STFT) function in MATLAB (normalised to the maximum energy of each signal), is shown in Figures 3.3(j)–3.3(l), and shows the differences between the harmonic components of the signals in greater detail. Here, maximum energy is shown in red, and confirms maximum relative harmonic scatter at below resonance. A bubble of radius $R = 1.6\mu\mathrm{m}$ will produce a relatively stronger harmonic signal than a bubble at $R = 4.54\mu\mathrm{m}$, and the signal is constant with time. This dominant harmonic is observed in bubbles of radii up to $R = 3.62\mu\mathrm{m}$, corresponding to 24.6% of the peak fundamental scatter. This nonlinear scatter will therefore make up a significant amount of the signal from a sample of contrast agent. That the peak signal is shown to have reduced second harmonic scatter (with fundamental nearly seven times stronger), provides an identifying factor for fundamental resonance behavour in individual bubble signals.

3.5.2 Affect of a size distribution

How these energy variations effect a real sample of Definity bubbles can be investigated using the experimentally measured radial distribution (Figure 3.1). The Mastersizer results measured a total of 35380 bubbles, with a resolution of $0.1\mu\mathrm{m}$. The above energy density results were used to calculate the minimum bubble size that can be measured experimentally. This was calculated using the noise floor of the experimental system, which was defined as the level of signal recorded when no bubbles were present (i.e. the electrical noise of the system). The size of such a bubble which would scatter with this level of signal was then calculated, and this radius used to threshold the size distribution. For example, in response to a 1.6MHz 550kPa six cycle pulse, the fundamental energy density noise-floor of the system has been calculated at $1 \times 10^{-6}\mathrm{Pa}^2\mathrm{s}$, which corresponds to a bubble of size $R_0 = 1.76\mu\mathrm{m}$. At these imaging parameters a large proportion of bubbles (88% of the scatterers by number) produce scatter at levels below this level, which is due to the peak in the size distribution at sub-micron radii

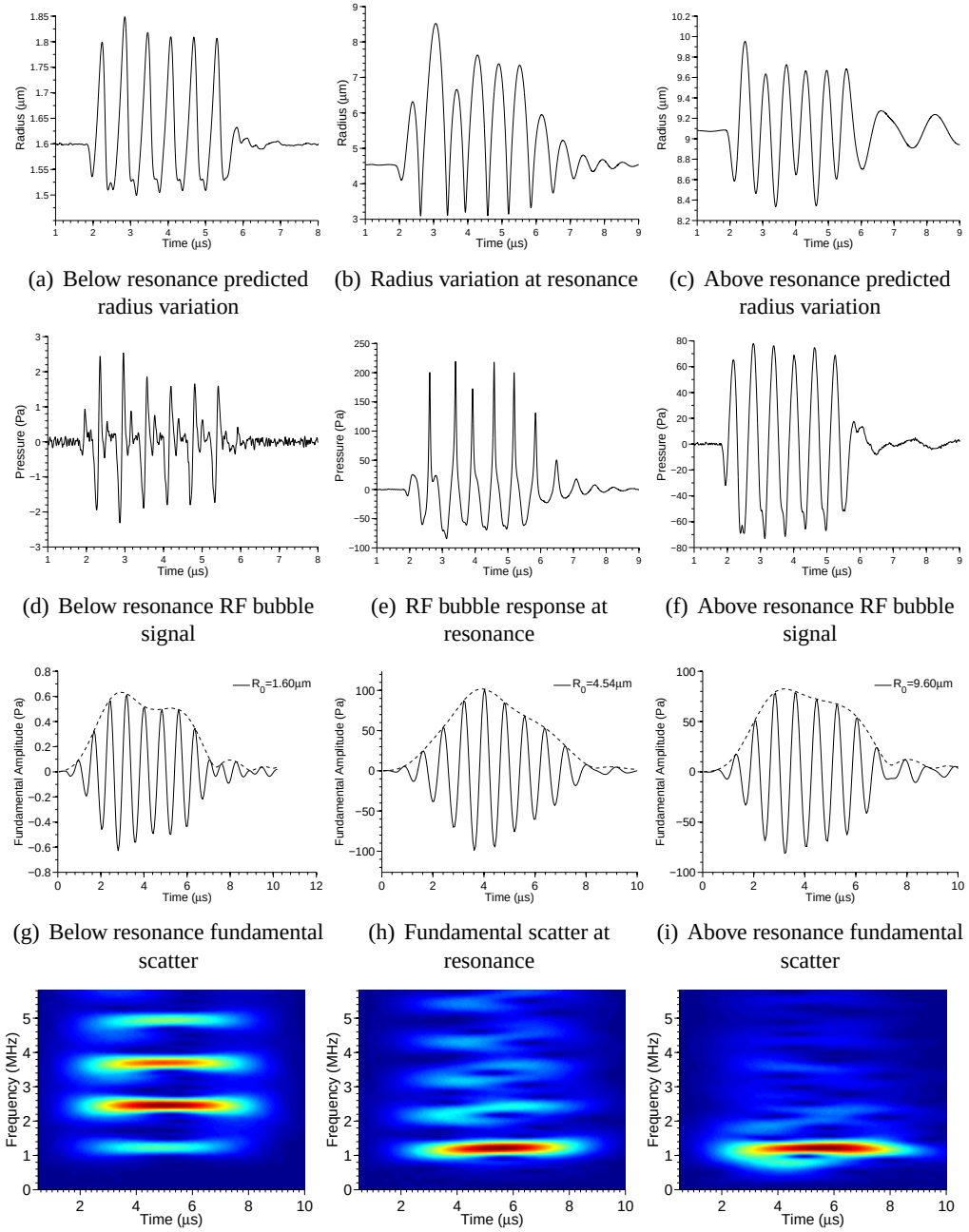

(a) Below resonance predicted radius variation

(b) Radius variation at resonance

(c) Above resonance predicted radius variation

(d) Below resonance RF bubble signal

(e) RF bubble response at resonance

(f) Above resonance RF bubble signal

(g) Below resonance fundamental scatter

(h) Fundamental scatter at resonance

(i) Above resonance fundamental scatter

(j) Below resonance RF bubble signal, STFT representation

(k) Bubble response at resonance, STFT representation

(l) Above resonance RF bubble signal, STFT representation

Figure 3.3: *Variation in bubble response below ($R_0 = 1.6\mu\mathrm{m}$), at ($R_{res} = 4.54\mu\mathrm{m}$) and above ($R_0 = 9\mu\mathrm{m}$) resonance, where R_{res} is defined as maximum fundamental scatter. Figures (a)-(c) show radial excursions of the driven bubbles, (d)-(f) show R.F. scatter, (g)-(i) fundamental components of scatter, and (j)-(l) show normalised short time Fourier transform (STFT) representation, as calculated in MATLAB, showing the relative components of harmonic scatter present in each signal.*

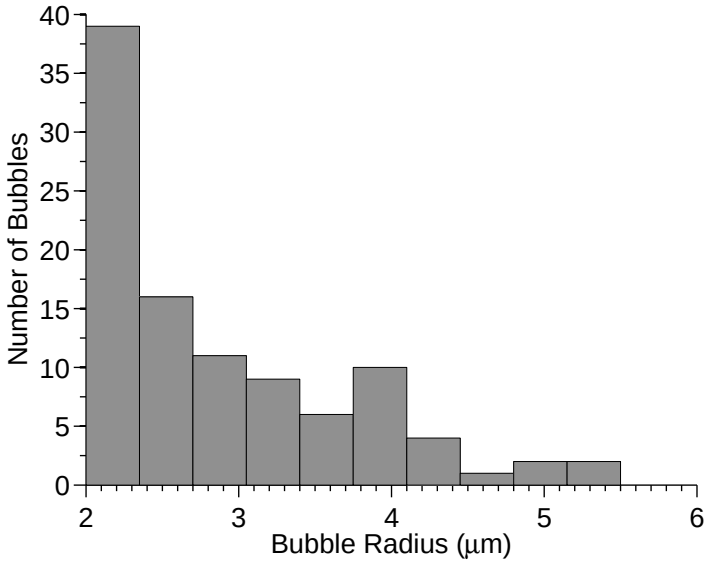

Figure 3.4: *A random sample of 100 Definity microbubbles whose scatter is above the noise level of the experimental system, as taken from the Mastersizer measured distribution of 35380 Definity bubbles.*

measured in the Mastersizer.

This thresholded size distribution of 4246 bubbles was then used to randomly sample 100 initial bubble radii, producing the sample distribution shown in Figure 3.4. This has in turn been used to calculate 100 bubble signals in response to a 1.6MHz 550kPa pulse, as shown in the scatter plot in Figure 3.5. The responses have been plotted with the signals decomposed into fundamental energy density (on the x-axis) and the 2nd harmonic (on the y-axis). Frequency dependent experimental error, as calculated in Chapter 2 from a series of well-characterized solid sphere measurements, was added to the energy densities of these bubbles (7.1% fundamental and 5.5% harmonic standard error for the imaging parameters used here). This allows the data to be compared to experimentally measured values.

Figure 3.5 shows a scatter plot of the energy distribution of 100 theoretically calculated responses from a 1.6MHz 550kPa pulse. Signals have been decomposed into the various components of harmonics, and plotted as fundamental versus 2nd harmonic. A two population response in the fundamental scatter is present as can clearly be seen in both the scatter plots and the histograms of scatter (Figure 3.6), due to the steep increase of scattered energy at resonance. These two populations, of resonant scatter and off resonant scatter have been classified in Figure 3.5 using cluster analysis methods[123]. Here, each scattered signal is considered as an

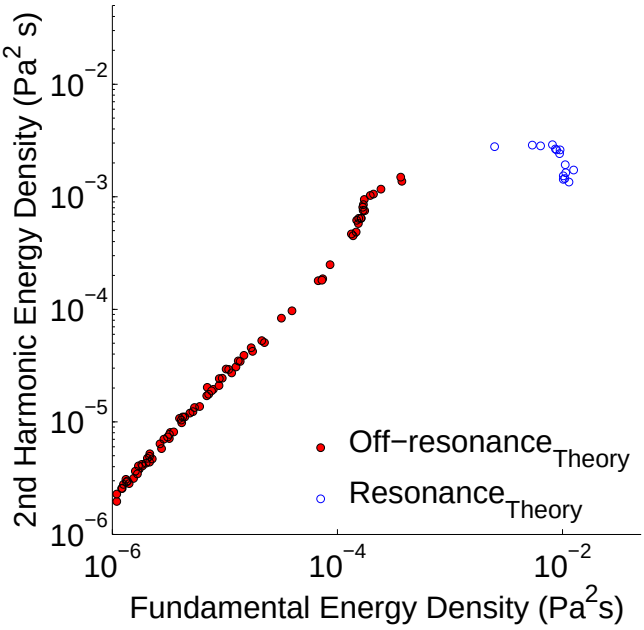

Figure 3.5: *Variation in bubble response, as calculated using the random sample of 100 bubbles shown in Figure 3.4 (1.6MHz 550kPa six cycle incident pulse). Experimental error has been added to the simulated bubble signals. A significant difference in fundamental energy density is observed between those bubbles which produce maximum scatter (16% by number) and those at lower energy scatter. Bubbles have been classified as resonant or off-resonance using cluster-analysis methods.*

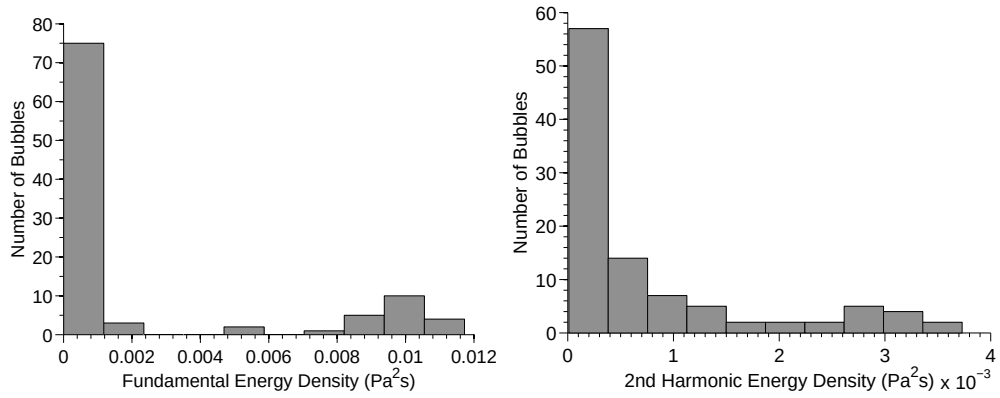

(a) Histogram of fundamental energy densities (b) Histogram of harmonic responses

Figure 3.6: *In response to a 1.6MHz 550kPa six cycle pulse, the distribution of 100 bubbles shown in Figure 3.4 produces a two population response in the fundamental scatter. The difference in harmonic signal of the highest scatterers and those with lower energy is less pronounced than the difference in fundamental energy.*

x-y coordinate (fundamental- 2nd harmonic energy density), and by calculating the Euclidean distance between each sample point a dissimilarity matrix has been calculated (implemented with the 'pdist' function has in MATLAB Statistics Toolbox 6). This information has been used to group the data into a relevant number of clusters (using the 'linkage' function in MATLAB), producing the two populations shown in Figure 3.5 showing a clear separation.

3.5.3 Effect of varying the shell parameters

Figure 3.2 shows the variation in energy of response for a distribution of bubbles, modeled with a shell stiffness of $G_s = 50\mathrm{MPa}$ (incident pressure of 1.6MHz, 550kPa six cycles pulse). This value of G_s was chosen from the mean of a variety of values quoted in the literature for Definity, as previously outlined. Figure 3.7 shows the effect of varying this parameter on the resonance peak response (for the same incident pulse). For increased values of shell stiffness (up to $G_s = 60\mathrm{MPa}$ shown here), the greater constraint that the stiffer shell places on the bubble leads to less relative expansion and contraction, leading to lower energy signals for a bubble of the same radius. For a $R_0 = 4.0\mu\mathrm{m}$ bubble, fundamental energy density of scatter reduces from $5 \times 10^{-}3Pa^2s$ for $G_s = 10\mathrm{MPa}$ to $2 \times 10^{-}4Pa^2s$ for $G_s = 80\mathrm{MPa}$. However, the resonance frequency is also dependent on shell stiffness, and increasing G_s gives a larger value for resonance radius R_{res}. This leads to larger bubbles being at resonance for greater values of G_s, which in turn leads to higher values of peak scatter, for the range of bubble radii investigated here.

Figure 3.7 shows how the peak fundamental energy density of scatter decreases from $0.0233\mathrm{Pa}^2\mathrm{s}$ for $G_s = 100\mathrm{MPa}$ at a resonance radius of $R_0 = 4.0\mu\mathrm{m}$ to $0.0040\mathrm{Pa}^2\mathrm{s}$ for $G_s = 10\mathrm{MPa}$ at a resonance radius of $R_0 = 3.2\mu\mathrm{m}$. This change in shell viscosity parameter is shown in Figure 3.8, with the fundamental and 2nd harmonic energy of scatter of a $R_0 = 4.0\mu\mathrm{m}$ bubble plotted for a variety of G_s values. Due to this increase in resonance radius with shell stiffness, both fundamental and 2nd harmonic values increase with shell stiffness from $G_s = 0 - 30\mathrm{MPa}$, where a maximum value of fundamental is reached. Maximum 2nd harmonic is achieved at a value of $G_s = 40\mathrm{MPa}$, due to this stiffness giving a 2nd harmonic resonance peak closest to the bubble radius. Stiffer values than this show significant decrease in fundamental scatter, due to reduced bubble movement.

Figure 3.9 shows how changing this value of stiffness affects the overall response from the experimentally measured distribution of bubbles shown in Figure 3.1. Changing the value of

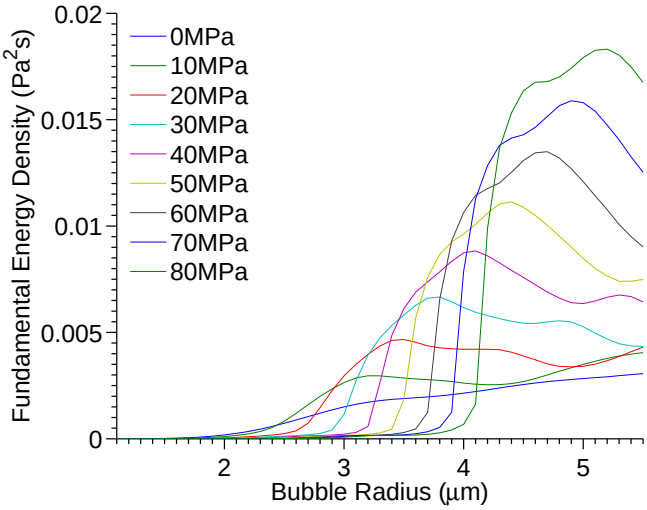

(a) Fundamental Energy Density

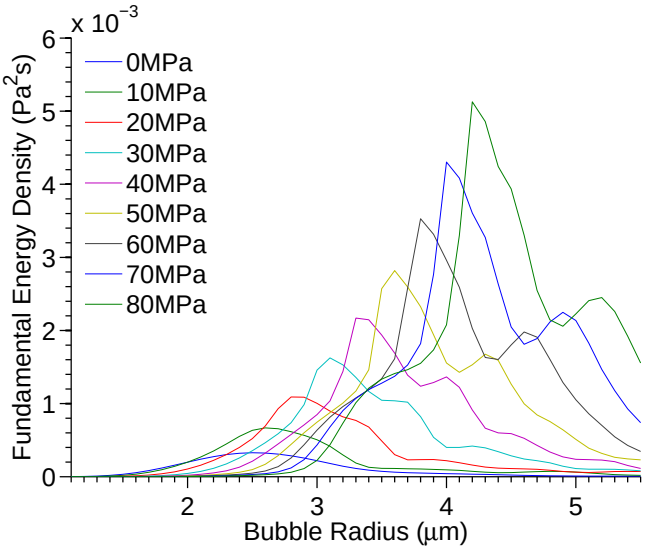

(b) 2nd Harmonic Energy Density

Figure 3.7: *Variation in energy of response for a variety of shell stiffnesses. Maximum peak scatter is seen for the largest shell stiffness ($G_s = 80\text{MPa}$), due to the increased resonance radius. However, for a fixed bubble radius, increasing shell stiffness can lead to either an increase or decrease in scatter, as shown in Figure 3.8.*

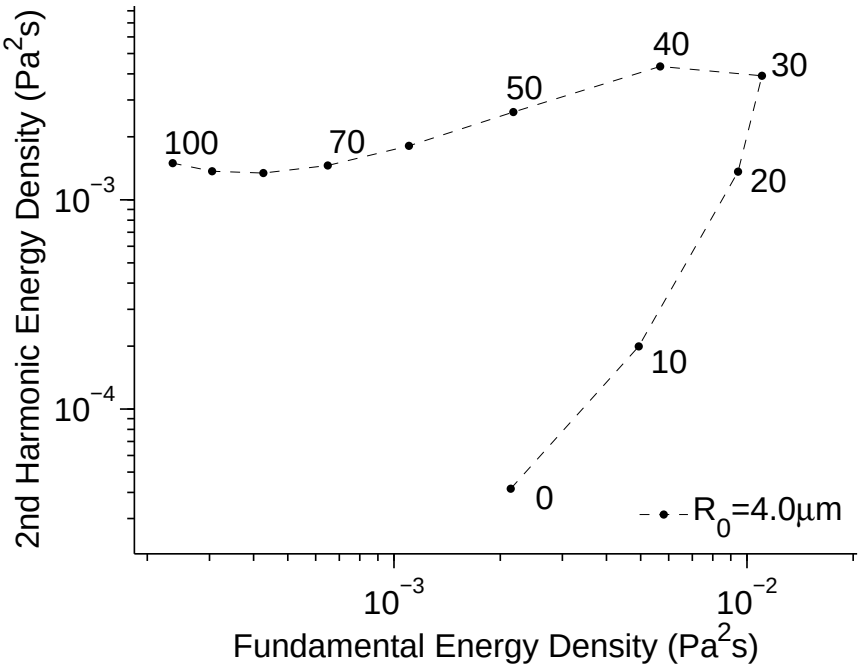

Figure 3.8: *Variation in response from a $R_0 = 4.0\mu\mathrm{m}$ bubble for a variety of shell stiffnesses (the numbers on the plot have units of MPa). The scatter shows maximum fundamental energy of scatter at $G_s = 30\mathrm{MPa}$, whereas maximum 2nd harmonic scatter is reached at $G_s = 40\mathrm{MPa}$. The value of shell stiffness which leads to peak scatter is dependent on the bubble radius, as shown in Figure 3.7. Shell stiffness therefore has a complex relationship with the energy of scatter from a distribution of bubbles.*

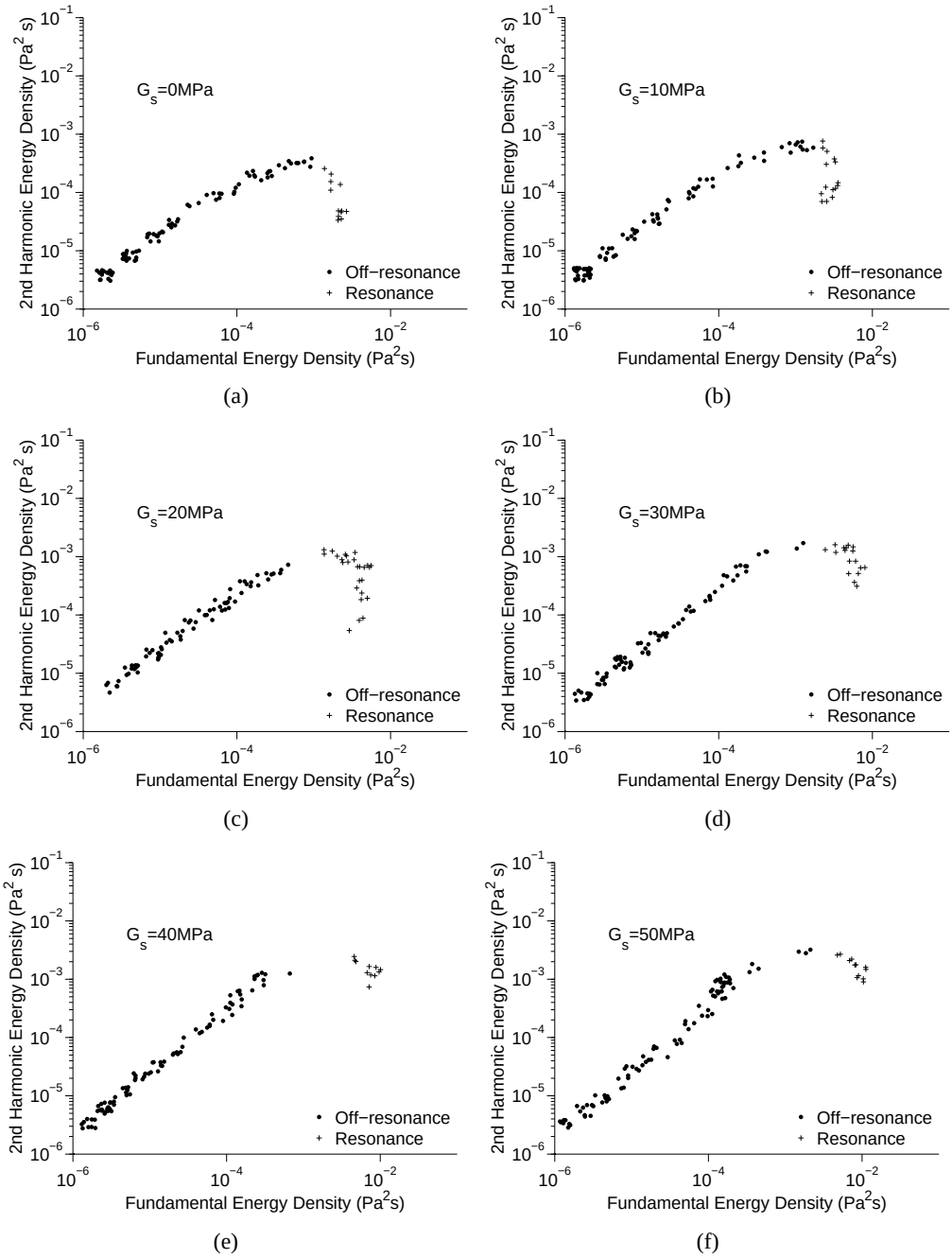

Figure 3.9: *Variation in energy of response for a variety of shell stiffnesses, for a random sample of 100 bubbles from the experimentally measured size distribution shown in Figure 3.1. Maximum peak scatter is seen for the largest shell stiffnesses ($G_s = 50\mathrm{MPa}$), due to the increased resonance radius.*

G_s has a greater effect on the population of bubbles defined to be at resonance than those off resonance. Figure 3.5 shows the distribution obtained using a shell stiffness parameter of $G_s = 50\text{MPa}$, which gives a mean resonance fundamental scatter of $0.0091Pa^2s$, with 15% of bubbles defined to be at resonance. For a value of $G_s = 10\text{MPa}$, peak fundamental scatter corresponds to a significant drop from the peak in 2nd harmonic scatter, as shown in Figure 3.9(b). This resonant population has a mean fundamental energy of scatter of $0.0033Pa^2s$, with 12% of bubbles defined to be at resonance. Figure 3.9 shows how this resonant population increases in energy in both fundamental and 2nd harmonic scatter with increasing shell stiffness, and thus the difference between the resonant and off-resonant population is also increased. However, due to the changing resonance radius, the numbers of bubbles that are defined to be at resonance decreases for larger values of stiffness for the distribution of bubbles used here. Even though the mean energy of resonant scatter increases for an increase from 10MPa - 90MPa, as shown in Figure 3.10, the number of scatterers included in this population reaches a peak at $G_s = 40\text{MPa}$ of 18.8%. The mean values of scatter have been calculated from 10 different random samples of bubbles. The error in the numbers of bubbles defined to be at resonance increases at lower values of shell stiffness due to the difference between the two populations being less than that at higher values (leading to larger differences between two random samples of bubbles).

Increasing the value for the shell viscosity has the opposite effect of increasing the shell stiffness, although on a smaller scale. Figure 3.11 shows how the energy density varies with increasing values of shell viscosity η_s, which shows increasing resonance radius corresponds to decreasing peak scatter. Due to the small differences between the peak values and the resonance radii concerned, changing the value for shell viscosity has little effect on a population response from the distribution of Definity bubbles measured earlier. This change in shell stiffness parameter is shown in Figure 3.12, with the fundamental and 2nd harmonic energy of scatter of a $R_0 = 4.0\mu\text{m}$ bubble plotted for a variety of η_s values.

3.5.4 Envelope effects

Figure 3.3 shows the variations predicted by the strain softening Mooney-Rivlin model for bubbles with radii below, at and above the resonance radius of $R_{res} = 4.54\mu\text{m}$, in response to a typical rectangular medical imaging pulse at 1.6MHz, 550kPa containing six cycles. Investigating the approach to resonance further shows that the envelope of the predicted signals changes

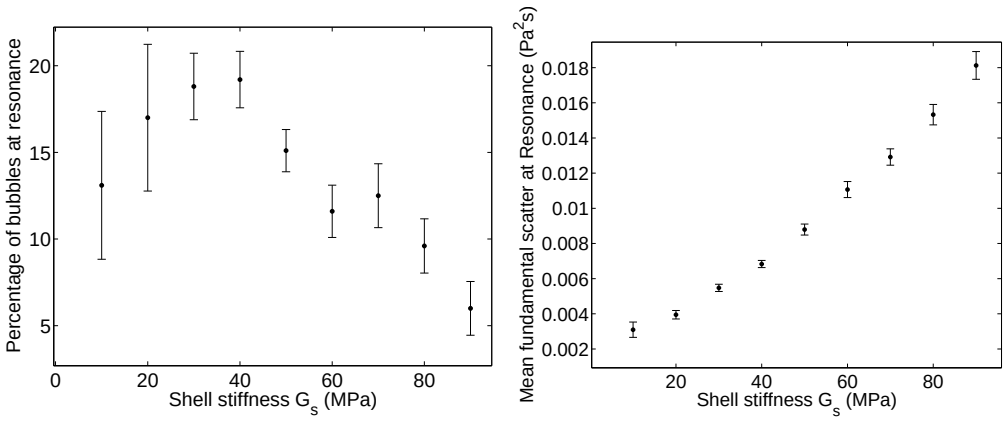

(a) Percentage of bubbles at resonance (b) Resonant fundamental energy density

Figure 3.10: *Variation in energy of resonant response for a variety of shell stiffnesses. Maximum peak scatter, and thus the largest difference between resonant and off-resonant scatter, is seen for the largest shell stiffnesses ($G_s = 60\mathrm{MPa}$), due to the increased resonance radius. The percentage of bubbles at resonance reaches a maximum at $G_s = 40\mathrm{MPa}$. Mean values ($\pm$ standard deviations) have been calculated from ten random samples of 100 bubbles.*

as the radius increases, as can be seen in Figure 3.13. Below resonance a fundamental signal is produced which is similar in shape to the fundamental incident pulse (both are slightly distorted from the rectangular incident RF pulse by the bandwidth of the transducer). The envelope of such a signal can be accurately calculated using a quadrature amplitude demodulation method (a function included in the MATLAB Signal Processing Toolbox(TM) 6.0, Mathworks), and is observed to be very similar to the incident pulse. As the bubble radius is increased toward resonance, this fundamental signal becomes distorted, with the envelope of the signal having increasing negative skew, which indicates an increasing fundamental signal with time, over the six cycle response. This effect of increasing amplitude at resonance is expected from simple harmonic oscillator theory, and has been observed in literature for forced damped oscillators[124]. The effect is at a maximum at radii corresponding to resonance, with fundamental scatter increasing to a peak in the first half of the six cycle response, and decreasing in the latter half of the response. This is similar to the predicted transient response of a simple forced harmonic oscillator.

This effect of increasing amplitude of scatter has been observed previously[8,125], but has not previously been identified as a feature of an encapsulated microbubbles approaching resonance. This may provide a useful tool in both analyzing experimental bubble data, and understanding

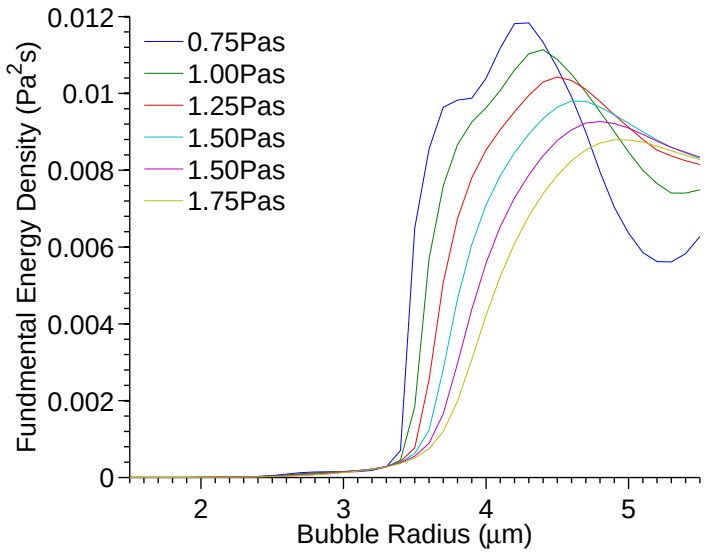

(a) Fundamental Energy Density

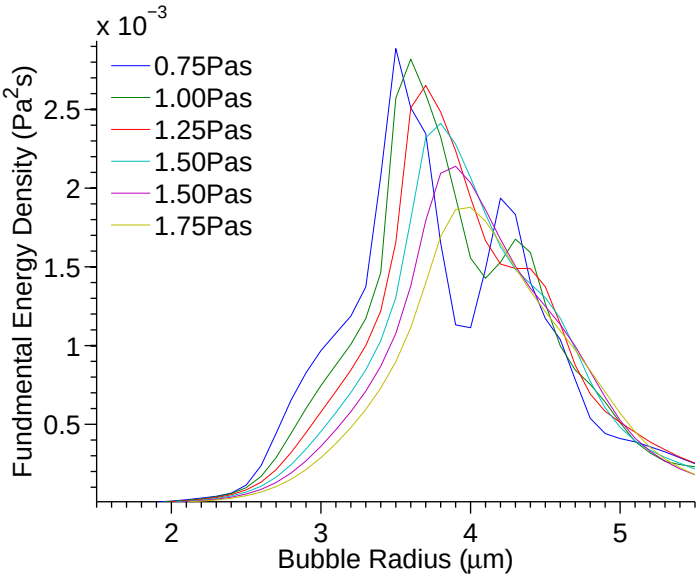

(b) 2nd Harmonic Energy Density

Figure 3.11: *Variation in energy of response for a variety of shell viscosities. Maximum peak scatter is seen for the smallest shell viscosity ($\eta_s = 0.75\mathrm{Pas}$), even though this occurs at a slightly reduced resonance radius*

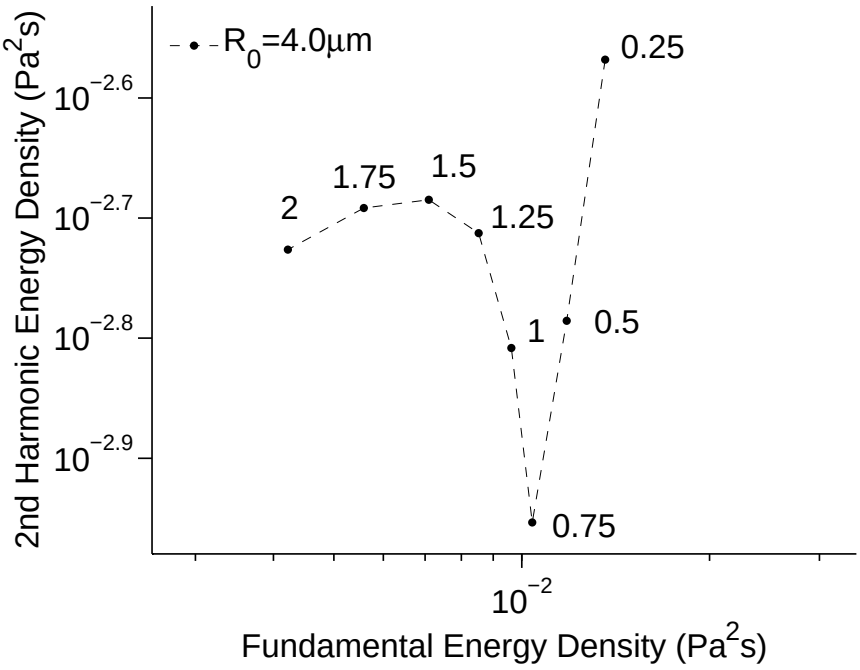

Figure 3.12: *Variation in response from a $R_0 = 4.0\mu\mathrm{m}$ bubble for a variety of shell viscosities (the numbers on the plot have units of* Pas*). The scatter shows maximum fundamental and 2nd harmonic energy of scatter at $\eta_s = 0.25\mathrm{Pas}$, although minimum harmonic scatter does not correspond to minimum fundamental scatter. The variations in scatter are less than that observed when varying the shell stiffness parameter G_s.*

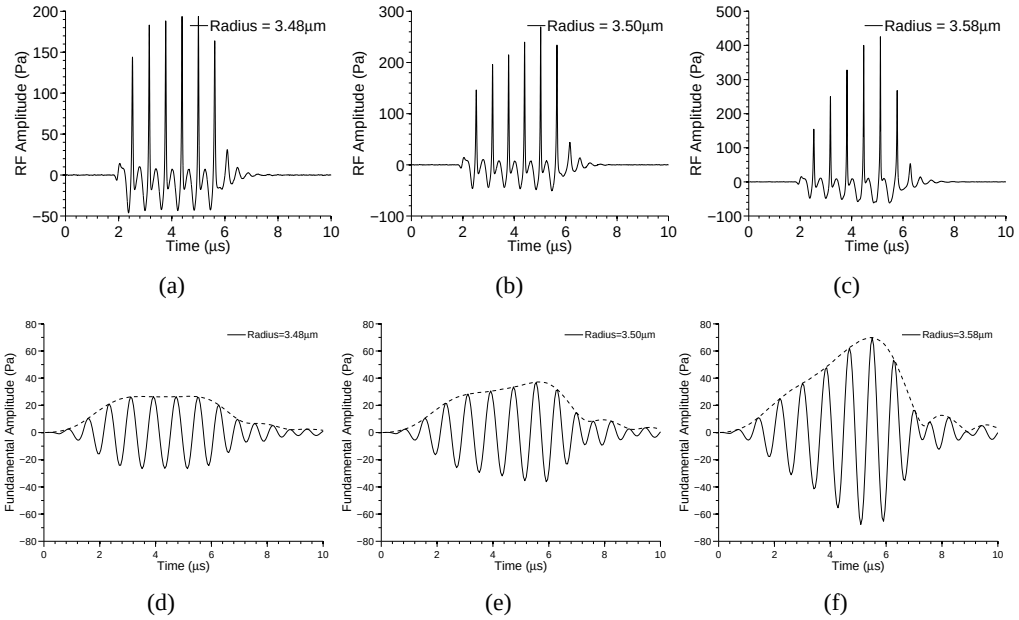

Figure 3.13: *As bubble radius is increased toward resonance, the signals show an increasing component of fundamental scatter across the six cycle response. Figures 3.13(a) – 3.13(c) show R.F scatter for increasing radius, and Figures 3.13(d) – 3.13(f) show the corresponding fundamental components of scatter.*

how the parameters of the soft lipid shell effect a bubble's response. The explanation for this increasing fundamental component of scatter lies in how a bubble at resonance absorbs the energy from the incident pulse, and has been previously described for simple harmonic oscillators[124]. As shown in Figure 3.3, the increasing fundamental component of scatter, whether increasing over the whole of the six cycle response, or increasing up to a peak and then decreasing back to steady state, coincides with an increasing maximal radius excursion. At a radius below resonance maximum radius is reached with the first cycle of the incident pulse, which is then followed by a bubble collapse to minimum radius. This collapse gives rise to the bubble shell acceleration which produces the maximum scattered pressure signal, which is then repeated over the six cycle incident pulse, leading to a constant amplitude of scatter. At an increased radius, closer to the resonance radius, although the first cycle leads to almost exactly the same radius increase (relative to the initial radius), the subsequent radial excursions then increase linearly up to a maximum, leading to an increasing component of scatter with time. At the resonance radius, this maximum scatter is reached in the third cycle, which is then followed by a decreasing scatter, leading to an approximately symmetrical envelope of scatter shown above (Figure 3.3).

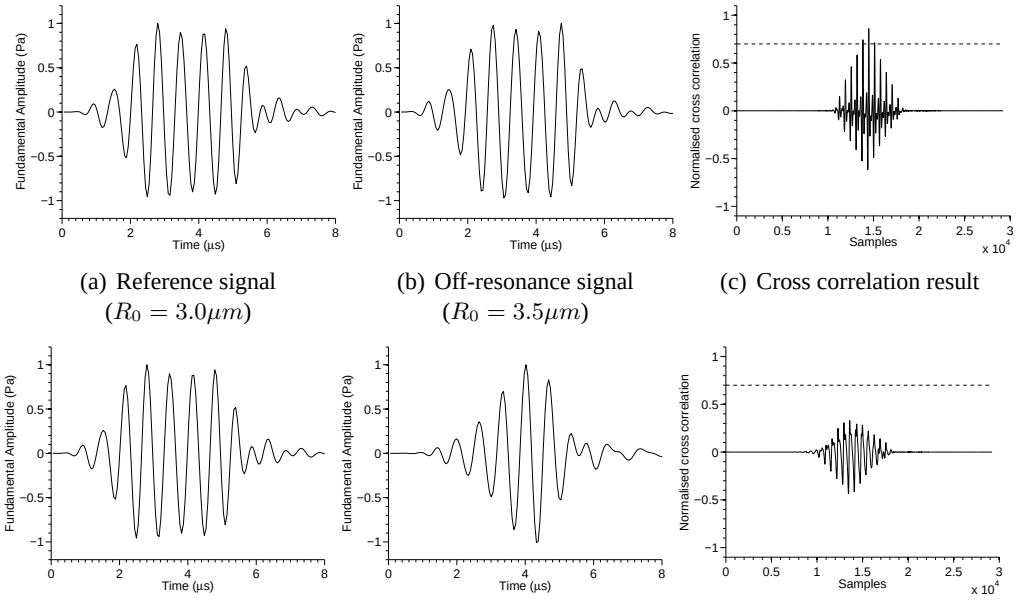

(a) Reference signal ($R_0 = 3.0\mu m$)

(b) Off-resonance signal ($R_0 = 3.5\mu m$)

(c) Cross correlation result

(d) Reference signal ($R_0 = 3.0\mu m$)

(e) Resonant signal ($R_0 = 4.3\mu m$)

(f) Cross correlation result

Figure 3.14: *Normalised cross correlation results can be used to compare the envelope of different signals . Using an off-resonance reference signal (a) with constant envelope (fundamental signal normalised to peak scatter shown), the difference between off-resonant (b) and resonant (e) normalised scatter can be determined by the peak cross-correlation results (c) and (f). Normalised cross correlation of RF signals shown, with a threshold peak of 0.7 shown.*

This effect can be quantitatively described by using a normalised cross correlation technique to compare the envelope of signals from different radii. It can be easily shown that when compared to a 'reference' off-resonant bubble signal of constant amplitude, a signal with increasing amplitude over time (resonant signal) has a decreased peak normalised cross correlation than one with similar constant amplitude, as shown in Figure 3.14. The incident pulse could also be used as the reference signal here, but would give reduced resolution in categorizing bubble signals, due to the expected differences between bubble signal envelopes and the incident pulse envelope. Figure 3.14(a) shows a reference (off-resonance) signal of constant amplitude ($R_0 = 3.0\mu\mathrm{m}$). When correlated with a $R_0 = 3.5\mu\mathrm{m}$ signal with similar envelope 3.14(b) this produces a signal of peak near one, whereas when correlated with a $R_0 = 4.3\mu\mathrm{m}$ resonant signal of increasing envelope with time 3.14(e), this gives a signal with peak of 0.36. Figure 3.15 shows how the peak cross correlation varies with radius, for a sample of scatterers.When plotted against fundamental energy density, a clear two population response can be observed by thresholding non-resonant behaviour at a peak correlation value of 0.7, leading to an identical classification as that calculated using cluster analysis earlier (Figure 3.16). As the bubble size is increased to well above resonance, the envelope of signal is predicted to be again similar to the incident pulse, as shown in Figure 3.3.

Although this technique does not use a precise description of the envelope to characterize each signal, the results agree well with the classification of signals using energy of scatter alone, confirming this as a valid technique with which to classify scatter.

3.5.5 Effect of increasing incident frequency

The transmitted frequency will affect the total response gained from a single distribution of bubbles, not only due to the total energy transmitted, but also due to the number of bubbles being present in each population. Figure 3.17 shows how the fundamental and 2nd harmonic energy densities vary with increasing frequency. As the frequency is increased, the transmitted energy in a six cycle pulse is decreased, and thus the peak scatter predicted by the Mooney Rivlin model decreases, with maximum peak scatter at 1.4MHz.

At larger frequencies, the resonant peak becomes less obvious, and eventually disappears. Figure 3.17 shows the results for nine frequencies at 550kPa. Above an incident frequency of 3.4MHz no resonance peak can be observed, leading to a reduction in the characteristic resonance behaviour as described above. Figure 3.19(a) shows the number of scatterers defined to

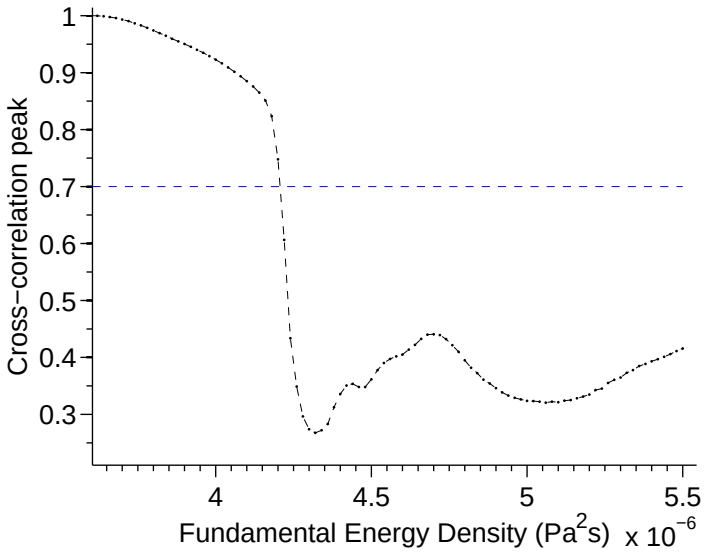

Figure 3.15: *Variation in normalised cross-correlation peaks for increasing bubble radii. As can be seen a threshold at 0.7 separates the two populations well, when using an off-resonance reference signal.*

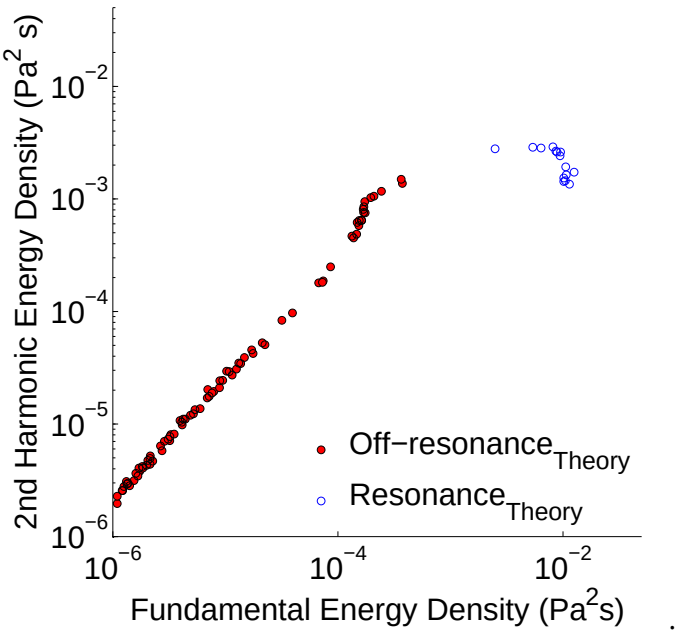

Figure 3.16: *Variation in bubble response, as calculated using the random sample of 100 bubbles shown in Figure 3.4 (1.6MHz 550kPa six cycle incident pulse). Bubbles have been characterized as resonant or off-resonance using a normalised cross correlation method, thresholded at a peak value of* 0.7*. This classifies the same number at resonance (*16%*) as the cluster analysis methods using energy density values alone (Figure 3.5)*

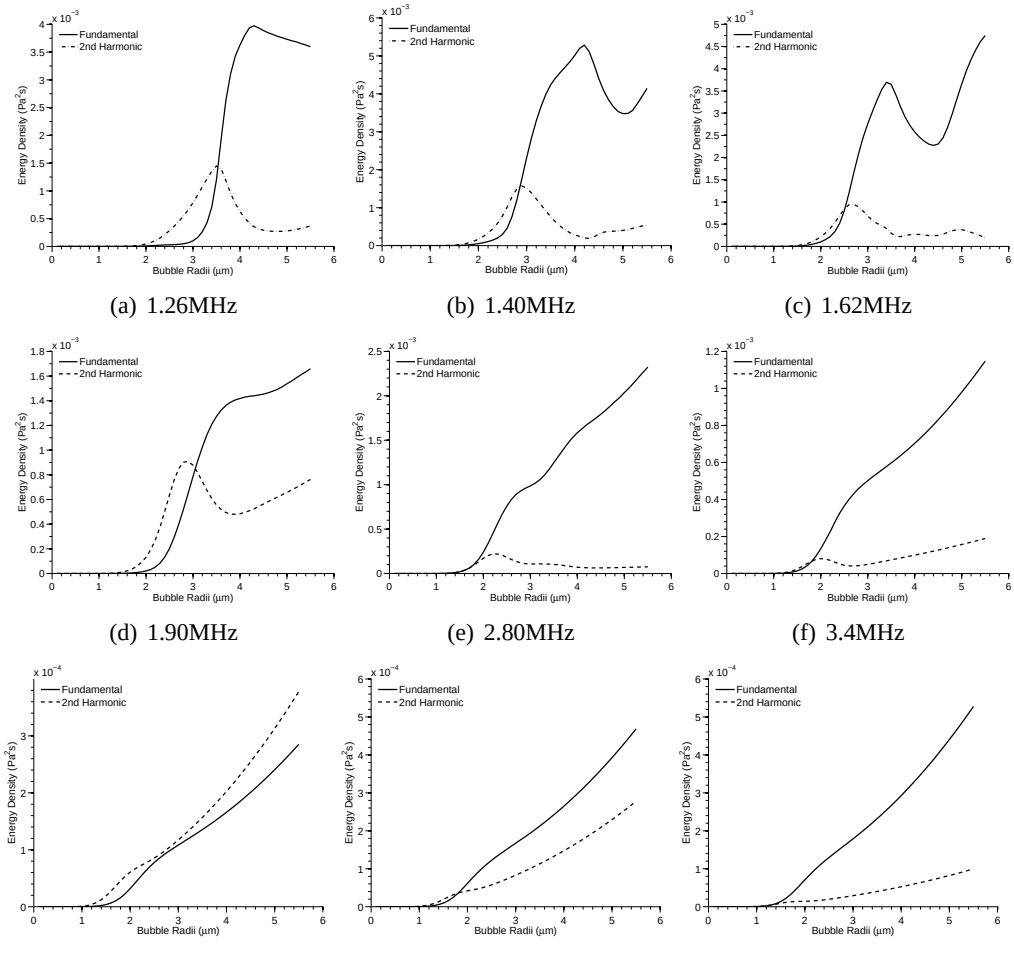

(a) 1.26MHz (b) 1.40MHz (c) 1.62MHz

(d) 1.90MHz (e) 2.80MHz (f) 3.4MHz

(g) 4.12MHz (h) 4.60MHz (i) 5.18MHz

Figure 3.17: *Variations in energy density with increasing frequency (550kPa, six cycle) imaging pulses. Above 3.4MHz no resonance peak is detectable, and the scatter can no longer be separated into resonant and off resonant scatter.*

be at resonance by the normalised cross correlation method described above. Resonant scatter decreases to less than 5% for frequencies above 3.5MHz.

The results from all four transducers calibrated in Chapter 2 are shown in Figure 3.19 and 3.18. In order to take into account the decreasing pulse energy density for increasing frequency, root mean square (RMS) pressures (Pa) are used to calculate a 'back-scattering cross section' (BSCS)-like quantity, to compare results from different transducers. To allow direct comparison of this with experimental results, which do not contain information on bubble size, BSCS has been modified to exclude the radius of each bubble, giving Equation 3.8. Mean fundamental scatter for each population has been plotted in 3.19. Figure 3.18 shows a scatter plot of the overall response from all four transducers. As can be seen in both figures, due to the resonance radius decreasing with increasing frequency, leading smaller bubbles being at resonance, the peak scatter is significantly reduced at higher frequencies. As the number of bubbles characterized as at resonance is also reduced significantly at higher frequencies, the off-resonance population shows an increase for higher frequencies.

$$\sigma = \frac{RMS_{Scatter}\ |^2}{RMS_{Incident}\ |^2} \tag{3.8}$$

3.5.6 Effect of increasing transmit amplitude

Results for varying acoustic pressures are presented for incident pressures of 1.6MHz six cycle pulses (as characterized in Chapter 2). A range of acoustic pressures, from 187kPa to 1.5MPa, were measured with the membrane hydrophone system previously outlined, and used as incident pulses in the above equations. The variation in energy densities is shown in Figure 3.20.

The number of bubbles classified to be at resonance increases with acoustic pressure, as shown in Figures 3.21 and 3.22. This in turn leads to a decrease in the mean scatter for off-resonance bubbles, as the mean size of off-resonant bubbles is subsequently decreased. The mean value of scatter for resonant bubbles increases with acoustic pressure due to the increased energy incident on the bubbles, as shown in Figure 3.22(b).

These results do not take into account any destructive effects caused by the high MI of the incident pulse, which is expected to take place. Pressures above a few hundred kPa have been shown to disrupt the encapsulating shell of soft-shelled microbubbles[4,72,92,95], and this is cur-

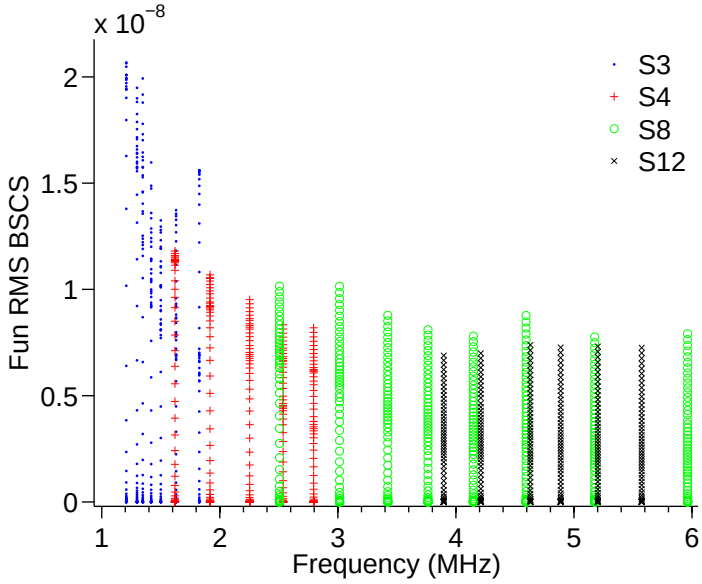

(a) Fundamental response

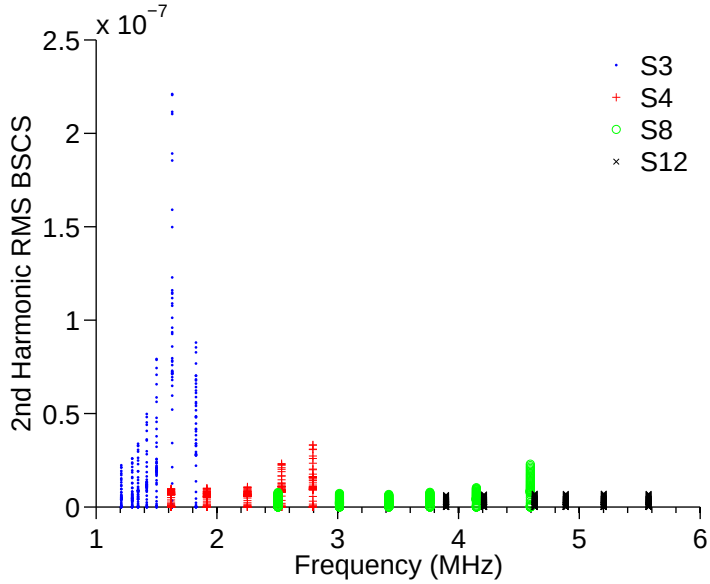

(b) Second harmonic response

Figure 3.18: *Response of a sample of Definity microbubbles to increasing frequency (550kPa, six cycle) imaging pulses. Results show back-scattering cross section-like results for all four transducers (*$1.2 < f < 5.5MHz$*). Peak scatter is achieved at 1.4MHz, and decreases with increasing frequency, due to the decreasing resonance radius.*

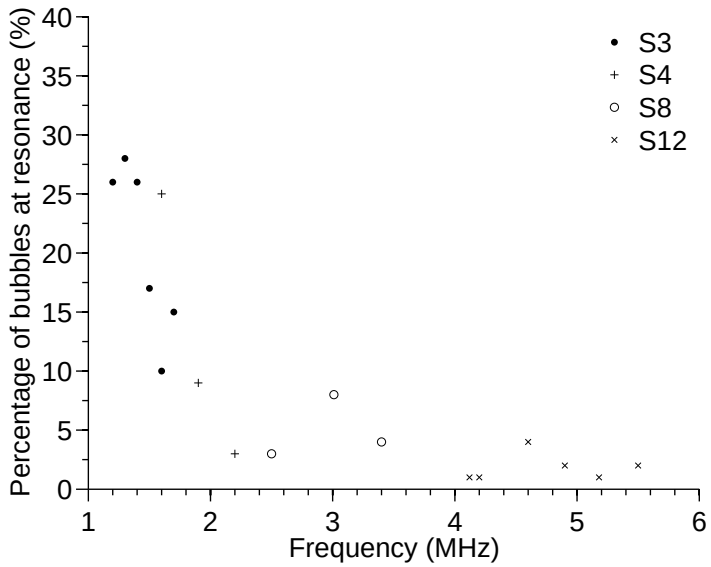

(a) Number of bubbles at resonance

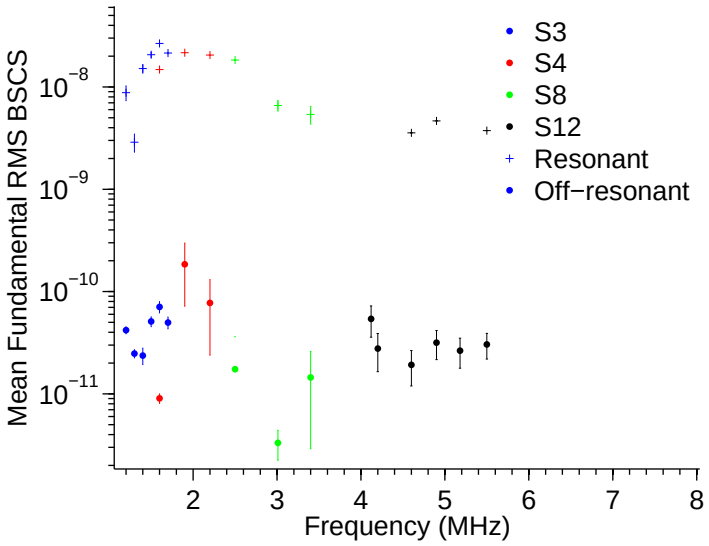

(b) Mean fundamental scatter for off-resonant and resonant bubbles

Figure 3.19: *Response of a sample of Definity microbubbles to increasing frequency (550kPa, six cycle) imaging pulses, calculated from the experimentally measured incident pulses from the four different transducers. (a) shows the number of bubbles classified as resonant by a normalized cross correlation analysis to be decreasing with frequency, due to the disappearance of the resonance peak. (b) shows back-scattering cross section-like results for all four transducers* ($1.2 < f < 5.5MHz$)*, with mean resonant (+) and mean off resonant scatter (.) shown. Peak scatter is achieved at 1.6MHz, and decreases with increasing frequency, due to the decreasing resonance radius.*

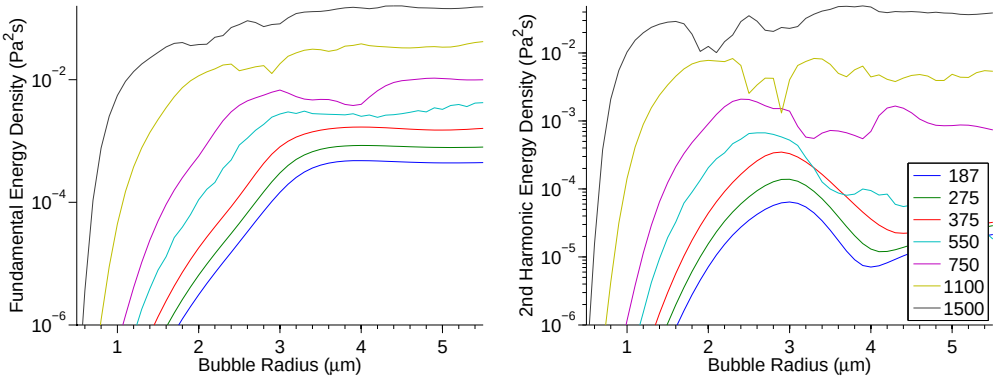

(a) Fundamental (b) 2nd Harmonic

Figure 3.20: *Effect of increasing acoustic pressure on bubble responses, from 187kPa-1.5MPa. The strong resonance peak in the 2nd harmonic, and the radial offset in peak response for fundamental and 2nd harmonic components, leads to the distinctive two population response outlined above for low to medium pressures. For a real sample of bubbles (as measured previously in Figure 3.1), the number of bubbles at resonance will increase with increasing acoustic pressure*

rently not included in the assumptions made for the theoretical model presented here. This will be investigated further in Chapter 6.

3.5.7 Higher harmonic resonance

The limitations of current transducer technology place the third harmonic at the edge of current imaging bandwidth. The above investigation has therefore concentrated on fundamental and second harmonic scatter. As shown in Chapter 2, the transducers used in the experimental investigation have the ability to measure third harmonic signals for a limited range of transmit frequencies at the lower end of each of the respective transducer's bandwidth. It has been shown that using higher harmonics has the potential for greatly improving the contrast to tissue ratio, depending on incident pulse parameters[126]. The variations of third harmonic scatter will briefly be investigated here.

Figure 3.23 shows the Mooney Rivlin results for fundamental, second and third harmonic variations in energy density with radius, in response to a 1.6MHz 550kPa six cycle pulse. As can be seen, each of the respective curves show peaks at decreasing radii, corresponding to the respective harmonic resonances. This leads to scatter at low radii being dominated by the higher order harmonics. Below $R_0 = 2.9\mu\mathrm{m}$ the scatter is dominated by the third harmonic scatter.

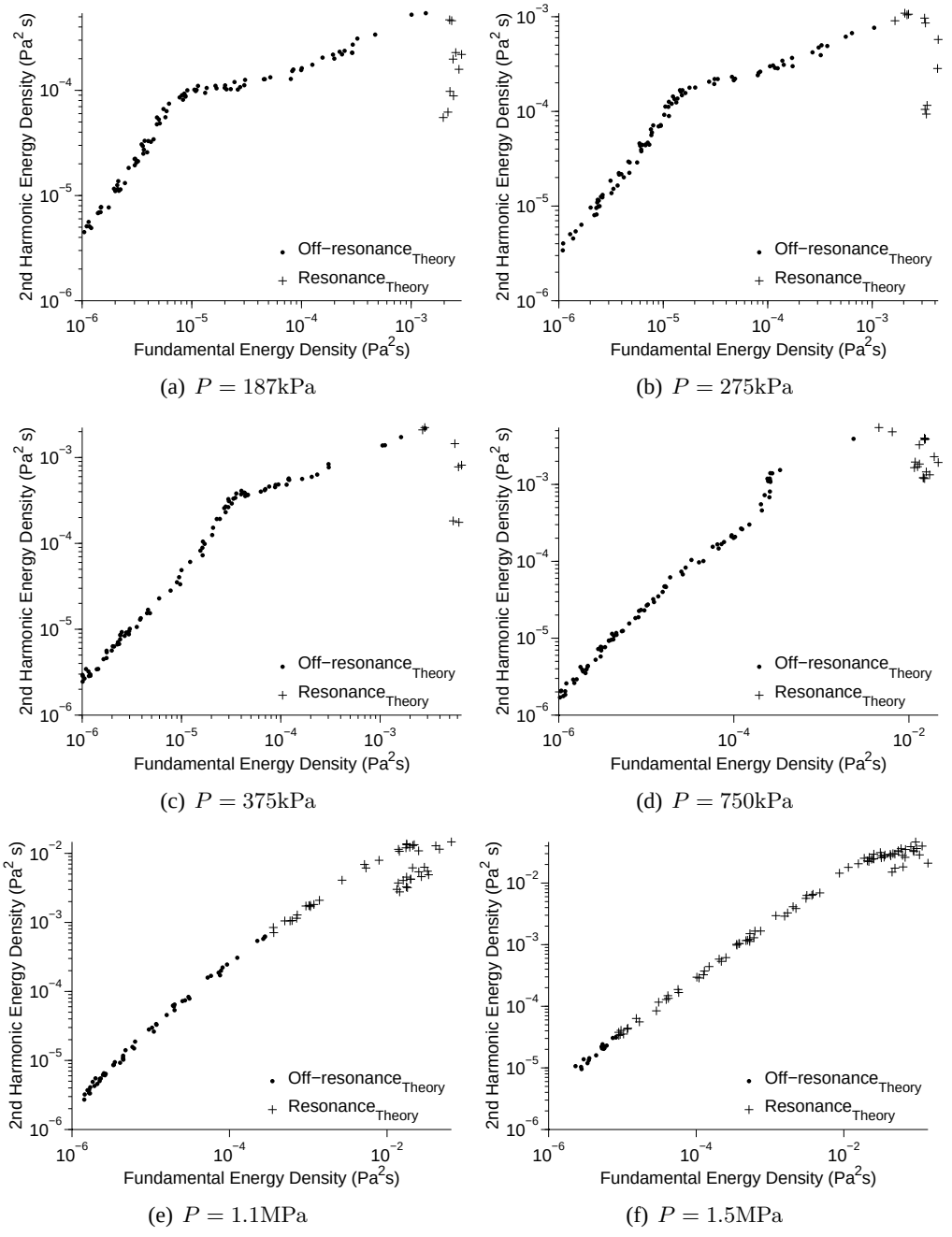

(a) $P = 187\text{kPa}$ (b) $P = 275\text{kPa}$

(c) $P = 375\text{kPa}$ (d) $P = 750\text{kPa}$

(e) $P = 1.1\text{MPa}$ (f) $P = 1.5\text{MPa}$

Figure 3.21: *Variation in energy of response for a variety of incident acoustic pressures (1.6MHz, six cycle pulses). Responses from a random sample of 100 bubbles from the experimentally measured size distribution shown in Figure 3.1, with shell stiffness value of $G_s = 50\text{MPa}$. The number of bubbles classified to be at resonance increases with incident pressure.*

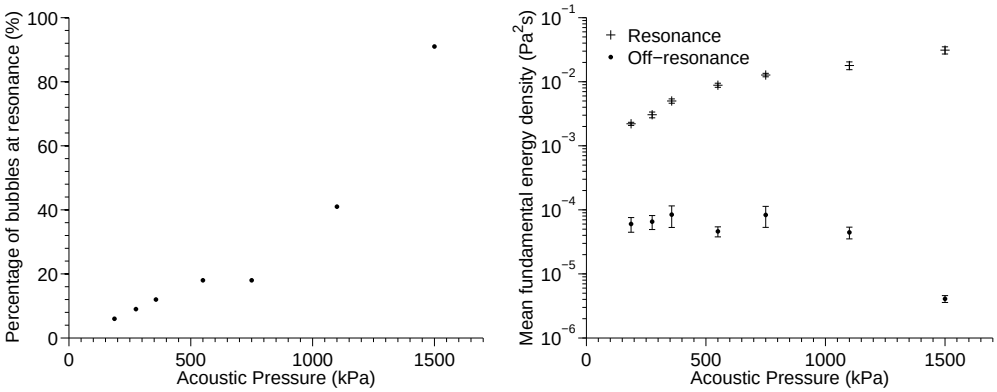

(a) Number of bubbles at resonance

(b) Mean values of scatter

Figure 3.22: *Effect of increasing acoustic pressure on bubble responses, from 187kPa-1.5MPa (fundamental scatter shown). The number of bubbles at resonance increases with increasing acoustic pressure, due to the decreasing resonance radius shown in Figure 3.20. This leads to an decreasing mean value of scatter for off-resonant bubbles. The mean value of resonant scatter increases with acoustic pressure due to the increased amount of energy incident on the bubbles.*

Between $R_0 = 2.9 - 3.62\mu\mathrm{m}$ the scatter is dominated by the second harmonic scatter. These regions correspond to the scatter previously described as 'off-resonance' (i.e below the fundamental resonance radius). Above $R_0 = 3.62\mu\mathrm{m}$ the scatter is predominantly fundamental, and has the characteristics of resonant scatter as outlined previously (i.e. increasing envelope and increased expansion to compression ratio). Figure 3.24 shows how this information can then be used to further classify the scatter, based upon the ratio of the fundamental and second harmonic to third harmonic scatter alone, into each of the three domains of resonance.

A distribution of 100 bubble signals, sampled from an experimental size measurement, in response to a 1.6MHz 550kPa six cycle pulse, is shown in Figure 3.24. 68% of bubbles by number are dominated by third harmonic scatter, 17% by the second harmonic and 15% by the fundamental. Although the majority of the bubbles by number are at third harmonic resonance, this population only accounts for 5.3% of the total RF scatter, due to their small sizes. 2nd harmonic resonant population accounts for 15.8% and fundmental resonant population accounts for 78.9% of total RF scatter.

As the incident frequency is increased, the resonance radius of each harmonic decreases, and thus the relative dominance of the three harmonics changes, as shown in Figure 3.25. Signals with third harmonic dominance decrease in both number and mean fundamental scatter with

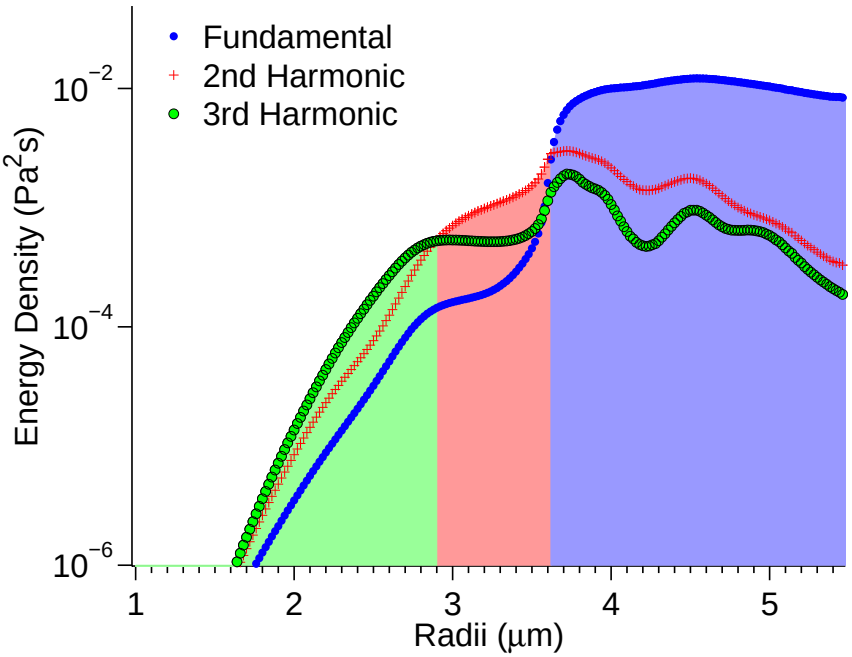

Figure 3.23: *Bubbles at lower radii have resonances at higher order harmonics. The dominance of the various components of harmonic scatter allow the scatter to be categorized into three regions, indicated by the shaded areas. Below $R_0 = 2.9\mu\mathrm{m}$ the third harmonic is dominant, between $R_0 = 2.9 - 3.62\mu\mathrm{m}$ the scatter is dominated by second harmonic scatter, and above $R_0 = 3.62\mu\mathrm{m}$ the scatter is predominantly fundamental, and displays the characteristics previously described as resonant. The 2nd and 3rd harmonic resonance populations are those bubbles previously described as 'off-resonance'.*

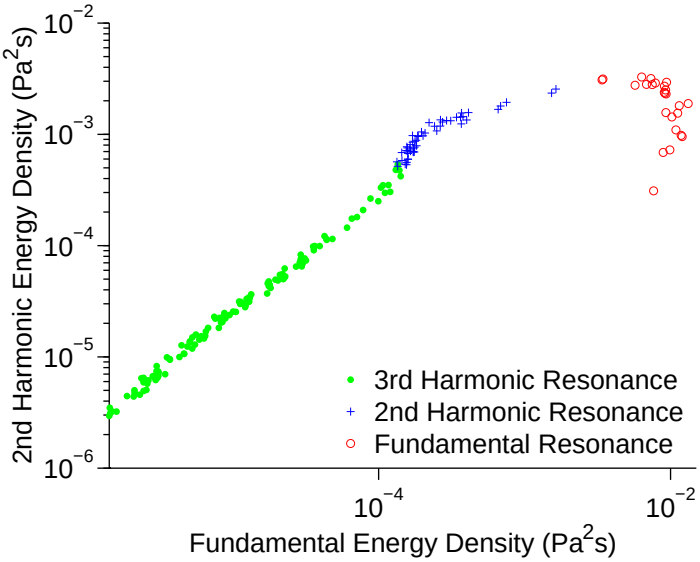

Figure 3.24: *Distribution of 100 bubbles sampled from a real size measurements, separated into three regions of harmonic resonance. In response to a 1.6MHz 550kPa six cycle pulse,* 68% *of bubbles are dominated by third harmonic scatter,* 17% *by the second harmonic and* 15% *by the fundamental. Although the majority of the bubbles by number are at third harmonic resonance, this population only accounts for* 5.3% *of the total RF scatter, due to their small sizes (2nd harmonic resonant population accounts for* 15.8% *and fundmental resonant population accounts for* 78.9%*.*

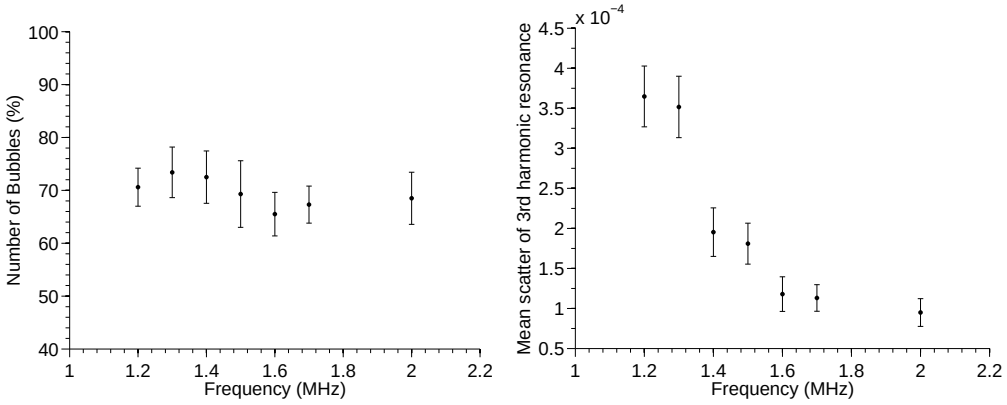

(a) Number of bubbles at 3rd harmonic resonance (b) Mean scatter at 3rd harmonic resonance

Figure 3.25: *The number of bubbles dominated by the 3rd harmonic reduces with increasing frequency, due to the inverse relationship of frequency and resonance radius. The mean scatter of this population decreases accordingly (calculated from ten random samples of 100 bubbles).*

increasing incident frequency. A similar effect is seen for increasing acoustic pressure, again due to the decreasing fundamental resonance radius which dominates the distribution of scatter.

The presence of these three regions of resonance will be investigated in the experimental data.

3.6 Discussion

The distribution of initial radii in a sample of Definity microbubbles, and the sharp increase in energy of response at resonance, leads to a significant separation in the response from resonant and off-resonant bubbles, leading to a two-population response in a sample of single bubble signals. The size and separation of the two populations, as predicted by the above model, is dependent upon the incident pulse parameters and the parameters which describe the shell.

Varying values of shell stiffness have been found to significantly effect the response from a distribution of bubbles. For larger values of shell stiffness, even though the bubble movement is restricted to a greater extent, the change in resonance radius leads to a distribution with increased scatter at resonance. The parameter of shell viscosity also has an effect, but on a much smaller scale.

Increasing frequency has been shown to reduce the value of peak scatter, due to the decreasing resonance radius, which directly relavent to improving the contrast to tissue ratio which can be achieved in clinical imaging techniques. At higher frequencies ($f > 3.4\mathrm{MHz}$) the number of bubbles defined to be at resonance decreases due to a reduction in the resonance peak, which reduces the characteristics of resonant scatter. In response to increasing acoustic pressures, it has been shown that peak bubble responses increase in energy exponentially, with an increased number of bubbles scattering around resonance. The energy response flattens out as the incident acoustic pressure is increased, which leads to a reduction in the resonance radius, and therefore the number and mean energy of off-resonant scatter.

Third harmonic response has briefly been analyzed, and used to further classify off-resonant scatter as either third harmonic or second harmonic dominated response. The proportion of third harmonic dominated scatter reduces with increasing frequency, due to decreasing resonance radius.

3.7 Conclusion

The results above present a theoretical prediction of the signals produced by a soft-shelled contrast agent in response to various single pulses, as predicted by a numerical model realized in MATLAB. The results have been presented to allow direct comparison with a sample of experimentally measured single bubble responses. Various characteristics of resonant scatter have been identified, with a view to identifying this behaviour in experimental data.

Within a typical sample of contrast agent, a small population of bubbles has been identified which shows a significantly increased overall scatter (Figure 3.6). These resonant bubble's scatter contain increased fundamental components with respect to the components of higher harmonics. In approaching the radius of peak scatter, the signals are observed to show increasing fundamental scatter with time over the duration of the transmitted pulse, with a maximum signal observed with a symmetric envelope at resonance. Increased radial expansion to compression ratio is also observed at resonance, leading to large high-frequency spikes in the RF signals (although the model does not take into account frequency dependent sound damping in the medium, which will act to reduce the energy of these spikes[127]). Compression dominated behaviour, which has been previously observed in experimental studies[50,80], is not predicted by the model used here, and this will be investigated further in the analysis of experimental data (Chapter 4).

Resonance behaviour, as predicted by the Mooney Rivlin model, can thus be characterized by:

- Increased energy of scatter.
- Increased fundamental to harmonic ratio.
- Increasing envelope with time.
- Increased expansion to compression ratio.

In the next chapter, experimental data will be analyzed to determine which model parameters correctly predict the bubble dynamics of a lipid based microbubble such as Definity, concentrating on the characteristics of peak scatter, fundamental to second harmonic ratio and signal envelope related to resonant scatter. By identifying these resonance characteristics in such a way, it will be possible in future work to tune the transmit parameters used in imaging to maximize the scatter from a sample of microbubbles which contains a wide-distribution of sizes,

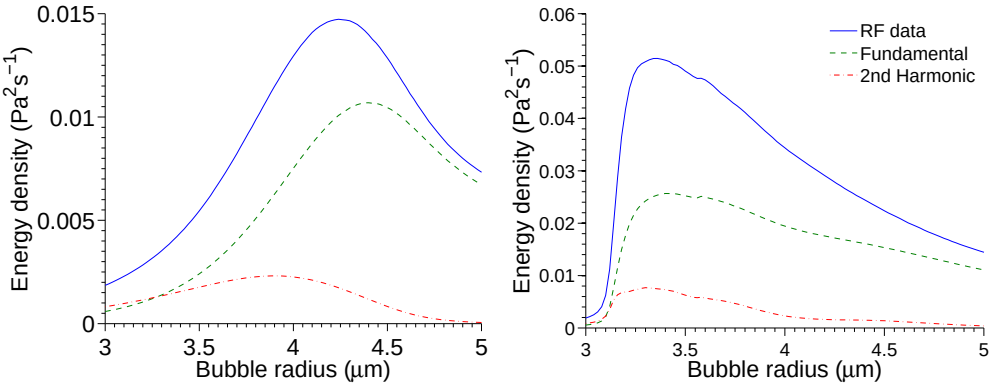

(a) Skalak, Strain Hardening Model

(b) Hoff Model

Figure 3.26: *Variation in resonance peaks for the Skalak and the Hoff shell models.*

as is the case for the agent used here. The comparison of experimental results with the theoretical results presented here will allow the model to be improved, and future models to more accurately predict the behaviour of oscillating microbubbles.

3.8 Further work

The results from strain softening Mooney Rivlin shell model have been presented here. Further work is needed to compare the results of this model to other models available in the literature, including the similar models of Hoff[128] and Skalak (a strain hardening model)[85].

The Hoff model, Figure 3.26(b), uses the Church shell model[129] for a viscoelastic shell, which uses an exponential law for the stress-strain relation, and thus defines the shell properties as follows;

$$P_{shell} \equiv 12\frac{d_{Se}}{R_o}\left(\frac{1}{8}G_S\left(1-e^{-8\frac{R-R_0}{R_0}}\right)+\eta_S e^{-4\frac{R-R_0}{R_0}}\frac{\dot{R}}{R_0}\right) \tag{3.9}$$

The Skalak model, Figure 3.26(a), defines the shell properties as follows;

$$P_{Shell} \equiv \frac{2d_{Se}G_S}{R}\left(\left(\frac{R}{R_0}\right)^2(1-C)+C\left(\frac{R}{R_0}\right)^6-1\right)+\frac{12\dot{R}\eta_S d_{Se}}{{R_0}^2} \tag{3.10}$$

Where C is a measure of the hardening of the shell, and can range from 1-10. For a small amount of shell hardening, as is likely to be relevant here, it is set to 1.

Initial results show that the Mooney Rivlin results agree reasonably well with these alternative models, as shown in Figure 3.26. All models show the same characteristics of resonance outlined above, but predict varying resonance peaks, and therefore differing responses from a distribution of bubbles. Further work is needed to investigate the response from varying imaging frequencies and acoustic pressures of these alternative models, in order to define the best model for Definity. A comparison of the results will allow further analysis of the shell parameters.

Chapter 4
Single bubble experiments with the contrast agent Definity®

4.1 Introduction

Definity® (Luminity in Europe) is an FDA(United States Food and Drug Administration) and MHRA (UK Medicines and Healthcare products Regulatory Agency) approved ultrasound contrast agent, developed by ImaRx, and marketed Bristol Meyers Squibb for cardiac imaging (now Lantheus Medical Imaging, Inc). It is licensed in the United States and Europe for cardiac use, and for radiological use in Canada. Definity started life as MRX-115, or Aerosomes™(ImaRx, Tucson, AZ), and was designed as a 'blood pool agent', to improve on previous albumin coated agents such as Albunex used in cardiac imaging. Albumin coated agents were shown to give effective contrast improvement as 'first pass cardiac agents', but most bubbles were observed to disappear before recirculation through the heart, limiting their use as arterial agents. Perfluorocarbons were originally seen as an alternative, as they offered more persistent contrast enhancement, but were shown to need relatively high doses. The original Aerosome™agent consisted of liposomes, composed of phosphatidyecholine, filled with nitrogen, and offered large amounts of contrast enhancement, at low doses. This original version of the agent lead to the development of Definity®, consisting of perflutren lipid microspheres encapsulating an octofluoropropane gas. When used in vivo, it recirculates well in the blood, traveling throughout the vascular system in a similar way to red blood cells. Fluorocarbon gases are then cleared from the blood by the lungs.

4.2 Aim of chapter

The aim of this chapter is to investigate the characteristics of resonant scatter, as observed in experimental single microbubble scatter, and to compare this data with the previously presented theoretical results (Chapter 3), and thus confirm the validity of the model. As stated in the previous chapter, resonance behaviour is the integral part of ultrasound contrast which allows

improved diagnostic imaging, but is not yet fully exploited in current imaging schemes, as a sample of ultrasound contrast agent contains a relatively wide distribution of bubble sizes, and current clinical pulses used can only excite a small proportion of these bubbles. Single bubble multi-method investigations such as this have the potential to both optimise the transmit parameters in order to increase the contrast to tissue ratio by increasing the scatter from a distribution of bubbles, and also to discover bubble-specific responses which will be masked by large concentration studies.

Thus the aim of this chapter is to develop a well-characterized micro-acoustic system, with which large amounts of single bubble RF data can be collected from commercially available contrast agents, in response to a variety of clinically relevant imaging parameters. The analysis of such data, in comparison with the previously presented results from relevant theoretical models, will allow physical insight into the response of microbubbles to ultrasound to be gained, with a view to improving the microbubble signal and thus the contrast to tissue ratio available to clinical diagnostic techniques. The clinical techniques which currently use microbubble contrast, as outlined in Chapter 1, can all benefit from improved resolution and contrast which can be gained from improved knowledge of the variation of microbubble scatter in response to a variety of incident parameters.

4.3 Contrast agent stability

Definity is supplied in 1.5mL vials, and is activated by shaking for 45 seconds in a manufacturer supplied device. This activates the microspheres by forcing the gas which is stored in the head space into the liquid lipid solution, creating the milky white suspension of microbubbles. For in vivo work, the manufacturers recommend immediate use once activated, as the agent does not contain any bacterial preservative. Bacterial contamination can therefore occur following the puncture of the “elastomeric septum” which seals the Definity vial, but for in vitro use this is not an issue. The microbubbles remain in suspension within the vial for five minutes, but can be easily resuspended by 10 seconds of hand agitation. For in vivo use, the agent is viable for up to 12 hours from the time of initial activation.

The stability of Definity microbubbles has been shown to be independent of the oxygen content of its surroundings[101].Differences in Definity stability over time may occur in vitro between solutions of saline and blood, and it has been suggested that the ultrasound contrast effect from

Definity may last significantly longer under ultrasound exposure in blood than in saline, for equivalent MI's[130]. Although acoustically very similar, there are differences in viscosity, pH, microscopic structure (e.g. the presence of red blood cells), which would explain this. This does not invalidate work done in vitro in water/saline solutions, but should be kept in mind when direct comparisons with in vivo work are made.

4.4 Single bubble system

The in vitro studies presented in Chapter 1 demonstrate that large variations in microbubble signals have been observed, in response to a clinical imaging pulse. Various optical systems have been designed that allow the visualization of a single microbubble's oscillations in response to specific ultrasound pulses, and have produced many interesting results[89,98,131–133]. While these techniques produce high resolution images for analysis, they are not without their drawbacks. Because the working distances of microscope objectives are just a few millimeters, the experimental setups are very small, and usually have many surfaces and reflectors close to or in the path of the ultrasound. This makes the actual transmitted acoustic signal hard to define at the region of interest, due to multiple reflections and reverberations associated with the optical microscopy system. Even with the use of a needle hydrophone, the accuracy of the calibration of ultrasound signal incident on the bubble has not been defined. In order to precisely align the imaging optics, the microbubbles are usually tethered to a surface, or placed within a system of tubes, both of which may affect their acoustic response to ultrasound[134,135]. This leads to the larger drawback however, of limiting the usefulness of any of the current optical systems. Attaching or tethering a microbubble on the order of $1-3\mu\mathrm{m}$ in diameter is a time consuming process, and as such it is difficult to record the oscillations of a large number of individual microbubble's scatter using optical techniques, and thus investigating the differences observed in a population of microbubbles.

This investigation is based on the design of a micro-acoustic system, which allows the scatter from a large number of microbubbles to be measured, in response to a large number of well-defined clinical ultrasound pulses. The use of a clinical scanner with a wide band commercial piezoelectric transducer allows high sensitivity measurements to be made, and has been fully characterized on both transmit and receive (as described in Chapter 2).

4.4.1 Requirements of system design

The system to measure single scattering events was originally based on a single particle optical sizer[136]. The aim was to be able to place individual microbubbles easily and precisely within an uninterrupted and clearly defined ultrasound field, free from reflections and reverberations. The system should be quickly and easily aligned, and allow a large throughput of microbubbles, in order to build up large data sets of single scattering events to define microbubble populations. Microbubble signals should be collected from bubbles being insonated for the first time, and then all signals from subsequent insonations recorded (until either the bubble is destroyed, or enough useful information about the dynamics of bubble response to subsequent pulses is gained). Once insonated, microbubbles should be removed from the measuring field, or region of interest (ROI), so that subsequent measurements can be made with confidence that no contamination of the signal takes place.

Other acoustic experimental systems use tubes together with a system of syringes or flow pumps to control the path of the bubbles into and out of the ultrasound field, and while this gives easy control over the placement of the bubbles, can add restrictive pressures to the bubble's surroundings that may effect the bubble's behaviour in an ultrasound field (the effect of the tube diameter on the oscillations of microbubbles has been shown optically[137]). A flow system was designed that gave ease of control, without these increased pressure effects, to allow measurement of truly 'free' microbubble signals. A relatively large flow tank that could be lined with acoustic absorbing material was used. This employed a directing flow together with hydrodynamic focusing, to allow microbubbles released into the stream to travel in a narrow (sub-millimeter) and well defined path toward a suitably placed transducer.

4.5 Methodology

A system was designed that allowed single RF microbubble data to be captured from a flow of dilute contrast agent flowing vertically toward a downward facing transducer.

A low voltage pump was used together with a system of filters and tubing to flow a narrow stream of water though the tank. This entered the tank at the base, connected with a weakly focused nozzle to produce a hydrodynamically focused path through the center of the tank. Dimensions were determined to produce the best tightness of focus so as to ensure a well defined linear flow through the tank. Initial designs of the system employed a closed-loop system so

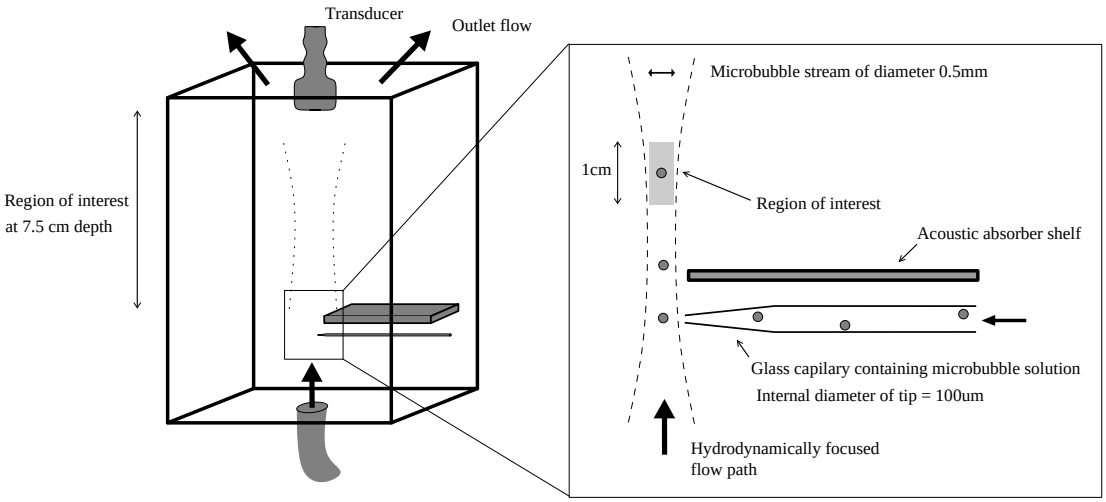

Figure 4.1: *Single bubble acoustic measurement system, employing a hydrodynamically focused flow to capture single RF microbubble data*

that the water flowing in the tank was removed from the top of the tank and re-circulated, after being filtered of all injected contrast agent. However, it was found that even with the use of high quality micro-pore filters it was not possible to ensure the full removal of contrast agent from the re-circulated water, especially when using the soft-shelled phosphor-lipid agents such as Definity. Any contrast agent re-entering the tank through the flow path would have been previously insonated, and so would not meet the conditions of the experiment. Thus it was decided that a simpler system that used a steady supply of fresh water flowing through the tank was a better solution. Although this requires large amounts of suitably 'degassed' water for a series of experiments, this was achieved by overnight cooling of a large (thirty litre capacity) open top tank of pre-filtered and boiled water (boiling the water will remove the majority of air suspended in the liquid). This water was then filtered prior to insertion into the tank, to remove any dust particles which may have settled on the surface of the water during cooling. Microbubbles inserted into the tank then followed the flow of the water out over the top of the tank, and into a waste receptacle. This was confirmed using coloured dye to show the path of the injected contrast agent. This was determined to be the most reliable way of removing contrast agent solution so as to ensure an uncontaminated flow of microbubbles, and to ensure each recorded microbubble was only insonated by a single series of pulses.

The insertion flow was limited to ensure a laminar flow path in which to insert single microbubbles. Microbubble insertion was done using a glass capillary pipette, which was made using

a micropipette puller (Sutter Instruments Co., Novato, CA). Various tapers and diameters of pipette were tested to find the angle best suited to inserting microbubbles smoothly into a laminar flow, and it was found that a pipette with taper length of 35mm, cut to an internal diameter of $80\mu\mathrm{m}$ (external diameter of original glass cylinder was 1mm) allowed a smooth transition from the relatively high pressure slow velocity internal environment of the pipette to the lower pressure, relatively high velocity of the insertion flow of the tank. This pipette was covered from the ultrasound field by a shelf of acoustic absorber mounted directly above it, to prevent premature insonation.

4.5.1 Microbubble solution

The microbubble solution, once suitably diluted, was inserted into the pipette through a system of tubes, by a gravity fed open topped container. The container was part of a magnetic stirrer system, which gently agitated the microbubble solution to avoid settling of the microbubbles within the container. The solution was fed slowly down through 10mm diameter tubes into the micro-pipette connected directly to the side of the tank, and then individual microbubbles fed through the micro-pipette into the insertion flow. The speed of this gravity fed flow could then be easily controlled by increasing or decreasing the height of the reservoir of contrast agent solution. It was found that with an internal diameter pipette of $80\mu\mathrm{m}$, the reservoir should be suspended at a height of 15cm above the point where the pipette enters the base of the tank.

4.5.2 Concentration

The concentrations used in the experiments were defined by a combination of numerical calculations of required dilution, and experimental trial and error, to ensure that the contrast agents were suitably diluted so as to give single scattering events in response to suitably triggered ultrasound. It was decided that as a compromise between ensuring a small probability of having multiple bubbles present in each frame, and the time needed to capture suitably large data sets, an average of one bubble should be present in the region of interest every three captured frames (triggered at 0.5Hz). Over a series of repeated experiments, in response to a single set of imaging parameters, 1000 frames of ultrasound therefore produced approximately 200 suitable single microbubble signals (excluding signals that are partially out of the region of interest).

An increased concentration flow (approximately five bubble signals present in the 9cm image

region, per frame) was used in aligning the transducer over the insertion flow to ensure optimal positioning, and then reduced by dilution to the capture concentration of one bubble per three frames in the region of interest.

4.5.3 Alignment of flow profiles

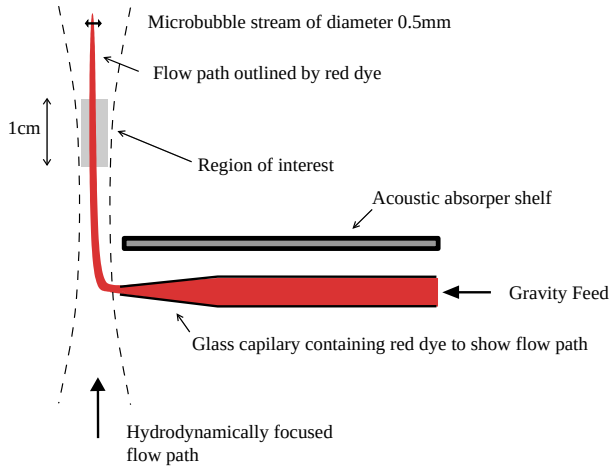

Figure 4.2: *The flow profile of the system was visualized using red food dye to show the path of the microbubble solution.*

The alignment of the flow profile of the system was done using red cochineal dye (common food dye) to trace the path of the flow out of the pipette, and ensure a well defined 0.5mm narrow vertical flow path, as shown in Figure 4.2. With the experimental conditions setup identical to those to be used for data collection (i.e. transducer clamped in place at the top of the tank, and a suitably diluted microbubble solution flowing into the tank through the pipette), a few drops of cochineal dye was added to the gravity feed, and the flow of the microbubble solution through the tubes system and into the insertion flow into the tank therefore traced. A smooth and laminar flow into the tank of approximately 0.5mm in diameter was achieved when flow speeds of both insertion flow and gravity fed flow are optimized. The microbubble solution flow became turbulent when the insertion flow was increased to above optimal, and also if the velocity of the gravity feed was too high (in this case the microbubble solution was not taken up by the insertion flow, and circulated at the bottom half of the tank). It was also important for alignment of the ultrasound transducer that the flow profile is vertical, and this is again controlled by the speed of the gravity flow, and also the positioning of the tip of the pipette in the insertion flow.

4.5.4 Alignment of transducer

The transducer is aligned in two steps. First, cochineal dye is used for a course alignment. Following this, to ensure the microbubble signal is maximized in the M-mode data capture mode of the scanner, an acoustic alignment is performed. As shown in Fig 4.1, this was done by mounting the transducer on a three dimensional micro-manipulator above the tank. With a relatively high concentration of microbubbles flowing through the system (high enough so that a stream of microbubbles can be traced out on the scanner screen, but not high enough so that the flow profile changes due to an increase density of microbubble solution), the flow can be observed easily on the scanner screen. The optimal position of the transducer can be found where the microbubble signal is brightest (corresponding to largest received signal), by translating the transducer in the elevation plane. This positioning can then be fine-tuned by capturing a signal and analyzing the position and intensity of the bubble echoes, and repositioning the transducer as necessary. The transducer captures 128 lines of received ultrasound, and so by ensuring that the peak received signal is maximized in the center line (line 62), and that the lines either side of the center line (line 61 and line 63) are of less and equal amplitude, the transducer can be positioned very accurately.

4.5.5 Data manipulation

The custom designed software enables individual lines of RF echo to be captured and recorded, and stores the data in a file format similar to a Matlab structure. Once the microbubble signals have been captured, they can then be read into Matlab, and easily converted to a text file for further analysis.

Each frame of captured ultrasound data contains the signals from a number of lines, which is specified by the back-door command ‘agt’ and ‘sector size’ commands (as outlined in Chapter 2). For the majority of Definity single pulse data (to be covered in this chapter), this is set to seven lines, unless otherwise specified. Once read into Matlab this gives a matrix of 2300 x 7 samples for each frame, sampled at the RF sampling rate of 19,636,363Hz. This can then easily be time-gated to select only the region of interest (e.g. 7-8cm for the S3 transducer), and separated into the respective lines. The next task necessary to analyze bubble signals is to identify the bubble signals themselves, and to separate them from the blank signals that have been captured (due to the concentration levels as defined above, an average of two out of every three frames will be empty at the region of interest). This is done by employing a sum-squares

technique to identify bubble signals that are above a threshold noise signal, and to detect the start and end of each signal. Automatic rejection of any signals close to the edge of the region of interest was employed, to ensure the full bubble signal was always recorded.

A sum squares method gives an accurate and robust way of detecting a large number of bubble signals above noise, and gives a rough estimate of start and end positions, as shown in Figure 4.3. This is used together with the Matlab graphical selection function 'ginput' to visually correct any discrepancies in the method. The function allows points from a plotted signal to be selected from the figure, using the mouse for cursor positioning, and then inputted back into the signal to fine-tune the edge detection method.

Once each individual bubble signal is identified, it can then be filtered and decomposed into components of fundamental and harmonic scatter. A similar filtering scheme was used as described in Chapter 2, so as to maintain continuity of signals. Each bubble, and its components of scatter (fundamental, second harmonic and third harmonic), were then stored in an individual MATLAB structure, together with relevant data, such as fundamental frequency, peak scatter, RMS scatter and energy density. This allowed the signals to be easily cataloged, and recalled for analysis.

4.5.6 Data analysis

Once the bubble signals have been decomposed into the various components of harmonic scatter, they can be calibrated and information about their behaviour, structure and resonance characteristics extracted. Initial analysis was done to investigate the response of the microbubbles to each individual transmit pulse, to investigate the possible presence of any sub-populations of scatter. The effect of increasing parameters such as frequency and acoustic pressure was then observed, to find any trends that appeared across the transmit parameters.

Responses from single Definity microbubbles were recorded for a range of frequencies, acoustic pressures and pulse lengths, and the data has been extensively analyzed. Up to 200 signals for each transmit signal were recorded, allowing a meaningful statistical analysis to be performed.

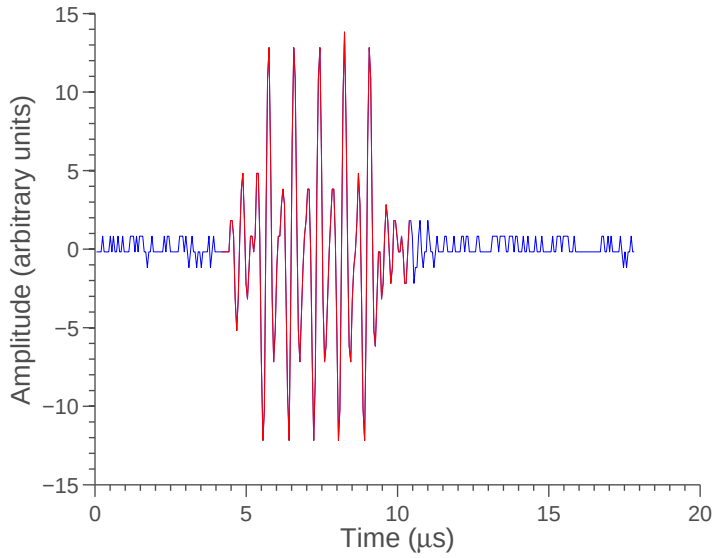

Figure 4.3: *Example of a typical RF signal from a Definity microbubble in response to a 1.2MHz, 550kPa 6 cycle pulse, with the sum-squares algorithm applied to identify the signal above noise.*

4.6 Results

A typical single Definity microbubble response to a low frequency medium amplitude pulse is shown in Figure 4.3. The received RF data is plotted in blue, with the sum-squares selected bubble signal plotted in red. The signal shows the six cycle of the transmit pulse (in this case 1.2MHz, 550kPa) has been cleanly repeated, as can be seen by the distinct six cycle signal, and the bubble signal has been calculated to be $6.26\mu s$ in duration (similar to the length of the incident pulse). The frequency spectra of the signal can be determined by observing the Fourier transform of this signal, as shown in Figure 4.4. Overlayed on the Fourier transform are the filters used to separate the various components of harmonic frequencies.

As can be seen in Figure 4.4, the microbubble shows a dominant second harmonic response, and a strong third harmonic response upon receive. The bandwidth and transfer function of the transducer was taken into account at this stage, and the receiver calibration as calculated in the previous chapter was applied. This allows the RF data captured from RF signal in AFLink (Figure 4.3) to be converted to filtered components of frequency in units of Pascal, as shown in Figure 4.5.

As can be seen in Figure 4.5, the filtered components show the strengths of the various com-

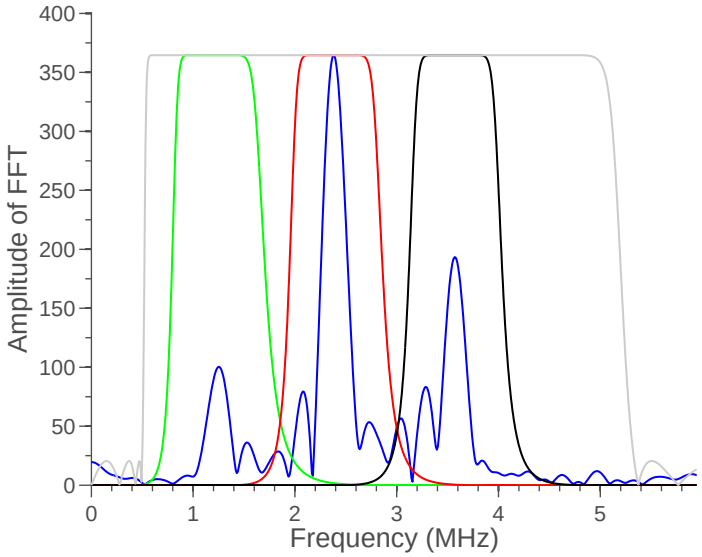

Figure 4.4: *Example a typical RF signal from a Definity microbubble in response to a 1.2MHz, 550kPa 6 cycle pulse, showing strong responses in the fundamental, second and third harmonic frequencies. Filters used to separate out the components are shown in green, red and black respectively, with an RF offset filter shown in gray.*

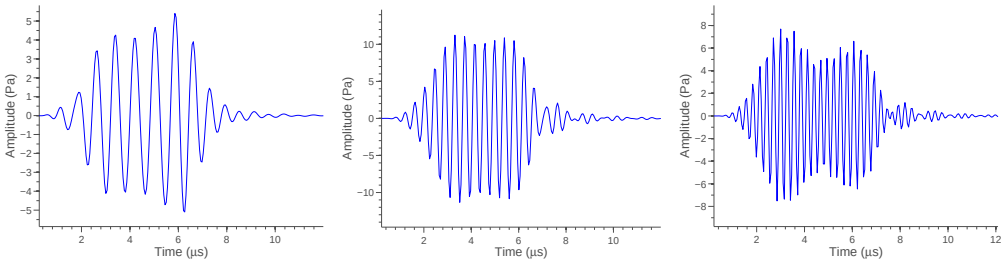

(a) Fundamental components of scatter

(b) Second harmonic components of scatter

(c) Third harmonic components of scatter

Figure 4.5: *Filtered Definity scatter signal, showing the fundamental, second and third harmonic components of scatter, in units of Pascals*

ponents. For the bubble shown, the second harmonic component is the strongest, with peak amplitude of 11.32Pa and an energy density of $2.27 \times 10^{-4} Pa^2 s$. The fundamental scatter from this bubble is approximately five times weaker than the second harmonic in terms of total energy, with a peak amplitude of 5.35Pa, and an energy density of $4.59 \times 10^{-5} Pa^2 s$. The third harmonic scatter is also stronger than the fundamental, by a factor of two in terms of energy, with peak scatter of 7.69Pa and an energy density of $9.99 \times 10^{-5} Pa^2 s$.

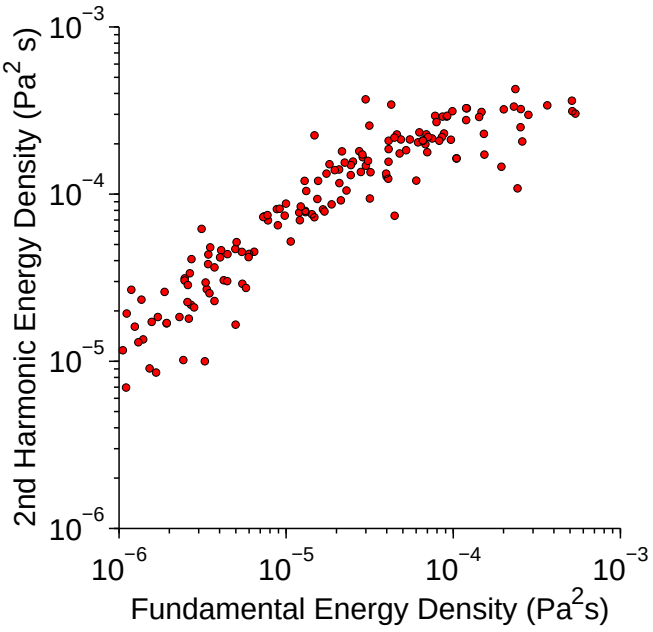

Figure 4.6: *Distribution of scatter from 117 Definity microbubble signals, in response to a 1.2MHz, 550kPa six cycle pulse. Signals have been decomposed into fundamental and second harmonic energy densities (note log-log axis)*

Once a large number of bubble response have been collected, the variations of scatter can be analyzed, and the variations in total energy, ratio of frequency components, and length of scatter can be plotted. Figure 4.6 shows the variations in fundamental and second harmonic scatter for 182 bubbles in response to the same 1.2MHz 550kPa six cycle pulse. The bubble signals have a mean energy density of $4.64 \pm 8.8 \times 10^{-5}$ and $1.11 \pm 1.06 \times 10^{-4} Pa^2 s$ (fundamental and 2nd harmonic respectively). The energy densities of the respective components have been plotted against each other in Figure 4.6 (note log-log axis), so any differences in harmonic component with increasing echo amplitude can be identified. Here, a single distribution of response is observed. The average ratio of fundamental to second harmonic energy density is 0.36 ± 0.45. The length of the signals are normally distributed about a mean of $5.82 \pm 1.02 \mu s$ as can be seen

in Figure 4.7.

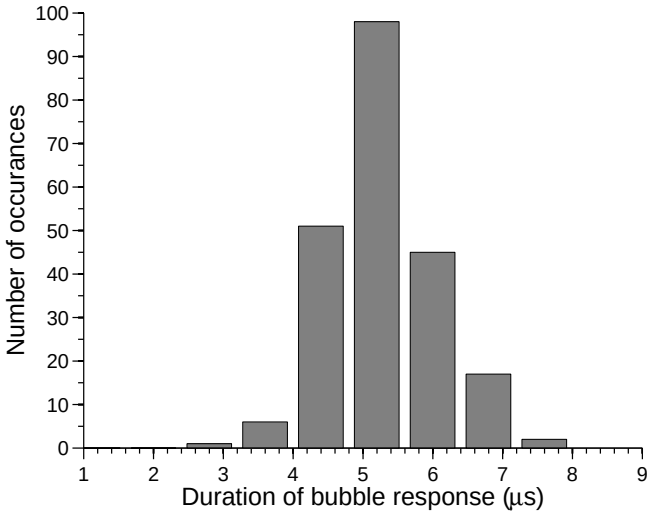

Figure 4.7: *Distributions of bubble signal durations in response to a 1.2MHz, 550kPa six cycle pulse. The distribution is approximately normal, with mean of* $5.27\mu s \pm 0.8\mu s$ *(of similar length to the incident pulse of* $4.95\mu s$*).*

4.6.1 Example of multiple populations of response

The data above shows an example of a single population of scatter in response to a single transmit pulse, as expected from basic microbubble theory, and as exploited by the many pulse sequences employed to improve the contrast to tissue ratio. However, this is not always the case for Definity scatter, when bubble data from a higher frequency transmit pulse is analsyed.

In response to a 1.6MHz, 550kPa six cycle transmit pulse, the distribution of scatter from a large number of single scatterers is markedly different from that behaviour shown in Figure 4.6. Figure 4.8 clearly shows two separate behaviours of scatter, with the populations defined using the cluster analysis methods as described in Chapter 3. Increased fundamental scatter, at the expense of the second harmonic, suggests that these signals are from the bubbles identified from theory to be at or approaching resonance (see Chapter 3). This classifies 44 (19%) bubbles to be at resonance, similar to the results from the Mooney Rivlin model presented previously. Off-resonance scatter has a mean energy of scatter of $9.90 \pm 9.28 \times 10^{-5}$ and $1.93 \pm 1.54 \times 10^{-4} \mathrm{Pa}^2\mathrm{s}$ (fundamental and 2nd harmonic respectively), and a fundamental to second harmonic ratio of 0.53 ± 0.4. Resonance scatter shows an increased mean energy of $1.90 \pm 0.76 \times 10^{-3}$ and $3.60 \pm 1.55 \times 10^{-4} \mathrm{Pa}^2\mathrm{s}$ (fundamental and 2nd harmonic respectively), and a significantly

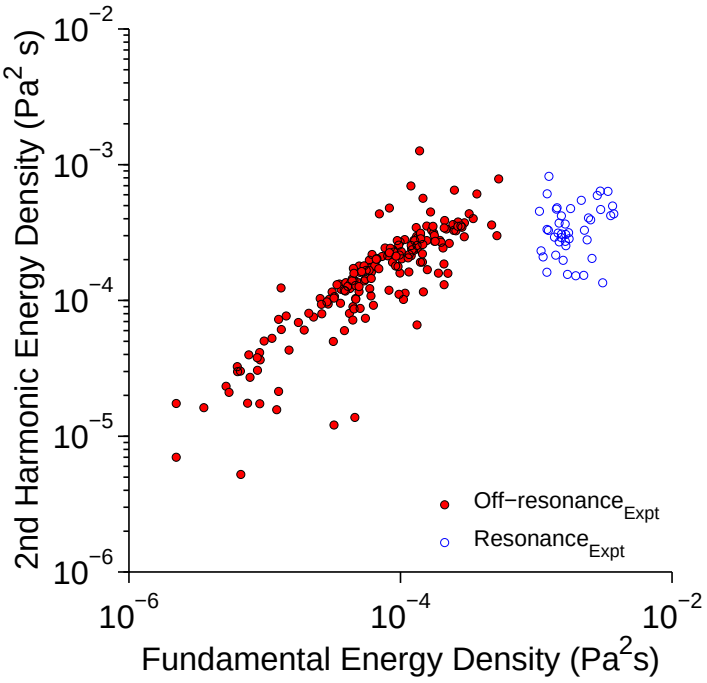

Figure 4.8: *Distributions of scatter from 235 Definity bubbles in response to a 1.4MHz, 550kPa six cycle pulse. Two distinct populations are present, as defined here using cluster analysis methods. 44 bubbles are classified to be at resonance, corresponding to* 19% *of the scatterers by number, with a mean energy of* $1.90 \pm 0.76 \times 10^{-3}$ *and* $3.60 \pm 1.55 \times 10^{-4} \mathrm{Pa}^2\mathrm{s}$ *(fundamental and 2nd harmonic respectively), and a mean fundamental to harmonic ratio of* 6.45 ± 3.8.

increased ratio of 6.45 ± 3.8. This separation in energy between the two populations has been observed for a variety of frequencies and acoustic pressures, although is less obvious at higher frequencies (as outlined in subsequent sections).

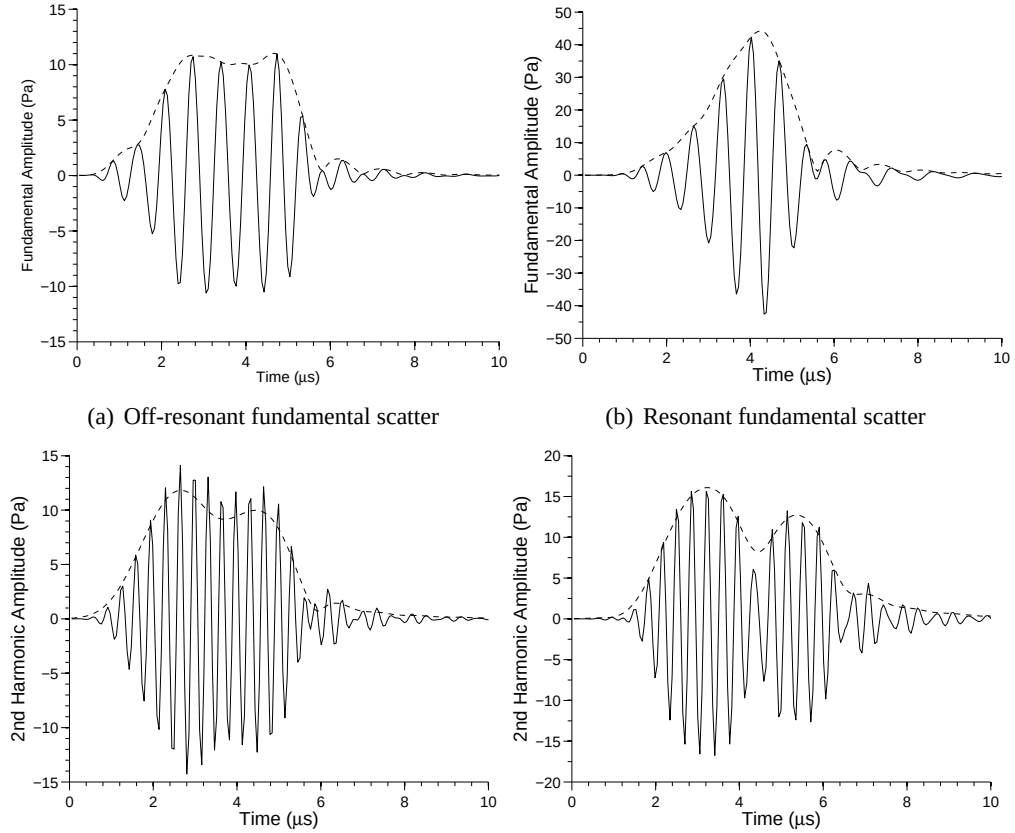

(a) Off-resonant fundamental scatter

(b) Resonant fundamental scatter

(c) Off-resonant 2nd harmonic scatter

(d) Resonant 2nd harmonic scatter

Figure 4.9: *The difference in the typical envelopes of response can clearly be seen between the two populations. Quadrature amplitude modulation has been performed to display the envelopes of the respective signals. Resonant scatter shows an increasing envelope of fundamental scatter, with peak fundamental corresponding to a dip in the harmonic scatter. This compares to the approximately constant envelope of off-resonant scatter, in both the fundamental and second harmonic components.*

4.6.2 Envelope effects

Further investigation of the individual bubble signals shows that the envelope of the response from these specific bubbles has increasing fundamental components with time across the six cycle transmit pulse, which is another feature predicted to be associated with resonance in Chapter 3. As can be clearly seen in Figure 4.9(b), a typical resonant scatter signal has a strongly in-

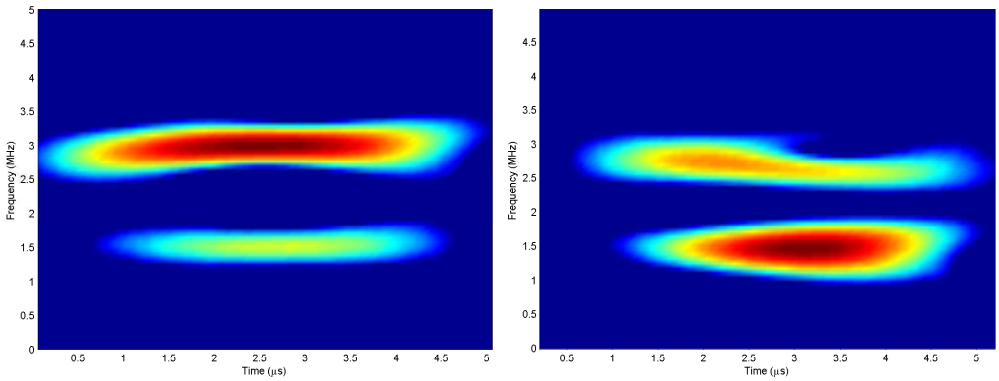

(a) Example of scatter from population 1 shows a constant harmonic and fundamental component across the $6\mu s$ duration of scatter.

(b) Example of population two scatter shows the increasing fundamental scatter

Figure 4.10: *Short-time Fourier transform representations of signals show the increasing fundamental energy in the Population 2 scatter, as compared to the constant envelope of response in Population 1 scatter*

creasing fundamental component which peaks at approximately $2.5\mu s$ after the onset of scatter, as compared to the constant amplitude components of both fundamental and second harmonic scatter in the typical off-resonance response, Figure 4.9(a). The difference in the fundamental envelope shapes is clearly obvious when the quadrature demodulated amplitude is plotted, as shown in Figure 4.9. This has been performed in MATLAB, using the 'demod' function in the signal processing toolbox, as previously described in Chapter 3. Figure 4.10 shows time-frequency representations of the signal (normalized short-time Fourier transform, performed in MATLAB), showing how this increasing amplitude relates to increased fundamental to harmonic ratio. When observing the harmonic scatter, it can be seen that at resonance the peak fundamental scatter corresponds to a dip in the second harmonic, and this will be addressed in the next section (Compression and expansion effects).

This property of increasing energy over the six cycle response is hard to quantify exactly in experimental data, given the variations in scatter over a large number of bubbles (Figure 4.11 shows the natural variations between three signals from each population). It was found that a cross-correlation method as outlined in Chapter 3 was able to accurately identify scatter of either constant or increasing scatter in the RF bubble response. Using a 'typical' bubble response from population one (the bubble signal similar to the most number of other bubble signals, as defined by the most number of signals with a normalized cross correlation peak above 90%),

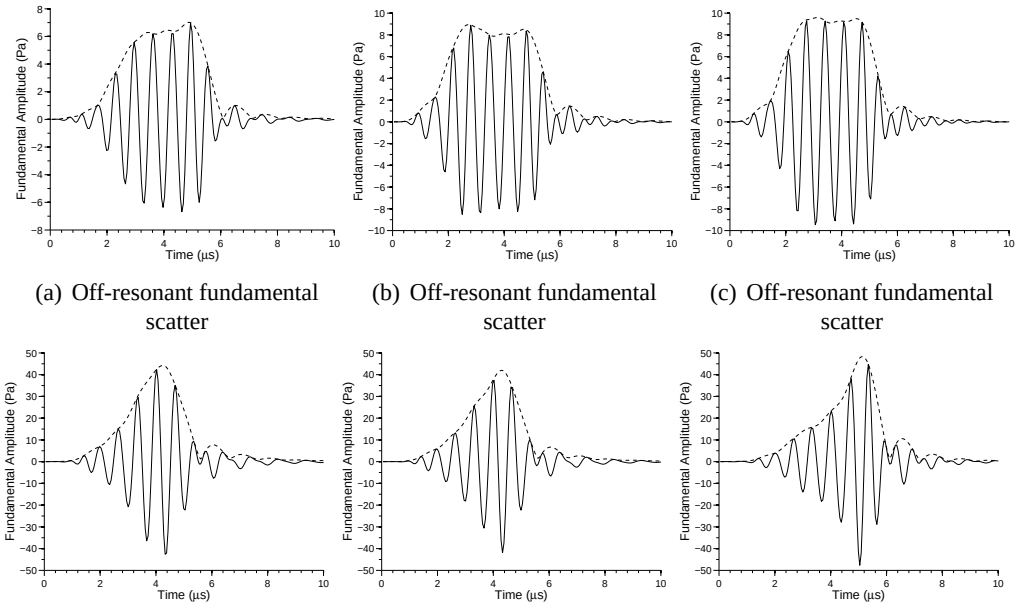

(a) Off-resonant fundamental scatter (b) Off-resonant fundamental scatter (c) Off-resonant fundamental scatter

(d) Resonant fundamental scatter (e) Resonant fundamental scatter (f) Resonant fundamental scatter

Figure 4.11: *Three examples of both populations are shown. Figures 4.11(a) – 4.11(c) are examples of off-resonance fundamental scatter, and Figures 4.11(d) – 4.11(f) are examples of resonant fundamental scatter. Within each population of scatter, similar envelopes of scatter can be observed, but small variations exist in the onset and peak scatter in both populations which make them difficult to classify automatically.*

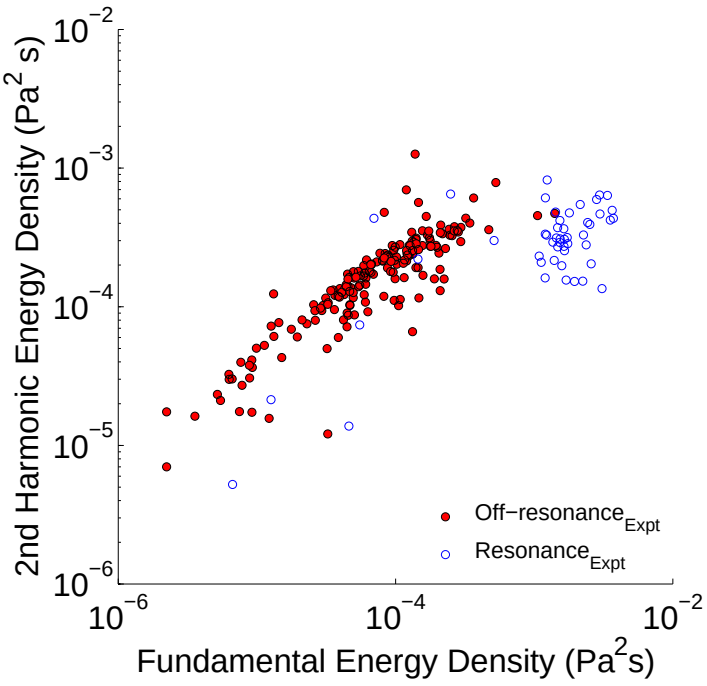

Figure 4.12: *Experimental signals from 235 single bubbles, in response to a 1.6MHz 550kPa six cycle pulse. Signals have been decomposed into fundamental and 2nd harmonic scatter. The scatter has been classified as resonant or off-resonant scatter, using a normalized cross-correlation method thresholded at 0.7 to distinguish between different envelopes of scatter. The method clearly shows a two population response, with a significant difference in energy between the resonant and off-resonant populations. Cross-correlation appears to overestimate the number of bubbles at resonance (52 compared to 44 using cluster analysis method), as can be seen by those bubbles with low energy scatter which have been mis-categorized as at resonance.*

bubble signals were compared using a normalised cross correlation technique to find differences in signal envelope alone. It was found that all population two scatter could be separated from population one by a threshold of 70% (same value used in Chapter 3) peak-cross correlation value, as shown in Figure 4.12. As can be seen, differences in shape leading to values below this threshold for the off-resonance bubbles in population one are mis-catorgorised in an insignificant number of instances (as shown by the blue bubble signals at low amplitude of scatter), but the majority of bubbles above a fundamental energy density of approximately $1 \times 10^{-3} Pa^2 s^{-1}$ are shown to have this distinctive difference in shape. Although this technique does not use a precise description of the envelope to characterize each signal, the results agree well with the cluster analysis method applied to the same data above, showing this is a valid technique for separating experimental data into populations of scatter.

4.6.3 Compression and expansion effects

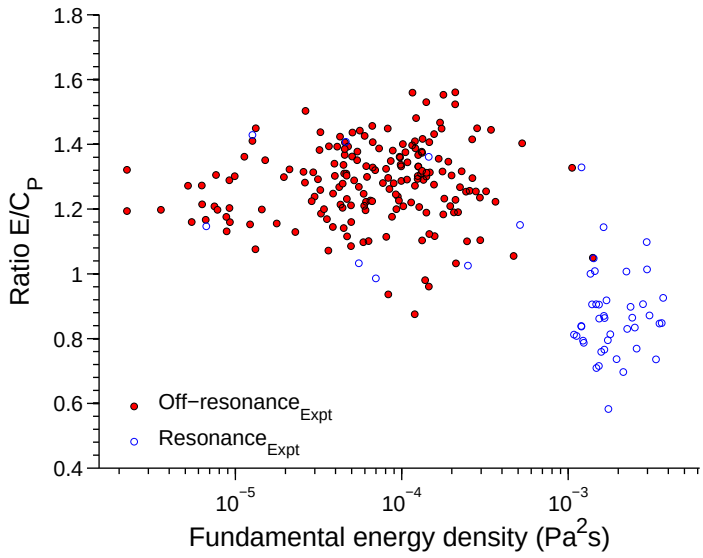

Figure 4.13: *Variation in ratio E/C_P between the two populations of scatter measured in response to a 1.6MHz 550kPa six cycle pulse. Off-resonance scatter has a mean ratio of 1.28 ± 0.12, whereas resonant scatter has an decreased ratio of 0.88 ± 0.15. Bubbles have been classified using normalized cross-correlation as described above.*

As described in Chapter 3, theoretical simulations using the Mooney Rivlin shell model predict increased expansion to compression ratio at resonance ($E/C_R = R_{max}/R_{min}$). This leads to increased positive to negative pressure ratio in the emitted signal, due to greater acceleration and

velocity upon contraction than upon expansion, which can be measured in the experimentally measured signals ($E/C_P = P_{max}/P_{min}$).

However, as shown in Figure 4.13, an increased ratio is not observed for those experimental signals identified to be at resonance, which contradicts the Mooney Rivlin results. Ratios E/C_P have been calculated from R.F. signals, as filtered signals will be symmetric by definition. These bubbles show a reduced mean expansion to compression ratio ($\overline{E/C}_P = 0.88 \pm 0.15$) in comparison to off-resonance scatter ($\overline{E/C}_P = 1.28 \pm 0.12$), suggesting E/C_R of less than one. Figure 4.14 shows examples of how this decreased ratio arises from the R.F. signals, due to greater acceleration and velocity upon contraction than upon expansion, which can be measured in the experimentally measured signals ($E/C_P = P_{max}/P_{min}$).

An expansion to compression ratio of less than one implies that the bubbles are dominated by the compression phase of the oscillation, and similar behaviour has been observed previously using optical techniques. Emmer et al[80] have modeled the soft lipid shelled BR14 (Bracco Research SA, Geneva, Switzerland) using a modified Rayleigh-Plesset model (RPNNP) to predict bubble response, and the Hoff model[128] to predict shell behaviour, and shown that when the simulations predict dominant expansion ($E/C_R > 1$), values of radii oscillations measured with the high speed Brandaris128 camera show compression dominated scatter ($E/C_R < 1$). Marmottant et al[50] have also described so-called "compression only" bubble scatter in lipid based agent BR14. They theorize that the forces in the lipid monolayer which encapsulate the gas, and therefore restrict both expansion and compression of the bubble, can be overcome by a driving pulse of sufficient pressure, suggesting buckling or folding of the monolayer, and producing a bubble that is more easily compressed than expanded.

Similar behaviour can be seen in the R.F. signals from the resonant population of scatter defined above, as shown in Figure 4.14(a)-(c). The R.F. envelope of scatter from a resonant bubble increases linearly for 3-4 cycles, showing expansion dominated behaviour ($E/C_P > 1$) as predicted by the Mooney Rivlin model, and producing the increasing fundamental amplitude seen in Figure 4.14 (d)-(f). This is then interrupted by a strong negative pressure spike over the following full cycle of response, giving the dip in harmonic scatter shown in Figure 4.14 (g)-(i), and leading to a decreased expansion to compression ratio for the signal as a whole ($E/C_P = P_{max}/P_{min}$). As the restriction to the oscillations of the bubble by the encapsulating shell leads to the harmonic components of scatter, this is thus reduced when the shell's integrity is compromised, as observed in the harmonic response, Figure 4.14 (g)-(i). This behaviour is

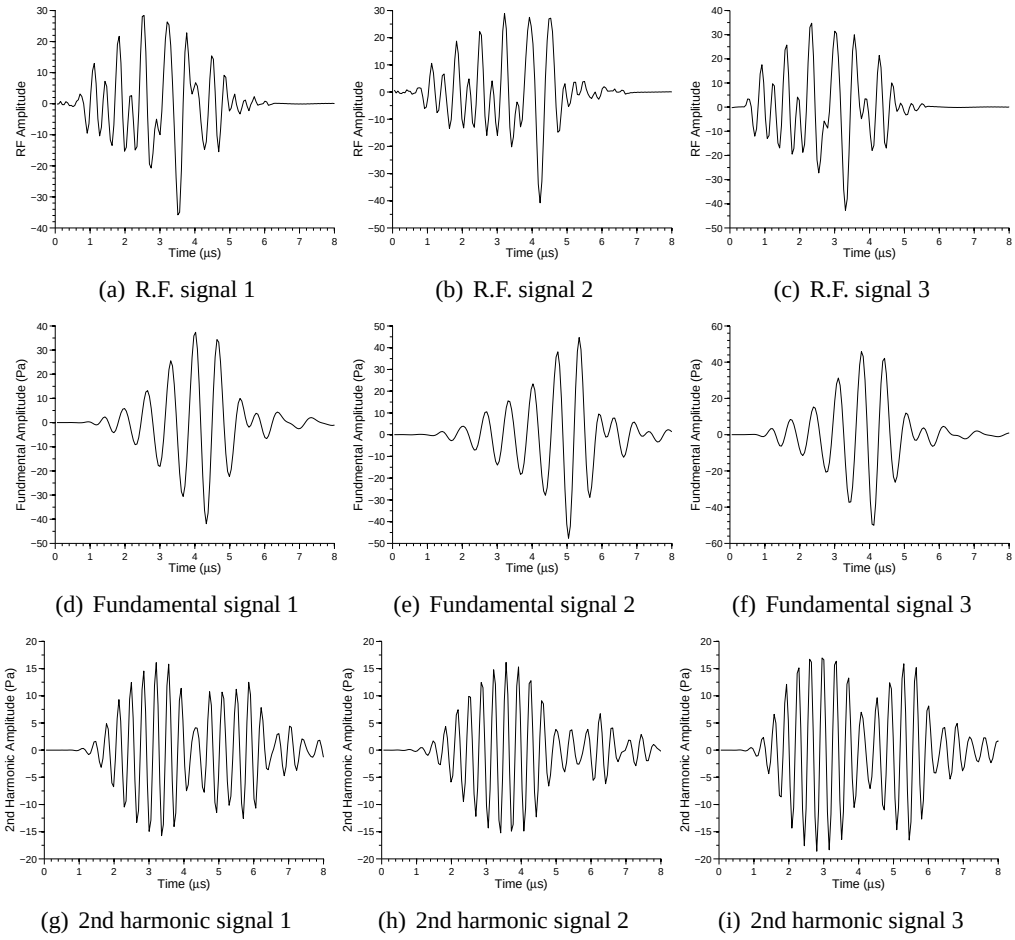

(a) R.F. signal 1 (b) R.F. signal 2 (c) R.F. signal 3

(d) Fundamental signal 1 (e) Fundamental signal 2 (f) Fundamental signal 3

(g) 2nd harmonic signal 1 (h) 2nd harmonic signal 2 (i) 2nd harmonic signal 3

Figure 4.14: *Examples of resonant scatter showing a negative pressure spike occurs after 4-5 cycles of the incident pulse. Strong negative pressure spikes are observed in the R.F. data (uncalibrated R.F. scatter shown) at* $t = 3.5\mu$s *(a),* 4.2μs *(b),* 3.3μs *(c). Until these spikes appear, the scatter is dominated by the expansion phase (*$E/C_P > 1$*), as previously predicted by the Mooney Rivlin model, and has increasing envelope of fundamental scatter (d)-(f). These negative pressure spikes give the signals an overall ratio* $E/C_P < 1$*, and lead to a dip in the respective 2nd harmonic envelopes of scatter at* $t = 4.3\mu$s *(g),* 5.4μs *(h),* 4.0μs *(i). This is not observed in the off-resonant scatter. Filtered signals are shifted slightly with respect to the R.F., as a consequence of the elliptical filters used to separate the respective components.*

not predicted by the Mooney Rivlin model (Chapter 3). That this behaviour is only observed in signals of increased scatter (i.e. is not observed in off-resonant signals), and only after a number repeated cycles of symmetric scatter, suggests that this is caused by structural forces in the lipid monolayer being overcome by the stresses caused by repeated oscillations of the bubble, as previously suggested[50].

A model for this non-linear behaviour is presented by Marmottant et al[50], based on a description of the shell properties defined by a buckling radius, shell compressibility and a maximum shell tension term, and this predicts the behaviour well. Differences in experimental setup exist however between these optical measurements and the acoustic ones made here, which may explain any discrepancies in response. The main difference is possibly the use of a capillary tube to position the bubbles, which the authors admit will therefore be affected by buoyancy forces driving the bubbles toward the capillary wall. The use of capillaries has previously been shown to effect bubble oscillation amplitude and symmetry[134,137].

4.6.4 Frequency and acoustic pressure dependence

Figure 4.15 shows results from a variety of incident frequencies (550kPa, six cycle pulses), with signals classified using normalized cross-correlation as described above. A resonance population as described above, and was observed from 1.4MHz up to 2.0MHz, as shown in Figure 4.16. Above 2.0MHz no resonance behaviour was detected using this criteria.

The results from increasing acoustic pressures are displayed in Figure 4.18, showing a scatter plot of the fundamental components of response, and grouped into the two populations as defined by the cross correlation study, in response to transmit pressures up to 1.5MPa. Similar results are seen across the range of frequencies, and these are in good agreement with the theoretical results shown previously. The lowest acoustic pressure at which Definity bubble signals could be measured above noise was 187kPa. At these low acoustic pressures (less than 550kPa), very few bubbles signals are recorded to be at resonance (less than 10% of bubbles measured). However, even at the lowest pressure measured (187kPa) these instances do exist, suggesting that there is no absolute threshold of acoustic pressure for resonance behaviour, within the acoustic pressures measured here. As the transmit pressure is increased to medium pressures (550kPa), the instances of this resonance behaviour increases to 18.5% of bubbles measured, and becomes a significant proportion of the total scatter from a sample of microbubbles (70% of the fundamental and 15% of the second harmonic scatter). At high pressures, above 1MPa,

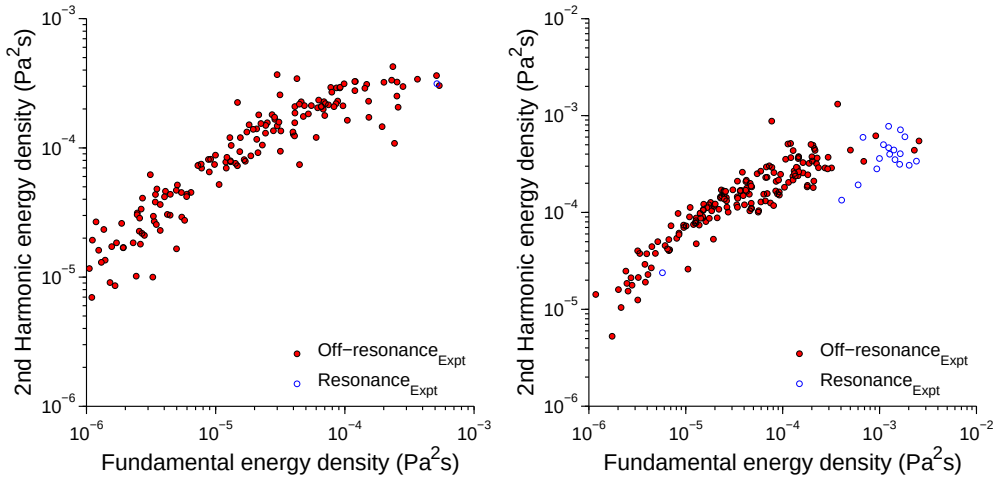

(a) 1.26MHz (b) 1.30MHz

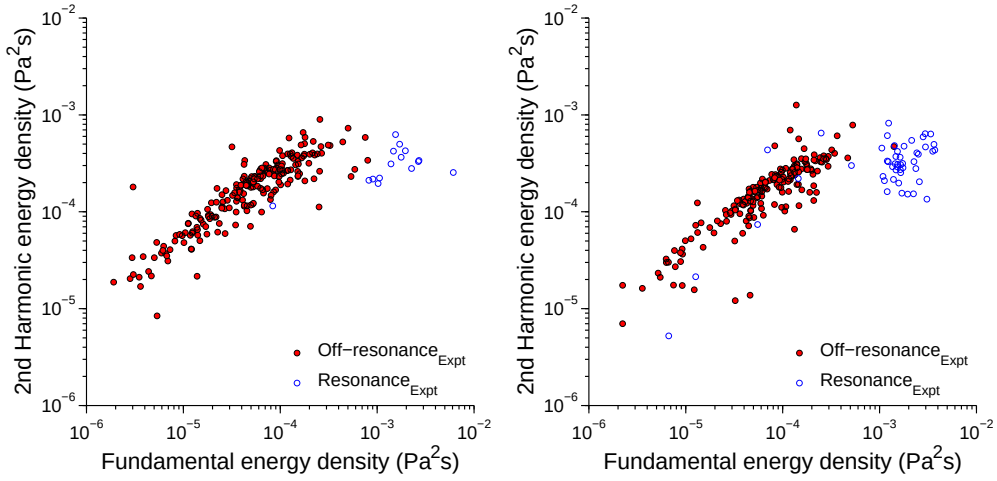

(c) 1.4MHz (d) 1.6MHz

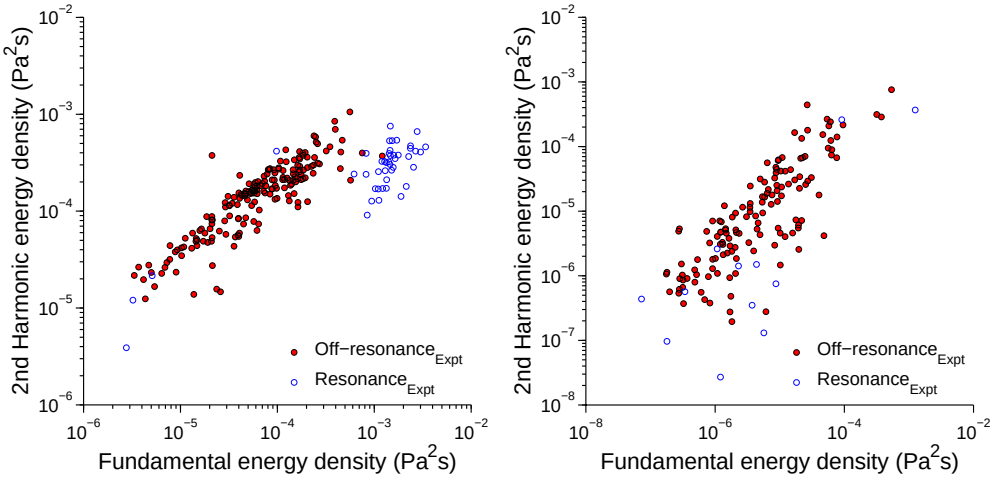

(e) 1.70MHz (f) 2.5MHz

Figure 4.15: *Variations in energy density with increasing frequency (550kPa, six cycle) imaging pulses. Above 2.0MHz no resonance behaviour is detectable at increased energy of scatter.*

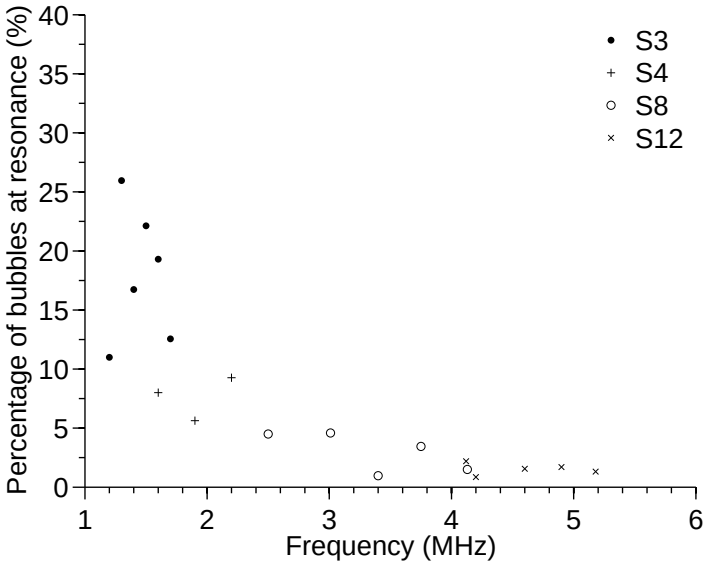

(a) Number of bubbles at resonance

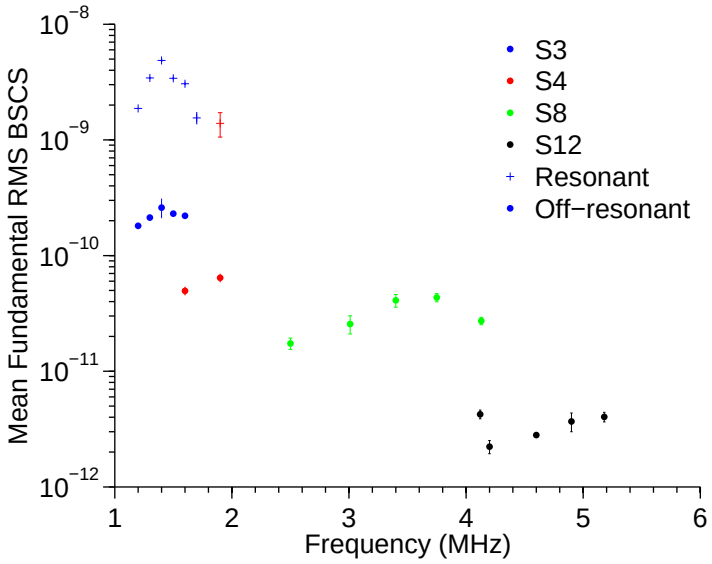

(b) Mean fundamental scatter for off-resonant and resonant bubbles

Figure 4.16: *Experimental results to increasing frequency (550kPa, six cycle) imaging pulses. (a) shows the number of bubbles classified as resonant by a normalized cross correlation analysis to be decreasing with frequency, in agreement with Mooney Rivlin results. (b) shows back-scattering cross section-like results for all four transducers ($1.2 < f < 5.5MHz$), with mean resonant (+) and mean off resonant scatter (.) shown. A resonant population is observed for frequencies up to 2MHz. Peak scatter is achieved at 1.4MHz (as compared to 1.6MHz predicted by theory), and decreases with increasing frequency. RMS pressures have been shown here to allow comparison between different incident frequencies.*

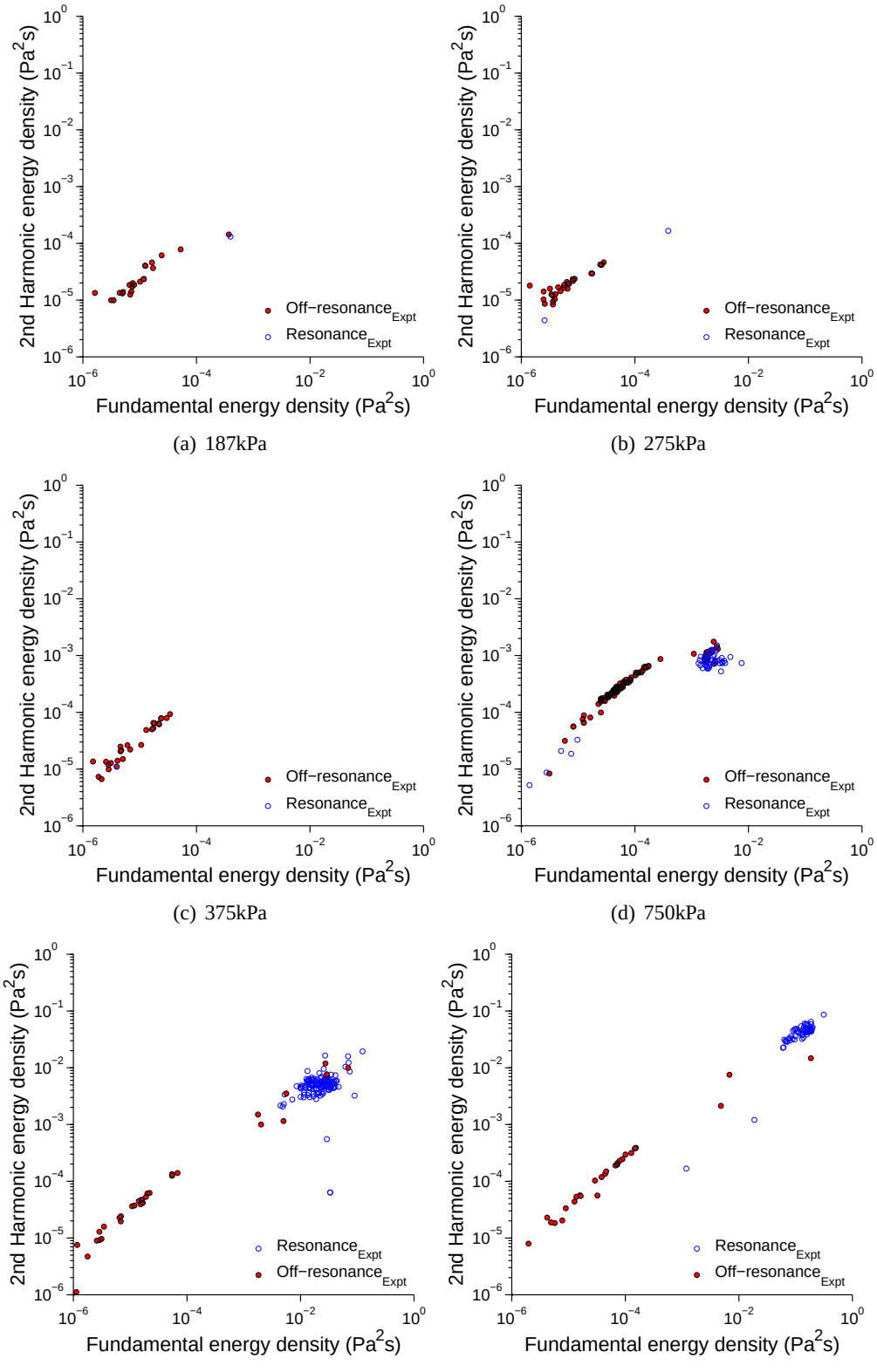

Figure 4.17: *Variations in energy density with increasing acoustic pressure (1.6MHz, six cycle) imaging pulses.*

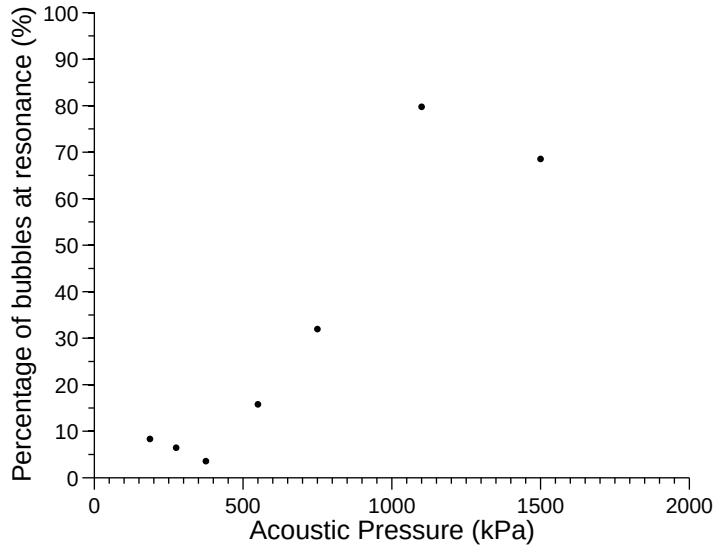

(a) Number of bubbles at resonance

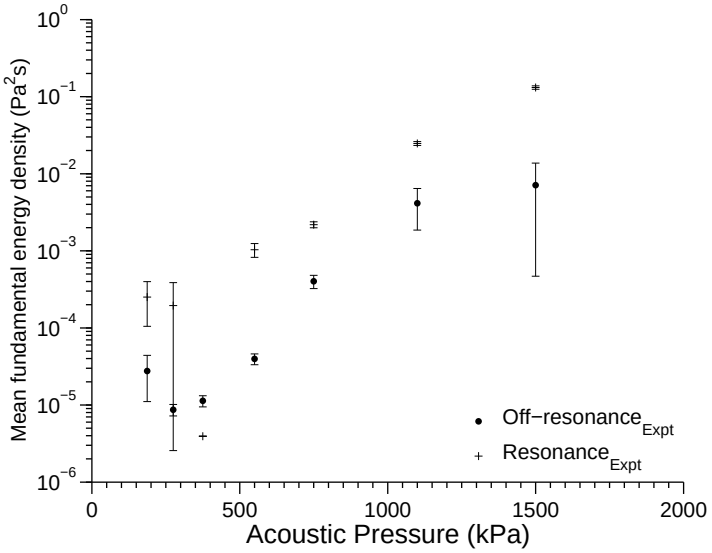

(b) Mean fundamental scatter for off-resonant and resonant bubbles

Figure 4.18: *Experimental results to increasing incident acoustic pressure (1.6MHz, six cycle). (a) shows the number of bubbles classified as resonant by a normalized cross correlation analysis to be increasing with acoustic pressure, in agreement with Mooney Rivlin results. (b) shows mean resonant (+) and off resonant scatter (.), also increasing with acoustic pressure.*

more than 80% of the bubbles measured are at resonance. This shows good agreement with the Mooney Rivlin results.

At pressures above 700kPa, the mean energy of scatter increases exponentially with incident acoustic pressure, and is dominated almost completely by the population two scatter (up to 85% by both number of scatterers and total energy of scatter of fundamental and harmonic components). This agrees well with the Mooney Rivlin data previously presented.

At these high acoustic pressures the destruction of bubbles may become significant, even in the first pulse scatter results shown here. The effects of acoustically induced fragmentation and diffusion will be covered in more detail in Chapter 5, but evidence of this can be seen in the lack of the scatter at medium energy densities for incident pressures above 1MPa (Figure 4.17), which is not present in the Mooney Rivlin results.

4.6.5 Comparison between experiment and theory

Figure 4.19 shows how the experimental signals compare with the results from the Mooney Rivlin model, in response to a 1.6MHz, 550kPa six cycle pulse. At low energy of scatter, the model predicts a higher concentration of scatterers, which can be explained by lack of sensitivity of the receiver. In using a shell stiffness value of $G_s = 50MPa$, the theoretical results overestimate the values of the peak scatter, Figure 4.19(a). Mean energies of resonant scatter are calculated to be 9.8×10^{-3} and $1.8 \times 10^{-3} Pa^2 s$ (fundamental and 2nd harmonic respectively), as compared to 1.9×10^{-3} and $3.6 \times 10^{-4} Pa^2 s$ measured experimentally. With a reduced shell stiffness value of $G_s = 10MPa$, the theoretical results show improved agreement with the experimental results, as shown in Figure 4.19(b), with theoretical mean energies at resonance of 2.9×10^{-3} and $4.5 \times 10^{-4} Pa^2 s$ (fundamental and 2nd harmonic respectively). Similar improvements have been observed at a range of frequencies and acoustic pressures.

4.6.6 Higher harmonic resonance

As shown in Chapter 3 (Figure 3.23), third harmonic resonance can be identified in a distribution of scatterers. The number of bubbles measured experimentally to be dominated by the third harmonic component of response is reduced as compared with that predicted by the Mooney Rivlin model. Figure 4.20 shows this third harmonic scatter in response to a 1.2MHz 550kPa six cycle pulse (this is at the lower end of the transducers bandwidth, and offers greater ac-

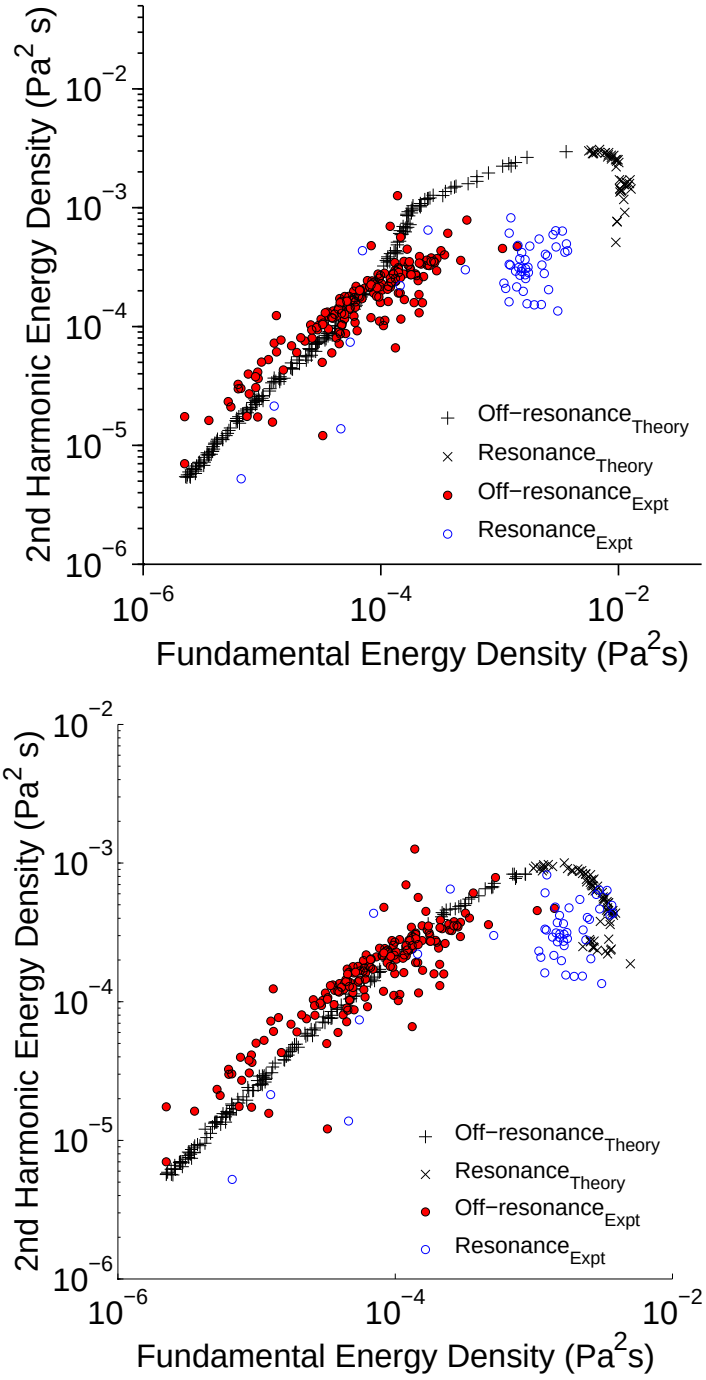

Figure 4.19: *Comparison of 235 experimental signals with 235 randomly sampled theoretically simulated signals. Incident pulse is 1.6MHz, 550kPa six cycle in both theory and experiment. In Figure (a) the shell stiffness variable has been set to $G_s = 50MPa$, which leads to overestimation of the energy density in bubble signals at resonance. Figure (b) shows the improved agreement observed when a shell stiffness of $G_s = 10MPa$ is used.*

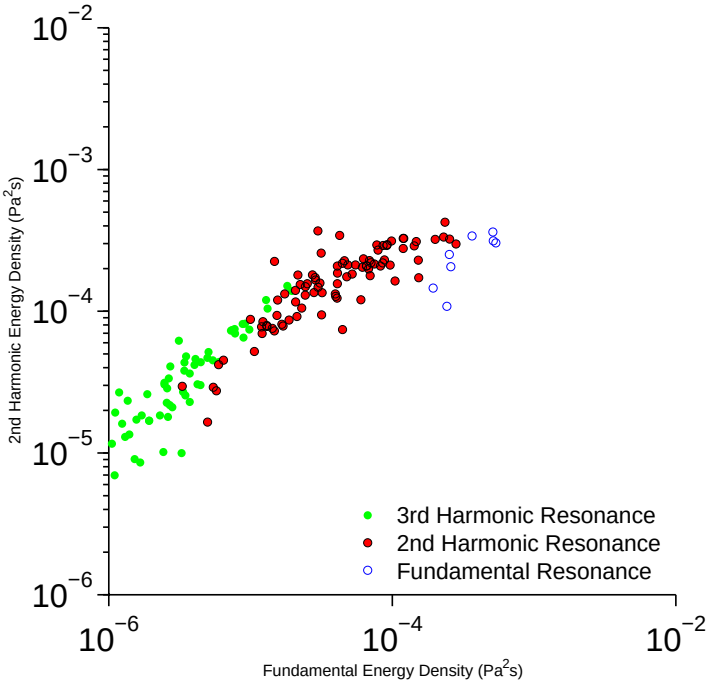

Figure 4.20: *Scatter has been classified by the dominance of the respective components of harmonic scatter, as shown in Chapter 3 (Figure 3.23). In response to a 1.2MHz 550kPa six cycle pulse,* 37% *of bubbles are dominated by the third harmonic,* 49% *are dominated by the second harmonic, and only* 14% *are dominated by the fundamental component. The third harmonic resonance population accounts for* 10.2% *of the total R.F. energy of scatter for the sample of bubbles. Due to the bandwidth of the transducer, an incident frequency of 1.2MHz gives greater sensitivity at the third harmonic, as compared to 1.6MHz.*

cess to the third harmonic bubble response). 49% of bubbles are dominated by third harmonic (10.2% of the total R.F. energy of scatter) compared to 71.4% (7.8% of the total R.F. energy of scatter) as predicted by the Mooney Rivlin model. This reduction could be explained by lack of detection at these low energies of scatter (as outlined above). Also observed is increased overlap between the regions of resonance, explained by the greater variation of bubble responses (as defined below).

The results to an incident frequency of 1.2MHz are shown here, as at this frequency the S3 transducer has maximum sensitivity of the third harmonic response, due to the transducers bandwidth. Figure 2.16 in Chapter 2 shows how the third harmonic receive sensitivity drops off sharply for increasing frequencies. This limits the ability to investigate the higher harmonic response experimentally, and it was not possible to produce experimental graphs of increasing incident frequency, equivalent to the theoretical ones shown in Chapter 3 (Figure 3.25).

4.6.7 Variation in experimental response

The experimental data in Fig. 4.19 displays a variance greater than experimental error calculations predict. The theoretical data shown has experimental error added as random variations to the energy densities (7.1% fundamental and 5.5% harmonic standard error for the imaging parameters used here). Figure 4.21 shows the comparison between the two data sets' variance (1.6MHz 550kPa incident pulse in both cases), as calculated using a simple second-order polynomial model for the off-resonance population, and calculating a 95% confidence interval. Although this doesn't accurately model the data, it does provide a simple metric for mean variance with increasing energy of response.

Experimental data shows a mean variance of 21.6%, compared to 6.3% theoretical. Variations of up to 150% in the maximal excursions of optically identical bubbles have been measured previously[117], attributed to differences in elastic properties of individual shells, and may explain these inconsistancies. A full analysis of variance and comparison with optical results will be the subject of further work.

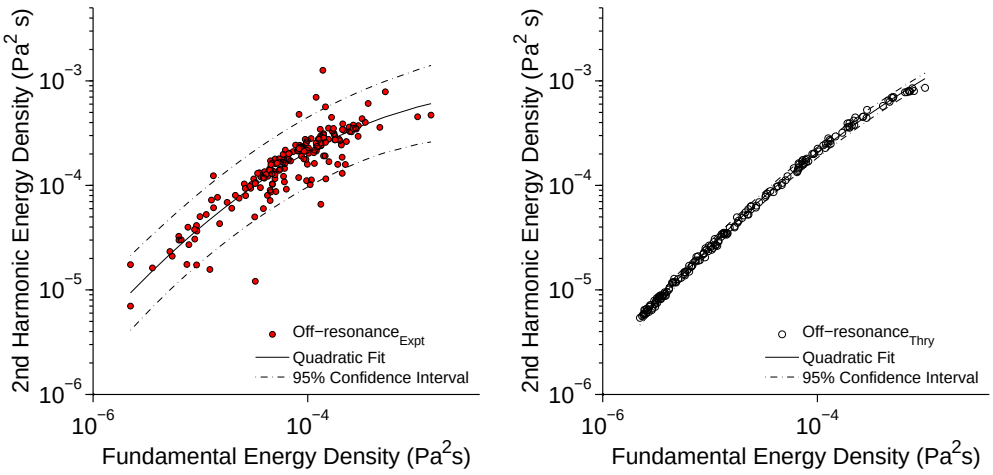

(a) Experimental variance

(b) Theoretical variance

Figure 4.21: *Variation in experimental off-resonance signals is greater than that for theoretical values including experimental error (21.6% experimental as compared to less than 1% theoretical), as added to the Mooney Rivlin results. The incident pressure in both cases is 1.6MHz 550kPa six cycle pulses. A second-order polynomial model has been fitted to the off-resonance population of each data set, and the 95% confidence interval plotted.*

4.7 Discussion

Data has been produced that has allowed a comparison between theoretical and experimental single bubble results. Resonance behavior has been identified from the theoretical modeling of bubble dynamics using the Mooney-Rivlin shell model to estimate the soft lipid shell of Definity microbubbles. In a previouse chapter it has been shown that bubbles at and above resonance are predicted to respond with significantly larger signals than those below, and this has been observed experimentally. These resonant bubbles have been shown to have reduced second harmonic components of scatter with respect to the fundamental, and a similar characteristic has been observed experimentally in bubbles with large responses. A clear distinction between the two populations of resonant and off-resonant bubbles has been observed, for a range of frequencies and acoustic pressures. A second characteristic of resonance is observed in the increasing fundamental envelope of bubbles around resonance, in both the theoretical and experimental results, which has been quantitatively defined using a normalized cross-correlation method. Experimental resonant bubbles have been shown to consist of a compression dominated response, which is in disagreement with the Mooney Rivlin results. This disagreement

between experimental results and simulation has been observed in the literature previously, and suggests the Mooney Rivlin model, as presented here, does not fully describe the dynamics of lipid shelled microbubbles.

Results are also presented, both theoretical and experimental, showing the effect of increasing frequencies and acoustic pressures on the two populations. For increasing frequencies, both data sets show decreasing energy of scatter, due to the decreasing resonance radius effecting the value of peak scatter. For increasing acoustic pressure, the experimental values agree well with the predictions from the Mooney Rivlin model, showing exponential increase of scatter energy and increasing numbers of bubbles defined to be at resonance. Discrepancies exist however in a lack of experimentally observed medium-energy scatter at high acoustic pressures, which suggests the destructive effects of the incident pulse become dominant. The effect of acoustically driven destruction and diffusion will be investigated further in Chapter 6.

4.8 Conclusion

In conclusion, experimentally measured single bubble data has been produced using a well characterized commercial ultrasound system. A two population response has been observed in response to a single set of imaging parameters. A theoretical model of the forced oscillations of soft-shelled encapsulated gas microbubbles has been used to identify these populations as below resonant and resonant scatter. Indicators which allow the classification of acoustic bubble signals as resonant scatter have been identified and observed experimentally.

This has allowed the identification of resonant scatter in acoustic single bubble experimental data for the first time. The techniques presented here provide significant insight into resonant populations of bubble scatter, providing the basis for improved imaging techniques based upon more intelligent pulse sequence design and/or improved signal processing. As stated in the aims of the chapter, this knowledge can directly improve current clinical techniques which suffer from poor resolution or limited contrast, both of which can be improved by using improved pulse sequences which are designed to increase the amount of bubbles which are at resonance.

4.9 Further work

The work presented here is a qualitative comparison between theory and experiment. In order to improve the model by fitting the parameters used to model the soft phospholipid shell of Definity, a more rigorous statistical analysis is needed. A one-to-one map associating each experimental signal with a one specific simulated signal (with optimized parameters) would allow a complete analysis of parameter variance (for example, using Monte Carlo methods to show the significance of any disagreement[138,139]), and determine if optimal parameters exist for an ensemble of microbubbles. This approach has the potential to further improve the understanding of the shell's effect on soft shelled microbubbles.

Further experimental results will also improve understanding of the Definity response to ultrasound imaging pulses. In particular, the effect of differing incident pulse lengths on the response from the resonance populations will be investigated.

Chapter 5

Single bubble experiments with the contrast agent biSphere™

5.1 Aim of chapter

This chapter presents and discusses theoretical and experimental data for the albumin shelled contrast agent biSphere™ (Point Biomedical Corp., San Carlos, CA), in response to a variety of incident pulse parameters, in order to gain physical insight into the response of such microbubbles to various ultrasound parameters. Knowledge gained from previous chapters will be used to reach conclusions on the scatter from this agent, with respect to the differences from a lipid shelled agent.

5.2 Introduction

BiSphere™ (POINT Biomedical, San Carlos, CA, USA), consists of a double layered shell which encapsulates an air bubble. The inner shell, consisting of biodegradable biopolymers, gives the bubbles their physical structure. The outer albumin layer is designed to operate as a biological interface, and can be independently tailored to specific diagnostic or therapeutic applications. The mean diameter of the bubbles is $4\mu m$. The double layer shell gives the bubbles increased resilience to ultrasound destruction as compared to single shelled albumin agents.

The encaspulated gas is air, which is soluble in water. This dramatically reduces the lifetime of the agent once the shell is broken, and optimizes the agent for destruction techniques such as harmonic power Doppler imaging [140]. Other variants of the agent, for example PB127, with the same shell construction containing nitrogen as the encapsulated gas core, are available but are not investigated here.

5.3 Methodology

The single bubble microacoustic imaging system described in Chapter 4 (Figure 4.1) was used to investigate the contrast agent biSphere. The agent is supplied in dry powder form and is reconstituted with sterile water prior to use, by adding water to a vial of the dry powder and shaking by hand to yield a suspension of microbubbles. A suitable concentration of microbubbles was found by trial and error method, which gave an average of one bubble in the region of interest per three imaging frames, as was the same with Definity. In this way the results can be directly compared. The flow path and acoustic imaging systems were aligned as described in Chapter 4, and the captured RF files were analysed in the same way as with Definity signals. The imaging parameters used in Chapter 4 were again used here to investigate the response of biSphere bubbles to a range of frequency and acoustic pressures.

5.4 Results

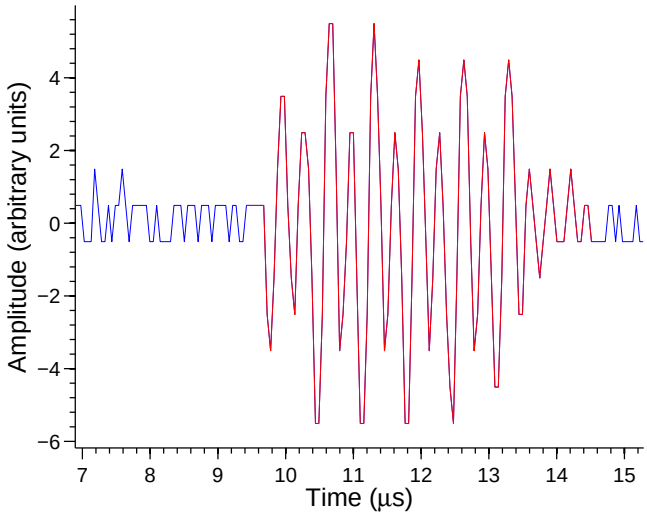

Figure 5.1: *Example a RF signal from a biSphere microbubble in response to a 1.6MHz, 550kPa 6 cycle pulse, with the sum-squares algorithm applied to identify the signal above noise. The R.F. signal is* $5.09\mu s$ *in duration, and contains six cycles in response to the incident pulse.*

Figure 5.1 shows a six cycle biSphere echo, in response to a 550kPa 1.6MHz six cycle pulse. The R.F. signal is $5.09\mu s$ in duration, and contains six cycles in response to the incident pulse, as can clearly be seen. The signal has been filtered into its fundamental and second harmonic

components, using the same elliptical filters as outlined in previous chapters (Chapters 2, 3 and 4), as shown in Figure 5.2. The signal is strongly harmonic, and the second harmonic component of scatter is stronger than the fundamental, with peak amplitude of 6.83Pa and an energy density of $8.71 \times 10^{-5}\mathrm{Pa}^2\mathrm{s}$. The fundamental scatter from this bubble is approximately six times weaker in terms of total energy, with a peak amplitude of 3.05Pa, and an energy density of $1.32 \times 10^{-5}\mathrm{Pa}^2\mathrm{s}$.

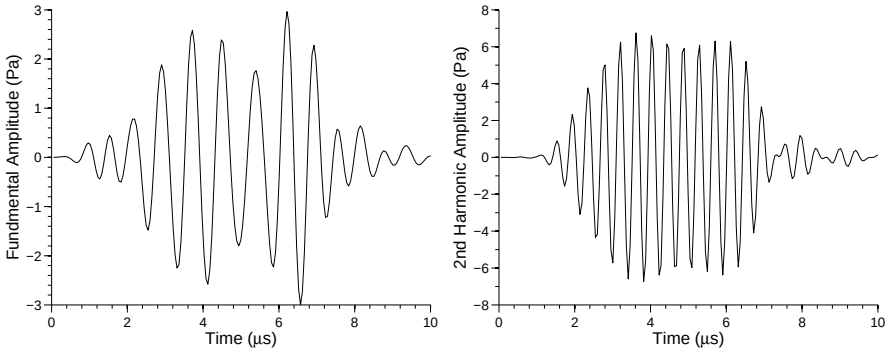

(a) Fundamental components of scatter (b) Second harmonic components of scatter

Figure 5.2: *Filtered biSphere signal, showing the fundamental and second harmonic components of scatter, in units of Pascals*

However, in addition to this type of echo signal, which is of approximately the same length as the incident signal (approximately 4μs, and containing six cycles of the fundamental frequency), biSphere echoes of a large variety of signal lengths have been measured. Figure 5.3 shows a short response of only 1.94μs in length (R.F. signal), containing only one clear visible cycle. The filtered components of this signal are shown in Figure 5.4, and the differences in energy density of each respective frequency component can be seen, due to the shorter duration. The distribution of echo signal lengths are shown in Figure 5.5, showing a large distribution of scatter, with a mean duration of $3.87 \pm 1.35\mu$s. The accuracy of the signal duration calculation is dependent on the semi-automatic edge detection method outlined in Chapter 4. The amplitude of responses (shown instead of energy densities, to allow direct comparison between signals of different duration) from this distribution are shown in Figure 5.6, with the duration of the responses shown on the associated color bar. In order to simplify the following analysis, the durations of response have been arbitrarily separated into two populations, using the binary classification scheme shown in Figure 5.7 (taken from the dual-population distribution shown in Figure 5.5). Signals of durations less than $\Delta t = 0.75\Delta t_{incident}$ account for 45% of scatterers by number, and have a mean scatter of $2.52 \pm 0.09 \times 10^{-6}$ and $7.39 \pm 4.15 \times 10^{-6}\mathrm{Pa}^2\mathrm{s}$

fundamental and 2nd harmonic components respesctively. In this case, $0.75\Delta t_{incident} = 2.8\mu$s (this values differs depending on incident frequency). This compares to those with durations greater than $\Delta t = 2.8\mu$s, whose mean scatter is $1.16 \pm 5.15 \times 10^{-4}$ and $0.42 \pm 0.51 \times 10^{-4}$Pa^{2}s fundamental and 2nd harmonic components respesctively. This simple classification helps to limit the effect of the error in the duration calculation, as errors in very short signals will not be sufficient to cause them to be misclassified, and the two populations can be analaysed with confidence.

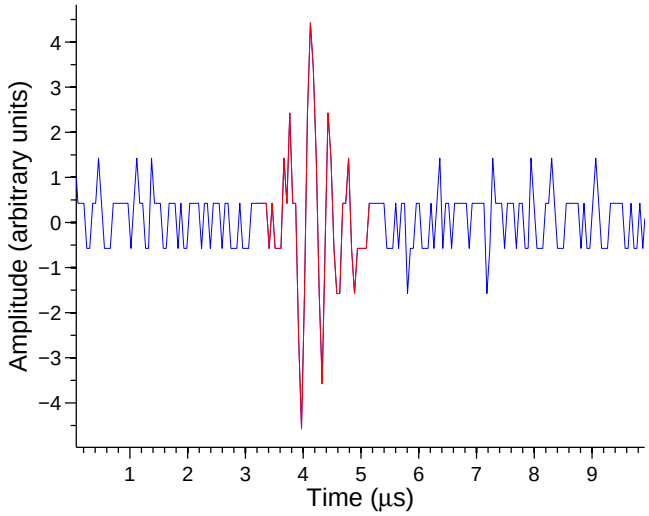

Figure 5.3: *Example a RF signal from a biSphere microbubble in response to a 1.6MHz, 550kPa 6 cycle pulse, with the sum-squares algorithm applied to identify the signal above noise. The R.F. signal is* 1.94μs *in duration, and contains only one clear visible cycle in response to the incident pulse of six cycles.*

5.4.1 Response to increasing incident frequency

Figure 5.8 shows the variation in amplitude of scatter, in response to increasing incident frequency pulses (550kPa, six cycle pulses). Figure 5.9 shows the responses from higher frequency pulses (2.52MHz to 5.2MHz). The signals have been separated into two populations, using the above description of those with signal durations $\Delta t > 0.75\Delta t_{incident}$ and those with signal durations $\Delta t < 0.75\Delta t_{incident}$. This ranges from $\Delta t = 3.46\mu$s to $\Delta t = 0.87\mu$s.

Figure 5.10 shows that the number of partial echoes observed decreases significantly with increasing frequency. Below 2.0MHz approximately 30% of the scatterers measured are of duration $\Delta t < 0.75\Delta t_{incident}$. The difference between mean amplitude of scatter of the two

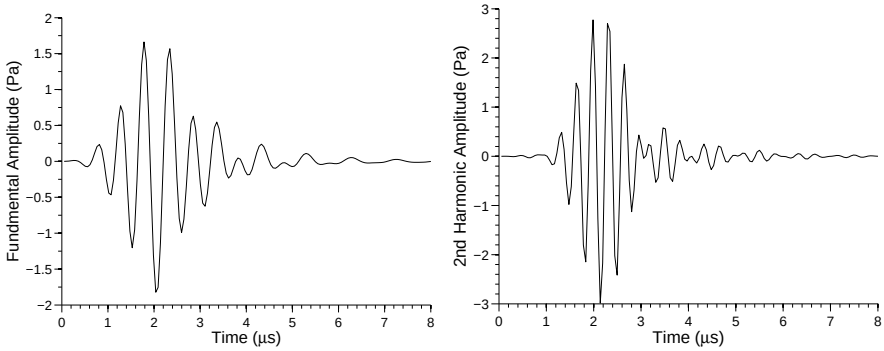

(a) Fundamental components of scatter (b) Second harmonic components of scatter

Figure 5.4: *Filtered biSphere signal shown in Figure 5.3, showing the fundamental and second harmonic components of scatter, in units of Pascals*

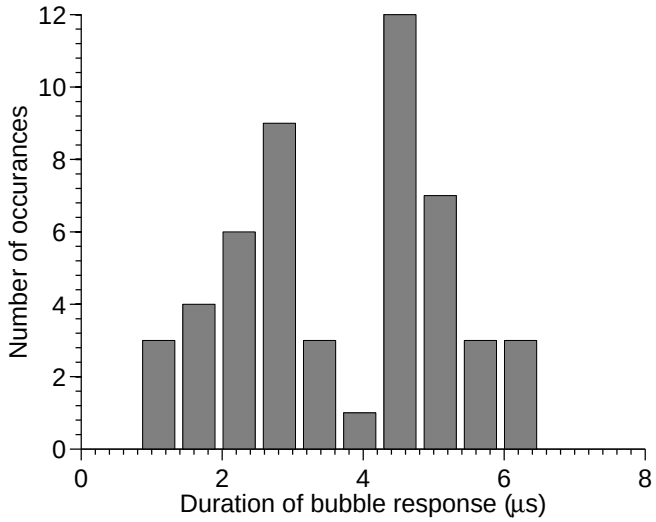

Figure 5.5: *Distribution of biSphere echo durations in response to a six cycle 1.6MHz 550kPa.*

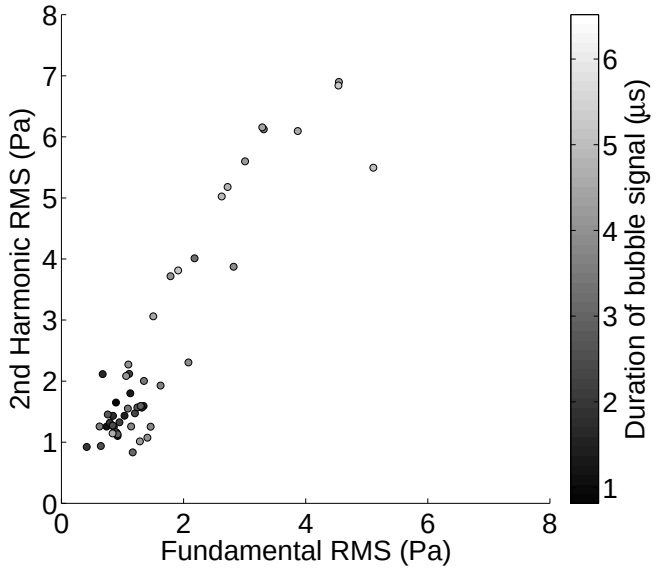

Figure 5.6: *Distribution of the duration of biSphere echo responses in response to a six cycle 1.6MHz 550kPa. The gray-scale shading of the symbols relates to the duration of the respective signals, as shown in the associated color bar (darker symbols indicating longer echo signals). As can be clearly seen, shorter signals relate to those of lower amplitude scatter. RMS signals are shown here to allow direct comparison between those of different durations.*

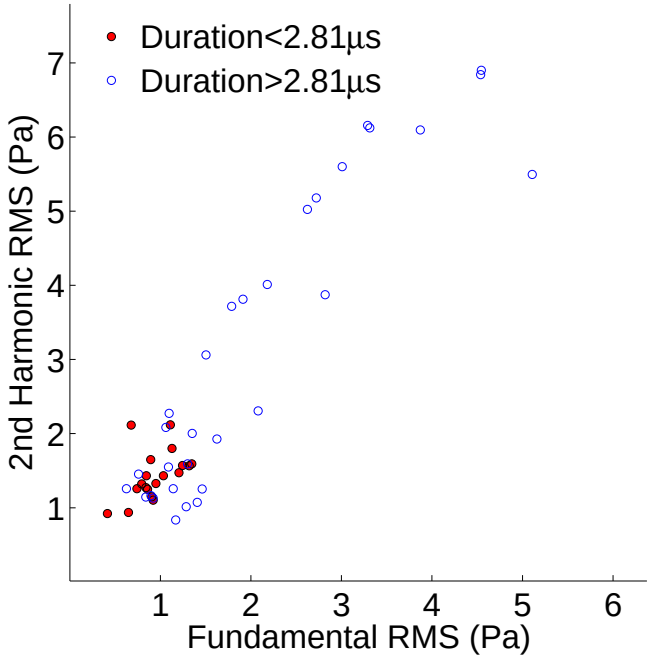

Figure 5.7: *Distribution of biSphere echo responses in response to a six cycle 1.6MHz 550kPa. The gray-scale shading of the symbols in the previous plot (Figure 5.6) has been replaced by an arbitrarily chosen binary classification scheme, separating signals by length into two populations: those with signal durations $\Delta t < 2.8\mu$s and those with signal durations $\Delta t > 2.8\mu$s, as defined by the length of the incident pulse. A clear relation to signal length and amplitude of scatter can be seen.*

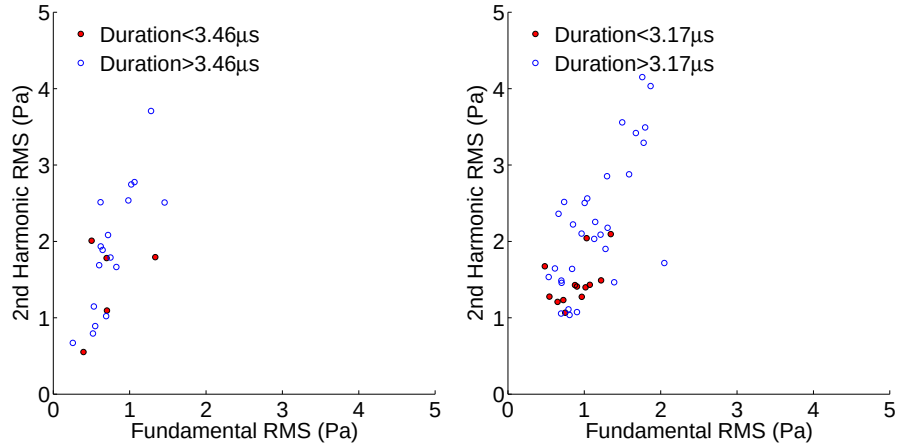

(a) 1.3MHz

(b) 1.42MHz

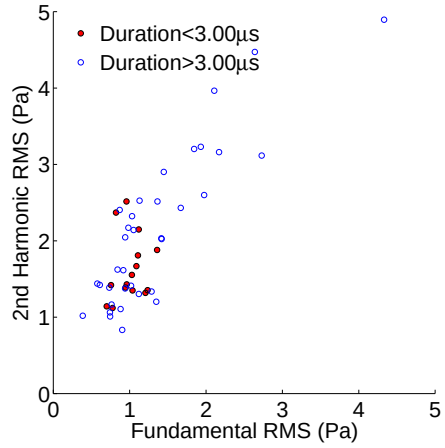

(c) 1.5MHz

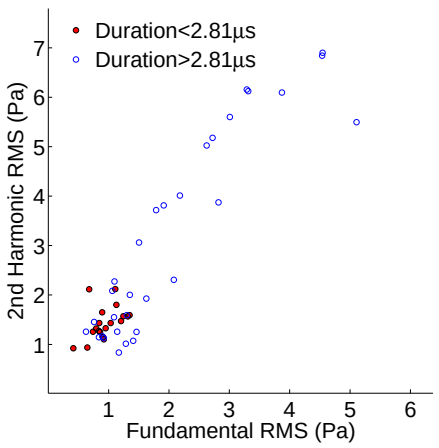

(d) 1.62MHz

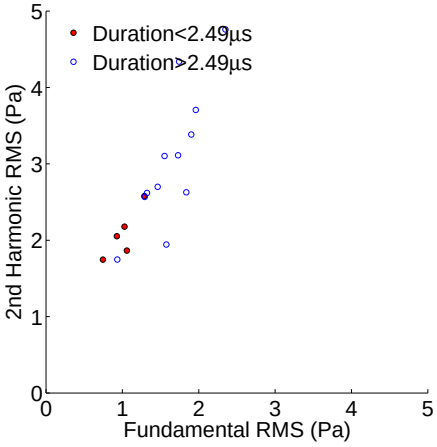

(e) 1.81MHz

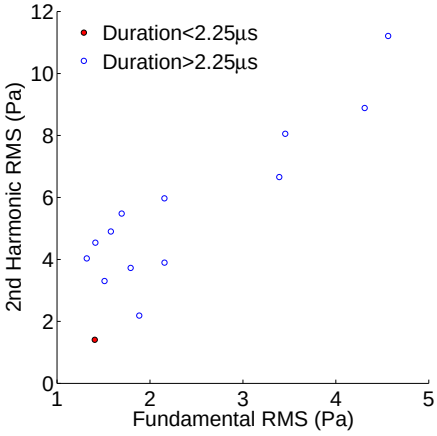

(f) 2.0MHz

Figure 5.8: *Variation in amplitude of biSphere signals in response to increasing incident frequency (550kPa, six cycle pulses), from 1.3MHz to 2.0MHz, separating signals by length into two populations, as defined by the length of the incident pulse.*

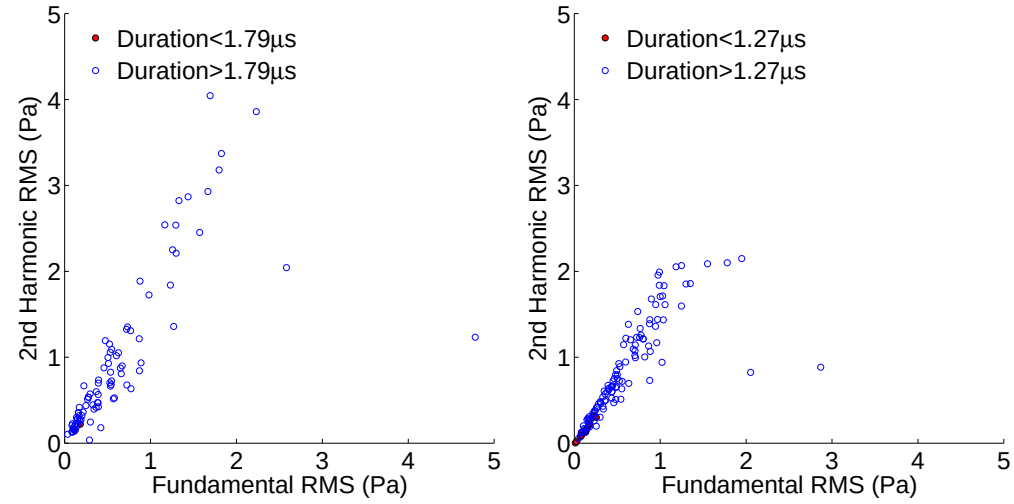

(a) 2.52MHz

(b) 3.55MHz

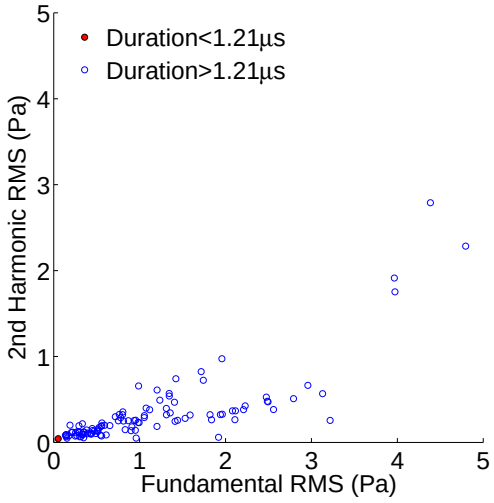

(c) 3.71MHz

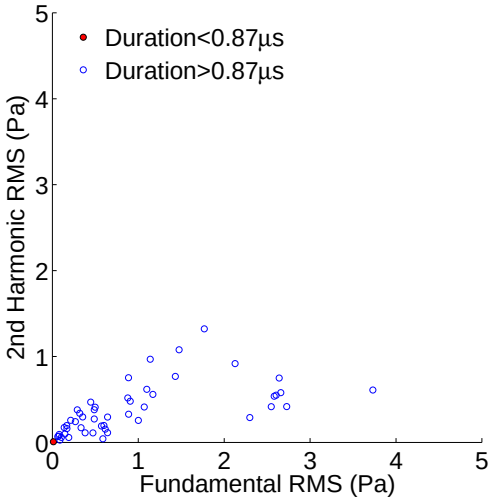

(d) 5.2MHz

Figure 5.9: *Variation in amplitude of signals from biSphere bubbles in response to increasing incident frequency (550kPa, six cycle pulses), from 2.5MHz to 5.2MHz. Signals have been separated into two populations, depending duration of signal defined by the incident pulse length. RMS signals are shown here to allow direct comparison between those of different durations.*

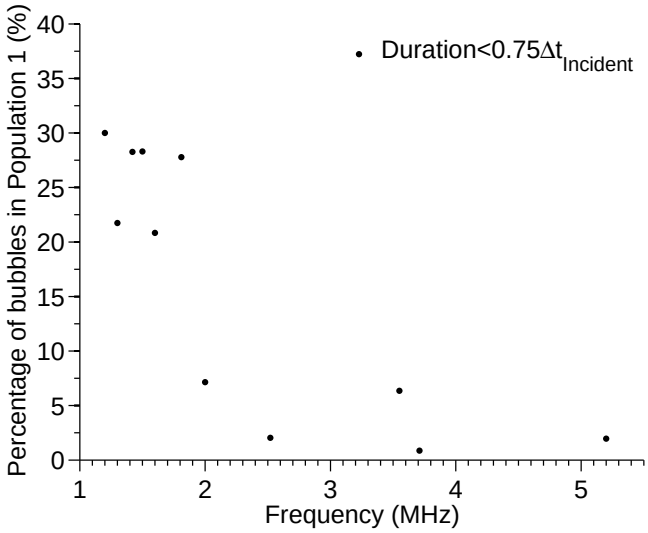

Figure 5.10: *Number of biSphere signals of duration $\Delta t < 0.75\Delta t_{incident}$, as a percentage (%) of the total number of scatterers measured. A clear relation to frequency can be seen, with the percentage of shorter echoes (relative to the incident pulse length) decreasing with increasing frequency.*

populations, in both fundamental and second harmonic, is approximately equal for frequencies less than 2.0MHz. As the frequency increases the small number of signals of partial echo are of significantly less amplitude than the those with durations approximately equal to the incident pulse, although here mean amplitude is calculated from $< 10\%$ of the scatterers measured (< 10 bubbles for each set of imaging parameters) and so may be effected by outliers. Figure 5.11 shows mean energy density of scatter, and Figure 5.12 shows mean amplitude of signals from each population for comparison.

5.4.2 Response to increasing incident acoustic pressure

As shown in Figure 5.13, in response to lower acoustic pressures biSphere bubbles show a more regular duration of response than is observed at the higher pressure of 550kPa, and the dual-response behaviour documented above is not observed. The durations of these scattered signals are approximately normally distributed around the incident pulse length of $\Delta t = 4.95\mu$s, and are all greater than $\Delta t = 2.8\mu$s. Figure 5.14 shows the amplitude of responses from biSphere bubbles to increasing acoustic pressures, from 160kPa to 335kPa.

As the acoustic pressure is increased further, the behaviour documented earlier in this section

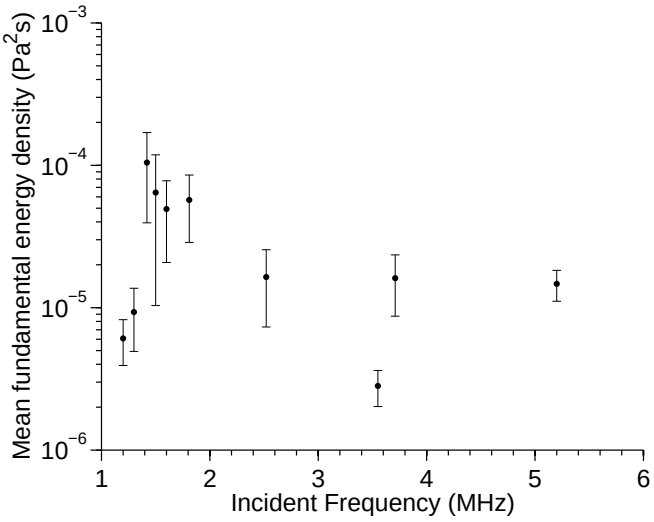

(a) Mean fundamental components of scatter

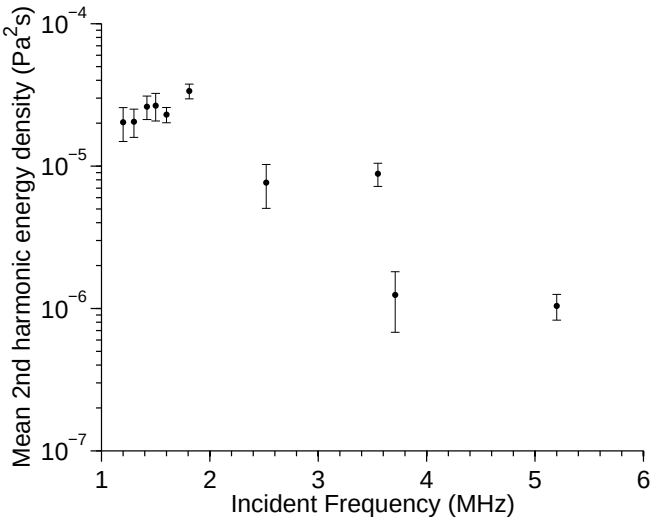

(b) Mean second harmonic components of scatter

Figure 5.11: *Mean energy densities of biSphere bubbles in response to increasing incident frequencies (550MHz, six cycles).*

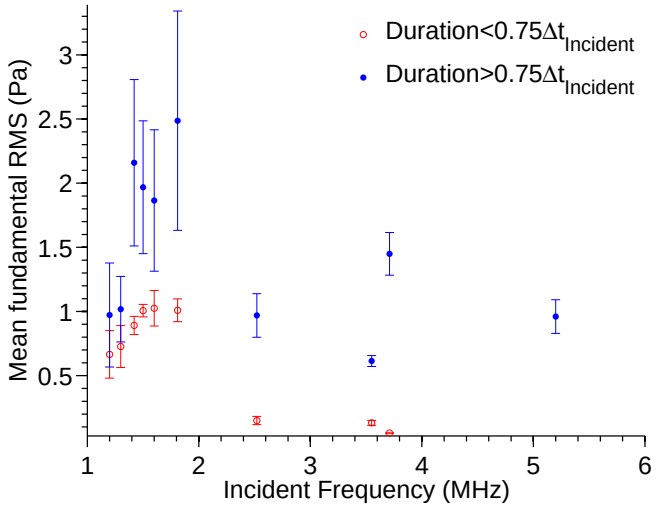

(a) Mean fundamental components of scatter

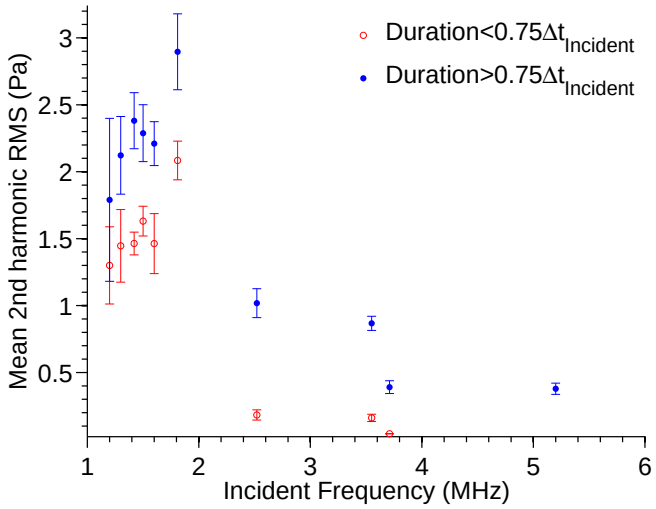

(b) Mean second harmonic components of scatter

Figure 5.12: *Mean amplitude of biSphere signals in response to increasing incident frequencies (550kPa, six cycles), as separated into two populations: those with signal durations* $\Delta t < 0.75\Delta t_{incident}$ *and those with signal durations* $\Delta t > 0.75\Delta t_{incident}$

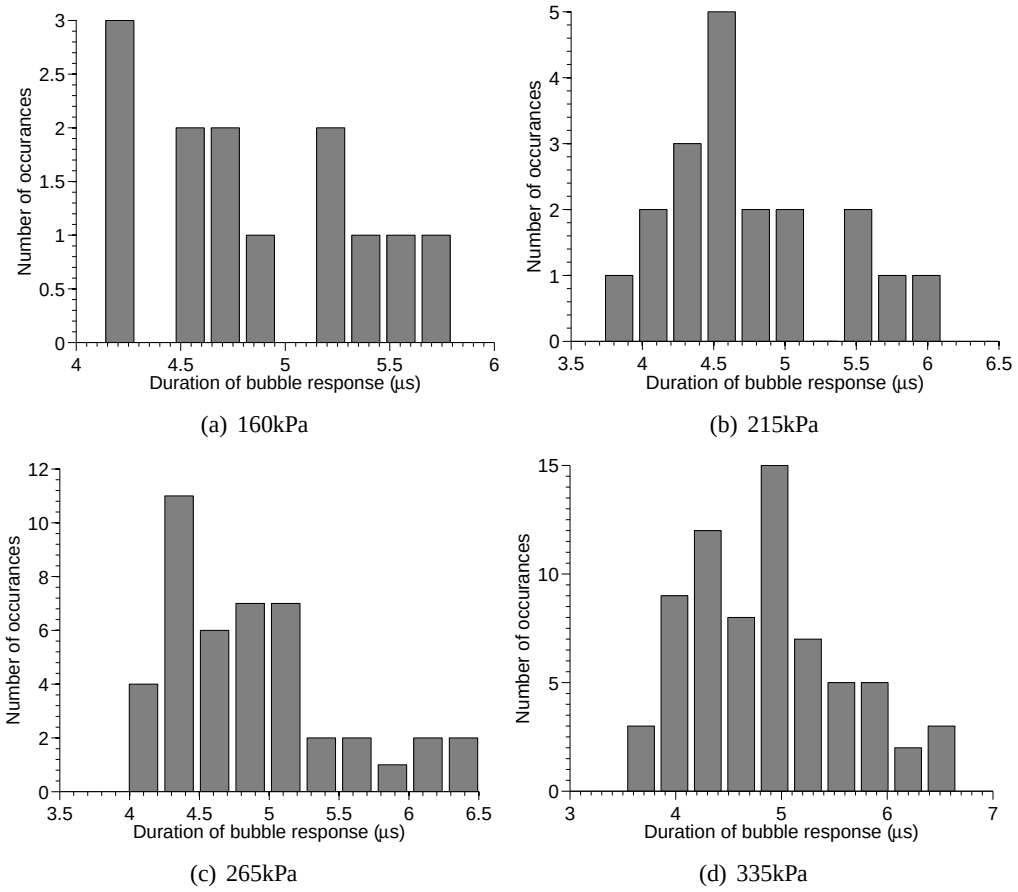

(a) 160kPa (b) 215kPa

(c) 265kPa (d) 335kPa

Figure 5.13: *Variation in durations of signals from biSphere bubbles in response to increasing acoustic pressures (1.6MHz, six cycle pulses), from 160kPa to 335kPa. In response to these lower acoustic pressures, the duration of bubble responses show approximately normal behaviour, and all signals recorded are of greater than* $\Delta t = 2.8\mu$s *in duration.*

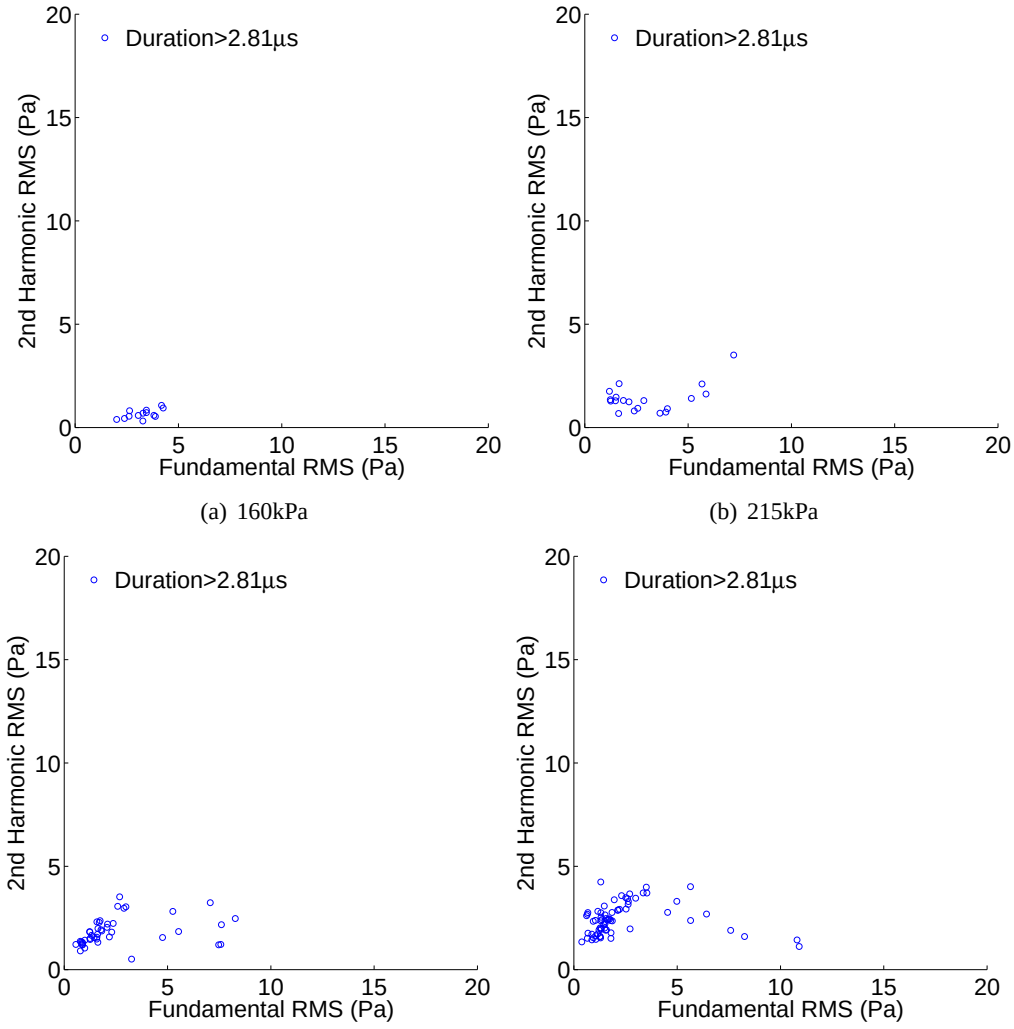

(a) 160kPa

(b) 215kPa

(c) 265kPa

(d) 335kPa

Figure 5.14: *Variation in amplitude of signals from biSphere bubbles in response to increasing acoustic pressures (1.6MHz, six cycle pulses), from 160kPa to 335kPa. All signals recorded are of greater than* $\Delta t = 2.8\mu$s *in duration.*

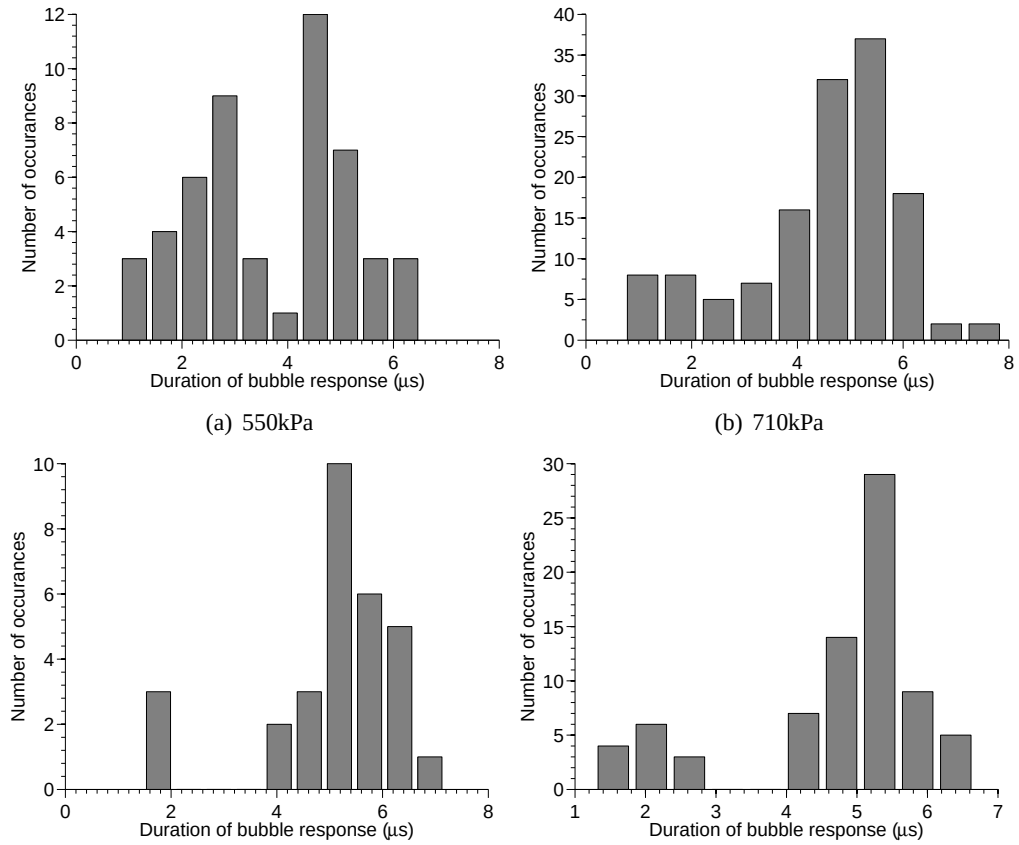

(a) 550kPa (b) 710kPa

(c) 850kPa (d) 1020kPa

Figure 5.15: *Variation in durations of signals from biSphere bubbles in response to increasing acoustic pressures (1.6MHz, six cycle pulses), from 160kPa to 335kPa. In response to these lower acoustic pressures, the duration of bubble responses show approximately normal behaviour, and all signals recorded are of greater than* $\Delta t = 2.8\mu$s *in duration.*

is observed. Figure 5.15 shows the distribution of echo signal durations in response to acoustic pressures from 550kPa to 1020kPa (1.6MHz six cycle pulses), and a two population response is observed. Figure 5.16 shows the amplitudes of the two populations, and again it can clearly be seen that the energy of scatter is strongly dependent on the duration. Bubble responses have again been separated into those with signals longer than $\Delta t = 2.8\mu$s and those shorter than $\Delta t = 2.8\mu$s.

At lower acoustic pressures (160kPa to 335kPa, the maximum energy and amplitude of fundamental scatter observed increases with acoustic pressure, as expected from linear scattering theory. Increasing acoustic pressure from 160kPa to 335kPa also reduces the minimum am-

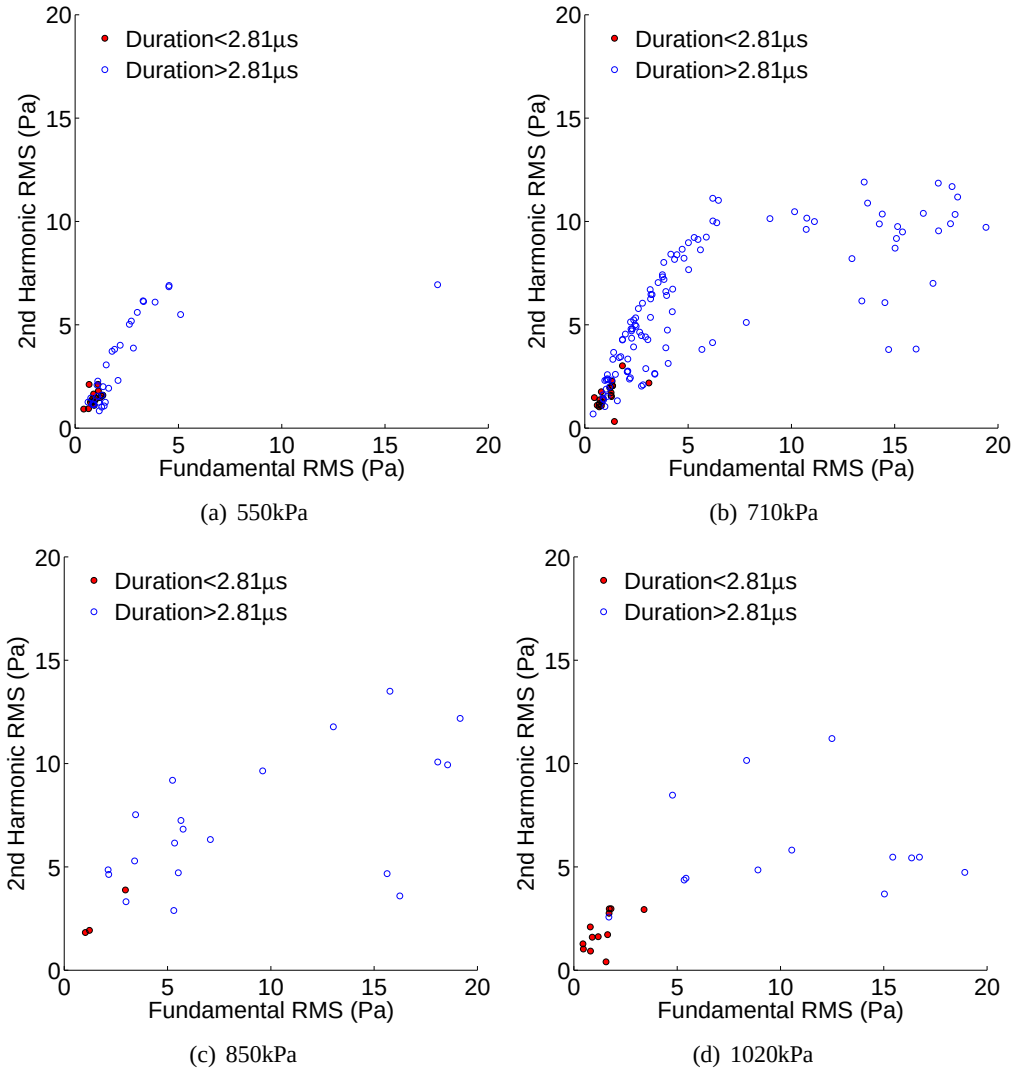

(a) 550kPa

(b) 710kPa

(c) 850kPa

(d) 1020kPa

Figure 5.16: *Variation in amplitude of signals from biSphere bubbles in response to increasing acoustic pressures (1.6MHz, six cycle pulses), from 550kPa to 1020kPa. A binary classification scheme has been used to separate signals by length into two populations: those with signal durations $\Delta t < 2.8\mu$s and those with signal durations $\Delta t > 2.8\mu$s. A clear relation to signal length and amplitude of scatter can be seen.*

plitude of scatter, as can be seen in Figure 5.14. In combination, this leads to no significant increase in the mean amplitude of scatter, as shown in Figure 5.18. The harmonic scatter of all responses increases sharply with acoustic pressure, as expected due to both increased nonlinear propagation of the incident pulse and nonlinear bubble behaviour.

As the incident acoustic pressure is increased to 550kPa and above, the minimum amplitude of fundamental scatter remains the same, suggesting the noise floor of the experimental system has been reached (at 1.6MHz the minimum signal detectable is approximately $1 \times 10^{-6}\mathrm{Pa}^2\mathrm{s}$). Increasing pressures above 550kPa produce significant increase in both fundamental and second harmonic mean scatter of those bubbles with responses longer than $\Delta t = 2.8\mu\mathrm{s}$. However, the amplitude of those signals with durations less than $\Delta t = 2.8\mu\mathrm{s}$ shows less relation to incident acoustic pressure, in both fundamental or second harmonic components of scatter. The number of bubbles classified as such show a slight decrease with increasing pressure (Figure 5.17).

Figure 5.18 shows mean energy densities of scatter in response to increasing acoustic pressure, for comparison. The mean amplitude of scatter, as separated into the two observed populations, is shown in Figure 5.19, and as can be seen the mean scatter of these shorter signals shows only a small increase in amplitude of response to 550kPa to 1020kPa.

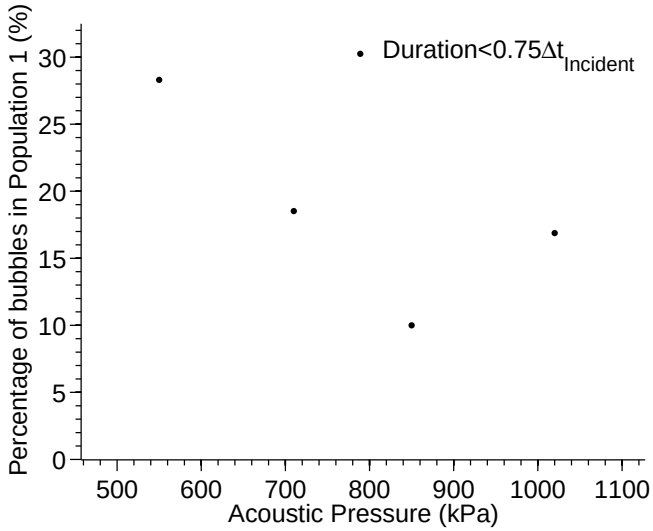

Figure 5.17: *Number of biSphere signals of duration $\Delta t < 0.75\Delta t_{incident}$, as a percentage (%) of the total number of scatterers measured, from 550kPa to 1020kPa. Below 550kPa no signals of duration $\Delta t < 0.75\Delta t_{incident}$ were measured.*

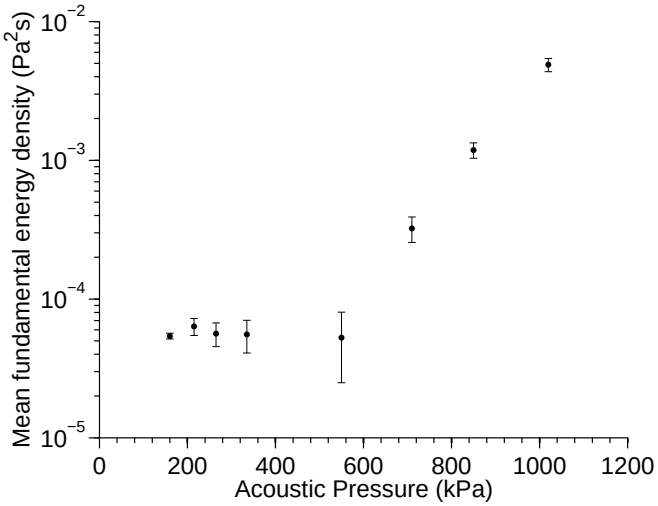

(a) Mean fundamental components of scatter

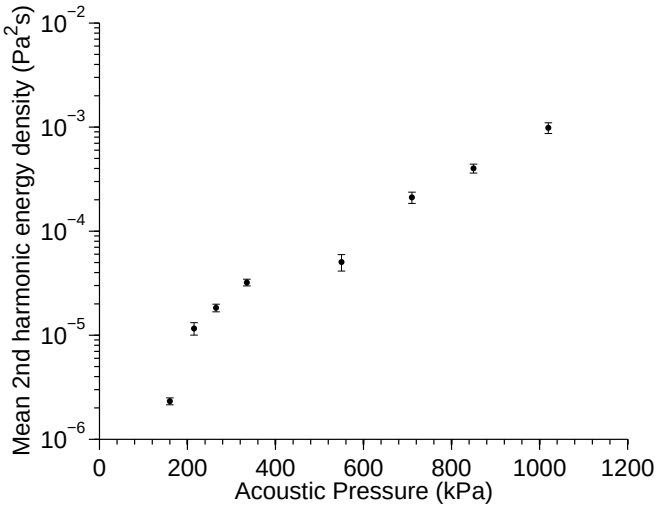

(b) Mean second harmonic components of scatter

Figure 5.18: *Mean energy densities of biSphere bubbles in response to increasing acoustic pressures (1.6MHz, six cycles).*

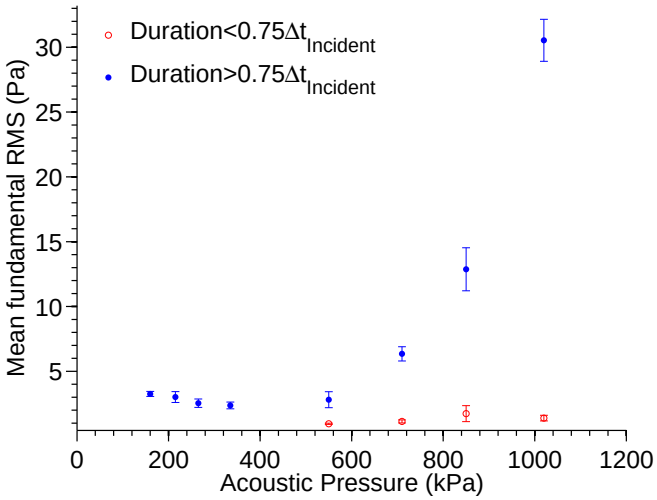

(a) Mean fundamental components of scatter

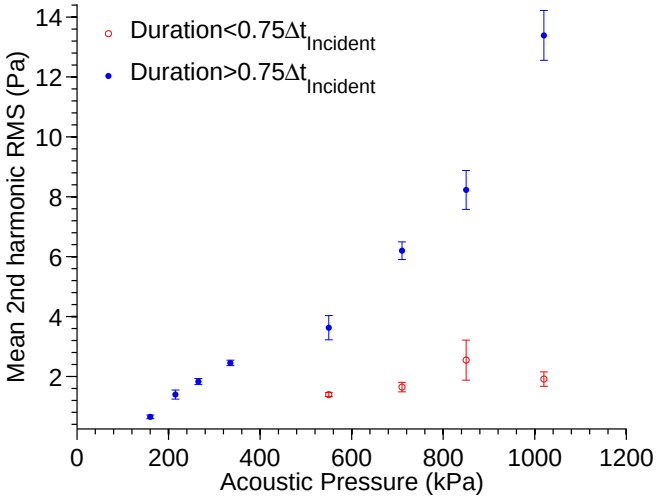

(b) Mean second harmonic components of scatter

Figure 5.19: *Mean amplitude of biSphere signals in response to increasing acoustic pressures (1.6MHz, six cycles), as separated into two populations: those with signal durations* $\Delta t < 2.8\mu$s *and those with signal durations* $\Delta t > 2.8\mu$s

5.5 Discussion

Previous results in the literature have shown that hard shelled albumin based agents show no visible oscillation in response to even large amplitude ultrasound imaging pulses[65], although scatter from single bubbles has been observed[58,65,71]. The resonance behaviour observed in Definity scatterers (Chapters 3 and 4) is not observed here. This suggests that biSphere scatter is due to gas escaping from the bubbles, as a result of slight disruptions in the shell. Frinking et al[65] describe the response from Quantison, an agent similar to biSphere, agents as being 'dualistic', relating to the applied acoustic pressure. At low pressures (Frinking state the 'threshold for shell rupture' is less than approximately 100kPa), they show that the agents behave as encapsulated gas bubbles, and are stable linear oscillators, which can be modeled by the Rayleigh-Plesset model or similar[94] (as described in Chapter 1). In response to acoustic pressures above this threshold, the bubbles rupture and the encapsulated gas is released. The applied pulse is now incident upon a free gas bubble, which is not constrained by the shell, and will quickly dissolve into the surrounding liquid (depending on the solubility of the gas). This behaviour has since been observed in optical experiments using high speed cameras[4,53,87–91,98]. The shell itself is not destroyed by the incident pulse, even by very high amplitudes[65], suggesting that the encapsulated air is replaced by the surrounding liquid.

The results shown here agree with this analysis. As the pressures investigated are greater than that expected to be the threshold for shell rupture, it can be assumed that the signals observed are from free air bubbles. The response in Figure 5.1 is highly nonlinear, and similar to the expected response shown by Frinking et al[65]. However, the 'partial echo' response shown in Figure 5.3 suggests are more complex behaviour than a free gas bubble echo. The shorter duration of approximately $\Delta t = 1.94\mu$s suggests that a partial echo is achieved in response to the incident pulse of six cycles. This could arise from various physical mechanisms. Dissolution of the ejected gas bubble into the liquid, in a time scale shorter than the incident pulse, would explain the shorter echo signal. However, static diffusion for free gas bubbles on this scale has not been observed (Chomas et al[4] observed that static diffusion of Albumin-shelled agents, after insonation with a 240kPa pulse, was on the order of seconds). Chomas et al also show that acoustically driven diffusion can change the bubble diameter during the transmitted pulse at sufficiently high pressures, although complete diffusion of gas bubbles in time scales less than 1ms has not been previously observed.

Another possible mechanism is the delayed rupture of the shell. If the shell is resilient enough to

survive the first few cycles of the incident pulse without leaking gas, no above noise echo would be measured. A rupture in the shell necessary to release the encapsulated gas may occur part way through the incident six cycle pulse. This will lead to the escaped gas bubble producing an echo from only the remaining incident cycles, explaining the short echo signal shown in Figure 5.3. This would also explain the range of durations shown in Figure 5.6, explained by differently resilient bubbles releasing gas at different stages of the incident pulse. Optical experiments have also observed more complex interactions between ruptured shells and the released gas bubbles, including partial release, and the attraction of ejected free gas bubbles to the shell material, due to secondary radiation forces[141], which could again lead to reduced echo durations. Combined optical and acoustic experiments would give more information on this behaviour, and its causes.

It has been shown that the size distribution of albumin bubbles changes significantly after an insonation above the destruction threshold, and that the resulting distribution is dependent on the insonant frequency[65] (for example smaller bubbles remain in response for a higher frequency). The difference in the size of remaining bubbles could arise from different parts of the bubble distribution being excited by different frequencies. Frinking et al show that a wider size range is disrupted by higher frequencies which are more efficient at disrupting the shell, and leads to only smaller bubbles remaining intact. Previous studies have also shown that the number of single scattering events is dependent on the acoustic pressure[71], as albumin shells are more easily disrupted by higher pressure pulses. This frequency and acoustic pressure dependence of shell disruption agrees with the data shown above. At lower frequencies we have observed an increased number of partial echoes, suggesting the incident pulses are not sufficient at disrupting the shell in order to give a full echo from the released gas bubble. At higher frequencies (which have been shown to have a greater destructive effect on the shell) less partial echoes are observed, an indication that all bubble signals arise from free gas bubbles responding to the entire pulse, due to early disruption of the shell.

Below an incident acoustic pressure of 550kPa no partial echoes have been observed, suggesting a smaller size range of bubbles is effected by the lower energy pulses. A higher minimum scatter is also observed, due to the lack of partial echo. Both these characteristics suggest that all echoes recorded at these lower amplitudes are from free gas bubbles whose shell's are disrupted by the first cycle of the imaging pulse. As the acoustic pressure is increased beyond 550kPa, partial echoes are observed, suggesting a larger distribution of bubbles are affected by

the larger amplitude imaging pulses. In response imaging pulses of 550kPa and above, partial echoes account for approximately 30% of scatterers measured, suggesting partial release of gas from bubbles which would otherwise remain intact and produce no signal at lower amplitudes. A significant increase in both fundamental and second harmonic scatter is observed, which is expected from free bubble scatter. However, the signals of shorter duration which are observed show reduced mean echo when compared to the longer duration echoes. They show no significant increase with acoustic pressure, and there is a clear difference between the two populations, especially at the maximum pressure measured here (1020kPa), indicating that the oscillations of these gas bubbles are somehow restricted. Restriction could possibly arise from the presence of the remaining shell, for example if the gas bubble remains in contact with the shell material. Optical experiments would provide further information into this phenomenon.

As the low energy scatter signals are close to the noise level of the experimental system, they are thus dependent on the accuracy of the processing of the RF data in identifying the echo signals from the electronic noise. A simple threshold is employed, as described in Chapter 4, to perform this, and as such bubble signals very close to noise may not be identified. However, this is the same for the range of incident parameters investigated here, and it can be assumed that similar errors in bubble detection occur in all data sets, for each of the incident parameters. Higher resolution combined acoustic and optical measurements, with more acoustic pressures investigated, would give more information on this, and determine if there is an acoustic pressure threshold at which the shell is disrupted.

5.6 Conclusion

In conclusion, the well characterized microacoustic system previously in Chapter 4 has been used to measure the scatter from single biSphere microbubbles. A range of incident frequencies and acoustic pressures have been used, and results show that scatter from the hard-shelled albumin agent biSphere is significantly different to soft-shelled lipid based Definity. No conclusive evidence for resonance behaviour in biSphere has been detected here. The results presented agree well with previous studies, which define the mechanism of scatter from hard shelled albumin agents to be shell disruption and gas release. Partial echoes, shorter than the incident pulse duration, have been observed for low frequency pulses of sufficient amplitude, suggesting partial release of gas from bubbles. The lack of this echo at lower amplitudes suggest these arise from a population which otherwise remain intact and produce no signal, unless a sufficient

acoustic pressure is incident upon them. This agrees with previous studies, which show the disruption of an albumin shell is frequency dependent, and that an acoustic pressure dependence exists for the number of single scattering events produced from a sample of contrast agents. The responses measured and the conclusions made here are directly relevant to improving imaging using albumin shelled agents, as it is clear that a resonance response has not been achieved using the imaging parameter used here, and that pulses which optimise the scatter from disrupted shelled bubbles should be used to improve diagnostic techniques.

5.7 Further work

Although the above experimental results allow us to observe various behaviours as documented above, in order to achieve a fuller understanding of the behaviour of hard shelled albumin contrast agents such as biSphere a theoretical description of the bubble responses is needed for comparison. Further experimental results also offer potential for improving the understanding of the behaviors observed here. In particular, the effect of differing incident pulse lengths will provide extra information on the differing durations of response observed. Optical observations of the different responses will also give confirmation of bubble shell integrity, and information on the destruction and remnants of shells.

Measurements of bubble radii, using the optical techniques described in Chapters 3 and 4, will add information about the disruption and subsequent dissolution of microbubbles due to the imaging pulses. It has been shown that the size distribution of albumin bubbles changes significantly after an insonation above the destruction threshold is incident upon the sample of bubbles, and that the resulting distribution is dependent on the insonant frequency[65]. This information will add significant confidence to the above analysis.

Chapter 6
Microbubble response from consecutive imaging pulses

6.1 Aim of chapter

The aim of this chapter is to investigate the effect of consecutive imaging pulses on microbubble response, with respect to the the lifetime and evolution of response. Experimental results from Definity® and biSphere™ will be presented, and comparisons with theoretical data used to infer how the microbubble response is affected by diffusion and destruction.

6.2 Introduction

The microbubbles which make up the contrast agents described in previous chapters have a finite lifetime. The length of this lifetime depends on many factors including, among others, the local environment of the bubble, the properties of the shell, the properties of the encapsulated gas, and acoustic pressure incident on the bubble. Acoustic signals collected from the single bubble system described in Chapter 4 are used here to investigate the lifetime and evolution of signals, and comparisons with the theoretical microbubble model presented in Chapter 3 will be used to infer any changes in microbubble structure. Results from both the lipid based agent Definity and the albumin shelled agent biSphere are presented here. The previous chapters have dealt with the first pulse response from the two agents, and this chapter builds on this knowledge.

6.2.1 On the fragility of microbubbles

A microbubble is described as being destroyed when the shell has been disrupted entirely, allowing the gas to escape, and therefore can no longer provide an echo in response to an imaging pulse. The processes involved in causing this destruction, and the time scales involved in each of them, are interesting for a variety of reasons. First it is obvious from any in vivo

scan using contrast agents that the contrast caused by the injected microbubbles disappears after only a few minutes, due to static diffusion. This destruction is accelerated mainly by increased pressure in the lungs and other organs[98], which will affect the limits of contrast enhancement in terms of time within the circulation[95], directly affecting the clinical diagnostic and therapeutic applications which can be improved using contrast enhancement. In addition to static diffusion, microbubbles have also been observed to disappear much more rapidly due to the interaction with the imaging ultrasound pulse. This unique property of ultrasound contrast agents (the only contrast agent which undergoes changes after interaction with the imaging technique) has offered the development of improved imaging[142] and, more recently, therapeutic techniques[143,144]. While the exact mechanisms of this destruction are not yet known, experimental evidence has shown that a variety of mechanisms may be present. While many more may exist, the three main mechanisms of contrast agent destruction have been identified to be fragmentation, acoustically driven diffusion, and static diffusion[4], with the relative importance of each being dependent on bubble properties, local environment and the parameters of the incident pulse. Improved knowledge of these behaviours may directly lead to improved diagnostic and therapeutic techniques which can be used to improve the clinical applications of contrast enhancement listed in Chapter 1.

6.2.2 Previous studies

Statistical analysis of single bubble acoustic data, similar to that produced here, has been presented previously[72] to provide information on the dissolution and destruction characteristics of various agents, and differing spectral signatures within a microbubble sample have been identified.

The optical techniques outlined in Chapter 1 also offer potentially large improvements in the understanding of the radial excursions of microbubbles during insonation. A variety of mechanisms for destruction have been observed optically, including gas release from hard shells[53,92,97,98], asymmetric collapse leading to gas-jet formation[53], ultrasound-induced coalescence of two or more microbubbles[53,135], fragmentation of a microbubble into smaller bubbles[4,53,87–91] and acoustically-driven diffusion (where the incident acoustic pressure forces gas out of the encapsulated bubble)[4,91,92].

Using high speed optical and acoustical observations, Dayton et al[92] have shown that under certain conditions, destruction occurs due to ultrasound induced shell rupture. At acoustic pres-

sures of several hundred kPa disintegration of a microbubble was observed optically to produce a symmetrical array of shell fragments around the original center of the bubble, and the encapsulated gas quickly dissolved away. This behaviour which has been termed 'fragmentation' by Stride et al[95], is predicted to occur when the stresses produced within the shell exceed its strength, and has been shown by Chomas et al[4] to cause complete disappearance of a received echo over a time scale of microseconds (dependent on the solubility of the encapsulated gas). They propose that any disappearance in echo over this time scale demonstrates the occurrence of fragmentation.

Incident ultrasound pulses have also been shown to cause bubbles to decay over longer time periods. Chomas et al[4] show acoustic signals from a microbubble, assumed to be intact over a sequence of transmitted pulses, which significantly decrease in amplitude and duration over a sequence of pulses separated by 1ms. An increase in center frequency of the scattered pulse is observed, suggesting a decrease in bubble diameter due to the diffusion of the gas core, although the individual harmonic components are not distinguishable due to the large bandwidth signal. They note that due to the time scales involved, this diffusion must be acoustically driven, and not static diffusion of the encapsulated gas.

Both Dayton[92] and Chomas[4] show that significant differences in terms of destruction are observed when contrast agents of different shell materials (with the same encapsulated gas) are insonated by similar transmit pulses. In both the optical and acoustic results presented, microbubbles with phospholipid shells[4,92] appear to have increased resilience to the disruptive potential of the incident pulse, in comparison to albumin coated bubbles such as Albunex, Optison or biSphere. Considering bubble destruction to be a result of shell rupture (i.e. when the shell material undergoes stresses greater than its strength), predictions using the bulk parameters of the shells' corresponding constituent materials alone would expect the thicker-shelled and less viscous Albumin coated bubbles to experience less effective stress and be therefore harder to disrupt. However, due to the fluid nature of the lipid bilayers making up Definity shells, they appear to have the ability to deform without rupturing, avoiding bubble destruction upon compression. While an Albumin coated bubble which undergoes shell disruption will therefore lose its coherence as a bubble, due to the encapsulated gas fully diffusing out into the surroundings, a lipid shell will retain its ability to inhibit diffusion, and have an improved ability to provide multiple responses from subsequent imaging pulses.

Hard shelled microbubbles like Quantison and Optison have been observed to give gas release

in response to high MI incident pulses, leading to large scattered signals[92,98]. In response to low MI incident pulses, they have been shown to give neither gas release nor significant radial oscillations, suggesting a threshold pressure is needed to trigger gas release[94].

The soft lipid shells of contrast agents such as Definity have been observed optically to maintain their structural integrity in response to multiple imaging pulses at low MI[81,87,88,93]. They have been shown to exhibit diffusion at low MIs[4,92,96], and fragmentation at higher MIs.

The solubility of the encapsulated gas also plays a significant role on the lifetime of a microbubble. Perfluorochemicals have been shown to have advantages over air or nitrogen as the encapsulated gas due to their increased dissolution times[4,145]. For example, nitrogen filled lipid shelled Definity has been shown to decay faster than a perflourocarbon gas version of the same agent[100,146].

6.3 Methodology

In order to analyze multiple signals from individual microbubbles, in response to subsequent imaging pulses, it is necessary to ensure that the bubbles do not move significantly within the imaging field, which would subject them to differing acoustic parameters within the focused beam. It has been previously determined (Chapter 2, Figure 2.5) that the incident ultrasound field remains approximately constant over the region of interest that has been defined (1.5cm). The bubble signals from consecutive imaging frames can be analyzed using cross correlation to determine the amount of bubble movement that occurs between the imaging pulses. This movement arises due to the injection flow. The pulse repetition frequency (PRF) for imaging pulses used here was 1kHz, giving separation of 1ms between pulses.

Figure 6.1 shows the first and the seventh signals produced by a typical bubble in response to a series of 1.2MHz, 550kPa six cycle pulses, separated by 1ms. As well as a relative decrease in energy of the seventh response (discussed further below), the movement of the bubble in the 6ms between pulses can be seen. Seven pulses have been chosen as an illustration, as the movement between two pulses is too small to easily identify. Cross-correlation is used to find the exact shift in position, and has been calculated in this example to be just two samples, equal to distance of $76 \pm 38\mu\mathrm{m}$ (the calculation is limited by the sampling rate of 19.63MHz, which gives a resolution of $38\mu\mathrm{m}$ per sample). An average value of $120 \pm 70\mu\mathrm{m}$ was calculated from a sample of 20 bubbles (giving an average speed of $2 \pm 1\mathrm{cms}^{-1}$). This is well within the limits

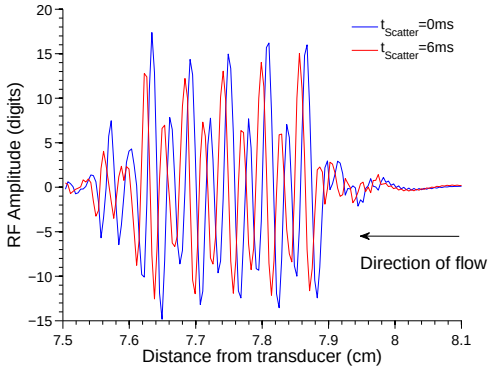

Figure 6.1: *A typical bubble shows a translation toward the transducer over a series of seven imaging pulses, due to the insertion flow. This can be seen in the shift to the left of the respective peaks, and has been measured using cross-correlation of the respective signals. Total translation during the 6ms of imaging was calculated to be* $76 \pm 38\mu\mathrm{m}$.

of the region of interest, and so we can say with confidence that for up to seven consecutive insonating pulses bubbles are being insonated by identical pulses. This allows the responses from subsequent imaging pulses to be used to determine the effect that the incident pulse has on the signals produced, and thus the bubbles themselves.

The results from seven consecutive imaging pulses with a PRF of 1kHz are presented here, giving a total imaging time of 7ms. The number of imaging pulses was limited by the m-mode of the scanner and by the size of data files which could be easily analyzed. Seven pulses were shown to be sufficient to analyze the effects of both destruction and diffusion of the agents used at the incident pulses parameters used here, and a significant decrease in amplitude of signals was observed at all imaging frequencies and acoustic pressures.

6.4 Experimental results

Experimental results are separated into two observed types of behaviour, defined as follows;

- Destruction event: Bubble signal decays to below noise level within $1\mathrm{ms}$.
- Diffusion event: Bubble signal decays gradually, showing reduced signals to each consecutive imaging pulse.

Examples of both types of behaviour observed from Definity bubbles is shown in Figure 6.2 (uncalibrated RF scatter shown). The first pulse responses from the two bubbles are similar in both fundamental and harmonic amplitude (both are examples of off-resonance response), but they differ greatly in response to the subsequent pulses.

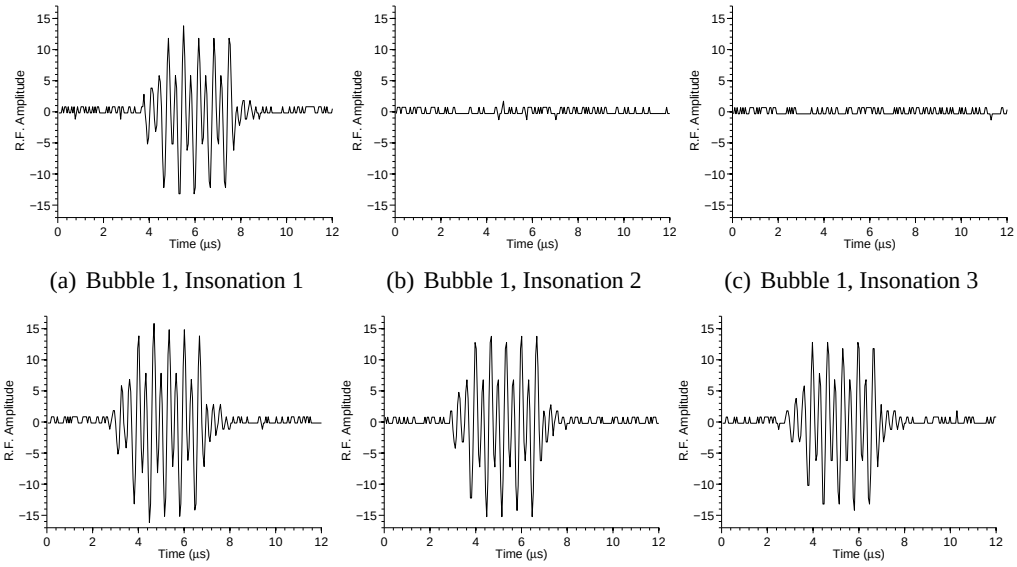

(a) Bubble 1, Insonation 1 (b) Bubble 1, Insonation 2 (c) Bubble 1, Insonation 3

(d) Bubble 2, Insonation 1 (e) Bubble 2, Insonation 2 (f) Bubble 2, Insonation 3

Figure 6.2: *Received RF signals from three consecutive imaging pulses of two example Definity bubbles (1.6MHz, 550kPa six cycle pulses), showing a destructive event in bubble 1 (a)-(c), and a diffusion event in bubble 2 (d)-(f). The amplitude of both the first pulse responses are similar, in both fundamental and harmonic components. A significant and rapid ($< 1ms$) reduction in scatter is classified as destruction in bubble 1 (no signal can be detected above noise in (b) and (c)), whereas a slow reduction in scatter over a series of subsequent pulses is defined as diffusion of gas out of bubble 2. Pulses are separated by 1ms (PRF=1kHz, 550kPa, 1.6MHz).*

6.4.1 Destruction

Destructive effects such as fragmentation, coalescence and jet formation are caused by the collapse of the microbubble concentrating sufficient energy to break the bubble apart, and will lead to a significant and rapid reduction in the scattering power of the bubble, as shown in Figure 6.2 (a)-(c). Examples of such rapid reduction in the scattered signals are presented here in response to imaging pulses with PRFs of 1kHz, and analyzed to show the effect of differing incident imaging parameters of frequency and acoustic pressure.

6.4.1.1 Definity

Figure 6.3 shows the effect of increasing incident frequency on the numbers of Definity bubbles which are detectable with successive imaging pulses (550kPa, six cycle incident pulses used). The responses from the first insonation are presented in detail in Chapter 4. The numbers of bubble signals are plotted as a percentage of the number of bubbles which were detected on the first imaging pulse, for each successive imaging pulse, showing the relative survival of bubble signals above noise. The data for increasing frequency for each imaging pulse has been modeled with a quadratic polynomial, which was calculated to give the best fit compared to a linear fit, using residual values to indicate goodness of fit (as shown in Table 6.1). A clear trend can be seen in the responses from each insonating pulse.

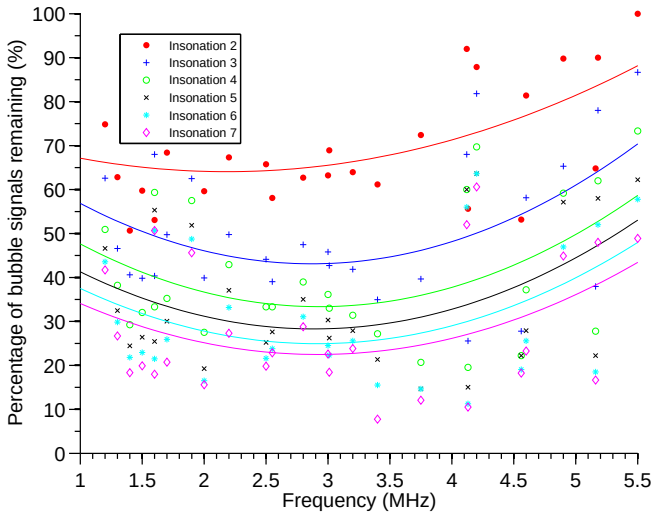

Figure 6.3: *Effect of increasing frequency on the number of bubbles signals detected above noise, with respect to the number detected by the initial imaging pulse (550kPa six cycle pulses used, R.F. signals shown). The percentage of bubble signals remaining decreases with each imaging pulse, as shown by the decreasing intercepts of the trend lines. Maximum number of remaining bubbles signals is observed at 5.5MHz. The frequency at which minimum detected bubble signals remain increases from 1.4MHz in the 2nd insonation, to 3.4MHz in the 7th insonation.*

The first imaging pulse has the largest effect on the number of remaining signals, with an average of $29.3 \pm 13.8\%$ of bubble signals being reduced to below noise across the range of frequencies measured. Maximum reduction in bubble signals (i.e. minimum percentage of bubble signals remaining in response to the second pulse) is observed at 1.4MHz. This corresponds to maximum first pulse response, as described in Chapter 4 (Figure 4.16), and

Insonation	2	3	4	5	6	7
Linear Fit	60.03	80.11	78.44	79.11	77.27	75.48
Quadratic Fit	56.49	71.27	69.89	71.54	70.36	69.59

Table 6.1: *Measures of goodness of fit, for linear and quadratic polynomial fits, as indicated by the sum of the squares of the residuals (a lower value signifies a better fit, and 0 is equal to an exact fit), for data from each insonating pulse. A quadratic fit is determined to be the best fit for each data set (as shown in Figure 6.3).*

also to maximum incident energy density, as shown in Chapter 2 (Figure 2.8), suggesting that both may play a role in the reduction of bubble signals to below noise levels. Subsequent imaging pulses also reduce the number of remaining signals, but with the effect reducing with each incident pulse. Maximum reduction in signals is observed for increasing frequency with increasing incident pulses, as seen by the increase in frequency of the quadratic trend line's minima for increasing insonations.

This reduction in the number of signals occurs more often in signals classified as off-resonance responses. Table 6.2 shows how the number of scatterers in the two populations are effected by the first imaging pulse, for a variety of frequencies, showing much greater survival of signals in the resonance population.

Frequency	1.2	1.3	1.4	1.5	1.62	1.7	2.0	(MHz)
Off resonance	39.4	32.1	47.1	44.1	57.5	29.85	40.3	(%)
Resonance	0	0	5.0	16.7	12.5	21.8	24.4	(%)

Table 6.2: *The percentage of Definity bubbles signals that are reduced to below noise by the first imaging pulse (550kPa, six cycle pulses), as displayed by population (classified using normalized cross correlation method).*

Figure 6.4 shows how the numbers of scatterers changes with consecutive imaging pulses for increasing acoustic pressures. Increasing incident acoustic pressure reduces the number of bubble signals detected above noise, with respect to the number detected by the initial imaging pulse (1.6MHz six cycle pulses used). In response to 710kPa and above, 83% of the bubble signals detected are reduced to below noise at the second imaging pulse. The percentage of bubble signals remaining decreases with each imaging pulse.

The survivability of a Definity bubble signal displays a dependence on the amplitude of the signal emitted by that bubble in response to a previous imaging pulse. Figure 6.5 shows first pulse responses classified as those which provide scatter to subsequent pulses, and those which do not. When plotted against fundamental energy density of initial signal, it can be clearly seen

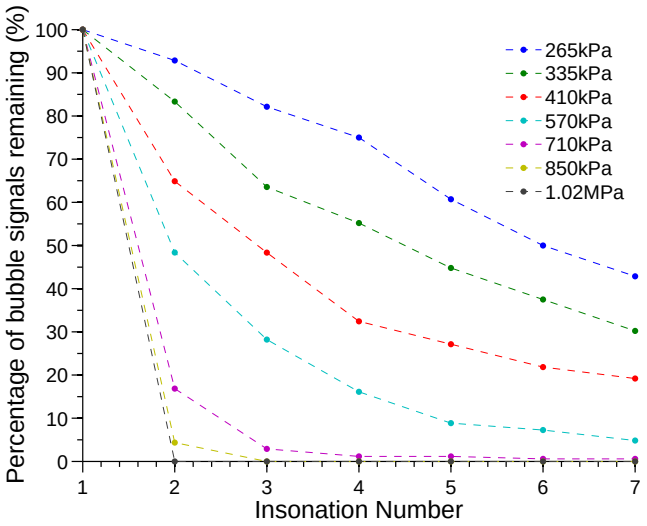

Figure 6.4: *Effect of increasing incident acoustic pressure on the number of bubble signals detected above noise, with respect to the number detected by the initial imaging pulse (1.6MHz six cycle pulses used). The percentage of bubble signals remaining decreases with each imaging pulse, and the effect increases with increasing acoustic pressure.*

that bubbles which respond in the first instance with higher fundamental energies (including, but not limited to, those classified to be at resonance) are more likely to provide an above noise signal in response to a second imaging pulse. Overlayed on Figure 6.5 is a fundamental energy density threshold, calculated using logistical regression analysis, as outlined below.

Using the Matlab 'classify' function (included in the MATLAB 2007 Statistics Toolbox), a discriminant analysis algorithm is employed to calculate a threshold for surviving bubble signals, as based on both the energy of the initial signal and the acoustic pressure of the incident pulse. This is equivalent to fitting a normal distribution to each of the two classes (here, 'subsequent signals' or 'no subsequent signals'), and using this information to interpolate the boundary, in terms of fundamental energy density, between the two classes. Here, a linear discriminant function is used to calculate the energy threshold, which has been plotted in black (Figure 6.5). Microbubbles below this threshold are most likely to provide no detectable signal in response to the following imaging pulse. The predicted destruction threshold increases from below the noise level of the experimental system ($2.5 \times 10^{-6}\mathrm{Pa}^2\mathrm{s}$) at 410kPa, to approximately $1 \times 10^{-2}\mathrm{Pa}^2\mathrm{s}$ at 750kPa. A linear discriminant function was shown to minimize the error (misclassifying 13.9% of recorded data) when compared to a quadratic discriminant function (which misclassifies 15.8% of recorded data), for pressures upto $710\mathrm{kPa}$. The linear classifi-

cation error was observed to increase when bubble signals from higher acoustic pressures were included in the data set (over 20% of the total recorded bubbles were misclassified when data over 800kPa were included). This is due to the sparsity of bubbles which produce subsequent signals at these higher pressures, which reduces the accuracy of the parametric model used to calculate the discriminant function.

At low incident pressures ($< 400\mathrm{kPa}$) it can be seen that some first pulse responses are close to the noise level of the system, meaning the subsequent lack of signal above could be explained by diffusion of gas leading to a small reduction of signal to below the noise level. However, in response to all incident acoustic pressures examples of signals at levels well above the noise threshold are observed to produce no subsequent signals, leading to the destruction threshold calculated here. For example, in response to an incident pressure of 550kPa the bubble which results in the largest first pulse response (fundamental energy density of $3.2 \times 10^{-3}\mathrm{Pa}^2\mathrm{s}$) produces no signal to subsequent incident pulses, suggesting a significant change in the integrity of the bubble.

6.4.1.2 biSphere

In response to low energy incident pulses ($< 400\mathrm{kPa}$), the majority of biSphere signals ($> 65\%$) measured are followed by signals above noise in response to subsequent incident pulses. Table 6.3 shows how the number of bubbles which emit no subsequent signals increases as the imaging pulse is increased to medium acoustic pressures (550kPa), and remains at a plateau for higher acoustic pressures (up to 1100kPa). The effect increasing pressure has on the responses from six subsequent pulses is shown in Figure 6.6, and it can be seen that even at 410kPa, very few bubbles (17%) survive to give a response to three imaging pulses.

This increase in destruction coincides with an overall increase in fundamental energy density of scatter, as outlined in Chapter 5. Figure 5.18 shows that as the destruction level increases, the level of mean fundamental and second harmonic scatter also increases sharply. At acoustic pressures of 410kPa, destruction levels of 33.3% are observed, which coincides with a mean fundamental scatter of $3.4 \times 10^{-5}\mathrm{Pa}^2\mathrm{s}$. At increased pressure of 710kPa, destruction levels of of 95.4% are observed, which corresponds to a mean fundamental scatter of $2.9 \times 10^{-4}\mathrm{Pa}^2\mathrm{s}$. This also corresponds to a change in the average duration of signal, as described in further detail in Chapter 5 (Figure 5.13).

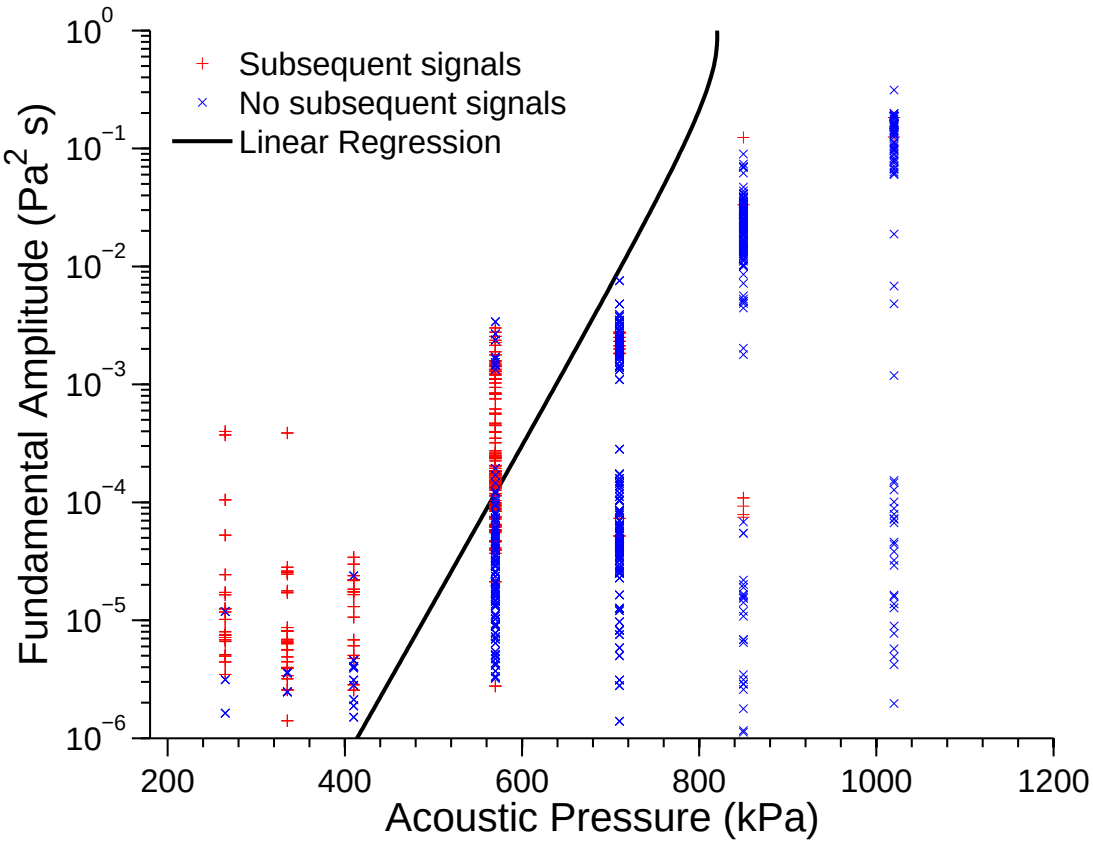

Figure 6.5: *Definity bubble responses to the first imaging pulse classified as those which give subsequent signals above noise, and those which do not. A dependence on the fundamental energy of the initial response can be seen, as well as the acoustic pressure of the incident pulse. Linear discriminant analysis has been used to plot the threshold between the two response types (black line) which separates the region of signal survival (red), and the region of no signal survival (blue).*

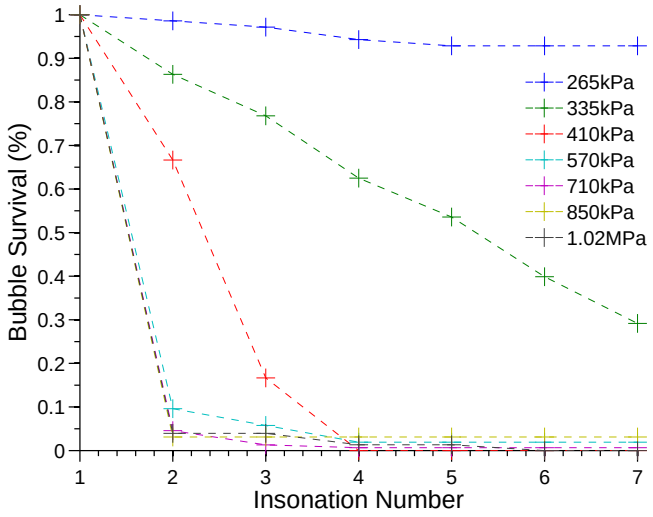

Figure 6.6: *The percentage of biSphere bubbles which provide above noise signal from a series of seven imaging pulses decreases with increasing acoustic pressure, and decreases with number of consecutive insonating pulses (1.6MHz, six cycle pulses). In response to 410kPa pulses the majority of bubbles (66%) produce multiple signals. In response to 550kPa and above, very few bubbles (3%) produce subsequent signals after the first imaging pulse.*

Acoustic Pressure	265	335	410	550	710	850	1025	(kPa)
Percentage of bubbles destroyed	1.4	13.7	33.3	97.1	95.4	96.9	96.0	(%)

Table 6.3: *The percentage of biSphere bubbles that produce no subsequent signals after the first imaging pulse (1.6MHz, six cycle pulses). A large increase is observed as acoustic pressure is increased above 500kPa*

6.4.2 Diffusion

Bubble signals which survive to produce successive signals have been observed to decay in amplitude, and evolve with respect to their harmonic content. Results are presented here in response to seven consecutive pulses (PRF=1kHz), allowing the evolution of above noise signals over 7ms to be analyzed. Chomas et al[89] have observed characteristics of acoustically driven diffusion over similar time scales in both albumin and lipid shelled bubbles.

6.4.2.1 Definity

A significant number of Definity bubbles (53% of the total sample measured) have been shown to produce surviving signals to subsequent imaging pulses of 550kPa. Figure 6.7 shows the

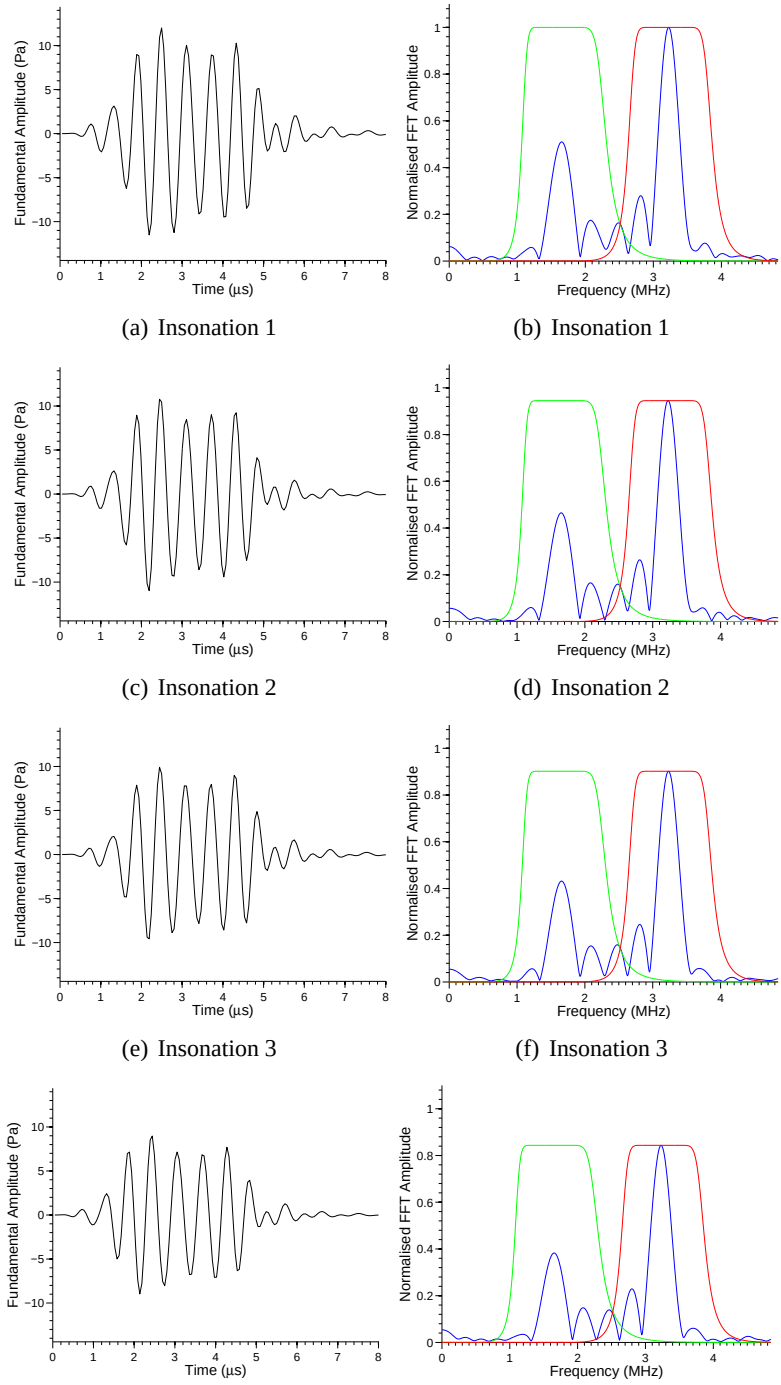

(a) Insonation 1 (b) Insonation 1

(c) Insonation 2 (d) Insonation 2

(e) Insonation 3 (f) Insonation 3

(g) Insonation 4 (h) Insonation 4

Figure 6.7: *Slowly decreasing signal from a typical off resonance Definity bubble, in response to 1.6MHz 550kPa six cycle pulses, and the respective Fourier transforms (normalized to peak component of scatter in the first response). The relative decrease in the fundamental and 2nd harmonic components is evident in the normalized FFT signals, showing a relative increase in harmonic components; the fundamental to harmonic energy ratio decreases from 0.66 to 0.52 over the four responses shown here.*

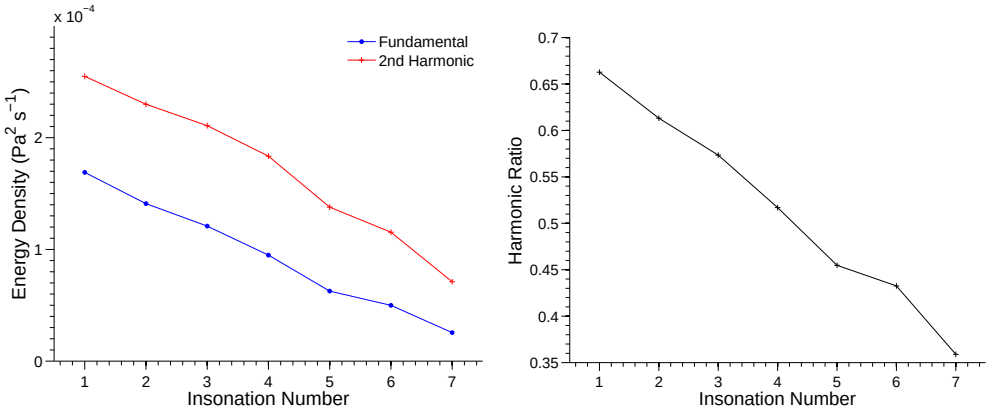

(a) Fundamental and harmonic components

(b) The ratio of fundamental to harmonic components

Figure 6.8: *The decreasing fundamental and 2nd harmonic components of the bubble shown previously in Figure 6.7. Both the fundamental and harmonic components decrease with each insonation (a), but the ratio of the two shows a much greater decrease in the fundamental components. Fundamental to harmonic ratio decreases from 0.66 to 0.36 over the seven insonations (b).*

surviving signals from a typical off resonance Definity microbbubble (identified as such by the normalised cross correlation method described in Chapter 4, Figure 4.12) in response to four consecutive 550kPa 1.6MHz six cycle pulses, each separated by 1ms. The signals each show all the properties previously identified to be indicative of off-resonant scatter in comparison to scatter at resonance (namely decreased fundamental to harmonic ratio, increased expansion to compression ratio, and a flat envelope showing a steady response with time over the six cycle incident pulse). The amplitude of the signals decrease with each insonation, showing a 75% decrease in total energy over seven insonations (the first four insonation responses are shown). When the frequency spectra of these consecutive signals are investigated further, it can be seen that the ratio of fundamental to harmonic energy decreases significantly over seven insonations (from 0.66 to 0.36), shown in Figure 6.8.

Figure 6.9 shows how this reduction in energy of signals effects the mean scatter of the two populations, in response to 1.6MHz 550kPa six cycle pulses. The numbers annotating the plot indicate the insonation number, and show the decrease in energy with increasing number of insonations. The bubbles have been separated into off-resonant and resonant populations using the normalized cross-correlation method described previously. Resonant bubbles show increased resilience to the imaging pulses, as shown in the plot of normalized mean values,

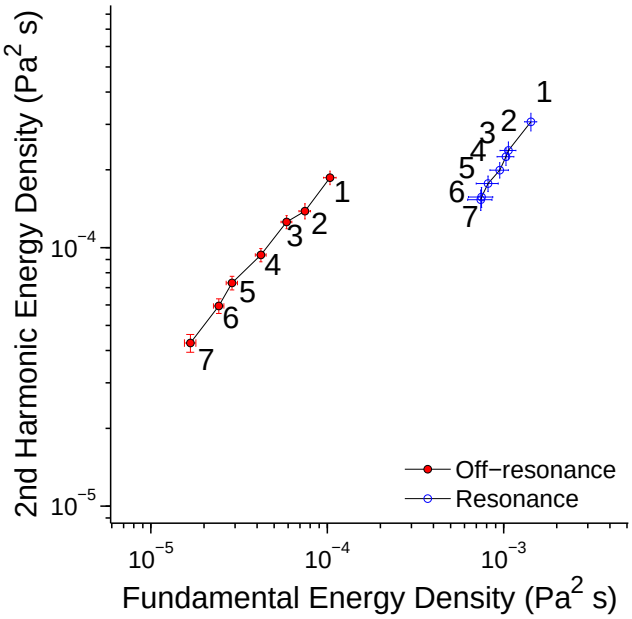

(a) Mean energy of scatter.

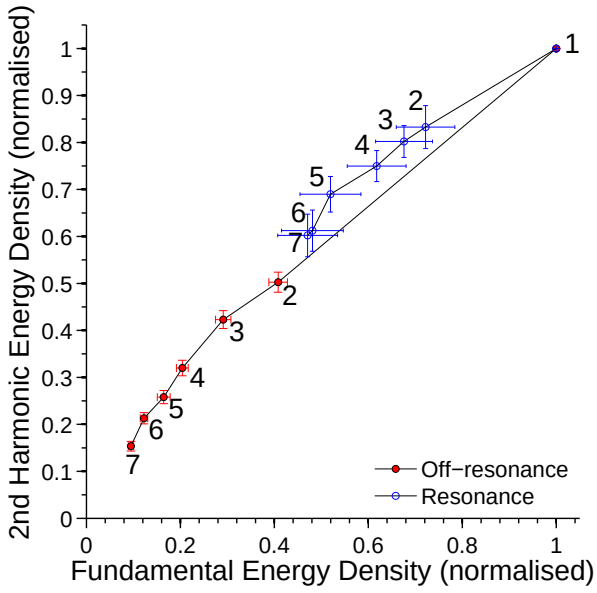

(b) Normalized energy of scatter

Figure 6.9: *Mean energy of scatter for the off-resonant (107 bubbles) and resonant (44 bubbles) populations of surviving bubble signals, in response to seven consecutive imaging pulses of 1.6MHz 550kPa. The numbers annotating the plot indicate the insonation number, and show the decrease in mean energy of scatter with increasing number of insonations. Resonant bubbles appear to be more resilient to the incident pulse, showing less relative reduction in energy of signal. (b) shows the mean values of bubble signals normalized to their respective first pulse response, showing the difference in resilience between the two populations.*

Figure 6.9(b). Here mean values have been calculated by normalizing bubble signals to the respective first pulse response of each individual bubble (insonation one in both populations therefore has a value of 1), to show the difference between the two populations. The effect of increasing frequency on the values of mean scatter from the second insonating pulse is shown in Figure 6.10, showing that in the majority of cases resonant scatter has a relatively increased second pulse response with respect to the off-resonant population.

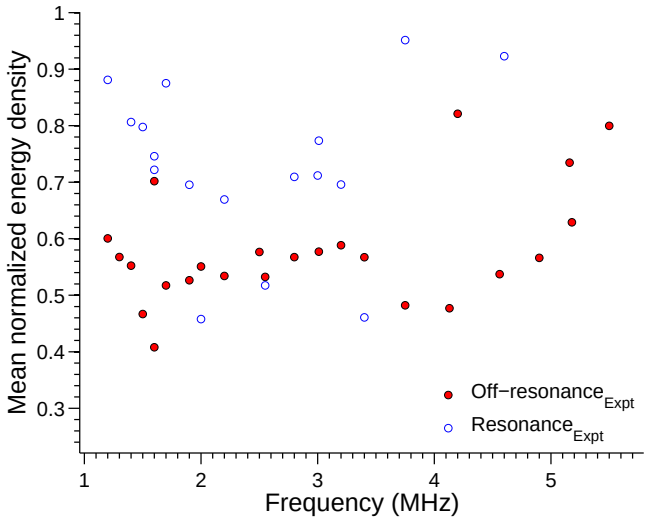

Figure 6.10: *Mean fundamental energy of scatter for the off-resonant and resonant populations of surviving bubble signals, in response to the second imaging pulse, normalized to the first pulse response (all values are less than one, indicating reduction of signal). Resonant bubbles appear to be more resilient to the incident pulse, showing less relative reduction in energy of signal. 550kPa six cycle pulses were used.*

The amount of reduction in energy for surviving bubble signals also appears to be related to the acoustic pressure of the incident pulse. Considering the response to the second insonation only, an increased mean drop in fundamental energy is observed in off-resonance response to increased acoustic pressures, as shown in Figure 6.11(a). Mean ratios of fundamental to second harmonic energy in off-resonant scatter are also shown to decrease with acoustic pressure, as shown in Figure 6.11(b). The mean difference in fundamental to second harmonic ratio (from the first to second response) changes from 0.8 ± 0.24 in response to 187kPa to 0.26 ± 0.34 in response to 750kPa.

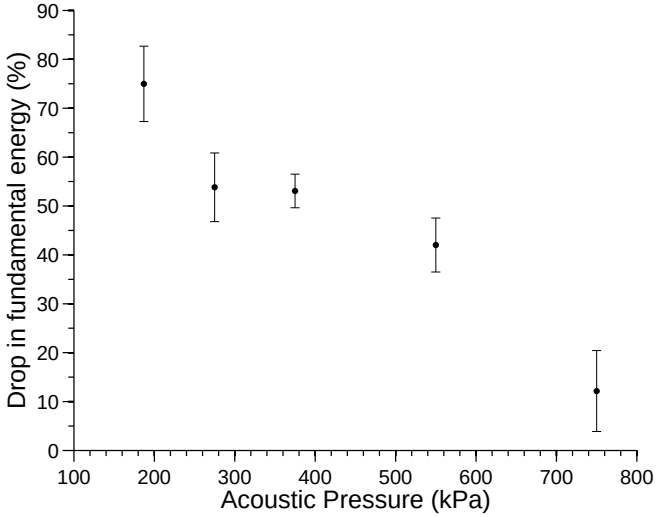

(a) Percentage drop in fundamental components

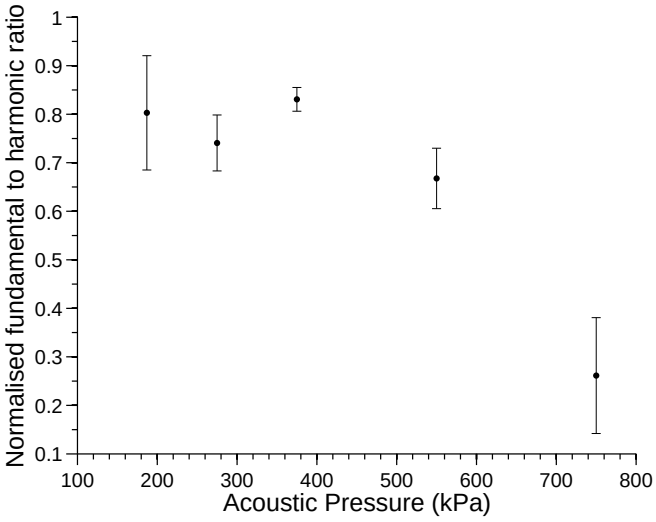

(b) Normalized reduction in ratio of fundamental to harmonic components.

Figure 6.11: *Mean levels of diffusion in off resonance scatter, as characterized by reduction in fundamental energy, and reduction in fundamental to second harmonic ratio, from the first to the second response. Both of these factors, which characterize acoustically driven diffusion, can be seen to increase with acoustic pressure. Acoustic pressures higher than 800kPa are not shown, due to lack of sufficient data from bubbles which survive the first imaging pulse.*

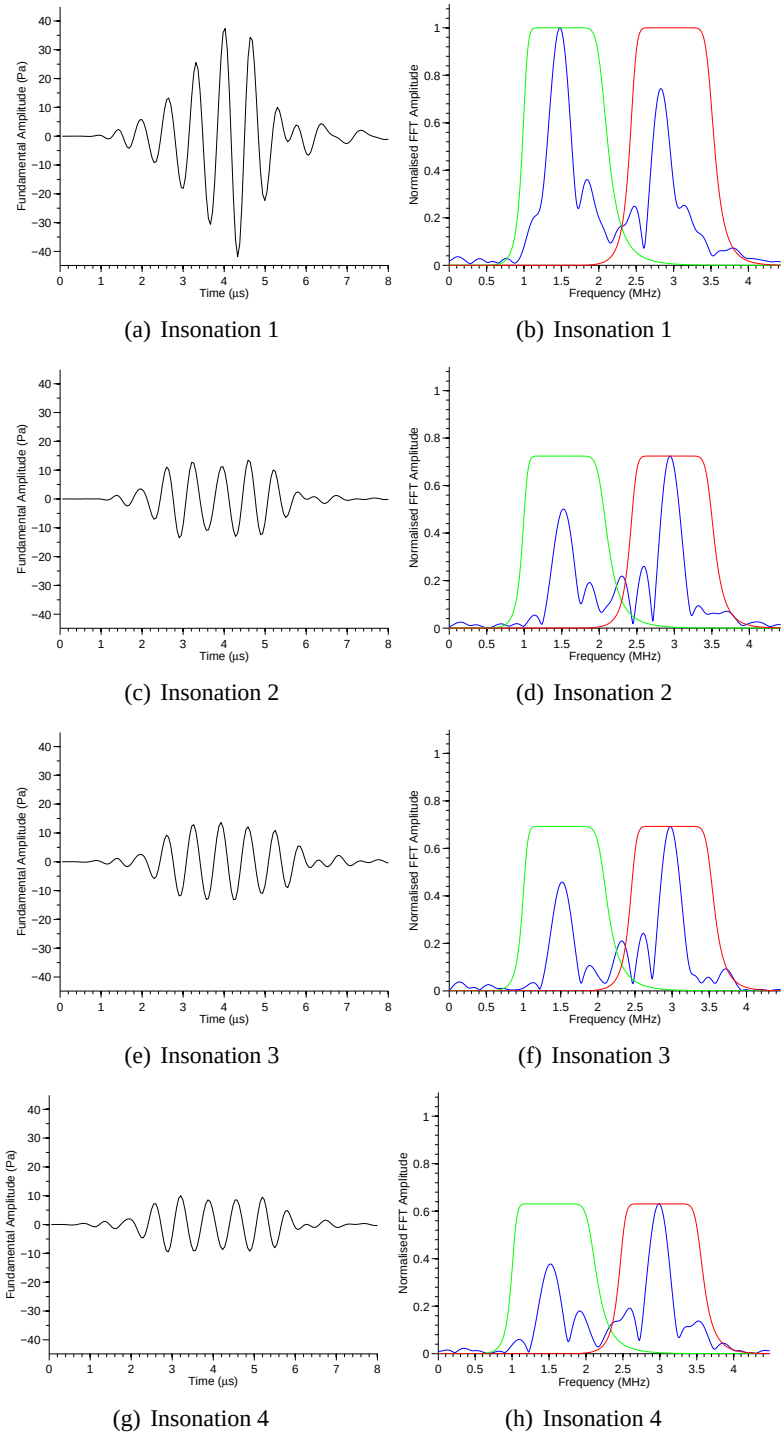

(a) Insonation 1 (b) Insonation 1

(c) Insonation 2 (d) Insonation 2

(e) Insonation 3 (f) Insonation 3

(g) Insonation 4 (h) Insonation 4

Figure 6.12: *Example of a bubble signal changing from resonant scatter in response to the first insonation, to a typical off resonant scatter in response to subsequent insonations. The first response shows all the properties identified to indicate a bubble at resonance. Subsequent responses indicate the bubble has changed to off-resonant scatter, displaying decreased overall scatter, and a relatively increased harmonic component. The incident pulses are 1.6MHz, 550kPa six cycle pulses, separated by 1ms.*

6.4.2.2 Migrating bubbles

Although it has been identified that resonant bubbles show more resilience to subsequent imaging pulses than the off resonance bubbles, certain bubbles have been identified that do not agree with this trend. Figure 6.12(a) shows a typical first insonation resonant bubble response. The signal shows the increased fundamental to harmonic scatter, decreased expansion to compression ratio, and increasing fundamental envelope with time that has been characterized as resonant scatter. However, in response to the second imaging pulse, the bubble signal which

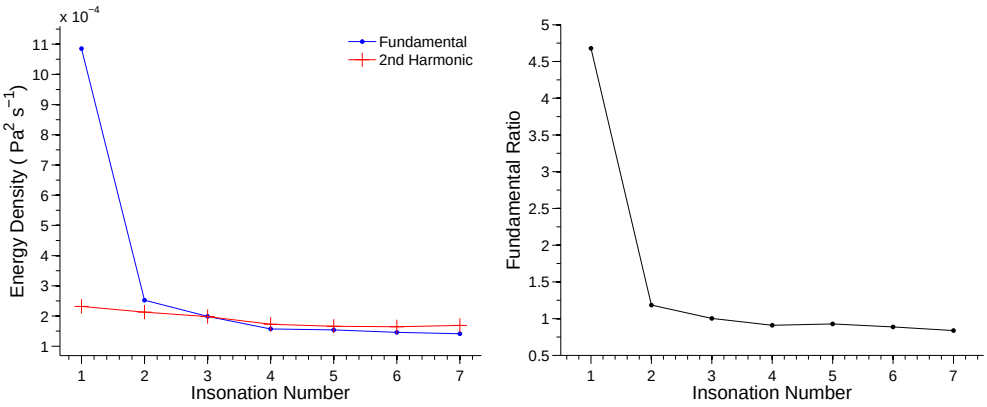

(a) Fundamental and harmonic components

(b) The ratio of fundamental to harmonic components

Figure 6.13: *The 'migrating bubble' shows a much greater reduction in fundamental than harmonic, on the first insonation only. The bubble then appears to behave as an off resonant bubble from then on, showing the relatively reduced reduction in fundamental to harmonic ratio observed due to acoustically driven diffusion.*

was initially classified as resonant scatter, has changed significantly to display all the characteristics of off-resonant scatter (Figure 6.12). An 80% drop in fundamental amplitude is observed. Following this large drop in fundamental amplitude, the bubble then appears to undergo the increased acoustically driven diffusion of an off resonant bubble in response to the following insonations (giving a drop of 50% over the next six insonations. Upon further interrogation of these subsequent signals, they are shown to have all parameters previously shown to be concurrent with off-resonant scatter, such as a constant envelope of scatter, and ratio of fundamental to harmonic scatter of approximately one. This change has been observed in a number of different resonant bubbles, for a variety of incident parameters, after varying number of insonations. The number of insonations needed to induce this large change in fundamental amplitude appears to have no significant correlation with intial bubble signal. No bubble signals have been observed

that show a change in scatter from off-resonant to resonant characteristics (which would indicate an increase in size).

Figure 6.14 shows how these changes in scatter appear when overlayed on the entire sample of responses (1.6MHz, 550kPa six cycle incident pulse). As can be seen in Figure 6.14(a), the two populations appear distinct in response to the first imaging pulse, as can be seen in the components of fundamental and harmonic energy. Figure 6.14(b) shows that in response to the second imaging pulse, six resonant bubbles have 'migrated' to become off-resonant scatter. The changes between the two populations are evident in the energy of the fundamental and harmonics components, the expansion to compression ratios, and the envelope of the signals. A reduction in the numbers of off-resonant scatter is also evident, due to reduction of signal below noise after the first insonation, as is a reduction in energy of the remaining bubbles due to the increased levels of diffusion in this population. The numbers of migrating bubbles in response to a variety of imaging frequencies and amplitudes are shown in Tables 6.4 (a) and (b).

(a) Acoustic pressure dependence (evaluated at 1.6MHz)

Acoustic Pressure	187	275	375	550	750	1100	1500	(kPa)
Number of migrating bubbles	0	0	0	9	7	0	0	
Surviving resonant bubble signals	2	1	0	25	8	1	0	

(b) Frequency dependence (evaluated at 550kPa)

Frequency	1.2	1.4	1.6	1.8	3.4	4.13	4.5	(MHz)
Number of migrating bubbles	0	19	9	9	9	13	17	
Surviving resonant bubble signals	0	28	25	31	15	25	31	

Table 6.4: *Number of resonant bubbles which migrate to become off-resonant scatter after one insonation*

Bubbles which display this migrating behaviour undergo large changes in the energy of their signals. Figure 6.14 shows that in response to a 550kPa pulse, bubbles have been observed which undergo up to 92% reductions in the energy of the signal (corresponding to a 98% drop in fundamental energy and a 15% drop in second harmonic energy), without destroying the bubble (i.e. all subsequent signals are above noise). This change in signal corresponds to a maximum change in fundamental to second harmonic ratio from 2.33 to 0.29. Comparing this directly to the Mooney Rivlin model, a similar decrease in fundamental to harmonic ratio relates to a reduction in bubble diameter from $3.84\mu\mathrm{m}$ (fundamental to harmonic ratio = 2.42) to $3.64\mu\mathrm{m}$ (fundamental to harmonic ratio = 0.30), which gives a similar (although slightly reduced) 80% reduction in overall energy. This is an overall decrease in radius of just 5.2% ($0.20\mu\mathrm{m}$), which is less than the maximum changes in radius of 18% ($0.74\mu\mathrm{m}$) previously observed optically in

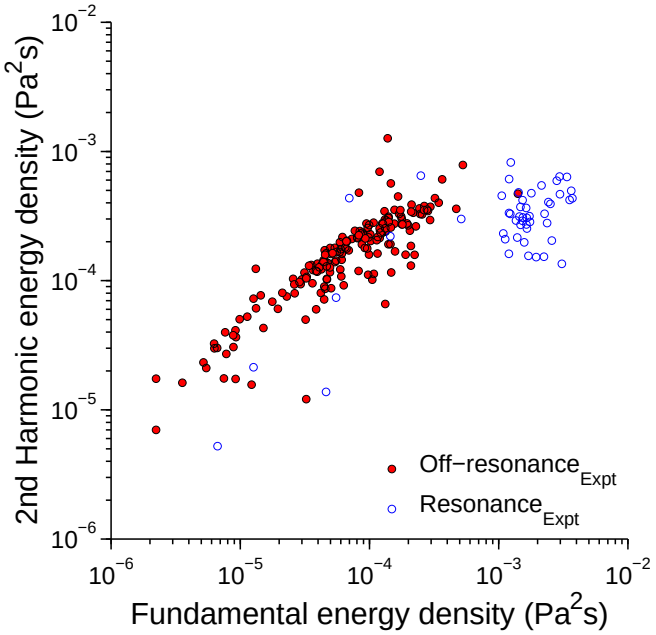

(a) Fundamental and harmonic components, first insonation.

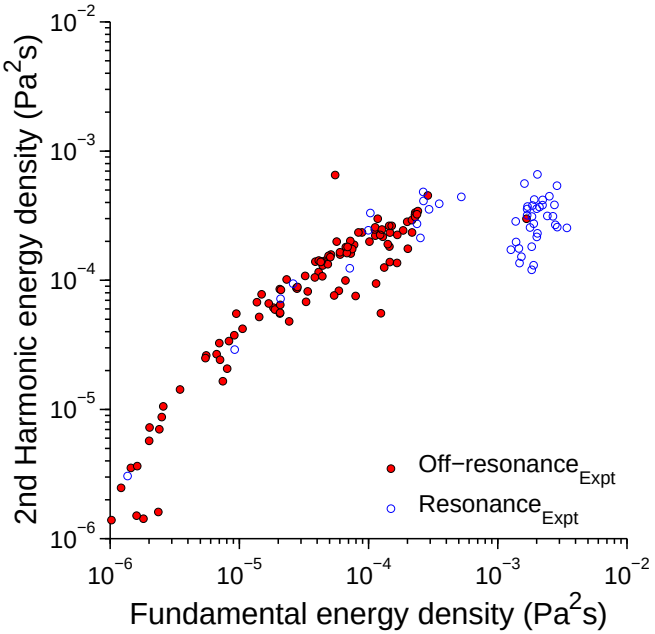

(b) Fundamental and harmonic components, second insonation.

Figure 6.14: *In response to the first insonation (1.6MHz, 550kPa, six cycle pulse), the two types of response can be clearly separated into two populations (as defined by normalized cross-correlation). In response to a second insonation, six resonant bubbles have 'migrated' to produce off-resonant scatter, as can be seen in the components of fundamental and harmonic energy. Similar changes can also be seen in the envelope of the signals and the ratios of expansion to compression (not shown here). A reduction in the numbers and energy of scatter of off-resonant scatter is also evident in response to the second insonation.*

surviving phospholipid bubbles[4].

6.4.2.3 biSphere

biSphere has been shown to have significantly different scatter to Definity, and no resonance population has been identified (Chapter 5). The characteristics of acoustically driven diffusion, namely a slow reduction in acoustic pressure, together with a relative increase in harmonic components, have not been detected in the biSphere bubble signals. Significant numbers of surviving bubble signals ($> 5\%$) have only been detected below an incident pressure of 400kPa, and the results are presented here.

Figure 6.15 shows an example of a biSphere bubble which survives to give a signal to four incident pulses of 1.6MHz, 335kPa six cycles pulses. As can be seen, while there is no significant change in the fundamental components of scatter, the harmonic component of scatter shows a small reduction in energy. Figure 6.16 shows the mean values of scatter calculated from 34 bubble signals which remain above noise, in response from seven consecutive incident pulses of 1.6MHz, 335kPa six cycles. The mean fundamental value of scatter shows no significant change throughout the seven insonating pulses (mean fundamental energy equal to $4.8 \pm 0.08 \times 10^{-5}$), whereas the harmonic scatter shows a small reduction with each pulse. This behaviour is significantly different from the characteristics of acoustically driven diffusion observed in Definity responses, and has been observed in response to acoustic pressures 160-335kPa (above which $< 5\%$ of bubble signals survive to give multiple responses). Figure 6.17 shows the mean responses from surviving bubbles in response to 160-335kPa, and the decreasing harmonic components is evident in response to 265kPa and 335kPa.

6.5 Discussion

Data has been presented that shows significant differences in the survival of bubbles between the two agents investigated. The various characteristics of the differing signals have been compared, when relevant, to theoretically predicted data produced using the Mooney Rivlin model, and to acoustic and optical results presented previously in the literature.

The destructive effects outlined in the introduction (such as jetting, coalescence and fragmentation of the microbubble), and the associated gas dispersion, are well accepted as the method

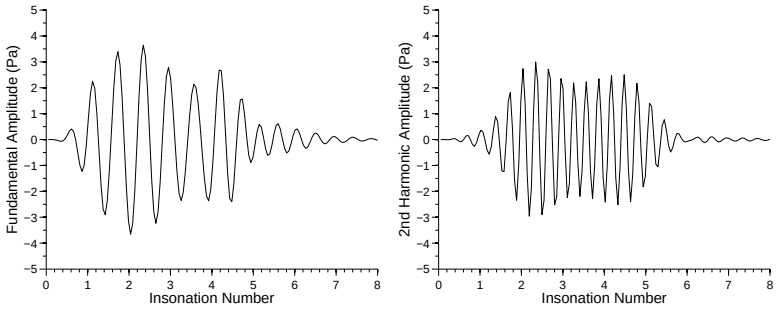

(a) Fundamental response, Insonation 1 (b) Harmonic response, Insonation 1

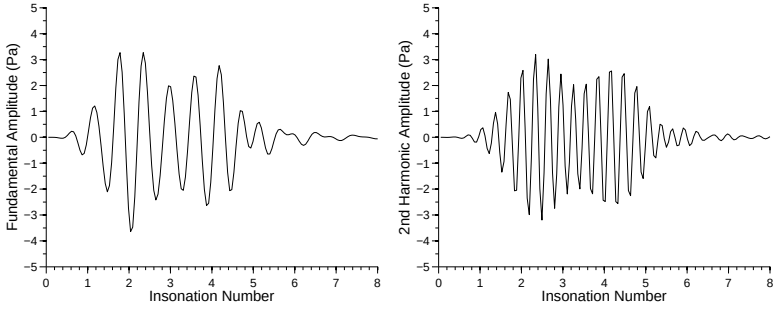

(c) Fundamental response, Insonation 2 (d) Harmonic response, Insonation 2

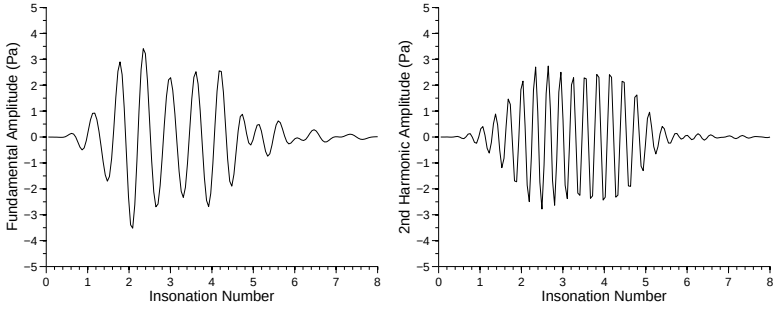

(e) Fundamental response, Insonation 3 (f) Harmonic response, Insonation 3

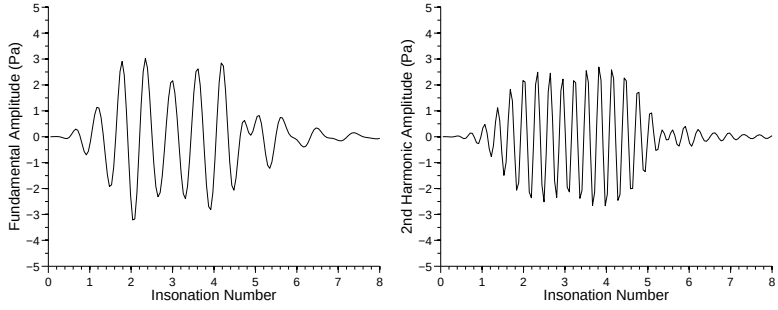

(g) Fundamental response, Insonation 4 (h) Harmonic response, Insonation 4

Figure 6.15: *Example of a biSphere bubble response which survives to give successive above noise signals to four incident pulses of 1.6MHz, 335kPa six cycles. The fundamental signals show very little change between insonations, whereas the second harmonic signals show a small reduction in amplitude. This is evidence of different behaviour from that observed in Definity.*

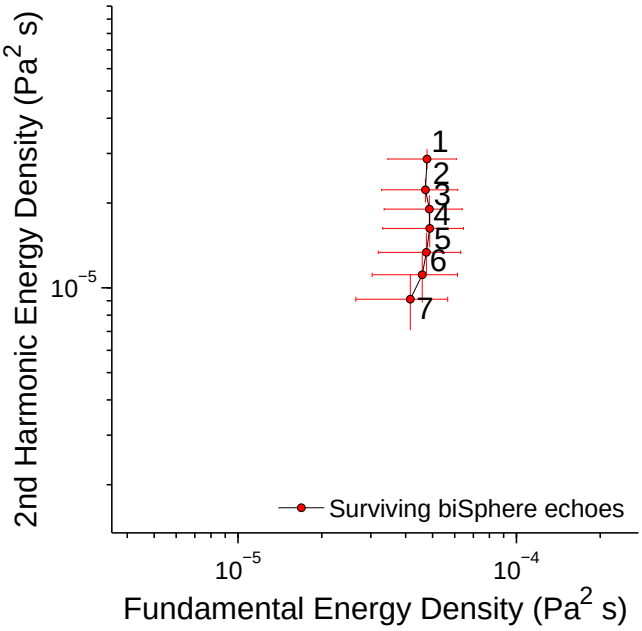

Figure 6.16: *Mean levels of energy density from the 34 remaining bubble signals to seven consecutive insonating pulses of 1.6MHz 335kPa. The mean values of energy density have been plotted as fundamental vs harmonic energy density components, with the numbers indicating the insonation number. The mean fundamental scatter remains at approximately constant level, with a reduction in mean harmonic component of energy only.*

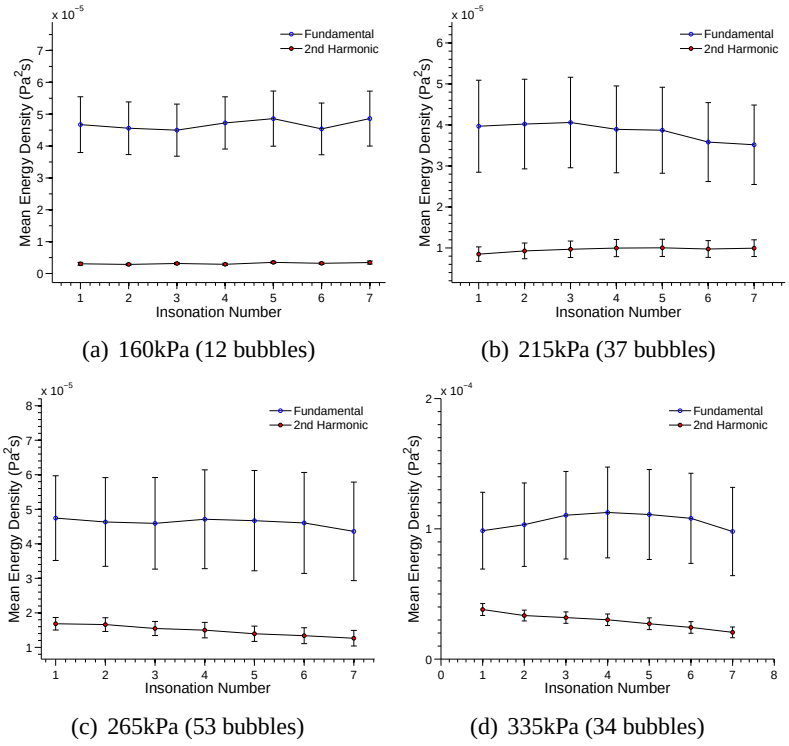

(a) 160kPa (12 bubbles) (b) 215kPa (37 bubbles)

(c) 265kPa (53 bubbles) (d) 335kPa (34 bubbles)

Figure 6.17: *Mean levels of energy density from the remaining bubble signals to seven consecutive insonating pulses. The mean values of fundamental and second harmonic energy density have been plotted against insonation number, showing the evolution of signals. The mean fundamental scatter remains at approximately constant level, with a reduction in mean harmonic component of energy evident in response to 265kPa and 335kPa pulses.*

for the destruction of a microbubble on a time scale of microseconds. On the other hand, the gradual reduction in resting diameter of a microbubble due to acoustically driven diffusion has been shown to occur on time scales of milliseconds. This order of magnitude difference in the time scales has been used to separate evolution of microbubble responses into two categories; destruction and diffusion.

The results presented here are limited by the noise level of the system, and therefore the destruction of microbubbles cannot be explicitly measured with this system. Emitted signals may evolve to below the noise level, but the bubble may remain intact. However, a significant change to the integrity of a microbubble can be defined as, if after producing a signal above noise from an initial imaging pulse, the bubble subsequently decays by such an extent that the next imaging pulse results in no detectable signal. The ability of a bubble to respond to subsequent pulses after such a change provides information about both the shell parameters and the solubility of the encapsulated gas. A significant and rapid ($t \leq 1\mathrm{ms}$) reduction in signal to below noise levels can therefore be defined as a destructive event; from the view point of the receiver, the bubble has been effectively destroyed (any shell or gas remnants which remain are incapable of producing sufficient scatter to be detected). A less rapid reduction ($t > 1\mathrm{ms}$) in scattered signal which results in above noise scatter to a subsequent pulse can therefore be classified as diffusion of gas out of the microbubble. This has been observed previously using both optical and acoustic techniques. In response to each imaging pulse, gas is forced out of the bubble, with a reduced volume of gas remaining in place to scatter subsequent signals.

6.5.1 Destruction

6.5.1.1 Definity

Results have been presented to show that although Definity bubbles have the ability to scatter ultrasound from multiple pulses, not all bubbles will do so. Those which emit lower energy signals, and thus according to the Mooney Rivlin model are below the resonance radius, are more likely to produce no subsequent scatter after the first imaging pulse. The relative numbers of Definity bubbles which survive to produce subsequent signals is higher than the equivalent number of biSphere signals, which suggests a strong role of the shell dynamics and encapsulated gas property in the destruction of bubble signals. This divergence in the lifetimes of lipid and albumin shelled agents has been observed previously. Stride et al[95] present a convincing reasoning behind this, based on the difference in the respective material's microstrucures,

specifically that van de Waals bound-phospholipid shells have the ability to 'repair' themselves after a moderate disruption, whereas the more rigid and 'much larger protein molecules cross-linked by covalent bonds' that make up an albumin based shell prevent repairable deformations, leading to increased amounts of shell rupture. Another significant difference between the two agents is the solubility of the encapsulated gases. Definity contains perfluorocarbon gas which can be considered insoluble in water, whereas biSphere contains soluble air. Chomas et al[4] show that the two gases have an order of magnitude difference between their respective dissolution times. For a $R_0 = 2\mu\mathrm{m}$ unshelled bubble, perfluorocarbon gas requires $t = 90ms$ to dissolve, whereas an equivalent air bubble requires only $t = 8ms$, which agrees with the increased resilience of Definity observed here.

Increased disappearance of echoes from lower energy Definity signals has been noted previously[72]. According to the Mooney Rivlin model results outlined above, these lower energy bubbles are most likely to have radii below the resonance radius, and it has been previously suggested that bubbles in this size domain are more likely to be disrupted[142,147]. Although the bubble responses measured here at low incident pressures ($< 400\mathrm{kPa}$) are close to the noise level of the system, and thus the subsequent lack of signal could be explained by a small reduction in signal to below noise levels, as the incident pressure is increased this is no longer the case. As shown in the example in Figure 6.2, bubbles well above noise are also observed to produce no subsequent signals. Relative destruction in the population of bubbles identified to be at resonance is much less than of those off-resonance (Table 6.2). This is in agreement with the work of Chomas et al[87], who have used optical experimental data together with a similar regression analysis as the one presented here to define a destruction threshold in terms of acoustic pressure and resting diameter. They show that bubbles with smaller initial radii are more likely to be destroyed, and that increasing transmission pressure increases the range of resting diameters for which destruction can be predicted.

Although these results agree with previous observations in literature, discrepancies exist. Chomas et al[87] have used a modified Rayleigh-Plesset model to relate microbubble destruction to the relative expansion (R_{max}/R_0) of a microbubble, similar to the Plesset and Mitchell stability criterion[148]. They show that in a phospholipid shelled microbubble relative expansion increases exponentially with decreasing diameter, and they present experimental data showing increased destruction for bubbles with lower resting diameters and increased relative expansion. The Mooney-Rivlin results (Chapter 3) presented here predict that bubbles at resonance show in-

creased relative expansion over those bubbles below resonance (Figure 6.18). According to the Plesset and Mitchell stability criterion, these bubbles at resonance would therefore have increased likelihood of destruction, due to the increased velocity and acceleration of the shell upon collapse, but the opposite has been observed here. However, Chomas et al have also optically observed increased destruction in smaller bubbles that exhibit lower relative expansions than larger bubbles (in response to differing incident pulses), and suggest that this effect is linked to the properties of the shell, which may not be uniform with respect to bubble size.

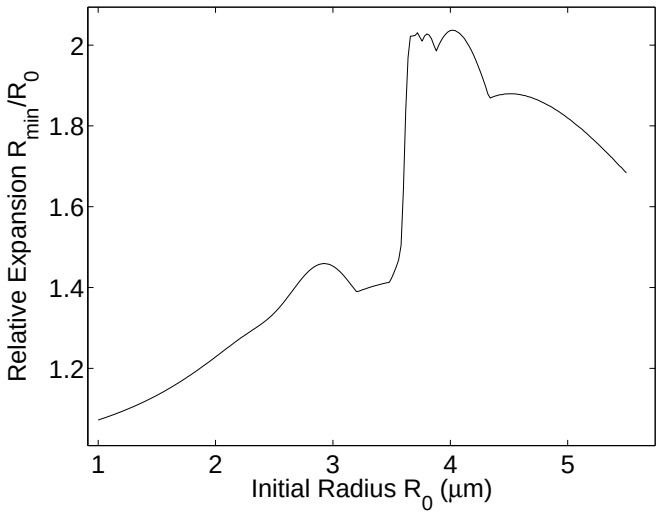

Figure 6.18: *Mooney Rivlin results for Definity in response to 1.6MHz, 550kPa six cycle pulse, showing relative expansion (R_{max}/R_0) with increasing radius. Maximum relative expansion occurs for bubbles at resonance (corresponding to maximum emitted fundamental response), which have been observed experimentally to show increased resilience. This is in contradiction to the Plesset and Mitchell stability criterion, which predicts increased destruction at increased levels of expansion.*

6.5.1.2 biSphere

Disappearance of biSphere echoes has been observed at all incident acoustic pressures used, but increases with acoustic pressure. That the net occurrence of destruction of biSphere bubble signals increases from 33% to over 97% for an increase in incident pressure from 410kPa to 540kPa, and that this level then stays at a plateau above 90%, suggests that a minumum pressure is neccessary to cause sufficient disruption to the majority of Albumin bubbles to reduce the scattered pressure to below the noise level of the experimental system. Similar effects have been observed in other Albumin shelled agents[4], using both optical and acoustic techniques.

Chomas et al have observed an increase from just 10% net destruction of bubbles at pressures of 800kPa, upto 80% net destruction at pressures greater than 800kPa. This also suggests that a minimum pressure is necessary to cause sufficient disruption to the Albumin shell. Wei et al[149] conclude from a combination of in vitro and in vivo experiments with Albumin shelled agents, that 'total power absorption', directly related to incident pressure, is the most important factor in destruction, and not resonance effects, which would agree with the results shown here. That both destruction and survival have been observed in response to a range of incident acoustic pressures (albeit in relatively different amounts), suggests that the integrity of biSphere bubbles varies, and the threshold pressure needed to disrupt them differs for individual bubbles.

Bouakaz et al[98] present optical results for biSphere, which show survival in response to much higher acoustic pressures than those observed here (bubbles up to $3\mu\mathrm{m}$ in diameter survive in response to a 1.3MPa, 1.7MHz, ten cycle pulse). They have also observed that smaller microbubbles are "harder to break", which is attributed to increased rigidity at smaller sizes. It may be that the presence of the optical components (or the tubing used to hold the bubbles in place) changes the acoustic field incident on the bubbles sufficiently to make direct comparison with results presented here not viable, and leading to the increased destruction threshold.

6.5.2 Diffusion

6.5.2.1 Definity

The characteristics of decreasing amplitude and relative increase of harmonic components shown in Figures 6.7 and 6.8, are similar to the increase in central frequency over a series of ten pulses shown by Chomas et al[4] in phospholipid shelled (MP211) bubble responses. This suggests that the mechanisms behind the effect are the same, namely a decrease in bubble diameter due to gas diffusion is taking place here. Again, due to the time scales involved (time between pulses equals $1\mathrm{ms}$), and the relatively low permeability of the phospholipid shell, this is very unlikely to be due to static diffusion alone, suggesting a strong role of acoustically driven diffusion in this decreasing bubble signal. Chomas et al[87] point out that this does not necessarily infer that a disruption in the shell, which allows the gas to escape, causes the diffusion alone. An alternative method could be an increased rate of static diffusion caused by the increased pressure gradient brought about by the compression of the bubble from the incident pulse, which would produce similar results. The data presented here alone does not offer any insight into which is more likely.

The bubble responses in Figure 6.7 can be directly compared to the Mooney Rivlin model presented previously. A similar decrease in fundamental to harmonic ratio (from 0.66 to 0.36) would be observed for a decrease in bubble diameter from $3.60\mu\mathrm{m}$ (ratio of 0.630) to $3.54\mu\mathrm{m}$ (ratio of 0.349), a decrease in size of just 1.6% ($0.06\mu\mathrm{m}$). This corresponds to a total decrease in energy of 53% (similar to, although less than, the 75% observed here). Decreases in diameter of upto 18% (maximum decrease of upto $0.74\mu\mathrm{m}$) in phospholipid shelled bubbles (MP2211) due to acoustically driven diffusion from a single acoustic pulse have been observed using high speed optical techniques[4], confirming that changes in diameter on this scale, over the timescales concerned (1-7ms), can occur without destroying the bubble.

It has been shown that the amount of initial energy scattered by a bubble relates directly to the amount of diffusion observed in subsequent pulses. Off resonance scatter shows, on average, higher levels of diffusion than those bubbles with increased levels of fundamental scatter classified to be at resonance. That the susceptibility of a bubble to acoustically driven diffusion is related to the bubble's level of scatter is not surprising, as these are both directly related to initial diameter. Chomas et al[4] have presented optical results that show a dependence on initial diameter of a bubble on the amount of decrease in diameter caused by acoustically driven diffusion. However, they observe that a bubble at resonance will be more susceptible to this effect, and that the effect will be reduced for bubbles less than $2\mu\mathrm{m}$ (relating to off resonance bubbles here). They suggest that at resonance increased convective diffusion, caused by increased wall velocity, would be responsible for increased reduction in bubble size. Results have been presented here where bubbles at resonance show the large reductions in fundamental scatter related to this increased diffusion (termed 'migrating bubbles' here). Although this behaviour is in the minority for bubbles at resonance (Table 6.4), the predicted changes in bubble radii are much greater than for those with characteristics of off-resonant scatter.

When comparing these results to the Mooney Rivlin model, the difference in the change of acoustic signals in the two populations can be understood in terms of shifts in initial radii of the bubbles. Due to the shape of the resonance curve (Figure 6.19), the Money Rivlin model predicts that a reduction in size for bubbles above the resonance radius will have less effect on the scattered signal than the same change for a bubble below the resonance radius. For example, a $0.5\mu\mathrm{m}$ reduction in size for a bubble approximately at resonance ($R_0 = 4.5\mu\mathrm{m}$, i.e. classified to be at resonance by the normalized cross correlation method used here) leads to a 17.5% reduction in fundamental component of scattered signal, whereas the same reduction in size for

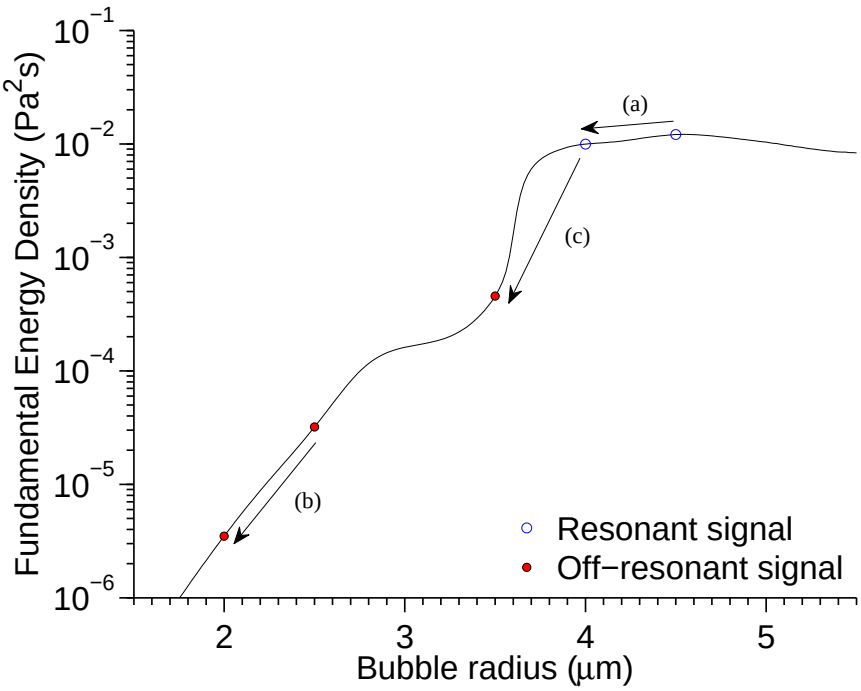

Figure 6.19: *Mooney Rivlin results for Definity in response to 1.6MHz, 550kPa six cycle pulse, showing fundamental component of scatter. A reduction in size of, for example,* $0.5\mu\mathrm{m}$ *for a bubble above resonance (*$R_0 = 4.5\mu\mathrm{m}$*) leads to a* 17.5% *reduction in fundamental component of scattered signal (a), whereas the same reduction in size for a below resonance signal (*$R_0 = 2.5\mu\mathrm{m}$*) leads to a* 89.1% *reduction in fundamental signal (b). The same decrease in size could lead the scattered signal 'migrating' between the two populations (c), depending on the initial size (e.g. a* $R_0 = 4.0\mu\mathrm{m}$ *resonant bubble undergoing a* $0.5\mu\mathrm{m}$ *reduction in radius, would produce off-resonant subsequent scattered signals).*

a below resonance signal (e.g. $R_0 = 2.5\mu\mathrm{m}$) leads to a 89.1% reduction in fundamental signal (although smaller bubbles are likely to diffuse faster). A bubble slightly above the resonance radius of $R_{res} = 4.54\mu\mathrm{m}$ (e.g. $R_0 = 4.0\mu\mathrm{m}$) which initially shows the characteristics of resonant scatter and then undergoes the same $0.5\mu\mathrm{m}$ decrease in radius would therefore see a large drop in scattered signal, and 'migrate' to below the resonance radius, as observed in the experimental results above. Thus, in relation to the optical results presented by Chomas et al[4], the relative increase in reduction of bubble radius they have observed at resonance may not result in an increased reduction of acoustic signals, when compared to smaller off-resonance bubbles. A combined optical and acoustic study into the effect of diffusion on the two populations is thus warrented, to provide further evidence.

Another explanation for the inferred large decrease in size observed in 'migrating bubbles' could lie in optical observations of so called 'fragmenting' bubbles. Both Chomas et al[4] and Dayton et al[92] show examples of fragmenting bubbles which result in intact 'daughter' bubbles. These bubbles have been shown to persist for timescales long enough to produce signals from subsequent pulses ($> 600\mathrm{ms}$ in the case of Chomas et al[4]). They are evidently much smaller than the original 'parent' bubbles, and therefore may result in the decreased amplitude of scatter observed in bubble signals after migration between populations. The data presented here offers no insight into whether this is more likely to be the case than incidents of large amounts of diffusion, and further investigation with combined optical and acoustic measurements is warranted to investigate this further.

6.5.2.2 biSphere

biSphere bubble signals which survive to produce above noise signals to successive incident pulses show approximately constant fundamental signals and energy of scatter. Neither of the two characteristics outlined above which would indicate the presence of acoustically driven diffusion (reduction in fundamental energy and decrease in fundamental to harmonic ratio), have been observed. Chomas et al[4] suggest that lack of diffusion is directly attributed to the mechanical properties of the Albumin shell. The stiffer and thicker Albumin shell presents a more rigid encapsulating structure around the gas core, which does not allow diffusion to take place as long as it retains its coherence. However, if the shell is disrupted, it may become ineffective in stopping dissolution taking place, and no longer have the ability to encapsulate the gas core. Albumin shelled agents have been shown to exhibit static diffusion after insonation[4],

giving much greater gas dissolution rates on the order of a free gas bubble, which would agree with the lack of acoustically driven diffusion over the millisecond timescales investigated here. Any biSphere bubble which has its shell sufficiently disrupted by an imaging pulse appears to give way to dissolution of its soluble nitrogen gas core, and thus does not survive to produce subsequent signals.

In the bubble signals which do survive to produce successive signals, no reduction in fundamental energy of emitted signal has been observed, and a relative decrease in harmonic components has been observed (unlike the relative increase in Definity). A reduction in the harmonic components of scatter without a corresponding reduction of fundamental scatter suggests a complex evolution of the bubble between imaging pulses. The harmonic component of scatter arises from the restrictive effect of the shell on the oscillation of the bubble, as previously observed optically[92], and thus removal of this constriction will lead to a reduced harmonic scatter. This reduction in harmonic signal has been observed previously at high acoustic pressures (above 600kPa), and related to destruction of microbubbles[103]. That it occurs here at lower acoustic pressures without significant reduction in total energy of scatter (i.e. bubble is not completely destroyed), suggests that the structure of the shell is altered sufficiently to remove the restriction on movement, but without allowing dissolution of the encapsulated gas. Fragments of an acoustically disrupted shell have previously been observed to affect the dissolution of the encapsulated gas, and thus affect the ability to produce an acoustic emission[92], and may be the mechanism behind the behaviour observed here.

6.5.3 Error analysis

The main source of error in this chapter arises from the experimental system's noise floor. The analysis of the data is based upon the reduction of microbubble signals to below the noise level of the Sonos ultrasound scanner relating to destruction of microbubbles. Single microbubbles have measured to scatter at a range of pressures, right down just above the detectable limit which arises from the ability to select a signal from the electrical noise present in the system. As stated in the Results section, this introduces the drawback that bubbles signals may reduce to below this lower limit, but the bubbles themselves with remain intact. This limitation has been overcome by large population single bubble study, which concentrates on the bubbles which can definitely be stated to have undergone a significant reduction or change in signal characteristics, as shown in Figure 6.2.

Other errors in the analysis are introduced by the lack of scatter at low amplitudes, and the limited ranged of acoustic pressures which have been measured (the minimum acoustic pressure used here was 265kPa), as shown in Figure 6.5. These issues limit the strength of the conclusions which can be drawn on the linearity of microbubble response to increasing pressures, but both of these issues can be improved upon by further experiments, using an improved ultrasound system, with a lower noise receive amplifier. A similar issue arises in the analysis of biSphere data, which shows only a small amount of signals can be measured from consecutive imaging pulses, due to the fragility of the agent. A reduced noise floor would add improved confidence that this is indeed evidence for microbubble destruction, as is suggested in the above discussion

6.6 Conclusion

Results from the single bubble system outlined in Chapter 3 have been used, together with a variety of statistical analysis methods, to produce understanding of the diffusion and destruction effects which microbubbles from samples of biSphere and Definity undergo, in response to increasing acoustic pressures and frequencies. The two different contrast agents show differing behaviour, which has been related to the constituent materials of both the encapsulated shell and the enclosed gas.

This improved knowledge of these agents and their corresponding behaviours may directly lead to improved diagnostic and therapeutic techniques, which can be used to improve the clinical applications of contrast enhancement listed in Chapter 1. The discussion above warrants further work with combined optical and acoustic measurements to investigate the structure of the lipid and Albumin shells.

6.7 Further work

The results presented here provide an insight into the evolution of contrast agents when in the presence of a range of clinical imaging parameters, but further work could provide an increased understanding of the effects described above. That lipid bubbles at resonance provide increased resilience over those bubbles off-resonance is not fully understood, and optical experiments recreating the conditions used here will provide further insight into the evolution of the respec-

tive populations.

The results presented here are in response to pulse repetition frequencies of 1kHz, giving 1ms separation between imaging pulses. Further work investigating the effect of pulse interval variation of the evolution of bubbles in the respective populations identified in Definity may elucidate the impact of diffusion on bubble signal evolution. Incident pulses with higher PRFs may provide information on how much effect the solubility of the gas has on the evolution of the signal as compared to the effect of the shell. This can also be investigated using contrast agents that are constructed with the same type of shell whilst containing different encapsulated gases.

A theoretical model for diffusion would improve the understanding of the experimental results presented here. A one-to-one map of experimental bubble signals to theoretical signals, as suggested for further work in Chapter 4, incorporating a change in bubble diameter between pulses to reflect the change in energy of signal, could provide better comparison with optical experiments which show examples of diffusion in the literature.

Chapter 7
The behaviour of single microbubbles under a power modulated pulse sequence.

7.1 Introduction

One important characteristic of the behavior of microbubble contrast agents is the dependence of their ultrasonic backscatter on acoustic pressure. It is generally considered that microbubble scatter can be classified into three domains: scatter through linear oscillation at low acoustic pressure, nonlinear behavior at intermediate pressures, and the creation of free bubbles at higher pressures[150–152]. The delineation of these domains is dependent on a number of factors, including specific microbubble characteristics, ultrasound beam properties and the bubbles local environment, which all add complexity to the relationship between acoustic pressure and microbubble behavior[62,103,153]. Previous studies have used high concentrations of contrast agent in vitro to infer the behavior of individual microbubbles[7,40,61,65,66,118,154–156]. These can lead to questionable results[58], which may be explained by the presence of multiple subpopulations of scatterers within a high concentration sample[101]. The use of fast acquisition microscopy has provided an unprecedented wealth of information on the behavior of microbubbles and has been reviewed recently[2]. The study of the acoustic response of single microbubbles, on the other hand, has offered over the recent years increasingly valuable insight, because it is directly related to their use in diagnostic imaging[2,67,69–72,74,76,157–160]. Our previously reported system offers accurate calibration of both the transmit and receive, providing absolute measurements of the pressure fields created by a point scatterer[72,75].

New imaging techniques use multipulse sequences to take advantage of microbubble nonlinear response and improve the contrast-to-tissue ratio. For example, pulse inversion (PI) uses inverted polarity transmit pulses (180° out of phase) to remove any linear scatter while preserving nonlinear echoes[161], and has been extended to incorporate Doppler processing techniques[64]. This allows spatial resolution to be improved, as compared to single pulse harmonic imaging,

by using sequences of short wideband pulses[162]. Another such technique, pulse amplitude modulation, uses a sequence of pulses (a half amplitude pulse followed by a full-amplitude pulse followed by another half-amplitude pulse) to enhance the nonlinear bubble to tissue response ratio. This technique relies on the increasing nonlinearity of the bubble signal in response to increasing insonating pulse amplitude to distinguish, in theory, between linear and nonlinear echoes[163]. Subtracting the echo response of two half amplitude pulses from the full-amplitude response should cancel out the linear components of the echo, whereas the remainder will be signal resulting from nonlinear scatter only.

7.2 Aims of chapter

The linearity of response to increasing amplitude pulses has not been tested previously with regards to Pulse Amplitude Modulation in vitro using single microbubble acoustic signals. The analysis of single scattering events will avoid the drawbacks which related to high concentration measurements such as self attenuation and pressure variation within a real ultrasound beam (as outlined in Chapter 1). Therefore single bubble measurements can offer more accurate results with respect to the range of response from varying acoustic pressures, which is directly related to the performance of pulsing schemes such as pulse amplitude modulation, and is investigated here at a range of diagnostic pressures. The aim of this chapter is to gain knowledge on the effectiveness of a current pulse sequence, and to investigate the potential for using this knowledge to improve the contrast to tissue ratio available in the clinical diagnostic techniques described in Chapter 1.

7.3 Pulse amplitude modulation

Pulse amplitude modulation (PAM) achieves linear echo cancellation by modulating the amplitude of the incident pulses (as opposed to the phase in pulse inversion imaging) and applying a series of gains to the received signals to exploit the nonlinearity of contrast echo. This approach was originally proposed by Brock-Fisher et al[164], and is based on transmission of varying amplitudes to exploit the nonlinearity of response of contrast agents. By applying suitable gain factors to the received signals, the nonlinear tissue echo can also be reduced. This method of increasing the contrast to tissue ratio has been included as an ‘on-board’ imaging method in the Philips Sonos 5500 scanner. This allows the transmit pulsing scheme and receiver gain se-

quence to be applied automatically, through the selection of 'contrast imaging' as a 'front-end' control. The response of single microbubbles to the pulse sequence is investigated here using the single bubble system described in Chapter 4. Results from the contrast agent Definity® are presented here, as it has been shown that Definity single microbubbles are more resilient to the incident pulse, and there is greater physical understanding of the response.

7.4 Methodology

7.4.1 Theoretical basis

The choice of the gain factors applied upon receive can have the effect of reducing the nonlinear echo signals arising from tissue, whilst preserving the nonlinear bubble signals. Brock-Fisher et al[165] outline the method based on the cancellation of so-called 'zero-memory' scatter. This 'zero-memory' scatter is solely dependent on the instantaneous acoustic pressure at the scatter, as is the case for both linear and nonlinear tissue echo. However, contrast agents have been observed to be affected by subsequent imaging pulses, even at low MIs, and as such are not classified as 'zero-memory' scatterers. The 'Brock-Fisher' technique of transmitting varying levels of incident pulse, and applying varying gains to the received signals, acts to minimize both the linear and nonlinear tissue echo, while preserving the nonlinear contrast echo. This shall be referred to as the 'PAM' technique henceforth.

Brock-Fisher et al[165] have calculated gain factors in response to an amplitude modulated pulse train by modeling tissue echo with a polynomial model representing both linear and nonlinear tissue echo (Equation 7.1).

$$y = ax + bx^2 + cx^3 + \cdots \tag{7.1}$$

where x, x^2, x^3 values represent the fundamental, second and third harmonic responses, and the parameters a, b, c are arbitrary constants. The higher order components above second harmonic can be ignored here for simplicity. In response to a series of three amplitude and inverted modulated transmit pulses (for example +0.5, +1, -0.5), the response from tissue becomes (Equation 7.2);

$$
\begin{aligned}
y_1 &= 0.5ax + 0.25bx^2 \\
y_2 &= ax + bx^2 \\
y_3 &= -0.5ax + 0.25bx^2
\end{aligned} \tag{7.2}
$$

The linear and nonlinear tissue signals can be reduced by scaling each of the received echo signals (y_n) by independent factors (k_n), so that the sum of the three responses (y_t) tends to zero, as follows (Equation 7.3);

$$
\begin{aligned}
y_t &= k_1 y_1 + k_2 y_2 + k_3 \\
y_t &= k_1(0.5ax + 0.25bx^2) + k_2(ax + bx^2) + k_3(-0.5ax + 0.25bx^2)
\end{aligned} \tag{7.3}
$$

By separating the fundamental and second harmonic terms, and setting each to zero, the gain factors can be found by substitution as follows (Equation 7.4);

$$
\begin{aligned}
\text{Fundamental;} \quad 0 &= 0.5k_1 ax + k_2 ax - 0.5k_3 ax \\
\therefore k_2 &= 0.5k_3 - 0.5k_1 \\
\text{2nd Harmonic;} \quad 0 &= 0.25k_1 bx^2 + k_2 bx^2 + 0.25k_3 bx^2 \\
\therefore 0.25k_1 &= 0.75k_3 \\
\Rightarrow k_3 &= k_1/3 \\
\Rightarrow k_2 &= k_1/6 - k_1/2
\end{aligned} \tag{7.4}
$$

By choosing gain factors which conform to this polynomial model of tissue scatter the fundamental and second harmonic scatter from the so-called 'zero-memory' tissue scatter is minimized, and the only significant response that will remain will be from contrast agent scatter (which does not conform to Equation 7.1). In the Sonos 5500 scanner's contrast mode the transmit gains employed are $[+1/2, +1, -1/2, 0]$ (an extra zero transmit line is used to minimize reverberations), which corresponds to equivalent receive gains of $[1/2, -1/6, 1/6, 1]$ to

minimize tissue echo (an arbitrary value of k_4 corresponds to the zero transmit pulse y_4). Signals received in response to each transmit pulse are then summed with the relevant gain factors applied upon receive, and the final result of each set of four pulses sent to the display processing electronics of the scanner. The result of the consecutively summed signals is passed to the R.F. data capture hardware and sampled by the custom designed 'Aflink' software described previously, meaning some simple post-processing is required to invert the summation and gains applied to each signal, in order to reconstitute the individual responses.

The results of this process, and the relative success in improving the contrast have been investigated for the two agents previously described. A variety of imaging parameters have been investigated, and the responses from the individual response have been looked at, specifically to investigate if the application of successive pulses of differing amplitude causes differing responses than single amplitude pulses cause.

7.4.2 Calibration

The transmit and receive functions of the scanner whilst in PAM imaging mode were calibrated as described in Chapter 2. It was confirmed by hydrophone measurements that the incident pulses employed were the same as the M-mode pulses used in previous chapters (Figure 7.1). Copper sphere measurements were performed to ensure that no significant differences exist in the receiver calibration settings (Figure 7.2).

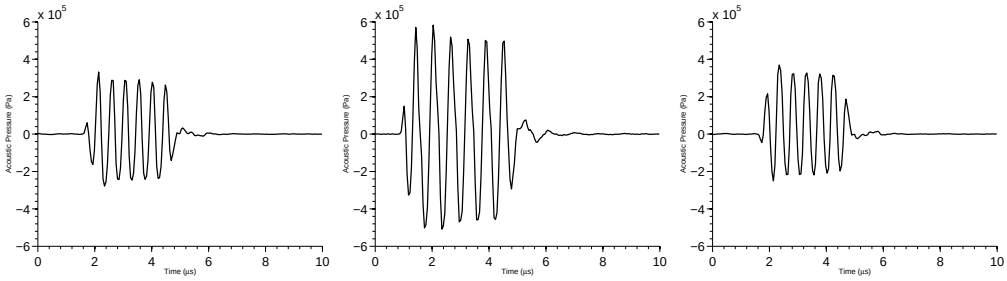

(a) Transmit pulse 1 (275kPa) (b) Transmit pulse 2 (550kPa) (c) Transmit pulse 3 (275kPa)

Figure 7.1: *The three amplitude modulated transmit pulses used in the Sonos 5500 on-board PAM contrast setting, with amplitudes 275,550,275kPa respectively (1.6MHz, six cycle pulses).*

Figure 7.1 shows the S3 calibration pulse of 1.6MHz 550kPa six cycles, when set to PAM imaging. The first and third pulses are identical in amplitude but inverted in phase, and have

peak negative pressure of half the imaging pressure (275kPa). Differences of less than 5% in the ratio between the full and half amplitude pulses were observed for a range of acoustic pressures and frequencies (which arise from the method which the scanner employs in generating the PAM pulse sequence).

7.4.3 Signal processing

The custom designed software package ('Aflink') allows the R.F. signals to be recovered from the amplitude modulated pulses. The software records each pulse after the relevant gain factor has been applied, and sums the result to the previous, giving the final Brock-Fisher PAM result on the final (fourth) line recorded. Therefore, in order to recover the raw RF signals, this processing must be 'un-done', as follows (Equation 7.5). Sx_l is the signal extracted from the scanner from insonation 'l' and Rx_l refers to the received signal from insonation 'l'. Gl is the gain signal applied to the respective signals.

$$\begin{aligned} Rx_1 &= \frac{Sx_l}{G1} \\ Rx_2 &= \frac{(Sx_2 - Sx_1)}{G2} \\ Rx_3 &= \frac{(Sx_3 - Sx_2)}{G3} \end{aligned} \tag{7.5}$$

The responses to the on-board amplitude modulation technique were initially measured using submilimeter copper spheres, as outlined in Chapter 2. This gives a bench mark for the amount of 'zero-memory' fundamental and second harmonic scatter that can be reduced using the multiple receive gain technique outlined above, and also allows a reliable test to the post-receive processing applied in order to recover the individual signals upon receive to be made. The difference between stationary and moving linear scatterers is investigated to show the effect of movement on the zero-memory theory upon which the technique is based. These results are then compared to single microbubble results for a range of acoustic pressures, and the relative effectiveness evaluated. Finally an alternative technique, a modified PAM technique, is presented, and the potential improvements shown.

7.5 Results

7.5.1 Introduction

Results have been produced for linear scatterers and Definity microbubbles in response to a range of PAM peak amplitudes. As stated previously, Definity was chosen over biSphere for this investigation because of its increased resilience to the incident pulses, allowing single bubbles to produce similar echoes from multiple transmit pulses.

7.5.2 Linear scatterer

Figure 7.1 shows the individual transmit pulses used in the PAM Contrast mode, as measured by the membrane hydrophone system outlined in Chapter 2. The time between pulses is 1ms, giving the same pulse repetition frequency (PRF) as that used in previous chapters. The amplitudes of transmit of the three are 275,550,275kPa respectively, and this shall be referred to as the 550kPa PAM pulse sequence from now on (with full amplitude peak negative being used as a descriptor for the pulse sequence). Figure 7.2 shows the response from a $43\mu m$ copper sphere attached to a membrane. The half, full, half amplitude modulation of the transmit pulses can clearly be seen in the sphere responses. The successful reduction in the fundamental scatter can be seen in the result to the gain modulated summation of all four received signals in Figure 7.2(d). The energy of scatter of each response is shown in Figure 7.3.

7.5.3 Definity

Figure 7.4 shows example signals from a Definity bubble, in response to the three amplitude modulated responses shown in Figure 7.1, followed by the PAM summation result. The non-linearity in response to the full amplitude (550kPa) transmit pulse can clearly be seen in the much larger second response, which contains much higher harmonic components. The first and third pulses, although similar, are not identical, which is presumably due to changes in the bubbles structure caused by one or both of the first two pulses, as outlined in the previous chapter (Chapter 5, Figure 6.7). This effect of acoustically driven diffusion will act to improve the relative increase in bubble signal compared to the 'zero-memory' tissue echo, which will remain similar across the imaging sequence.

As can be seen in Figure 7.4(d), although the PAM method of processing reduces the ampli-

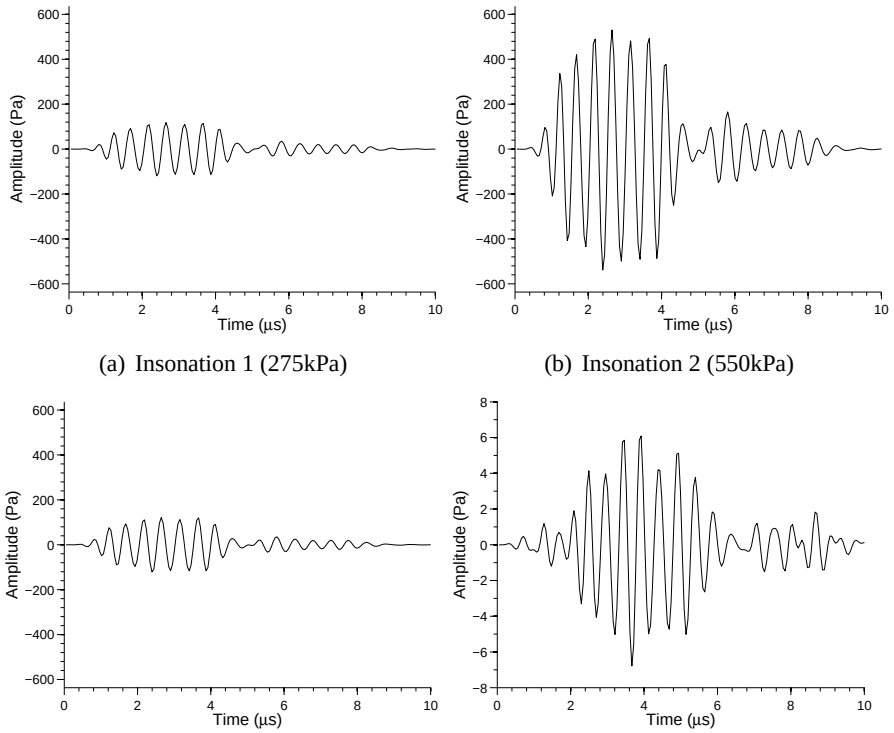

(a) Insonation 1 (275kPa)

(b) Insonation 2 (550kPa)

(c) Insonation 3 (275kPa)

(d) PAM result

Figure 7.2: *The fundamental components of scatter from an attached $43\mu m$ copper sphere in response to the amplitude modulated transmit pulses employed in contrast mode. Figure 7.2(d) shows the result of the PAM processing, showing a $39.19dB$ reduction in the fundamental component of scatter ($23.59dB$ reduction in the 2nd harmonic is also achieved).*

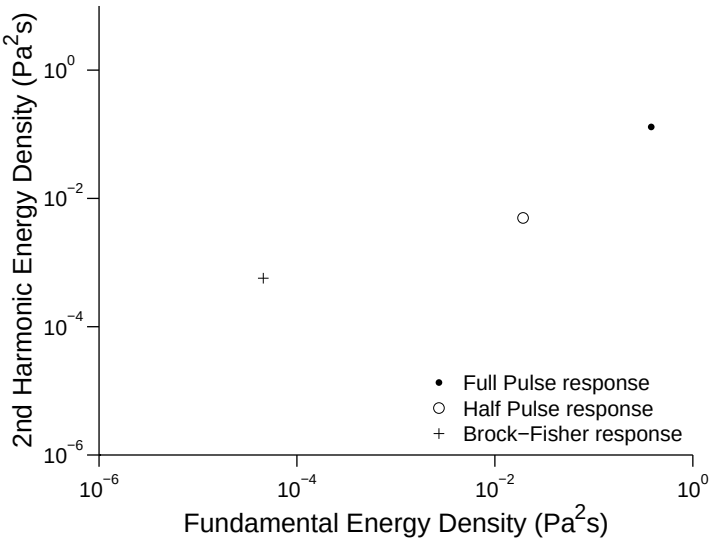

Figure 7.3: *Energy of scatter from the sphere signals shown in Figure 7.2, showing full pulse response, half pulse response, and the subsequent reduction in both fundamental and 2nd harmonic following the Brock-Fisher technique. Transmitted pulse sequence of 1.6MHz, 550kPa six cycle pulses.*

tude of the bubble signal (a 7.86dB and 7.85dB reduction in fundamental and 2nd harmonic respectively), it is successful in increasing the signal from a contrast bubble relative to scatter from a zero-memory linear scatterer (giving a relative increase of 31.34dB and 15.74dB in fundamental and 2nd harmonic respectively).

A second type of behavior to amplitude modulated pulses has been observed in Definity response, shown in Figure 7.5. Although the second full-amplitude transmit pulse produces a six cycle response as expected (Figure 7.5(b)), the initial half amplitude pulse produces no measurable signal above the noise level of the system. As shown in Figure 7.5(c), this bubble then produces no response from the third half-amplitude pulse. This is distinctly different behaviour to that shown in Figure 7.4, which produces a response to each of the three imaging pulses, and around which the PAM imaging method is designed. In a diagnostic imaging situation, when no microbubble signal is received on the first pulse the signal is purely from tissue and therefore could be exploited to provide a higher contrast to tissue ratio. The PAM method described above does not take this type of behaviour into account, and improvements in contrast to tissue ratio may be possible.

The signals from a large number of bubbles in response to varying acoustic pressure PAM

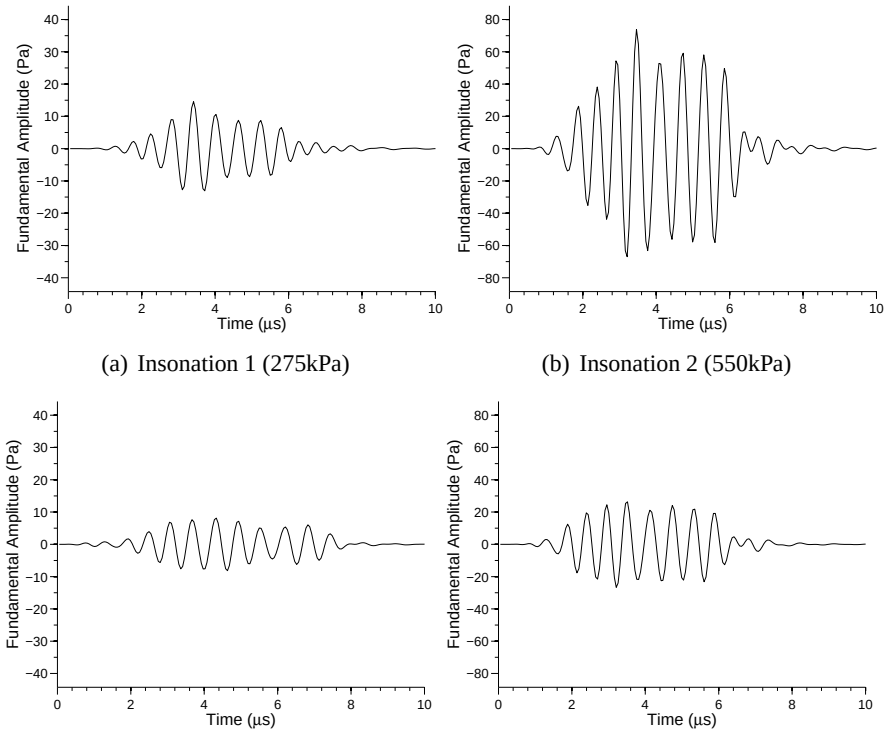

(a) Insonation 1 (275kPa)

(b) Insonation 2 (550kPa)

(c) Insonation 3 (275kPa)

(d) PAM Result

Figure 7.4: *Example of Definity bubble response to three amplitude modulated responses of 275kPa, 550kPa 275kPa (1.6MHz six cycle pulses). The responses to the first and third pulses are similar, although not identical, due to change in the bubble structure as described in Chapter 6. (d) shows the result of the PAM processing, showing a* $7.86dB$ *reduction in the fundamental (*$7.85dB$ *reduction in the 2nd harmonic) from the full amplitude response.*

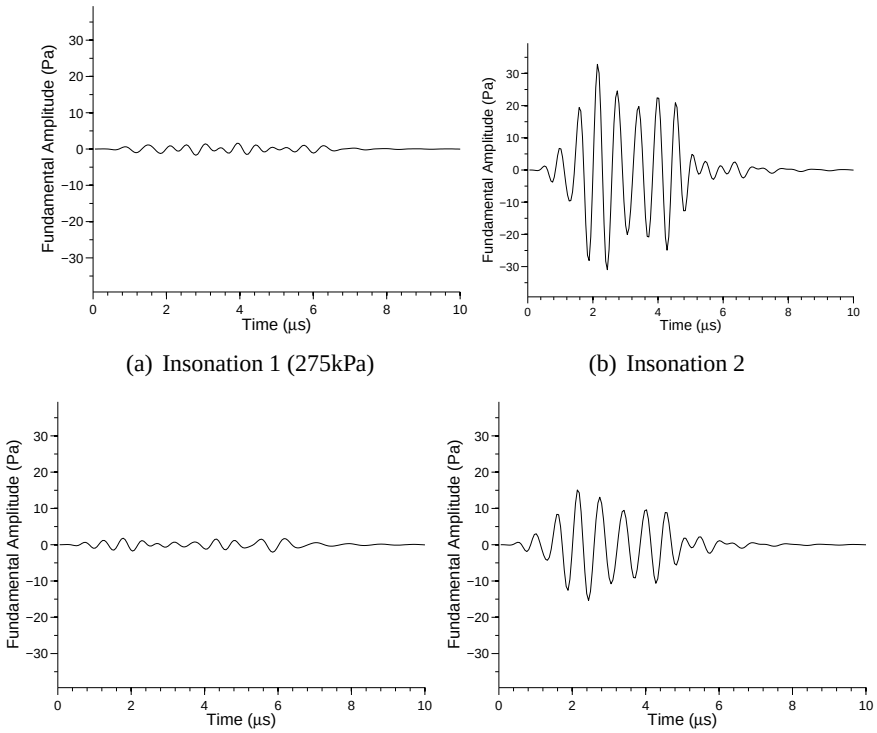

(a) Insonation 1 (275kPa)

(b) Insonation 2

(c) Insonation 3 (550kPa)

(d) PAM result

Figure 7.5: *Example of second type of Definity behaviour observed in response to three amplitude modulated responses of 275kPa, 550kPa 275kPa (1.6MHz six cycle pulses). No response above noise is observed in response to the first and the third incident pulses. The second full amplitude pulse gives a response as expected. (d) shows the result of the PAM processing, showing a* $6.59dB$ *reduction in the fundamental (*$6.39dB$ *reduction in the 2nd harmonic).*

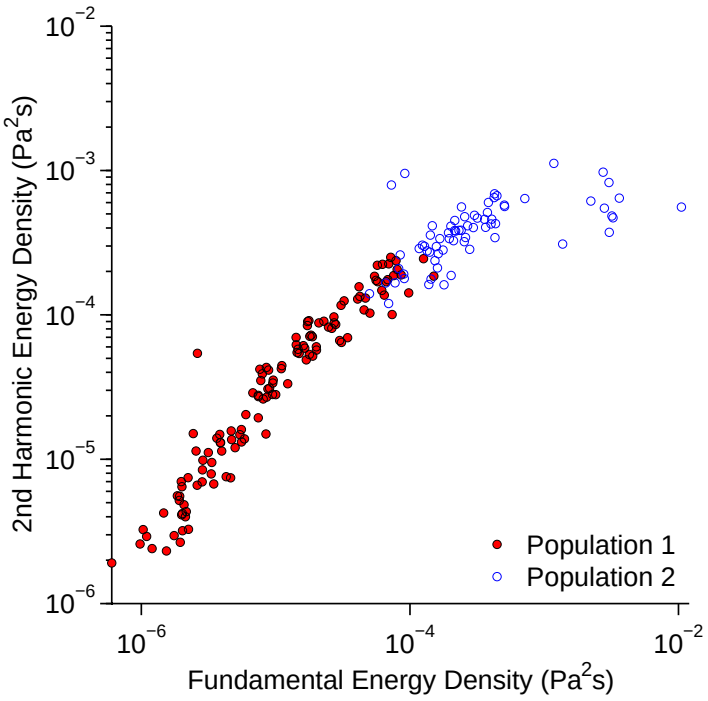

Figure 7.6: *2nd pulse (full amplitude) responses from 194 bubbles to a 1.6MHz, 550kPa PAM pulse sequence. Bubbles have been categorized as those for which the first signal in response to the first half amplitude pulse is below the noise level of the system (Population 1), and those which give an above noise signal (Population 2).*

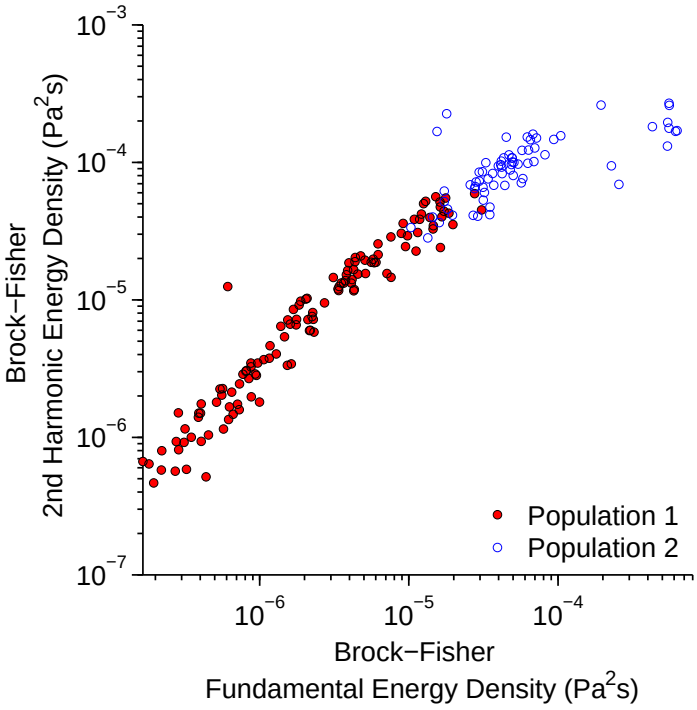

Figure 7.7: *The PAM method results in stronger signals from the higher energy Population 2 bubbles, in both the fundamental and 2nd harmonic components. The increased information that the lack of first response gives in Population 1 bubbles, is lost.*

pulse sequences have been analyzed. The behaviours of 194 bubbles in response to amplitude modulated pulses (1.6MHz, 550kPa peak negative pressure) are shown in Figure 7.6, with the bubbles categorized as those which do not give a response above noise to the first imaging pulse (Population 1), and those which do (Population 2).

The energy density of the second pulse response is shown here. As can clearly be see in Figure 7.6, the bubbles which give a first pulse response subsequently give a much stronger response to the second pulse, although there is some overlap in the mid-range energy densities. Therefore, in response to a 550kPa PAM sequence, the bubble response is dominated by the higher energy scatter of those bubbles which respond as predicted by theory, and the Brock-Fisher gain processing works well (Figure 7.7). Of the total energy of all responses measured at 550kPa, 64% belongs to Population 2 scatter.

This proportion of Population 2 response changes with the incident pressure of the PAM pulse sequence, as shown in Figure 7.9. Figure 7.8 shows the response to a range of incident acoustic pressure PAM pulse sequences (from 335kPa to 1.02MPa). In response to the maximum energy measured (1.02MPa), out of 110 bubbles measured, 65 bubbles (59.1%) belong to the Population 1 scatter which produces no response to the first half-amplitude (510kPa) pulse. These responses span the entire range of full pulse energy densities, and as such include a large number of high energy scatterers; in total adding up to 38% of the total energy measured (39% of the fundamental energy and 36% of the 2nd harmonic). This represents a significant increase in this type of scatter from the 550kPa responses, and in turn has significant effect on the effectiveness of the PAM method, as shown in Figure 7.11. As can be seen, the PAM responses from Population 1 are now a significant proportion of the total scatter (47% of the fundamental and 49% of the 2nd harmonic resulting energy), and the loss of information from the lack of first response is substantial.

7.5.4 Alternative PAM technique

An alternative post-processing method to the simple summation of responses is proposed here, to optimize contrast imaging based on the knowledge of the new behaviour presented in the previous section. In order to increase the energy of the signal when no response is observed, a simple division by the energy contained within this first response will act to reduce the 'zero-memory' tissue scatter further, while simultaneously increasing the energy of the Population 1 scatter. While this is a simplistic approach, and not necessarily the most efficient process

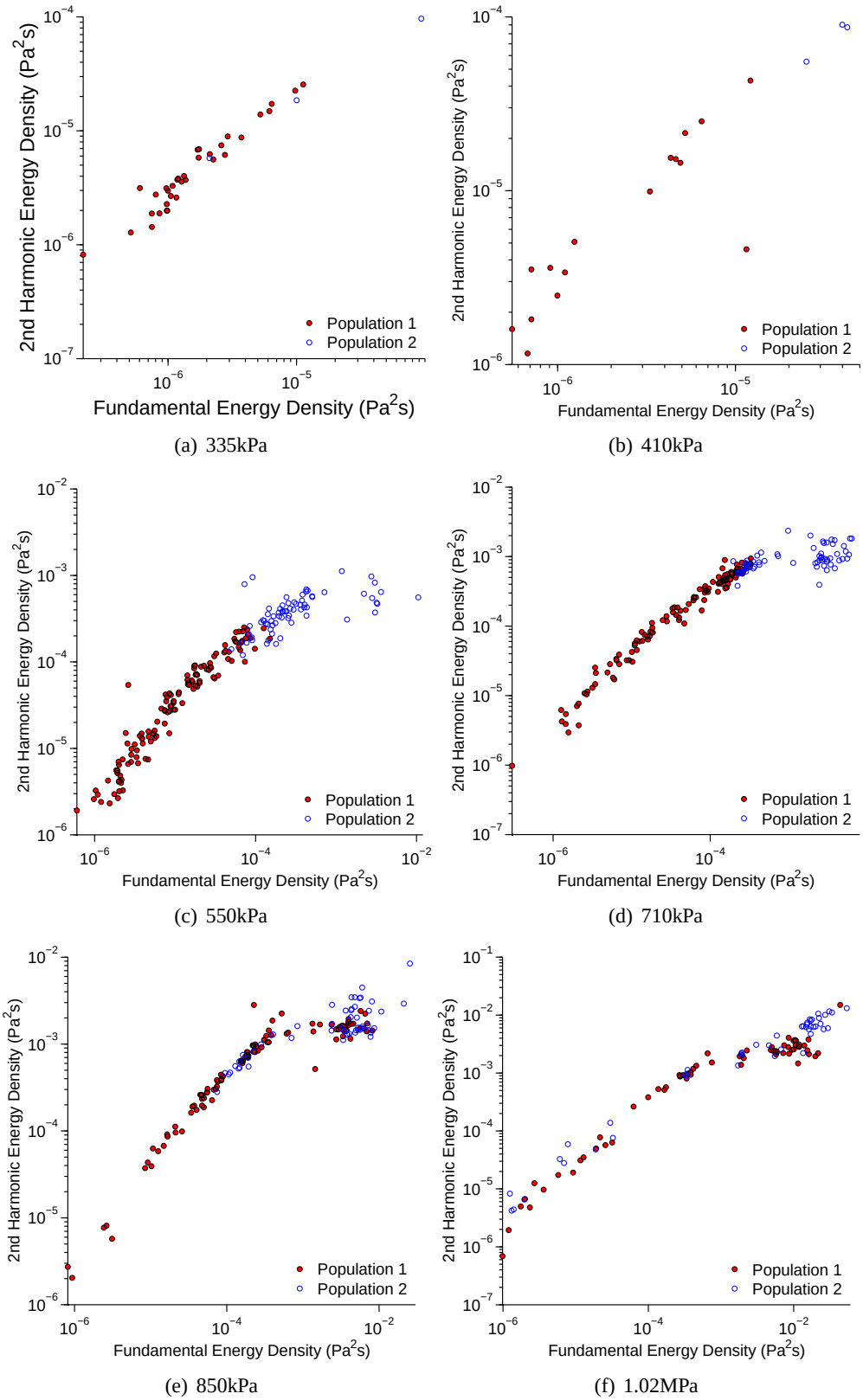

(a) 335kPa (b) 410kPa

(c) 550kPa (d) 710kPa

(e) 850kPa (f) 1.02MPa

Figure 7.8: *Variations in energy density with increasing acoustic pressure (1.6MHz). Bubbles have been categorized as those which the first signal in is below the noise level of the system (Population 1), and those which give an above noise response (Population 2).*

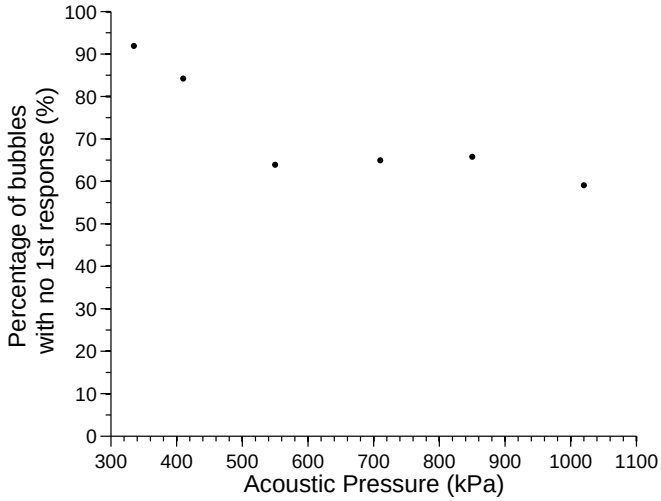

Figure 7.9: *Number of Definity signals which give no above noise signal to the first half amplitude pulse, as a percentage (%) of the total number of scatterers measured, from 335kPa to 1020kPa.*

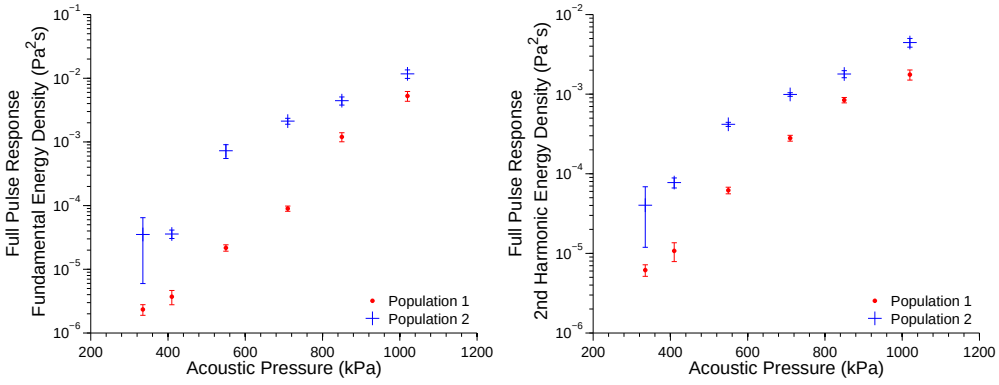

(a) Mean Fundamental Response (b) Mean 2nd Harmonic Response

Figure 7.10: *Mean 2nd pulse (full amplitude) responses from Definity signals to increasing acoustic pressure (1.6MHz, six cycle) pulse amplitude imaging pulses. Bubbles have been categorized as those for which the first signal in response to the first half amplitude pulse is below the noise level of the system (Population 1), and those which give an above noise signal (Population 2).*

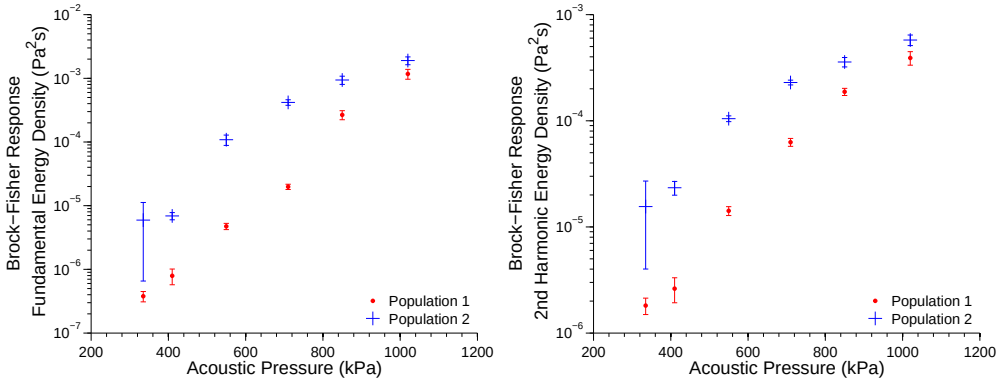

(a) Mean Fundamental Response (b) Mean 2nd Harmonic Response

Figure 7.11: *Mean PAM responses from Definity signals to increasing acoustic pressure (1.6MHz, six cycle) pulse amplitude imaging pulses. Bubbles have been categorized as those for which the first signal in response to the first half amplitude pulse is below the noise level of the system (Population 1), and those which give an above noise signal (Population 2).*

to implement into hardware or post-processing software, the validity of this approach will be investigated here to show that further improvements using more intelligent signal processing are possible.

Linear scatterer

Figure 7.12 shows the effect of division of the PAM result by the first half-amplitude response for a linear scatterer. For example, in the case of a linear scatterer such as a sub-millimeter copper sphere, or indeed response from human tissue, this first pulse response will always be finite and above noise, resulting in a reduction of the Brock-Fisher result upon division, as seen. For the stationary linear scatterer, the PAM method is very efficient in reducing nonlinear scatter, and no improvement is seen in the 2nd harmonic when this is divided by the first pulse response. An improvement of -3.3 dB is observed in the remaining fundamental scatter following division by first response (‘Alternative PAM’ response). However, for the moving scatterers, which are subject to decorrelation of signals between imaging pulses, the PAM method is less efficient at removing both linear and nonlinear scatter (as a ‘memory’ effect is introduced by the movement). An increased improvement (i.e. reduction of scatter) is seen by dividing the PAM result by the first response (‘Alternative PAM’ response), giving a mean 8.79dB reduction in fundamental and a mean 14.44dB reduction in 2nd harmonic. This shows that potential

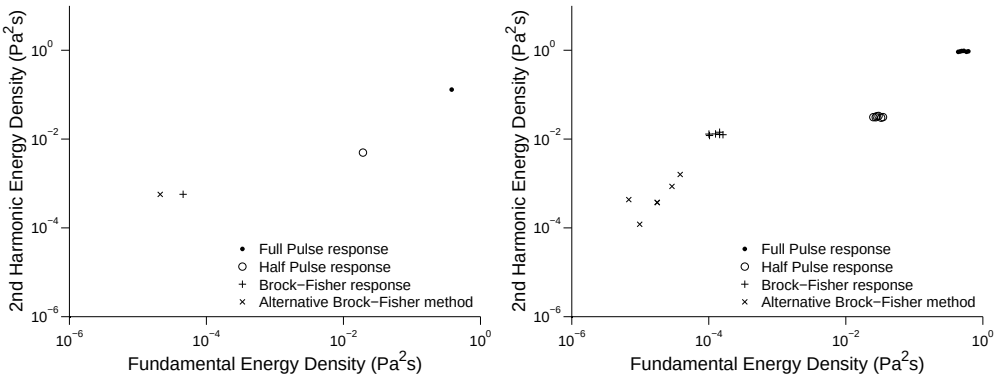

(a) Results from a stationary attached $43\mu m$ sphere.

(b) Results from 11 moving spheres subject to decorrelation (Sizes $35\mu m$ to $53\mu m$).

Figure 7.12: *Division of the PAM result by the finite first half-amplitude pulse response results in decreased fundamental scatter for a stationary linear scatterer (-42.53dB fundamental and -23.60dB 2nd harmonic reduction from full pulse response). For a moving linear scatterer, which is subject to decorrelation, the scatter is reduced further, in both the fundamental and the 2nd harmonic. Transmitted 1.6MHz, 550kPa PAM pulses.*

improvement in the contrast to tissue ratio is available when there is significant lack of first half-amplitude response from bubbles, which will increase the contrast signal in comparison to the linear scattered signal.

Definity

Figure 7.13 shows how this alternative processing effects the two populations previously identified. As compared to Figures 7.10 and 7.11, it can be seen that this Alternative PAM response brings the two populations of scatter closer in energy density. Above an incident acoustic pressure of 550kPa the responses from population one (no first pulse response) have greater mean scatter values than the population two scatter (those which do give a response to all pulses). Thus, by using the extra information which the PAM technique discards, the scatter can be increased when compared to a linear scatterer.

Figure 7.14 shows the mean responses from all bubbles measured (both population one and two), for increasing acoustic pressures. The increase in low energy scatter in response to lower incident acoustic pressures (335-410kPa) leads to the overall scatter being increased. In response to high pressures of 550kPa - 1.02MPa the two processing techniques produce similar

results (although the PAM is greater than the Alternative PAM). However, when compared to the reduction of $8.79dB$ and $14.44dB$ (fundamental and 2nd harmonic respectively) which the alternative processing gives to a moving linear scatterer, it can be seen that this gives a larger contrast-to-linear scatter ratio.

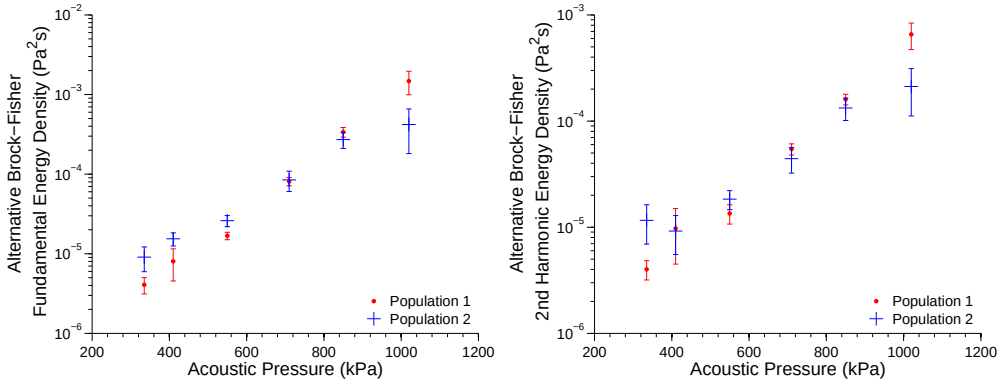

(a) Mean Fundamental Response

(b) Mean 2nd Harmonic Response

Figure 7.13: *Mean Alternative PAM responses from Definity signals to increasing acoustic pressure (1.6MHz, six cycle) pulse amplitude imaging pulses. Bubbles have been categorized as those for which the first signal in response to the first half amplitude pulse is below the noise level of the system (Population 1), and those which give an above noise signal (Population 2). The extra information from the lack of first pulse response has been used to increase the scatter from Population 1 bubbles, and above an incident acoustic pressure of 710kPa this population dominates the scatter from a sample of Definity bubbles, in both fundamental and 2nd harmonic components of scatter.*

7.6 Discussion

It is highly unlikely that bubble destruction takes place on the first pulse and creates no measurable signal, as is seen here. The existence of corresponding echoes in all the pulses of the sequence in the experimental data from linear (Figure 7.2) and nonlinear scatterers (Figure 7.4) confirm the robustness of the measurement system and the validity of the observed microbubble behavior. The lack of microbubble response to a medium or low transmitted pressure is not a new finding [71,80,97,101]. It has been shown that an increase in the number of Definity scatterers is observed as acoustic pressure increases [71], which is compatible with the results presented here.

There is no systematic study that deals with lipid-coated bubbles, which are generally seen as softer shelled and therefore able to provide oscillations at very low acoustic pressures. It

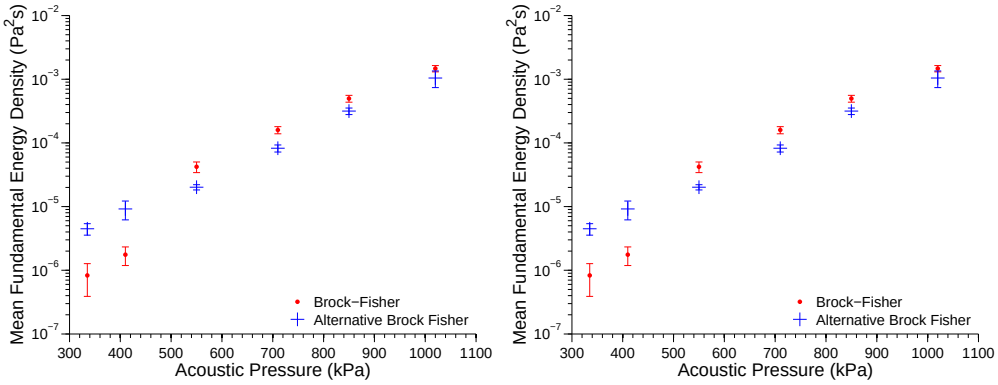

(a) Mean Fundamental Response (b) Mean 2nd Harmonic Response

Figure 7.14: *Mean PAM and Alternative PAM responses from Definity signals to increasing acoustic pressure (1.6MHz, six cycle) pulse amplitude imaging pulses. (a) shows the fundamental mean values and (b) shows the mean 2nd harmonic responses.*

seems, though, that there is a lower limit to acoustic pressure that will induce microbubble vibration for different microbubbles[80]. However, this threshold may fall within the limits of these optical techniques, and was measured at much lower acoustic pressures to the present experiments. This paper also reports cases of microbubbles that did not provide any oscillation even at higher acoustic pressures, more relevant to the results presented here. At the range of the acoustic pressures that the lack of signal was observed in the present experiments, Marmottant et al[50] observed compression-only oscillation that provided large oscillations (300kPa). It is possible that compression-only events provide very weak scatter, but it is generally difficult to compare the optical microscopy spatial thresholds with the acoustic threshold of the receiver in our experiments. It is therefore possible that a number of oscillating microbubbles do not provide a scatter strong enough to be captured by even the most sensitive of acoustic receivers. It is possible that in the second population of bubbles shown here, the larger acoustic pressures (i.e., the middle full pulse) that provide significant responses above measurement threshold may produce significant damage to the shell, and that the third half-pulse is recorded as a result of decreased resistance to oscillation.

As discussed, single bubble acoustic measurements are limited in detecting all microbubble echoes, because microbubble responses below noise are not accounted for. At higher concentrations in real imaging situations, where more than one microbubble contributes to a detectable echo, the effects from single bubbles below noise may become significant. In diagnostic imaging problems where small blood flows such as perfusion are investigated, it is expected that very

few microbubble are responsible for contrast enhancement; in such cases, single microbubble measurements are highly relevant, and the detection of as many bubbles as possible is important. Conversely, in situations where large microbubble concentrations are used, such as left ventricular opacification, the requirement for improvement of contrast-to-tissue ratio is not imperative. Although the pulse amplitude modulation sequence is effective in reducing the fundamental component from linear scatterers, it is not designed to exploit the behavior seen here, and thus microbubble information is lost. In a diagnostic imaging situation when no microbubble signal is received on the first pulse, the signal is purely from tissue and therefore could be exploited to provide a higher contrast-to-tissue ratio. It has been proposed that the presence of an acoustic pressure threshold in the microbubble response is suitable for an amplitude-modulated pulsing approach[80]. However, the different and relatively large half-amplitude response suggests that phase modulation combined with amplitude modulation may be more effective in this case, and further work is required here. The movement of the microbubble and the importance of the slight decorrelation mentioned previously may also have a role and need to be addressed in future experiments. At lower mechanical index (MI), where the lack of first pulse response is a small part of the total microbubble scatter, our data suggest that the current pulse sequence design is useful for imaging. Most pulse sequences are based on theoretical assumptions of the microbubble behavior that are then tested with experiments that use a microbubble suspension[64,163]. It is also assumed that microbubbles behave fairly uniformly, which was shown here to be incorrect. Single microbubble scatter measurements offer insight to the operation of pulse sequences and may be used to optimize them. In addition, it should be possible to address pulsesequence design using such measurements alone.

Figures 7.12-7.14 show how an improved processing technique can be employed to take advantage of the behaviour observed here. Although this is a simplistic approach, the potential for increased contrast to tissue ratio by using adaptive or more intelligent signal processing based on individual bubble responses can be seen.

7.7 Conclusion

The response to single Definity microbubbles to a simple pulse sequence has been investigated here for the first time. The results presented from single bubble scatter show that the linear response of microbubbles, as predicted from theory and upon which the pulse amplitude modulation is based, may not hold when bubbles are subject to varying amplitude pulses. Behaviours

have been observed which are not exploited by current pulsing schemes, and may offer increased contrast to tissue ratio to clinical diagnostic techniques when they are targeted by more sophisticated signal processing or transmit pulsing schemes. These effects have not previously been observed in large concentration measurements, which confirms the usefulness of single scattering events in advancing the current knowledge of the interaction between microbubbles and ultrasound.

7.8 Further work

The work presented in this Chapter will benefit from further work using an expanded set of incident acoustic parameters, especially applying pulses of lower amplitude. A comparison with other agents would also reveal any shell or gas dependent effects on the results shown here. A direct comparison of the results with optical measurements would offer greater understanding to the lack of first pulse response. Extension of the modified processing technique outlined here would require further testing, especially with higher concentrations of microbubbles and in combination with linear scatterers, to determine if any advantages in contrast to tissue ratio can be achieved.

Chapter 8
Conclusions and further work

8.1 Conclusions

As outlined in Chapter 1 of this thesis, present knowledge of the interaction of microbubbles with ultrasound is far from complete. The full potential of contrast agents in improving diagnostic and therapeutic techniques has not yet been achieved. This thesis a study of single microbubble scattering in order to gain understanding of the ultrasound microbubble interaction, as is relevant to diagnostic and therapeutic techniques. The study of the acoustic response of single microbubbles offers valuable insight, since it is directly related to their use in diagnostic imaging, and as shown in this thesis offers advantages over high concentration measurements which are limited by the presence of multiple subpopulations of scatterers within a high concentration sample. Quantitative information of microvasculature blood flow is highly desirable in the diagnosis and treatment of a number of diseases, and has the potential to add large benefits to both diagnosis and patient care, but this is not possible without quantitative in vitro measurements which define the range of responses from microbubbles, as is presented here. The experimental single bubble measurement system used in this work offers accurate calibration of both transmit and receive systems, providing absolute measurements of the pressure fields created by a point scatterer.

A novel type of analysis of acoustic single bubble signals has been introduced in Chapters 3-7, comparing the filtered components of fundamental and harmonic scatter of acoustic signals. This allows a direct comparison between experimental and theoretical data when combined with the statistical techniques introduced in Chapters 3 and 4. The logarithmic graphs of fundamental versus harmonic energy density shown in these chapters have not been used previously to analyze single bubble signals. They allow both qualitative and quantitative comparisons and conclusions to be made on the energy of scatter and nonlinearity, but also allow further features of microbubble scatter (such as compression to expansion ratio and envelope of response) to be probed in conjunction with these metrics.

These methods have shown that within a typical sample of contrast agent, a small population of

bubbles can be identified which show a significantly increased overall scatter. The scatter from these resonant bubbles contains increased fundamental components with respect to the components of higher harmonics. In approaching the radius of peak scatter, the signals are observed to show increasing fundamental scatter with time over the duration of the transmitted pulse, with a maximum signal observed with a symmetric envelope at resonance. Compression dominated behaviour, which has been previously observed in experimental studies, is not predicted by the model used here, and this will be investigated further in future studies. Indicators which allow the classification of acoustic bubble signals as resonant scatter have been identified and observed experimentally, including:

- Increased energy of scatter.
- Increased fundamental to harmonic ratio.
- Increasing amplitude of response.

This has allowed the identification of resonant scatter in acoustic single bubble experimental data for the first time. The techniques presented here provide significant insight into resonant populations of bubble scatter, providing the basis for improved imaging techniques based upon more intelligent pulse sequence design and/or improved signal processing.

In contrast to these Definity results, no conclusive evidence for resonance behaviour in biSphere has been detected. The results presented agree well with previous studies, which define the mechanism of scatter from hard shelled albumin agents to result from shell disruption and gas release. Partial echoes, shorter than the incident pulse duration, have been observed for low frequency pulses of sufficient amplitude, suggesting partial release of gas from bubbles. The lack of this echo at lower amplitudes suggest these arise from a population which otherwise remain intact and produce no signal, unless a sufficient acoustic pressure is incident upon them. This agrees with previous studies, which show the disruption of an albumin shell is frequency dependent, and that the number of single scattering events produced from a sample of contrast agents has an acoustic pressure dependence.

Results from the single bubble system have been used, together with a variety of statistical analysis methods, to produce understanding of the diffusion and destruction effects which microbubbles from samples of biSphere and Definity undergo, in response to increasing acoustic pressures and frequencies. Definity has been shown to exhibit more resilience to the destruc-

tive properties of the imaging pulse than biSphere, and this has been attributed to the increased stability of the lipid shell, perhaps due to the flexible nature of the phospholipid structure. The two populations of bubbles previously identified (off-resonance and resonance) show different characteristics of survivability. biSphere scatter has been shown to be more easily disrupted by the imaging pulses, due to the nature of the Albumin shell and the solubility of the encapsulated gas. Bubbles signals which do survive subsequent imaging pulses do not exhibit the characteristics of acoustically driven diffusion, suggesting that the Albumin shells are not affected in the same way as the lipid shells of Definity. These results warrant further work with combined optical and acoustic measurements to investigate effect of imaging pulses on the structure of the Albumin shells.

It is the hope of the author that the results and analysis set out in this thesis will be helpful for ongoing work investigating the response of contrast agents to ultrasound. The author believes that useful progress toward quantitative comparison of acoustic measurements and theoretical modeling has been made. The experimental system used here has drawbacks, and while an improved system may allow expansion on the range of parameters investigated, the analysis techniques introduced here will remain useful in any such future work.

The knowledge of the contrast-ultrasound interaction presented here can provide the basis for improved signal processing tools for contrast enhanced imaging, with potential benefits to both diagnostic techniques and microbubble manufacture.

8.2 Further work

The results from strain softening Mooney Rivlin shell model have been presented here. Further work is needed to compare the results of this model to other models available in the literature, including the similar models of Hoff[128] and Skalak (a strain hardening model)[85], and the Marmottant model for large amplitude oscillations of encapsulated bubbles which accounts for buckling and rupture of the soft lipid shell. Initial results show that the Mooney Rivlin results agree reasonably well with these alternative models. All models show the same characteristics of resonance outlined above, but predict varying resonance peaks, and therefore differing responses from a distribution of bubbles. Further work is needed to investigate the response from varying imaging frequencies and acoustic pressures of these alternative models, in order to define the best model for Definity. A comparison of the results will allow further analysis of

the shell parameters.

The experimental results shown here indicate good agreement with the theoretical predications. In order to improve the results from the Mooney Rivlin model, and fine tune the parameters used to model the soft phospholipid shell of Definity, a more rigorous statistical analysis is needed. A one-to-one map associating each experimental signal with a one specific simulated signal (with optimized parameters) would allow a complete analysis of parameter variance, and determine if optimal parameters exist for an ensemble of microbubbles. This approach has the potential to further improve the understanding of the shell's effect on soft shelled microbubbles. Further experimental results will also improve understanding of the Definity response to ultrasound imaging pulses. In particular, the effect of differing incident pulse lengths on the response from the resonance populations will be useful.

The experimental results with the albumin based contrast agent biSphere present various behaviours, but in order to achieve a fuller understanding of the behaviour of hard shelled albumin contrast agents a theoretical description of the bubble responses is needed for comparison. Further experimental results also offer potential for improving the understanding of the behaviours observed here. In particular, the effect of differing incident pulse lengths will provide extra information on the differing durations of response observed. Optical observations of the different responses will also give confirmation of bubble shell integrity, and information on the destruction and remnants of shells.

Measurements of bubble radii, using the optical techniques described in Chapters 3 and 4, will add information about the disruption and subsequent dissolution of microbubbles due to the imaging pulses. It has been shown that the size distribution of albumin bubbles changes significantly after an insonation above the destruction threshold is incident upon the sample of bubbles, and that the resulting distribution is dependent on the insonant frequency[65]. This information will add significant confidence to the above analysis.

The results presented in Chapter 5 provide an insight into the evolution of contrast agents when in the presence of a range of clinical imaging parameters, but further experimental work will provide an increased understanding of these effects. That lipid bubbles at resonance provide increased resilience over those bubbles off-resonance is not fully understood, and optical experiments recreating the conditions used here will provide further insight into the evolution of the respective populations. The results presented are in response to pulse repetition frequencies

of 1kHz, giving 1ms separation between imaging pulses. Further work investigating the effect of pulse interval variation on the evolution of bubbles in the respective populations identified in Definity may elucidate the impact of diffusion on bubble signal evolution. Incident pulses with higher PRFs may provide information on how much effect the solubility of the gas has on the evolution of the signal as compared to the effect of the shell. This can also be investigated using contrast agents that are constructed with the same type of shell whilst containing different encapsulated gases.

A theoretical model for diffusion would improve the understanding of the experimental results presented here. A one-to-one map of experimental bubble signals to theoretical signals, as suggested above, incorporating a change in bubble diameter between pulses to reflect the change in energy of signal, could provide better comparison with optical experiments which show examples of diffusion in the literature.

Appendix
List of publications

Journal publications

1. **D.H. Thomas**, P. Looney, R. Steel, N. Pelekasis, W.N. McDicken, T. Anderson, V. Sboros. Acoustic detection of a microbubble resonance. *Applied Physics Letters*, 94(24) 2439023, 2009.

2. **D.H. Thomas**, M.B. Butler, T. Anderson, R. Steel, S.D. Pye, M. Poland, T. Brock-Fisher, W.N. McDicken, V. Sboros. Microbubble Response Using Pulse Sequences: Initial Results. *Ultrasound in Medicine and Biology*, 35(1):112-119, 2008.

3. M.B. Butler, **D.H. Thomas**, S.D. Pye, C.M. Moran, W.N. McDicken, V. Sboros. The Acoustic Response from individual attached and unattached rigid shelled microbubbles. *Applied Physics Letters*, 93(22) 2239063, 2008.

Conference publications

1. **D.H. Thomas**, M. Emmer, H.J. Vos, V. Sboros, N. de Jong. Optical observations of microbubble oscillations in small tubes. In *Proceedings of IEEE International Ultrasonics Symposium*, Rome, poster presentation (student paper prize winner), September 2009.

2. **D.H. Thomas**, P. Looney, T. Anderson, N. Pelekasis, W.N. McDicken, V. Sboros. Acoustic detection of microbubble resonance. In *Proceedings of 14th European Symposium on Ultrasound Contrast Imaging*, Rotterdam, poster presentation, January 2009.

3. MB Butler, **D.H. Thomas**, S.D. Pye, C.M. Moran, W.N. McDicken, V. Sboros. Comparison of the acoustic response of attached and unattached BiSphere microbubbles. In *Proceedings of IEEE Ultrasonics Symposium*, Beijing, poster presentation, November 2008.

4. **D.H. Thomas**, M.B. Butler, T. Anderson, R. Steel, S.D. Pye, M. Poland, T. Brock-Fisher, W.N. McDicken, V. Sboros. Single Microbubble Acoustics And Signal Processing: Ini-

tial Experience With Amplitude Modulated Pulse Sequences. In *Proceedings of IEEE International Ultrasonics Symposium*, New York, poster presentation, November 2007.

5. **D.H. Thomas**, M.B. Butler, T. Anderson, R. Steel, S.D. Pye, M. Poland, T. Brock-Fisher, W.N. McDicken, V. Sboros. Single microbubble response using pulse sequences: initial results. In *Proceedings of International Congress on Ultrasonics*, Vienna, oral presentation, March 2007.

6. **D.H. Thomas**, M.B. Butler, T. Anderson, W.N. McDicken, V. Sboros. Initial results of an investigation into single bubble acoustics using amplitude modulation. In *Proceedings of 12th European Symposium on Ultrasound Contrast Imaging*, Rotterdam, oral presentation, January 2007.

Bibliography

[1] Flemming Forsberg and Joel S. Raichlen. *Ultrasound Contrast Agents*. Informa Health Care, 2001.

[2] V. Sboros. Response of contrast agents to ultrasound. *Advanced Drug Delivery Reviews*, 60(10):1117–1136, 2008.

[3] R. Gramiak and P. M. Shah. Echocardiogram of the aortic root. *Invest Radiol*, 3:356–366, 1968.

[4] J.E. Chomas, P. Dayton, J. Allen, K. Morgan, and K.W. Ferrara. Mechanisms of contrast agent destruction. *Ultrasonics, Ferroelectrics and Frequency Control, IEEE Transactions on*, 48(1):232–248, 2001.

[5] O. I.I. Soliman, M. L. Geleijnse, F. J. Meijboom, A. Nemes, O. Kamp, P. Nihoyannopoulos, N. Masani, S. B. Feinstein, and F. J. Ten Cate. The use of contrast echocardiography for the detection of cardiac shunts. *Eur J Echocardiogr*, 8(3):2–12, 2007.

[6] S. B. Feinstein, J. Cheirif, F. J. Ten Cate, P. R. Silverman, P. A. Heidenreich, C. Dick, R. M. Desir, W. F. Armstrong, M. A. Quinones, and P. M. Shah. Safety and efficacy of a new transpulmonary ultrasound contrast agent: initial multicenter clinical results. *Journal of the American College of Cardiology*, 16(2):316–324, 1990.

[7] H. J. Bleeker, K. K. Shung, and J. L. Barnhart. Ultrasonic characterization of albunex, a new contrast agent. *The Journal of the Acoustical Society of America*, 87:1792, 1990.

[8] L. Hoff. *Acoustic Characterization of Contrast Agents for Medical Ultrasound Imaging*. Kluwer Academic Publishers, 2001.

[9] Robert S. Hillman, Kenneth A. Ault, and Henry M. Rinder. *Hematology in clinical practice*. McGraw-Hill Professional, 2005.

[10] Emilio Quaia. Microbubble ultrasound contrast agents: an update. *European Radiology*, 17(8):1995–2008, 2007.

[11] B. A Kaufmann, K. Wei, and J. R Lindner. Contrast echocardiography. *Current Problems in Cardiology*, 32(2):51–96, 2007.

[12] K Iwakura, H Ito, S Takiuchi, Y Taniyama, Y Nakatsuchi, S Negoro, Y Higashino, A Okamura, T Masuyama, M Hori, K Fujii, and T Minamino. Alternation in the coronary blood flow velocity pattern in patients with no reflow and reperfused acute myocardial infarction. *Circulation*, 94(6):1269–1275, 1996.

[13] H Ito, A Maruyama, K Iwakura, S Takiuchi, T Masuyama, M Hori, Y Higashino, K Fujii, and T Minamino. Clinical implications of the 'no reflow' phenomenon. a predictor of complications and left ventricular remodeling in reperfused anterior wall myocardial infarction. *Circulation*, 93(2):223–228, 1996.

[14] C. Sonne, F. Xie, J. Lof, J. Oberdorfer, P. Phillips, E. Carr Everbach, and T. R. Porter. Differences in definity and optison microbubble destruction rates at a similar mechanical index with different real-time perfusion systems. *Journal of the American Society of Echocardiography*, 16(11):1178–1185, 2003.

[15] O. Kamp, W. Lepper, J. L Vanoverschelde, B. C. Aeschbacher, D. Rovai, P. Assayag, P. Voci, Y. Kloster, A. Distante, and C. A. Visser. Serial evaluation of perfusion defects in patients with a first acute myocardial infarction referred for primary PTCA using intravenous myocardial contrast echocardiography. *European heart journal*, 22(16):1485, 2001.

[16] S. Shimoni, N. G Frangogiannis, C. J Aggeli, K. Shan, M. A Quinones, R. Espada, G. V Letsou, G. M Lawrie, W. L Winters, M. J Reardon, et al. Microvascular structural correlates of myocardial contrast echocardiography in patients with coronary artery disease and left ventricular dysfunction: implications for the assessment of myocardial hibernation. *Circulation*, 106(8):950, 2002.

[17] J. R Lindner, F. S Villanueva, J. M Dent, K. Wei, J. Sklenar, and S. Kaul. Assessment of resting perfusion with myocardial contrast echocardiography: Theoretical and practical considerations. *American Heart Journal*, 139(2):231–240, 2000.

[18] A. Elhendy, E. L O'Leary, F. Xie, A. C McGrain, J. R Anderson, and T. R Porter. Comparative accuracy of real-time myocardial contrast perfusion imaging and wall motion analysis during dobutamine stress echocardiography for the diagnosis of coronary artery disease. *Journal of the American College of Cardiology*, 44(11):2185–2191, 2004.

[19] A. Micari, T. A. Belcik, E. A. Balcells, E. Powers, K. Wei MD, S. Kaul, and J. R. Lindner. Improvement in microvascular reflow and reduction of infarct size with adenosine in

patients undergoing primary coronary stenting. *The American Journal of Cardiology*, 96(10):1410–1415, 2005.

[20] J. M.A Swinburn, A. Lahiri, and R. Senior. Intravenous myocardial contrast echocardiography predicts recovery of dysynergic myocardium early after acute myocardial infarction. *Journal of the American College of Cardiology*, 38(1):19–25, 2001.

[21] David Owen Cosgrove. A revolution in liver ultrasound. *European Journal of Gastroenterology & Hepatology*, 19(1):1–2, 2007.

[22] S. R. Wilson and P. N. Burns. An algorithm for the diagnosis of focal liver masses using microbubble Contrast-Enhanced Pulse-Inversion sonography. *Am. J. Roentgenol.*, 186(5):1401–1412, 2006.

[23] T. Albrecht, M. J. K. Blomley, P. N Burns, S. Wilson, C. J. Harvey, E. Leen, M. Claudon, F. Calliada, J. Correas, M. LaFortune, R. Campani, C. W. Hoffmann, D. O. Cosgrove, and F. LeFevre. Improved detection of hepatic metastases with pulse-inversion US during the liver-specific phase of SHU 508A: multicenter study. *Radiology*, 227(2):361–370, 2003.

[24] S R Wilson, P N Burns, D Muradali, J A Wilson, and X Lai. Harmonic hepatic US with microbubble contrast agent: initial experience showing improved characterization of hemangioma, hepatocellular carcinoma, and metastasis. *Radiology*, 215(1):153–161, 2000.

[25] Min-Hua Chen, Wei Wu, Wei Yang, Ying Dai, Wen Gao, Shan-Shan Yin, and Kun Yan. The use of Contrast-Enhanced ultrasonography in the selection of patients with hepatocellular carcinoma for radio frequency ablation therapy. *J Ultrasound Med*, 26(8):1055–1063, 2007.

[26] R Vilana, L Bianchi, M Varela, C Nicolau, M Snchez, C Ayuso, M Garca, M Sala, J M Llovet, J Bruix, and C Bru. Is microbubble-enhanced ultrasonography sufficient for assessment of response to percutaneous treatment in patients with early hepatocellular carcinoma? *European Radiology*, 16(11):2454–2462, 2006.

[27] E. Quaia, M. Bertolotto, L. Calderan, E. Mosconi, and R. Pozzi Mucelli. Original Investigations-US characterization of focal hepatic lesions with intermittent High-Acoustic-Power mode and contrast material. *Academic Radiology*, 10(7):739–750, 2003.

[28] O. Catalano, F. Sandomenico, M. Mattace Raso, and A. Siani. Low mechanical index Contrast-Enhanced sonographic findings of pyogenic hepatic abscesses. *Am. J. Roentgenol.*, 182(2):447–450, February 2004.

[29] C. Nicolau, V. Catala, R. Vilana, R. Gilabert, L. Bianchi, M. Sole, M. Pages, and C. Br. Evaluation of hepatocellular carcinoma using SonoVue, a second generation ultrasound contrast agent: correlation with cellular differentiation. *European radiology*, 14(6):1092–1099, 2004.

[30] Christopher Harvey, Adrian Lim, Madeleine Lynch, Martin Blomley, and David Cosgrove. Applications of ultrasound microbubbles in the spleen. In *Contrast Media in Ultrasonography*, pages 205–219. 2005.

[31] Jean-Michel Correas, Michel Claudon, Franois Tranquart, , and Olivier Hlnon. The kidney: imaging with microbubble contrast agents. *Ultrasound Quarterly*, 22(1):53–66, 2006.

[32] T. Bragadeesh, I. Sari, M. Pascotto, A. Micari, S. Kaul, and J. R Lindner. Detection of peripheral vascular stenosis by assessing skeletal muscle flow reserve. *Journal of the American College of Cardiology*, 45(5):780–785, 2005.

[33] S. B. Feinstein. The powerful microbubble: from bench to bedside, from intravascular indicator to therapeutic delivery system, and beyond. *Am J Physiol Heart Circ Physiol*, 287(2):450–457, 2004.

[34] P. M. C. Morse and K. U. Ingard. *Theoretical Acoustics*. Princeton University Press, 1986.

[35] L. Rayleigh. *The Theory of Sound, Vol. II*. New York: McMillan and Co., Ltd, 1896.

[36] J. Ophir and K. J. Parker. Contrast agents in diagnostic ultrasound. *Ultrasound in Medicine & Biology*, 15(4):319–333, 1989.

[37] N. de Jong, P. J. Frinking, and A. Bouakaz. Basic acoustic properties of microbubbles. *Echocardiography*, 19(3):229–240, 2002.

[38] M. Minnaert. On musical air bubbles and the sounds of running water. *Phil. Mag*, 16(7):235–248, 1933.

[39] A. Prosperetti. Thermal effects and damping mechanisms in the forced radial oscillations of gas bubbles in liquids. *The Journal of the Acoustical Society of America*, 61:17, 1977.

[40] N. de Jong, L. Hoff, T. Skotland, and N. Bom. Absorption and scatter of encapsulated gas filled microspheres: theoretical considerations and some measurements. *Ultrasonics*, 30(2):95–103, 1992.

[41] W. Lauterborn. Numerical investigation of nonlinear oscillations of gas bubbles in liquids. *The Journal of the Acoustical Society of America*, 59(2):283–293, 1976.

[42] L. Rayleigh. On the pressure developed in a liquid on the collapse of a spherical bubble. *Philos. Mag*, 34:94, 1917.

[43] M. S. Plesset. The dynamics of cavitation bubbles. *J. Appl. Mech*, 16:277, 1949.

[44] L. Trilling. The collapse and rebound of a gas bubble. *Journal of Applied Physics*, 23:14–17, 1952.

[45] J. B. Keller and M. Miksis. Bubble oscillations of large amplitude. *The Journal of the Acoustical Society of America*, 68:628, 1980.

[46] J. B. Keller and I. I. Kolodner. Damping of underwater explosion bubble oscillations. *Journal of Applied Physics*, 27:1152, 2004.

[47] A. Prosperetti and A. Lezzi. Bubble dynamics in a compressible liquid. Part 1. First-order theory. *Journal of Fluid Mechanics Digital Archive*, 168:457–478, 2006.

[48] F. R. Gilmore. The collapse and growth of a spherical bubble in a viscous compressible liquid. *Calif. Inst. of Tech. Hydrodynamics Lab. Rep*, 1952.

[49] H. G. Flynn. Cavitation dynamics. I. A mathematical formulation. *The Journal of the Acoustical Society of America*, 57:1379, 1975.

[50] P. Marmottant, S. van der Meer, M. Emmer, M. Versluis, N. de Jong, S. Hilgenfeldt, and D. Lohse. A model for large amplitude oscillations of coated bubbles accounting for buckling and rupture. *The Journal of the Acoustical Society of America*, 118:3499, 2005.

[51] K. Vokurka. On rayleigh's model of a freely oscillating bubble. I. Basic relations. *Czechoslovak Journal of Physics*, 35(1):28–40, 1985.

[52] K. Wei, A. R. Jayaweera, S. Firoozan, A. Linka, D. M. Skyba, and S. Kaul. Quantification of myocardial blood flow with Ultrasound-Induced destruction of microbubbles administered as a constant venous infusion. *Circulation*, 97(5):473–483, 1998.

[53] M. Postema, A. van Wamel, C. T. Lance, and N. de Jong. Ultrasound-induced encapsulated microbubble phenomena. *Ultrasound in Medicine & Biology*, 30(6):827–840, 2004.

[54] P.J. Phillips. Contrast pulse sequences (CPS): imaging nonlinear microbubbles. In *Ultrasonics Symposium, 2001 IEEE*, volume 2, pages 1739–1745, 2001.

[55] C. Leavens, R. Williams, F.S. Foster, P.N. Burns, and M.D. Sherar. Golay pulse encoding for microbubble contrast imaging in ultrasound. *Ultrasonics, Ferroelectrics and Frequency Control, IEEE Transactions on*, 54(10):2082–2090, 2007.

[56] K. Chetty, J. V. Hajnal, and R. J. Eckersley. Investigating the nonlinear microbubble response to chirp encoded, multipulse sequences. *Ultrasound in Medicine & Biology*, 32(12):1887–1895, 2006.

[57] A. Bouakaz, S. van der Meer, M. Versluis, and N. de Jong. Chirp reversal ultrasound contrast imaging. In *Ultrasonics Symposium, 2006 IEEE*, pages 224–227, 2006.

[58] V. Sboros, K. V. Ramnarine, C. M. Moran, S. D. Pye, and W. N. McDicken. Understanding the limitations of ultrasonic backscatter measurements from microbubble populations. *Physics in Medicine & Biology*, 47(23):4287–4299, 2002.

[59] P. A. Dayton, J. E. Chomas, A. F. H. Lum, J. S. Allen, J. R. Lindner, S. I. Simon, and K. W. Ferrara. Optical and acoustical dynamics of microbubble contrast agents inside neutrophils. *Biophysical Journal*, 80(3):1547–1556, 2001.

[60] V Sboros, E Glynos, S D Pye, C M Moran, M Butler, J A Ross, W N McDicken, and V Koutsos. Nanomechanical probing of microbubbles using the atomic force microscope. *Ultrasonics*, 46(4):349–54, 2007. PMID: 17720211.

[61] N. de Jong and L. Hoff. Ultrasound scattering properties of albunex microspheres. *Ultrasonics*, 31(3):175–181, 1993.

[62] P. D. Krishna and V. L. Newhouse. Second harmonic characteristics of the ultrasound contrast agents Albunex and FSO69. *Ultrasound in Medicine & Biology*, 23(3):453–9, 1997.

[63] W. Zheng and V. L. Newhouse. Onset delay of acoustic second harmonic backscatter from bubbles or microspheres. *Ultrasound in Medicine & Biology*, 24(4):513–22, 1998.

[64] D.H. Simpson, Chien Ting Chin, and P.N. Burns. Pulse inversion Doppler: a new method for detecting nonlinear echoes from microbubble contrast agents. *Ultrasonics, Ferroelectrics and Frequency Control, IEEE Transactions on*, 46(2):372–382, 1999.

[65] P. J. Frinking, N. de Jong, and E. I. Cespedes. Scattering properties of encapsulated gas bubbles at high ultrasound pressures. *The Journal of the Acoustical Society of America*, 105(3):1989–1996, 1999.

[66] J.M. Gorce, M. Arditi, and M. Schneider. Influence of bubble size distribution on the echogenicity of ultrasound contrast agents: A study of SonoVue (TM). *Investigative Radiology*, 35(11):661, 2000.

[67] S. H. Bloch, R. E. Short, K. W. Ferrara, and E. R. Wisner. The effect of size on the acoustic response of polymer-shelled contrast agents. *Ultrasound in Medicine & Biology*, 31(3):439–444, 2005.

[68] V. Sboros, S.D. Pye, T. Anderson, C.M. Moran, M. Averkiou, C.A. MacDonald, and J. Gomatam. The measurement of backscatter from individual contrast agent microbubbles. In *Ultrasonics Symposium, 2002 IEEE*, volume 2, pages 1945–1947, 2002.

[69] A. L. Klibanov, P. T. Rasche, M. S. Hughes, J. K. Wojdyla, K. P. Galen, J. H. Wible Jr, and G. H. Brandenburger. Detection of individual microbubbles of an ultrasound contrast agent: fundamental and pulse inversion imaging. *Academic radiology*, 9:S279, 2002.

[70] A. L. Klibanov, P. T. Rasche, M. S. Hughes, J. K. Wojdyla, K. P. Galen, J. H. Wible Jr, and G. H. Brandenburger. Detection of individual microbubbles of ultrasound contrast agents: Imaging of Free-Floating and targeted bubbles. *Investigative Radiology*, 39(3):187, 2004.

[71] V. Sboros, C. M. Moran, S. D. Pye, and W. N. McDicken. The behaviour of individual contrast agent microbubbles. *Ultrasound in Medicine & Biology*, 29(5):687–94, 2003.

[72] V. Sboros, S. D. Pye, T. A. Anderson, C. M. Moran, and W. N. McDicken. Acoustic rayleigh scattering at individual micron-sized bubbles. *Applied Physics Letters*, 90(12):123902–3, 2007.

[73] M.B. Butler, V. Sboros, C.M. Moran, J. Ross, V. Koutsos, W.N. McDicken, and S. Pye. P1F-6 development of a novel experimental Set-Up to allow investigation of the ultrasonic backscatter from microbubble contrast agents attached to surfaces. In *Ultrasonics Symposium, 2006 IEEE*, pages 1362–1364, 2006.

[74] A. Y. Ammi, R. O. Cleveland, J. Mamou, G. I. Wang, S. L. Bridal, and W. D. OBrien Jr. Ultrasonic contrast agent shell rupture detected by inertial cavitation and rebound signals. *Ultrasonics, Ferroelectrics and Frequency Control, IEEE Transactions on*, 53(1):126, 2006.

[75] V. Sboros, S. D. Pye, C. A. MacDonald, J. Gomatam, C. M. Moran, and W. N. McDicken. Absolute measurement of ultrasonic backscatter from single microbubbles. *Ultrasound in Medicine & Biology*, 31(8):1063–1072, 2005.

[76] E. Biagi, L. Breschi, and L. Masotti. Transient subharmonic and ultraharmonic acoustic emission during dissolution of free gas bubbles. *Ultrasonics, Ferroelectrics and Frequency Control, IEEE Transactions on*, 52(6):1050–1056, 2005.

[77] S.H. Bloch, P.A. Dayton, and K.W. Ferrara. Targeted imaging using ultrasound contrast agents. *Engineering in Medicine and Biology Magazine, IEEE*, 23(5):18–29, 2004.

[78] J. Guan and T. J. Matula. Understanding the pulse-to-pulse evolution of microbubble clouds using light scattering. In *Ultrasonics Symposium, 2004 IEEE*, volume 1, 2004.

[79] WT Shi, F. Forsberg, A. Tornes, J. stensen, and BB Goldberg. Destruction of contrast microbubbles and the association with inertial cavitation. *Ultrasound in Medicine & Biology*, 26(6):1009–1019, 2000.

[80] M. Emmer, A. van Wamel, D. E. Goertz, and N. de Jong. The onset of microbubble vibration. *Ultrasound in Medicine & Biology*, 33(6):941–949, 2007.

[81] S. M. van der Meer, B. Dollet, M. M. Voormolen, C. T. Chin, A. Bouakaz, N. de Jong, M. Versluis, and D. Lohse. Microbubble spectroscopy of ultrasound contrast agents. *The Journal of the Acoustical Society of America*, 121:648, 2007.

[82] C. T. Chin, C. Lance, J. Borsboom, F. Mastik, M. E. Frijlink, N. de Jong, M. Versluis, and D. Lohse. Brandaris 128: A digital 25 million frames per second camera with 128 highly sensitive frames. *Review of Scientific Instruments*, 74:5026, 2003.

[83] N. de Jong, P. J. Frinking, A. Bouakaz, M. Goorden, T. Schourmans, X. U. Jingping, and F. Mastik. Optical imaging of contrast agent microbubbles in an ultrasound field with a 100-MHz camera. *Ultrasound in Medicine & Biology*, 26(3):487–492, 2000.

[84] K. E. Morgan, J. S. Allen, P. A. Dayton, J. E. Chomas, A. L. Klibaov, and K. W. Ferrara. Experimental and theoretical evaluation of microbubble behavior: effect of transmitted phase and bubble size. *Ultrasonics, Ferroelectrics and Frequency Control, IEEE Transactions on*, 47(6):1494–1509, 2000.

[85] K. Tsiglifis and N. A. Pelekasis. Nonlinear radial oscillations of encapsulated microbubbles subject to ultrasound: the effect of membrane constitutive law. *The Journal of the Acoustical Society of America*, 123(6), 2008.

[86] M. X. Tang, R. J. Eckersley, and J. A. Noble. Pressure-dependent attenuation with microbubbles at low mechanical index. *Ultrasound in Medicine & Biology*, 31(3):377–384, 2005.

[87] J. E. Chomas, P. Dayton, D. May, and K. Ferrara. Threshold of fragmentation for ultrasonic contrast agents. *Journal of Biomedical Optics*, 6:141, 2001.

[88] S. H. Bloch, M. Wan, P. A. Dayton, and K. W. Ferrara. Optical observation of lipid- and polymer-shelled ultrasound microbubble contrast agents. *Applied Physics Letters*, 84:631, 2004.

[89] J. E. Chomas, P. A. Dayton, D. May, J. Allen, A. Klibanov, and K. Ferrara. Optical observation of contrast agent destruction. *Applied Physics Letters*, 77:1056, 2000.

[90] D. J. May, J. S. Allen, and K. W. Ferrara. Dynamics and fragmentation of thick-shelled microbubbles. *Ultrasonics, Ferroelectrics and Frequency Control, IEEE Transactions on*, 49(10):1400–1410, 2002.

[91] Y. Sun, D. E. Kruse, P. A. Dayton, and K. W. Ferrara. High-frequency dynamics of ultrasound contrast agents. *Ultrasonics, Ferroelectrics and Frequency Control, IEEE Transactions on*, 52(11):1981–1991, 2005.

[92] P. A. Dayton, K. E. Morgan, A. L. Klibanov, G. H. Brandenburger, and K. W. Ferrara. Optical and acoustical observations of the effects of ultrasound on contrast agents. *Ultrasonics, Ferroelectrics and Frequency Control, IEEE Transactions on*, 46(1):220–232, 1999.

[93] J. Chomas, P. Dayton, D. May, and K. Ferrara. Nondestructive subharmonic imaging. *Ultrasonics, Ferroelectrics and Frequency Control, IEEE Transactions on*, 49(7):883–892, 2002.

[94] P.J. Frinking and N. de Jong. Acoustic modeling of shell-encapsulated gas bubbles. *Ultrasound in Medicine & Biology*, 24(4):523–533, 1998.

[95] E. Stride and N. Saffari. On the destruction of microbubble ultrasound contrast agents. *Ultrasound in Medicine & Biology*, 29(4):563–73, 2003.

[96] M.A. Borden, D.E. Kruse, C.F. Caskey, Shukui Zhao, P.A. Dayton, and K.W. Ferrara. Influence of lipid shell physicochemical properties on ultrasound-induced microbubble destruction. *Ultrasonics, Ferroelectrics and Frequency Control, IEEE Transactions on*, 52(11):1992–2002, 2005.

[97] M. Postema, A. Bouakaz, M. Versluis, and N. de Jong. Ultrasound-induced gas release from contrast agent microbubbles. *Ultrasonics, Ferroelectrics and Frequency Control, IEEE Transactions on*, 52(6):1035–1041, 2005.

[98] A. Bouakaz, M. Versluis, and N. de Jong. High-speed optical observations of contrast agent destruction. *Ultrasound in Medicine & Biology*, 31(3):391–399, 2005.

[99] V. Sboros, E. Glynos, M. Butler, C.M. Moran, J. Ross, S.D. Pye, W.N. McDicken, and V. Koutsos. Microbubble nano-interrogation using the atomic force microscope. In *Ultrasonics Symposium, 2005 IEEE*, volume 2, pages 985–987, 2005.

[100] A. Kabalnov, J. Bradley, S. Flaim, D. Klein, T. Pelura, B. Peters, S. Otto, J. Reynolds, E. Schutt, and J. Weers. Dissolution of multicomponent microbubbles in the bloodstream: 2. Experiment. *Ultrasound in Medicine & Biology*, 24(5):751–60, 1998.

[101] V. Sboros, C. M. Moran, S. D. Pye, and W. N. McDicken. Contrast agent stability: a continuous B-mode imaging approach. *Ultrasound in Medicine & Biology*, 27(10):1367–77, 2001.

[102] J. Guan and T. J. Matula. Using light scattering to measure the response of individual ultrasound contrast microbubbles subjected to pulsed ultrasound in vitro. *The Journal of the Acoustical Society of America*, 116(5):2832–2842, 2004.

[103] V. Sboros, C. M. Moran, S. D. Pye, and W. N. McDicken. An in vitro study of a microbubble contrast agent using a clinical ultrasound imaging system. *Physics in Medicine & Biology*, 49(1):159–73, 2004.

[104] G. ter Haar, F. A. Duck, and British Institute of Radiology. *The Safe Use of Ultrasound in Medical Diagnosis*. British Institute of Radiology, 2000.

[105] N. de Jong. Mechanical index. *European Journal of Echocardiography*, 3(1):73–74, 2002.

[106] Ed. Preston Roy C. *Output Measurements For Medical Ultrasound*. Springer, 1st edition, 1991.

[107] D. H. Evans and W. N. McDicken. *Doppler ultrasound: physics, instrumentation, and clinical applications*. John Wiley & Sons, 1989.

[108] A. C. Baker. Prediction of non-linear propagation in water due to diagnostic medical ultrasound equipment. *Physics in Medicine & Biology*, 36(11):1457–1464, 1991.

[109] P. D. Krishna, P. M. Shankar, and V. L. Newhouse. Subharmonic generation from ultrasonic contrast agents. *Physics in Medicine & Biology*, 44:681–694, 1999.

[110] S. H. Wang and K. K. Shung. An approach for measuring ultrasonic backscattering from biologicaltissues with focused transducers. *Biomedical Engineering, IEEE Transactions on*, 44(7):549–554, 1997.

[111] J. J. Faran Jr. Sound scattering by solid cylinders and spheres. *The Journal of the Acoustical Society of America*, 23:405, 1951.

[112] R. Hickling. Analysis of echoes from a solid elastic sphere in water. *The Journal of the Acoustical Society of America*, 34:1582, 1962.

[113] Mairead B. Butler, David H. Thomas, Stephen D. Pye, Carmel M. Moran, W. Norman McDicken, and Vassilis Sboros. The acoustic response from individual attached and unattached rigid shelled microbubbles. *Applied Physics Letters*, 93(22):223906–3, 2008.

[114] M. B. Butler, V. Sboros, C. M. Moran, J. Ross, V. Koutsos, W. N. McDicken, and S. Pye. P5B-9 investigation of the response of attached biSphere microbubbles to ultrasound. In *Ultrasonics Symposium, 2007 IEEE*, pages 2219–2222, 2007.

[115] L. Rayleigh. Pressure due to collapse of bubbles. *Phil. Mag*, 94, 1917.

[116] K. Tsiglifis. *Numerical simulation of bubble dynamics in response to acoustic disturbances*. PhD thesis, University of Thessaly, 2007.

[117] M. Postema, A. Bouakaz, Chien Ting Chin, and N. de Jong. Simulations and measurements of optical images of insonified ultrasound contrast microbubbles. *Ultrasonics, Ferroelectrics and Frequency Control, IEEE Transactions on*, 50(5):523–536, 2003.

[118] L. Hoff, P. C. Sontum, and J. M. Hovem. Oscillations of polymeric microbubbles: Effect of the encapsulating shell. *The Journal of the Acoustical Society of America*, 107:2272, 2000.

[119] D. E. Goertz, N. de Jong, and A. F. W. van der Steen. Attenuation and size distribution measurements of definity and manipulated definity populations. *Ultrasound in Medicine & Biology*, 33(9):1376–1388, 2007.

[120] K. Cheung, O. Couture, P.D. Bevan, P.N. Burns, and F.S. Foster. The effect of bubble size distribution and driving frequency on the "subharmonic" response from definity microbubbles. In *Ultrasonics Symposium, 2005 IEEE*, volume 2, pages 850–853, 2005.

[121] C.M. Moran, J.A. Ross, C. Cunningham, M. Butler, T. Anderson, D. Newby, K.A.A. Fox, and W.N. McDicken. Manufacture and acoustical characterisation of a high-frequency contrast agent for targeting applications. *Ultrasound in Medicine & Biology*, 32(3):421–428, 2006.

[122] D. B. Khismatullin. Resonance frequency of microbubbles: Effect of viscosity. *The Journal of the Acoustical Society of America*, 116(3):1463–1473, 2004.

[123] A. Jain, M. Murty, and P. Flynn. Data clustering: A review. *ACM Computing Surveys*, 31(3), 1999.

[124] L N. Hand and J. D. Finch. *Analytical Mechanics*. Cambridge University Press, 1998.

[125] D. E. Kruse and K. W. Ferrara. A new imaging strategy using wideband transient response of ultrasound contrast agents. *Ultrasonics, Ferroelectrics and Frequency Control, IEEE Transactions on*, 52(8):1320–1329, 2005.

[126] N. de Jong, A. Bouakaz, and F. J. Ten Cate. Contrast harmonic imaging. *Ultrasonics*, 40(1-8):567–573, 2002.

[127] S. Hilgenfeldt, D. Lohse, and M. Zomack. Sound scattering and localized heat deposition of pulse-driven microbubbles. *The Journal of the Acoustical Society of America*, 107:3530, 2000.

[128] L. Hoff. Nonlinear response of sonazoid. numerical simulations ofpulse-inversion and subharmonics. In *Ultrasonics Symposium, 2000 IEEE*, volume 2, 2000.

[129] C. C. Church. The effects of an elastic solid surface layer on the radial pulsations of gas bubbles. *The Journal of the Acoustical Society of America*, 97:1510, 1995.

[130] J. Lazewatsky, M. Kagan, and J.A. Barrett. The effect of dilution medium on the measurement of in-vitro properties of ultrasound contrast agents. In *Ultrasonics Symposium, 1999 IEEE*, volume 2, pages 1737–1742, 1999.

[131] K.E. Morgan, J.S. Allen, J.E. Chomas, P.A. Dayton, and K.W. Ferrara. Experimental and theoretical analysis of individual contrast agent behavior. In *Ultrasonics Symposium, 1999 IEEE*, volume 2, pages 1685–1688, 1999.

[132] Yang Sun, D.E. Kruse, P.A. Dayton, and K.W. Ferrara. High-frequency dynamics of ultrasound contrast agents. *Ultrasonics, Ferroelectrics and Frequency Control, IEEE Transactions on*, 52(11):1981–1991, 2005.

[133] S.M. van der Meer, M. Versluis, D. Lohse, C.T. Chin, A. Bouakaz, and N. de Jong. The resonance frequency of SonoVue/spl trade/ as observed by high-speed optical imaging. In *Ultrasonics Symposium, 2004 IEEE*, volume 1, pages 343–345, 2004.

[134] S. Zhao, K. W. Ferrara, and P. A. Dayton. Asymmetric oscillation of adherent targeted ultrasound contrast agents. *Applied Physics Letters*, 87:134103, 2005.

[135] M. Postema, P. Marmottant, C. T. Lance, S. Hilgenfeldt, and N. Jong. Ultrasound-induced microbubble coalescence. *Ultrasound in Medicine & Biology*, 30(10):1337–1344, 2004.

[136] E. G. M. Pelssers, C. Stuart, and G. J. Fleer. Single particle optical sizing (SPOS). i. design of an improved SPOS instrument and application to stable dispersions. get the document, find related information or use other SFX services. *J. Colloid Interface Sci*, 137:350–361, 1990.

[137] C. F. Caskey, D. E. Kruse, P. A. Dayton, T. K. Kitano, and K. W. Ferrara. Microbubble oscillation in tubes with diameters of 12, 25, and 195 microns. *Applied Physics Letters*, 88:033902, 2006.

[138] J. Besag and P. Clifford. Generalized monte carlo significance tests. *Biometrika*, 76(4):633–642, 1989.

[139] A. C. Hope. A simplified monte carlo significance test procedure. *Journal of the Royal Statistical Society, Series B*, 30(3):582–598, 1968.

[140] A. Bouakaz and N. de Jong. WFUMB safety symposium on echo-contrast agents: Nature and types of ultrasound contrast agents. *Ultrasound in Medicine & Biology*, 33(2):187–196, 2007.

[141] P. Dayton, K. Morgan, M. Allietta, A. Klibanov, G. Brandenburger, and K. Ferrara. Simultaneous optical and acoustical observations of contrast agents. In *Ultrasonics Symposium, 1997 IEEE*, volume 2, pages 1583–1591, 1997.

[142] T. R. Porter and F. Xie. Transient myocardial contrast after initial exposure to diagnostic ultrasound pressures with minute doses of intravenously injected microbubbles demonstration and potential mechanisms. *Circulation*, 92(9):2391–2395, 1995.

[143] G. M. Lanza, K. D. Wallace, M. J. Scott, W. P. Cacheris, D. R. Abendschein, D. H. Christy, A. M. Sharkey, J. G. Miller, P. J. Gaffney, and S. A. Wickline. A novel Site-Targeted ultrasonic contrast agent with broad biomedical application. *Circulation*, 94(12):3334–3340, 1996.

[144] J. R. Lindner, J. Song, F. Xu, A. L. Klibanov, K. Singbartl, K. Ley, and S. Kaul. *Noninvasive Ultrasound Imaging of Inflammation Using Microbubbles Targeted to Activated Leukocytes*, volume 102. Am Heart Assoc, 2000.

[145] J. G. Riess. Fluorocarbon-based injectable gaseous microbubbles for diagnosis and therapy. *Current Opinion in Colloid & Interface Science*, 8(3):259–266, 2003.

[146] C. T. Chin and P. N. Burns. Investigation of the effects of microbubble shell disruption on population scattering and implications for modeling contrast agent behavior. *Ultrasonics, Ferroelectrics and Frequency Control, IEEE Transactions on*, 51(3):286–292, 2004.

[147] N. Kamiyama, F. Moriyasu, Y. Mine, and Y. Goto. Analysis of flash echo from contrast agent for designing optimal ultrasound diagnostic systems. *Ultrasound in Medicine & Biology*, 25(3):411–420, 1999.

[148] M. S. Plesset and T. P. Mitchell. On the stability of the spherical shape of a vapor cavity in a liquid. *Applied Mathematics*, pages 419–430, 1954.

[149] M. D. Wei, PhD Skyba, M. D. Firschke, PhD Jayaweera, M. D. Lindner, and M. D. Kaul. Interactions between microbubbles and ultrasound: In vitro and in vivo observations. *Journal of the American College of Cardiology*, 29(5):1081–1088, 1997.

[150] Harold Becher and Peter N Burns. *Handbook of Contrast Echocardiography: Left Ventricular Function and Myocardial Perfusion*. Springer, 1st edition, 2000.

[151] W. T. Shi and F. Forsberg. Ultrasonic characterization of the nonlinear properties of contrast microbubbles. *Ultrasound in Medicine & Biology*, 26(1):93–104, 2000.

[152] W. D. OBrien. Ultrasoundbiophysics mechanisms. *Progress in biophysics and molecular biology*, 93(1-3):212–255, 2007.

[153] V. Uhlendorf and C. Hoffmann. Nonlinear acoustical response of coated microbubbles in diagnosticultrasound. In *Ultrasonics Symposium, 1994 IEEE*, volume 3, 1994.

[154] F. Forsberg, Y. Wu, I. R. Makin, W. Wang, and M. A. Wheatley. Quantitative acoustic characterization of a new surfactant-based ultrasound contrast agent. *Ultrasound in Medicine & Biology*, 23(8):1201, 1997.

[155] J. N. Marsh, M. S. Hughes, C. S. Hall, S. H. Lewis, R. L. Trousil, G. H. Brandenburger, H. Levene, and J. G. Miller. Frequency and concentration dependence of the backscatter coefficient of the ultrasound contrast agent albunex. *The Journal of the Acoustical Society of America*, 104:1654, 1998.

[156] K. Sarkar, W. T. Shi, D. Chatterjee, and F. Forsberg. Characterization of ultrasound contrast microbubbles using in vitro experiments and viscous and viscoelastic interface models for encapsulation. *The Journal of the Acoustical Society of America*, 118:539, 2005.

[157] V. Sboros, C. A. MacDonald, S. D. Pye, C. M. Moran, J. Gomatam, and W. N. McDicken. The dependence of ultrasound contrast agents backscatter on acoustic pressure: theory versus experiment. *Ultrasonics*, 40(1-8):579–583, 2002.

[158] J. Guan, T. J. Matula, and M. Averkiou. Imaging the destruction of individual ultrasound contrast microbubbles with diagnostic ultrasound. *Acoustics Research Letters Online*, 5:165, 2004.

[159] E. Biagi, L. Breschi, E. Vannacci, and L. Masotti. Stable and transient subharmonic emissions from isolated contrast agent microbubbles. *Ultrasonics, Ferroelectrics and Frequency Control, IEEE Transactions on*, 54(3):480–497, 2007.

[160] H. J. Vos, F. Guidi, E. Boni, and P. Tortoli. Method for microbubble characterization using primary radiation force. *Ultrasonics, Ferroelectrics and Frequency Control, IEEE Transactions on*, 54(7):1333, 2007.

[161] J. J. Hwang and D. H. Simpson. *Two pulse technique for ultrasonic harmonic imaging*. US Patent 5,951,478, 1999.

[162] R. J. Eckersley, C. T. Chin, and P. N. Burns. Optimising phase and amplitude modulation schemes for imaging microbubble contrast agents at low acoustic power. *Ultrasound in Medicine & Biology*, 31(2):213–219, 2005.

[163] Victor Mor-Avi, Enrico G. Caiani, Keith A. Collins, Claudia E. Korcarz, James E. Bednarz, and Roberto M. Lang. Combined assessment of myocardial perfusion and regional left ventricular function by analysis of Contrast-Enhanced power modulation images. *Circulation*, 104(3):352–357, 2001.

[164] George A. Brock-Fisher, Mckee D. Poland, and Patrick G. Rafter. Means for increasing sensitivity in non-linear ultrasound imaging systems, 1996. U.S. Classification: 12866202 ; International Classification: A61B 800.

[165] George A Brock-Fisher. Contrast agent imaging with suppression of nonlinear tissue response, 2002. U.S. Classification: 600/458 ; International Classification: A61B 814.